UNIVERSITY OF CALIFORNIA SAN DIEGO

Atmosphere-Ocean Momentum Exchange by Extra-Tropical Storms

A dissertation submitted in partial satisfaction of the
requirements for the degree
Doctor of Philosophy

in

Oceanography

by

Momme Claus Hell

Committee in charge:

Sarah T. Gille, Co-Chair
Arthur J. Miller, Co-Chair
Bruce D. Cornuelle
Ian Eisenman
Jan Kleissl
Mark Merrifield

2020

The dissertation of Momme Claus Hell is approved, and it is acceptable in quality and form for publication on microfilm and electronically:

_____

_____

_____

_____

_____
Co-Chair

_____
Co-Chair

University of California San Diego

2020

DEDICATION

To my parents, who cultivated my curiosities from the beginning.

TABLE OF CONTENTS

LIST OF FIGURES

LIST OF TABLES

ACKNOWLEDGEMENTS

How did I end up pursuing a Ph.D. in Physical Oceanography at Scripps? One could say it was a semi-random walk. In hindsight, it might not have been that random, but who can tell if there is only one realization.

I grew up in the mids between nowhere and two marginal seas in northern Germany. Before the internet brought the world into my room, there was nothing more interesting to do than go outside. Flying a kite over gently sloped green fields, or staring at my dad as he navigated the small sailing boat through hours of pouring rain, probably did its part in my choice of education. Living on a boat during a few weeks in summer makes you realize that the ocean surface is always moving, winds are not constant, and the weather forecast in the LW radio determines if there is a rough sea next day or not. It turns out, that is a good zeroth-order summary of my Ph.D., which I knew even before I knew what a Ph.D. was. It just took another 20 years to write it down in a formal and condensed thesis, so that adults appreciate what a teenager can observe. I thank my parents and my sister for the endless support throughout my life, wherever I am and whatever I do, and for their continued effort to get me out of the house once I got internet.

The 25 years spent in one or the other educational institution left their marks on me. I had a few great teachers and mentors through high school and college. They helped me with my *Bildungsweg*, an un-translational expression that points out that education is more than acquiring knowledge and skills. Rather, it is essentially something that never ends and is not quantifiable.

My Ph.D. was not a single person's effort. With years of support from my advisors, my committee, and many other academic mentors, it just comes into place similar to a spider web that appears overnight. I gratefully thank my advisors, Art, Sarah, and Bruce. Art, thanks for your welcoming way, letting me go on my semi-random walk, and having my back when needed. I would have walked away if I hadn't met you. Sarah, thanks for the great advice on what to do and on any random question I had. It sometimes took a minute, or sometimes a month, or maybe years to understand its value. Bruce, you pushed the door open to a messy world of never-ending

optimization. Thanks for sending me down those loopholes. My thesis wouldn't be what it is without your help, and that is just fine. Thanks to all three of you for your patience when I came up with another idea every week, even though you knew it'd be just another distraction on my semi-random walk. I also want to thank Peter for involving me in the RIS project, funding me, and letting me see everything through my eyes. The same accounts for Mark, who simply had faith in my work before I had it. You made my grad student life way more comfortable.

Grad school is way more than just your advisors. There was a lot of other advice from mentors that made the last five years worth a two Ph.Ds. They were just there, whatever happened, or not. Thank you, Tapio, for all the support throughout the years. You helped me to get to the west coast, and also let me go. Without running into you, I would have never thought of going to the (great) United States of America or even of doing a Ph.D. at all. Thanks, Larry, for teaching a bit of fluid mechanics, insisting on changing perspective without losing the objective, and helping me swim against the flow. Thanks, Ian and Skipper, for introducing me to Scripps and having free Netscape capsules for at least some time. You also made me very drunk one night at Walter Munk's house without even realizing it. But who cares, since you always walk home on four feet anyways. And, thanks to Myrl for just being you. Everywhere my interests are going, your mind was there before. You told me that there is not enough time to learn, but also there is no way to overstrain your mind. Thanks to the polar group for adopting me for some time, giving me coffee and cakes on Friday mornings, even though I've never been on 79 North nor work with ICEsat2.

I have to mention all the other friends and grad students I met in San Diego. Thanks to the sandcastle occupants for experiencing all German grumpiness levels, and all friends that made my life way more enjoyable over the last five years. Many of them are overseas, or where ever they are on their semi-random walks. I met them during college, master, and summer schools in one or the other European mountain range. One day, some of them will maybe all be at one happy place, hiding from wildfires, floods, and heatwaves.

Science is a construct, made by people, and hence it is the result of human interaction

rather than pure logical extrapolation. I can't end these acknowledgments without thanking Scripps Institution of Oceanography as an institution of people. SIO is more than a brand, a collection of buildings, or an instructional unit. It is an "integrated systems of rules that structure social interactions"[1]. Many examples of discoveries in SIO history have shown that knowledge is local and new science appears from a social web that cannot be replaced by virtual meetings or singular excellence. All the best in maintaining and extending this institution of science, diversity, and integrity against all threats and enemies that there may come.

Chapter 2, in full, is a reprint of the material as it appears in the Journal of Atmospheric and Oceanic Technology, Hell, M. C., B. D. Cornuelle, S. T. Gille, A. J. Miller, and P. D. Bromirski, AMS, 2019. The dissertation/thesis author was the primary investigator and author of this paper.

Chapter 3, in full, is a reprint of the material as it appears in Journal of Geophysical Research: Oceans, Hell, M. C., Gille, S. T., Cornuelle, B., Miller, A. J., Bromirski, P. D., Crawford, A. D, Wiley, 2020. The dissertation/thesis author was the primary investigator and author of this paper.

Chapter 4, in part, is currently being prepared for submission for publication of the material: A simple model of swell generation under extra-tropical storms, Hell, M. C., Ayet, A, Chapron, B. The dissertation/thesis author was the primary investigator and author of this material.

Chapter 5, in full, has been submitted for publication of the material as it may appear in Journal of Climate, Hell, M. C., Cornuelle, B. D., Gille, S. T., Lutsko, N. J., AMS, 2020. The dissertation/thesis author was the primary investigator and author of this paper.

[1] Hodgson (2015 p. 501), Journal of Institutional Economics (2015), 11: 3, 497–505

VITA

2012	B. Sc. in Physics of the Earth System - Meteorology, Oceanography and Geophysics (*Magna Cum Laude*) Christian-Albrecht-University Kiel, Germany
2015	M. Sc. in Atmospheric and Climate Science (*Summa Cum Laude*) Swiss Federal Institute of Technology Zürich - Zürich, Switzerland
2015 - 2020	Graduate Student Researcher Scripps Institute of Oceanography University of California San Diego
2020	Doctor of Philosophy in Physical Oceanography Scripps Institution of Oceanography University of California San Diego

PUBLICATIONS

Atmospheric zonal flows and blocks from the perspective of Rossby-beta hydraulics
Hell, M. C. and Armi, L.
Journal of Atmospheric Science, *in preparation*

About the relation of moving fetches and swell fronts generated under extra-tropical cylones
Hell, M. C., Ayet, A, Chapron, B., Cournuelle B. D.
Journal of Geophysical Research: Oceans, *in preparation*

Time-varying empirical probability densities of Southern Ocean surface winds: Leading modes linked to SAM, the annual cycle, and product biases
Hell, M. C., Cornuelle, B. D., Gille, S. T., Lutsko, N. J.
Journal of Climate, *submitted*

Estimating Southern Ocean storm position with seismic observations
Hell, M. C., Gille, S. T., Cornuelle, B., Miller, A. J., Bromirski, P. D., Crawford, A. D
Journal of Geophysical Research: Oceans, **2020**, 125, e2019JC015898.

Atmospheric Circulation Response to Episodic Arctic Warming in an Idealized Model
Hell, M. C., Schneider, T., Li, C.
Journal of Atmospheric Science, **2019**, 77 (2): 531–549.

Identifying ocean swell generation events from Ross Ice Shelf seismic data
Hell, M. C., B. D. Cornuelle, S. T. Gille, A. J. Miller, and P. D. Bromirski
Journal of Atmospheric and Ocean Technology, **2019**, 36 (11): 2171–2189.

Integrated Observations of Global Surface Winds, Currents, and Waves: Requirements and Challenges for the Next Decade
Villas Bôas, A. B., and Coauthors including Hell, M. C.
Frontiers of Marine Science, **2019**, 6

Arctic change and possible influence on mid-latitude climate and weather: A US CLIVAR white paper
Cohen, J., and Coauthors including Hell, M. C.
US clivar Rep, **2018**

Investigation of the atmospheric mechanisms related to the autumn sea ice and winter circulation link in the Northern Hemisphere
King, M.P., Hell, M. C., and Keenlyside, N.
Climate Dynamics, **2016**, 46: 1185.

ABSTRACT OF THE DISSERTATION

Atmosphere-Ocean Momentum Exchange by Extra-Tropical Storms

by

Momme Claus Hell

Doctor of Philosophy in Oceanography

University of California San Diego, 2020

Sarah T. Gille, Co-Chair
Arthur J. Miller, Co-Chair

The Earth's climate warms with increasing greenhouse gases in the atmosphere. The Southern Ocean (SO) mixed layer dampens the speed and intensity of global warming by storing a large fraction of the anthropogenic CO_2 and heat. However, the mechanisms and hence the SO's future capabilities to store heat and CO_2 remain uncertain. This thesis aims to understand better how atmospheric wind forcing drives mid-latitude mixed-layer variability. It focuses on the wind forcing and swell generation under extra-tropical cyclones and links these to the large-scale atmospheric circulation.

A supervised machine learning method is developed to characterize events in wave's

spectrograms of Ross Ice Shelf seismometers. The events are used to show that wave origins under SO storms are systematically displaced compared to the highest wind speeds. This result is further explored by extending the optimization method to multiple wave buoys in the North Pacific to derive a common set of parameters that describe the origin and intensity of waves. The triangulated wave source location motivates developing an idealized swell generation model that mimics the time and spatially varying wind forcing as a 2D-Gaussian distribution that moves with a constant speed over the ocean. It shows that the location where wind stress and wave forcing are the strongest is not the same as the identified swell source location because non-linear wave-wave interaction prohibits wave dispersion. The Gaussian moving wind model reveals the sensitivity of the wave's spectral energy and peak frequency on extreme winds under storms because they influence the spatial gradients of the moving wind field.

Finally, an SVD decomposition of surface wind probability distributions from reanalysis and scatterometer winds over the SO is used to link changes in the extremes of the joint wind and stress probability density functions over the SO to the Southern Annular Mode. This reveals how the planetary-scale circulation drives surface wind extremes through storm intensity over the SO and suggests how the swell climate, related surface stress pattern, and mixed-layer ventilation may change with a drifting large-scale atmospheric circulation.

Chapter 1

Introduction

Earth's climate is undergoing rapid but long foreseen changes (Charney Report, National Research Council, 1979). Weather and climate began to change notably over the short period of my life, and they will continue to respond to more and more greenhouse gases in the atmosphere (Keeling and Keeling, 2017). This is creating tremendous pressure on the Earth's population to mitigate and adapt to changing weather, droughts, heatwaves, rising sea levels, and a general shifting climate. Even though there is no doubt that the Earth's surface temperature will continue to rise throughout my lifetime, the International Panel for Climate Change (IPCC) identified key factors that limit our ability to estimate the speed and path of global warming (Flato et al., 2014). The largest uncertainty in global climate projections comes from future human behavior. Humans have to understand that their existence is irrevocably intertwined with Earth and that only changes in their behavior can flatten the impact of the current and future generations (Weber, 2019).

To make our path of mitigation and adaption to a changing climate the least disruptive for us, we must improve our understanding of the Earth's climate system and its variability in unprecedented detail. This goes beyond understanding the climate system's long-term response to global warming, i.e., climate sensitivity (first done in the Charney Report and many others) since adaptation strategies rely on accurate prediction of the internal variability on sub-seasonal

to decadal-scales. Limiting damage from extreme weather or fire, efficient planning of renewable power, and crop management are the most prominent areas where an improved medium-range weather forecast is valuable.

The ocean plays a critical role in these mitigation and adaptation strategies. While the troposphere's decorrelation timescale generally does not exceed ten days, the ocean is a reservoir for long-term memory and the climate system's predictability. Because the upper 2.5 meters of the ocean has the same heat capacity as the integrated atmospheric column, the ocean's upper 50-100 meters can easily impact the atmospheric circulation on all timescales. It is estimated that the upper ocean has stored about 50% of the additional heat and 90% of anthropogenic CO_2 since the start of industrialization. If the ocean's ability to damp global warming is altered a few percent, this has notable consequences for global warming (Vaughan et al., 2013).

The global warming trend, as well as sub-seasonal to decadal variability, can be accessed with state-of-the-art Earth System Models (CMIP models, Taylor et al., 2012; Haarsma et al., 2016) or sub-seasonal to seasonal weather prediction models. But as these hyper-complex Earth System Models allow us to study all kinds of feedback between the atmosphere and ocean, they have one substantial weakness. They cannot explicitly resolve atmosphere-ocean interaction processes because these processes are on scales orders of magnitudes smaller than the resolution of climate or weather forecast models. They rely on parametrizations of the often turbulent, small-scale processes, like ocean waves or turbulent heat fluxes, which then feed back on the larger-scale (Cavaleri et al., 2012; Lorenz, 1969).

Climate models were initially designed to reproduce the general response of the sea surface temperature to greenhouse gas changes. The models mostly agree on the energy balance constraints of the Earth system. However, they still disagree in many fundamental aspects of Earth's circulation (Stroeve et al., 2012; Chang et al., 2012; Knutti and Sedláček, 2013; Masato et al., 2013; Barnes and Polvani, 2013, 2015; Huang et al., 2020; Zappa et al., 2013; Pithan et al., 2016; Lin et al., 2020, and many others). The discrepancies stem from the fact that the Earth

system is inherently chaotic, so misrepresented small-scale processes lead to biases even on the largest scales (Lorenz, 1963, 1967). Hence, our use of numerical models for predicting weather and climate relies on accurate understanding and parametrizations of small scale processes at the atmosphere-ocean interface.

Air-sea interaction is complex, ranges over many scales, and often involves turbulence (sec. 1.1). And because the air-sea exchange is generally the strongest under extreme weather, our understanding of air-sea fluxes is still hampered by limited observations. To circumvent this problem, one can use *remote constraints* on air-sea exchange statistics. As I will show, these constraints can be used to improve our understanding of remote observations and hence of the process itself.

This thesis aims to improve our understanding of how the atmosphere and ocean interact. It focuses on momentum transfer from the large-scale atmospheric circulation to ocean surface waves. Chapters 2, 3 and 4 show how remote swell observations can be used to understand swell generation better. Chapter 5 shows how angular momentum conservation can be used as boundary conditions for air-sea interaction.

1.1 Air-Sea interaction - a double boundary layer problem

The atmosphere-ocean interface sits between the ocean and the atmospheric boundary layer. Because there is friction between the fluids (no-slip condition), the atmosphere establishes a mechanical boundary layer (BL), where the boundary influences the fluid motion. The time-averaged velocity profile in the boundary layer is approximated by the "law of the wall" (von Kármán, 1931; Garratt, 1992, first published in the Nachrichten von der Gesellschaft der Wissenschaften zu Gottingen, 1930). This scaling law says the flow must be continuous between zero at the wall and the outer flow above and requires a logarithmic velocity profile for neutrally stratified turbulent flow. The turbulent flow at a high Reynolds number Re cascades momentum

from the atmosphere's interior to the surface, such that the boundary layer height generally depends on Re.

The atmospheric boundary layer (ABL) is more complex than this simple scaling law because it is rarelt never neutrally stratified. Radiative, turbulent, and sensible heat fluxes across the surface, as well as heat release from condensation, change the static stability of the ABL, which affects the turbulence and hence the resulting velocity profile (Monin and Obukhov, 1954). This changes the boundary layer turbulence's efficiency in transporting momentum to the boundary and other properties, like heat or moisture, away from the boundary.

These two fundamental relations – the law of the wall and its modifications due to stratification – lead to the universally used bulk formulas that describe fluxes of heat, momentum, and any other properties through the surface. In the most general form, they can be written as

$$\boldsymbol{\tau} = \rho \; C_D \; \Delta \boldsymbol{u} \; |\Delta \boldsymbol{u}| \tag{1.1}$$

$$H_0 = \rho \; c_p \; C_H \; \Delta \theta_v \; |\Delta \boldsymbol{u}| \tag{1.2}$$

$$E_0 = \rho \; C_W \; \Delta q \; |\Delta \boldsymbol{u}|, \tag{1.3}$$

where $\boldsymbol{\tau}$ is the surface stress vector, H_0 the turbulent sensible heat flux, E_0 the turbulent latent heat flux, ρ the density of air, $\boldsymbol{u}$ the wind vector, c_p the heat capacity of air, θ_v the virtual potential temperature, and q the specific humidity (Garratt, 1992). The capital delta Δ describes the finite difference of the quantity between two reference heights. The exchange coefficients for drag C_D, heat C_H, and water vapor C_W generally depend on the static stability of the boundary layer, the surface roughness, and the wind speed (Garratt, 1992). The simplicity of these bulk flux formulae put the complexity of the ABL in the formulation of these drag coefficients. They can be found in every climate or weather prediction model, such that any modeled interaction between atmosphere and ocean uses these equations.

The ocean boundary layer has a different character. The upper ocean's Re is generally

smaller, but still turbulent flow. An (observable) mechanical boundary layer in the ocean develops because the higher velocities appear at the interface rather than in the interior. Following the drag formulas (1.1), the momentum that is advected from the atmospheric interior to the boundary leads to stress at the interface that – in this simple framework – might push the ocean surface in the direction of the stress (Ferrari and Wunsch, 2010, "wind work"). It results in a velocity shear profile with decreasing velocities to the interior of the ocean, which will, with time, give rise to Ekman dynamics (Gill, 1982, chap.9).

However, this attractive and simplified picture of momentum transfer to the ocean has two fundamental flaws. First, the bulk flux formulas are tuned to a reference level of ten meters above the surface, due to the World Meteorological Organization (WMO) conventions. Second, and more importantly, the lower boundary is thought to be fixed, which means the surface does not move or react to perturbation by surface stress. That is not what one observes when one inspects the ocean surface. Because the ocean surface is an interface between two fluids and is highly susceptible to perturbations from both sides, it is permanently in motion. A flat ocean only appears when there is no wind, hence no turbulent fluxes, and the presence of wind instantaneously generates waves at the interface.

Waves excite orbital motions that decay in both fluids away from the surface. Because the atmosphere is so highly turbulent ($Re \approx 10^4$), atmospheric orbital motions are hard to observe. Instead, ocean surface waves appear for the ABL as a roughness pattern with characteristic scales, i.e., its wavenumber spectrum, that interact with the turbulence spectrum of the ABL.

Wave growth comes from continuous winds that transfer energy from the turbulent ABL to the ocean. Even though wave growth is still not completely understood, it is thought to be the result of instabilities and resonances of the surface that interact with the ABL (Phillips (1957); Miles (1957, 1960), or chap. 3 in Janssen (2004) and chap. 12 in Kinsman (2013)). For wave numbers lower than the spectral peak, the surface interacts with the corresponding scales of the ABL turbulence. Because the ABL is continuously forced by the large-scale atmospheric flow,

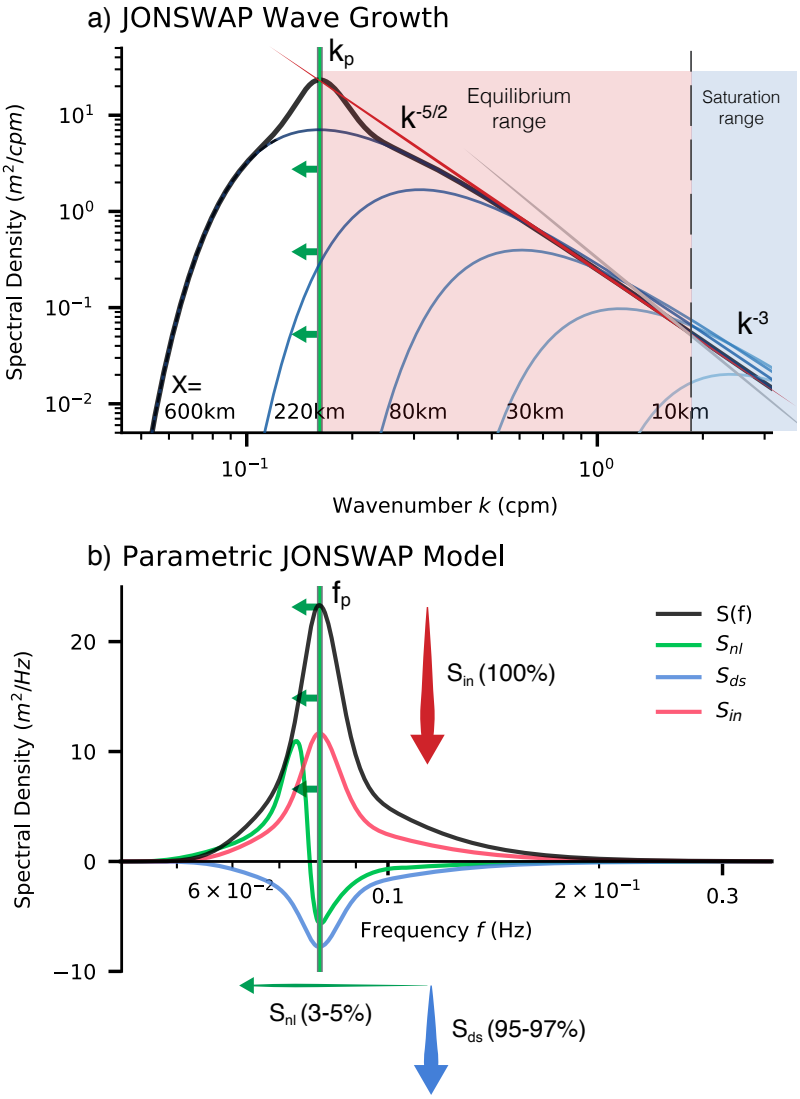

Figure 1.1: Schematic of wave growth and energy transfer from the atmosphere to the Ocean, adapted from Hasselmann (1974); Hasselmann et al. (1976); Elfouhaily et al. (1997); Phillips (1985). (a) JONSWAP spectrum for various fetch lengths with $U_{10} = 15m/s$ (blue lines). The estimated equilibrium range is is shown in red shading with a characteristic slope of $k^{5/2}$ (thin red line) and the saturation range in light blue with a characteristic slope of k^{-3} (thin gray line). The peak wave number k_p is indicated as a green line that migrates with longer fetch X to lower frequencies. (b) JONSWAP spectrum for a $X = 600$ km fetch (black), with the estimated energy input S_{in} (red), dissipation S_{ds} (blue), and wave-wave energy flux (green).

a resonance-like interaction between the ABL turbulence and the surface waves leads to wave growth for short waves. This continuous growth of wave energy in the "equilibrium range" is balanced by dissipation and interaction with waves of other scales (Phillips, 1958, Fig.1.1a,). Most of the energy in this range is gained from the atmosphere and is directly dissipated to the ocean (90-95%, Fig. 1.1b, blue arrow), while the rest goes into four-wave interactions (Hasselmann and Hasselmann, 1985, Fig. 1.1b, green arrow). This wave-wave interaction leads to a flux of wave-energy to longer wavelengths, which migrates the peak wave number to longer scales (Fig. 1.1, short green arrows). This shift of the peak frequency by weak wave-wave interactions of a small fraction of the total momentum flux drives the generation of swell and the growth of the characteristic wave spectrum (Pierson and Moskowitz, 1964; Hasselmann et al., 1973; Elfouhaily et al., 1997, Fig. 1.1a, blue lines). The shift of the wave's peak frequency also feeds back to ABL turbulence (Ayet et al., 2020; Zou et al., 2020).

Any significant atmosphere-ocean momentum transfer involves surface waves. The largest proportion of the ABL momentum is likely transferred through the equilibrium range to Reynolds-stress at the ocean surface. Other processes, like wave breaking and Stokes drift, can also significantly affect the momentum transfer (Cavaleri et al., 2012). All processes mentioned above depend on the frequency boundaries of the equilibrium range and hence on the wave spectrum's shape. The wave spectrum, in turn, is the result of prior wind forcing and hence introduces a non-local condition to the local turbulent fluxes, via changes in the transfer coefficient.

When models calculate surface stress and other turbulent fluxes, the complex processes outlined above are entirely parameterized in the drag coefficients C_D, C_H and C_W (Fairall et al., 2003; Edson et al., 2013). Any modification of the ABL by stratification, changes in surface wave roughness, and changes in the ABL turbulence balances modify C_d by some functional relation. But because wave growth and associated momentum transfer introduce non-local information, the estimation of surface fluxes from local conditions remains challenging. State-of-the-art flux formulas can account for surface roughness changes from short waves by using wave age (c_p/U_{10}),

assuming the wave's response time is generally much faster than model time steps (Edson et al., 2013). However, the effects of long waves and mature wave spectra are not considered in any of these parametrizations. One can speculate that non-local wave conditions are important in high and mature seas with extreme surface winds and strong fluxes of heat, momentum, and CO_2 (eq.1.1 Schulz et al., 2012; Ogle et al., 2018; Tamsitt et al., 2020). Even though extreme fluxes are modeled in flux formulas vi a squared dependence on the wind shear, there is essentially no validation of these estimates for extreme seas, or under extra-tropical storms.

Surface waves are the source of the momentum that drives the upper ocean circulation. However, the cascade of processes that connects the momentum dissipated by short waves, Stokes drift, or wave breaking to the ocean circulation remains unclear. Once the momentum crosses the interface, it somehow must end up in the much larger inertial scale, which is where most of the energy in the wake of a storm is observed (Ferrari and Wunsch, 2008). This thesis characterizes the scales of the surface wind and wave forcing to improve the understanding of how the surface wave momentum interacts with the many other processes in the upper ocean (Villas Bôas et al., 2019).

1.2 Large-scale drivers of synoptic-scale atmosphere-ocean interaction and weather extremes

Strong zonal winds near the tropopause dominate the atmospheric mid-latitude flow. Any changes in these zonal jets' variability and position significantly impact local climate, precipitation, and extreme weather by changing weather regimes (Held and Soden, 2006; Mitchell et al., 1987). The jets' variability also impacts atmosphere-ocean interaction through changes on the synoptic scale. The statistics of the small-scale processes mentioned above (sec. 1.1) are related to the large-scale changes in the atmosphere and ocean, which is implied in research about atmosphere-ocean coupling. For example, "The atmospheric Bridge" (Alexander et al., 2002),

"D-O events" (Stocker and Johnsen, 2003), trends in SAM drive trends in the SO circulation (Thompson et al., 2000; Thompson and Solomon, 2002) and so on. However, little is known about how larger-scale climate phenomena like the Northern or Southern Annular Mode (NAM, SAM), El ñino, the Pacific Decadal Oscillation, and other climate indices perturb the unresolved and under observed small scales of air-sea exchange. Hence, a better understanding of how the mid-latitude atmospheric circulation couples with small scales at the interface may reveal how planetary-scale phenomena drive atmosphere-ocean coupling.

1.2.1 Angular Momentum in the Atmosphere

All chapters of this thesis address the distribution and conservation of atmospheric angular momentum (AM). Earth's mid-latitudes are baroclinically unstable and create Rossby waves (Eady, 1949; Phillips, 1954; Charney and Stern, 1962) that transport relative angular momentum from the tropics to the high latitudes. That is, they transport AM in the region they are created (Peixoto and Oort (1992), chapt. 11 and Schneider (2006), and therein). Their momentum flux convergence leads to an excess angular momentum in mid-latitudes that has to be balanced by surface friction; otherwise, the zonal flow would infinitely accelerate. It is convenient to analyze the atmospheric angular momentum balance in the zonal mean because it simplifies the equations of motions along the axis of symmetry (Andrews et al., 1987, , for example). In the absence of form drag by topography, the instantaneous vertical integral of the Eulerian, zonal-mean momentum equation in mid-latitudes is

$$\frac{\partial}{\partial t}\langle[u]\rangle - f\langle[v]\rangle \;+\; \frac{\partial}{\partial y}\left(\langle[u][v]\rangle + \langle[u^*v^*]\rangle\right) \;= [\mathcal{F}_{tur}], \tag{1.4}$$

with u and v as zonal and meridional wind, f as the Coriolis parameter and $\mathcal{F}_{tur}$ as the turbulent drag in the surface boundary layer (Andrews et al., 1987). The zonal mean is written as $[\cdot]$, its deviations as $(\cdot)^*$ and the vertical integral as $\langle\cdot\rangle$. Eq. (1.4) shows that (eastward) zonal-mean

surface drag – the mechanical force on the ocean – balances the residual of four components in the zonal mean flow (Fig. 1.2): the acceleration of the zonal mean zonal wind, the southward advection of planetary momentum, and the divergence of momentum fluxes either by the mean flow or by eddies. Hence, the zonal mean mechanical work of the atmosphere on the ocean, called surface stress or surface friction, is related to large-scale atmospheric circulation processes.

In a steady-state, and for small Rossby radius, the vertical integral of eq. 1.4 can be written as

$$\partial_y \overline{\langle [u^* v^*] \rangle} = \left[\bar{\mathcal{F}}_{tur} \right], \qquad [m/s^2] \tag{1.5}$$

where the over-bar indicates a time-mean over typical Rossby wave scales ($\approx$ 5 days). Hence in the time-mean and in the absence of continents, the momentum flux convergence of the atmospheric column is the dominant source of zonal stress on the ocean surface.

In the Southern Hemisphere (SH) mid-latitudes, the ocean covers more than 99% of the surface (35°S to 63°S, Fig.1.2), similar to idealized GCM circulations where no continents are present. This is especially true for the small latitude band of Drake's Passage, where the balances eq. 1.4 and eq. 1.5 should be valid because there are no continents (Chapter 5).

1.3 Storms as catalysts of air-sea exchange

Mid-latitude storms funnel excess angular momentum to the synoptic-scale (Lorenz, 1955). The synoptic scale is about 1000 km and $3-5$ days and dominates the variability in mid-latitudes. Synoptic storms are depicted using several frameworks in the literature (review in Schultz et al., 2018), four of which are summarized here:

- **Low-pressure systems:** In contrast to high-pressure systems, storms are anomalies of low surface pressure that carry warm and cold fronts. This highly descriptive view of storms

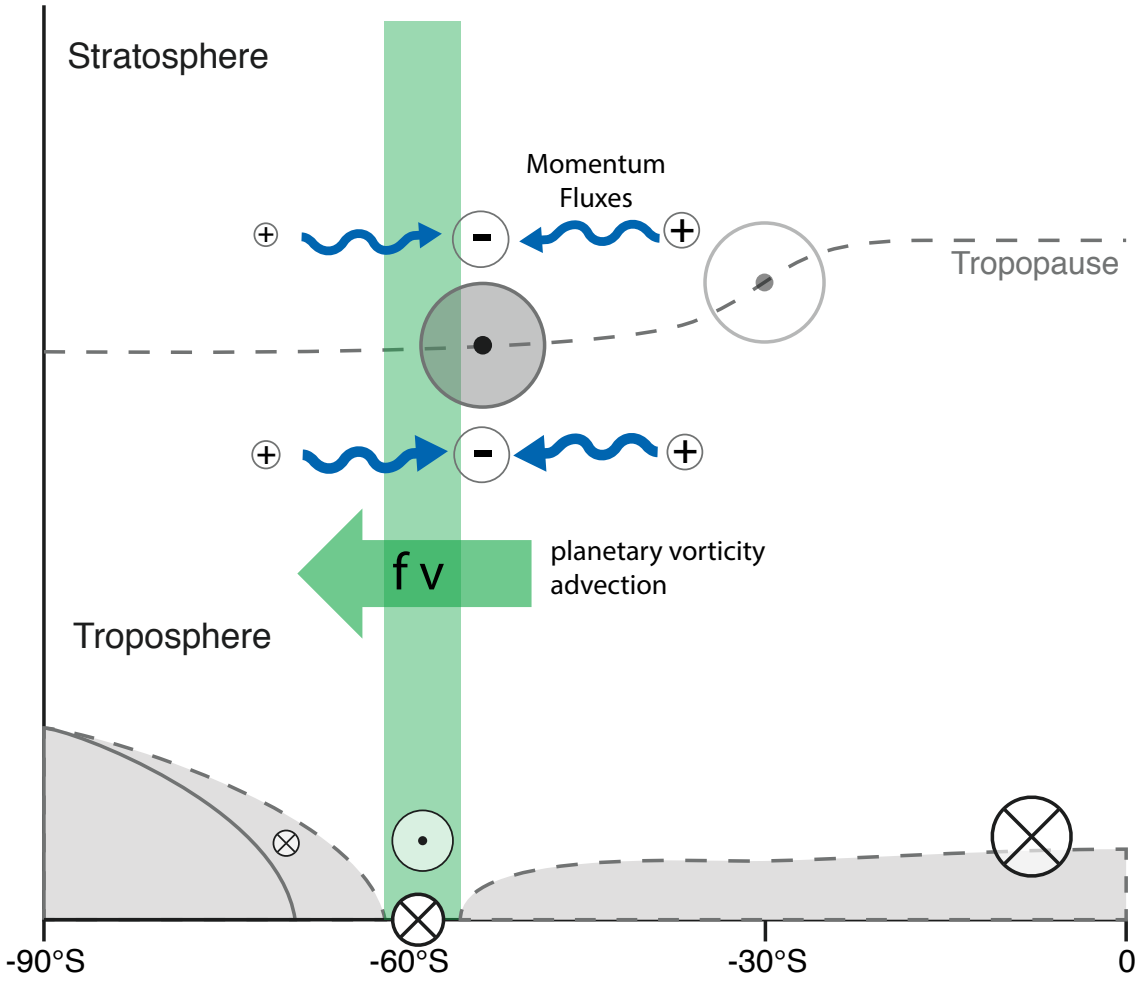

Figure 1.2: Atmospheric momentum balance in the Southern Hemisphere. Circles with a dot indicate strong zonal wind out of the page, while crosses show wind into the page. The blue arrows indicate angular-momentum fluxes from areas of wave breaking (divergence, pluses) to areas of wave generation (convergence, minuses). The green shading shows the atmospheric column over the drake passage where eq. 1.4 would be valid. The green arrow indicates the vertical integrated Eulerian momentum flux $f\ \langle [v] \rangle$. Dashed gray lines illustrate the mountain ranges in the latitude band.

and their lifecycle is used in the daily weather forecast and often referred to as the Bergen School of Meteorology (Bjerknes, 1919; Bjerknes and Solberg, 1921, 1922).

- **Baroclinic eddies:** With the development of a theory for the general atmospheric circulation, storms were referred to as *eddies* to describe their dynamical purpose better. These eddies must be understood in contrast to the mean flow, as they drive and balance the mean flow (Charney, 1947; Eady, 1949). Eddy-mean flow analysis is commonly used to explain changes in large-scale flow (Charney and Stern, 1962; Andrews and McIntyre, 1978; Edmon et al., 1980). Because this approach only describes eddy statistics in a highly chaotic circulation, it fails to explain individual storm strength or even their surface fields.

- **Extra-tropical cyclones:** Rossby-Ertel Potential Vorticity (PV) describes storms as PV anomalies on isentropic surfaces (Namias, 1939; Hoskins et al., 1985). It allows detailed analysis of the synoptic evolution of storms (cyclo-genesis and cyclo-lysis) in PV rather than pressure, which directly links synoptic and mesoscale phenomena to the general circulation (Simmons and Hoskins, 1978; Wernli et al., 2002; Schemm and Wernli, 2014, and others).

- **Noise in a honey world:** Because the time and spatial scales of large-scale oceanography are much larger than storms, their impact on the ocean is supposed to average out, such that the time and spatial mean of these "eddies" is the signal of interest. However, the assumption that single storms have only randomized impacts on the ocean can only be held when the ocean is modeled as a coarse-grained, large-scale flow (a "honey ocean" due to its large viscosity). However, there is observational and modeling evidence that air-sea coupling on the synoptic-scale has a significant non-random impact on the upper ocean and the large-scale circulation (Schulz et al., 2012; Ogle et al., 2018; Tamsitt et al., 2020; Giglio et al., 2017; White et al., 2017; Bharti et al., 2019).

Different communities of Earth science tend to one or the other of these mental models. This thesis can be seen as a pledge to use them all and harvest the synergies from analyzing air-sea

exchange from different perspectives on extra-tropical storms.

1.4 Ocean Swell as the residue of intense Air-Sea exchange

Swell waves have a unique role in linking atmospheric dynamics to upper-ocean variability. Because strong air-sea exchange is the result of turbulent processes that are sparsely observed (sec. 1.1), our understanding relies on remote observations that have to be interpreted with inverse models to reconstruct statistics of air-sea exchange. This is, for example, used in scatterometry.

Swell waves can be interpreted as another remote observation of air-sea exchange because they result from the continuous process of wave growth (Fig. 1.1). They are an encoded signal of the momentum fluxes that depend on the wind forcing scales and are altered by interacting with their carrying medium. After leaving its source, the wave energy spreads out and ages (measured by frequency dispersion). When it is observed at a location far remote from its origin, the waves' spectral shape still contains information about the source's intensity, location, and time.

Understanding swell is much more than just predicting local surf. Swell is an observation of intense remote air-sea exchange that shapes mixed-layer ventilation and long-term climate trends. Changes in the swell climate may result from changes in synoptic dynamics over the ocean. These dynamics are tied to the development of the low-level PV as well as to the large-scale flow.

Chapter 2

Identifying ocean swell generation events from Ross Ice Shelf seismic data

Abstract

Strong surface winds under extra-tropical cyclones exert intense surface stresses on the ocean that lead to upper ocean mixing, intensified heat fluxes and the generation of waves, that, over time, lead to swell waves (longer than 10 s period) that travel long distances. Because low-frequency swell propagates faster than high-frequency swell, the frequency dependence of swell arrival times at a measurement site can be used to infer the distance and time that the wave has traveled from its generation site. This study presents a methodology that employs spectrograms of ocean swell from point observations on the Ross Ice Shelf (RIS) to verify the position of high wind speed areas over the Southern Ocean, and therefore of extra-tropical cyclones. The focus here is on the implementation and robustness of the methodology in order to lay the groundwork for future broad application to verify Southern Ocean storm positions from atmospheric reanalysis data. The method developed here combines linear swell dispersion with a parametric wave model to construct a time and frequency-dependent model of the dispersed swell arrivals in spectrograms

of seismic observations on the RIS. A two-step optimization procedure (deep learning) of gradient descent and Monte Carlo sampling allows detailed estimates of the parameter distributions, with robust estimates of swell origins. Median uncertainties of swell source locations are 450 km in radial distance and 2 hours in time. The uncertainties are derived from RIS observations and the model, rather than an assumed distribution. This method is an example of supervised machine learning informed by physical first principles in order to facilitate parameter interpretation in the physical domain.

2.1 Introduction

Strong winds associated with extra-tropical cyclones act on the ocean surface and generate surface gravity waves. These waves propagate long distances and are observed as swell (Snodgrass et al., 1966). Long swell waves (in the range between $0.03 - 0.8$ Hz) can travel across ocean basins with minimal attenuation (Snodgrass et al., 1966). Because wave dispersion depends on frequency, swell observed at distant locations contains information about its position and time of generation. The idea of tracking storms using swell was first shown by Munk (1947) and by Barber and Ursell (1948). The objective of this study is to establish a methodology to use modern swell observations to learn about conditions at the swell's source region as well as the travel path of the swell.

The locations where swell waves originate experience intense atmosphere-ocean interaction. Some of the strongest events occur in the Southern Ocean, where the observing system is sparse and storm systems are not well characterized by direct observation (e.g. Bourassa et al., 2013). Strong surface winds lead to intense air-sea fluxes of heat, momentum and CO_2, with potential implications for ocean circulation changes and the ocean uptake of anthropogenic heat and CO_2 in the Southern Ocean (SO, Swart et al., 2018; Rintoul, 2018; Marshall et al., 2016; Munday and Zhai, 2017; Gruber et al., 2019).

Ocean swell spectra are routinely generated from autonomous wave buoy observations, GPS sensors, or seafloor pressure sensors (Munk et al., 1963; Collard et al., 2009; Delpey et al., 2010; O'Reilly et al., 2016), and they have also been observed by land-based seismic stations when swell interacts with the coast (Bromirski et al., 1999). The time series of swell arrivals at an observation site can be converted to a time evolving power spectrum, known as a spectrogram. Each set of swell arrivals detected in a spectrogram is related to the surface wind at the storm (Pierson and Moskowitz, 1964; Hasselmann et al., 1973; Elfouhaily et al., 1997) and can, as we will show, be interpreted as a *remote* observation of the storm itself.

This study adopts a unique approach by using seismic data collected not on land, but instead on a floating ice shelf, as part of the Ross Ice Shelf (RIS) Vibration Project (Wiens et al., 2014; Bromirski et al., 2017). The data from the RIS allow us to compute an extensive series of high-resolution spectrograms of surface gravity waves, similar to conventional wave observations. We use these data as a training set to develop a new method to characterize ocean swell observations.

Feature comparison in geophysical data is often challenging because the observations are noisy, and the models are too simple. As we outline below, the combination of optimization and Monte Carlo methods enables us to improve our model understanding of the data, while we use the model to identify the relevant data. This is a "machine learning" approach that is constrained by physical laws, with the benefit that it generates uncertainties based on the data and the model, rather than assuming an a priori uncertainty distribution (Marone, 2018).

We present a method to compare characteristic patterns in seismic spectrograms with a parametric model that is constrained by the physics of ocean gravity waves. We first briefly describe the physical background that motivates the model (section 2.2) and introduce the data set (section 2.3). Then, we introduce the governing cost function (section 2.4), the model (section 2.5), and the data preparation (section 2.6). The actual fitting procedure is explained in section 2.7, and its performance is shown in section 2.8 and discussed in sec-

tion 2.9. The developed code for this analysis will be publicly available in a github repository (`https://github.com/mochell/stormy_forerunners`) after completing the project.

2.2 Waves across the Pacific - physical background

Observations on the RIS record storm-induced swell events (Fig. 2.1), much like previously reported observations along coastlines (Munk and Snodgrass, 1957; Snodgrass et al., 1966). The gestalt of these coherent packages of swell energy is shaped by three processes:

1. The dispersion of deep water waves means longer waves travel faster, such that the longest wave generated by a storm arrives first (Munk, 1947; Barber and Ursell, 1948; Snodgrass et al., 1966; Gallet and Young, 2014). At any point in the ocean, an observer who records the arrival time of waves of different frequencies can estimate both the time of origin and the distance traveled, assuming all waves come from the same source. For continuous observations, like those provided by the RIS seismometers, the succession of wave arrivals results in a sloped line in the wave spectra (Fig. 2.1). The sloped line of these dispersed wave events is an indirect measure of the radial distance to the origin of the waves.

2. The spectrogram and it's shape are related to winds in the wave generation region. There is extensive literature about ocean wave spectra. See for example the compendial overviews of Massel (1996, 3.2.) or Elfouhaily et al. (1997). The most commonly used parametric models are the Pierson-Moskowitz (here after PM) spectrum for a fully developed sea or the Joint North Sea Wave Project (JONSWAP) spectrum (Fig. 2.2, Pierson and Moskowitz, 1964; Phillips, 1985; Hasselmann et al., 1973, 1976). Both models are possible functional forms for this optimization problem. The advantage of the JONSWAP spectrum is that it is more flexible and is not limited to fully developed seas. It also relates the peak frequency

f_m and the amplitude parameter α to the non-dimensional fetch $\tilde{X}$

$$f_m = \frac{3.5\ g}{U_{10}} \tilde{X}^{-0.33}, \tag{2.1}$$

$$\alpha = 0.033 \left(\frac{f_m U_{10}}{g} \right)^{0.67} = 0.076\ \tilde{X}^{-0.22}, \tag{2.2}$$

with

$$\tilde{X} = \frac{g\ X}{U_{10}^2}, \tag{2.3}$$

where X is the fetch in meters (defined as the horizontal distance over which wave-generating winds are able to act), U_{10} is the 10-meter wind speed over that area, and g is the acceleration due the Earth's gravity (Hasselmann et al., 1973). The JONSWAP relations can be inverted to infer speed and fetch at the location of the storm from the wave spectrum parameters α and f_m, detected at a remote location (Pierson and Moskowitz, 1964; Hasselmann et al., 1976). Both PM and JONSWAP spectra are based on theories of wave generation by winds (Phillips, 1957; Miles, 1957, 1960), and their only difference stems from the JONSWAP model's inclusion of additional parameters that vanish under the assumption of a fully developed sea (see section 2.5, Fig. 2.2 and Massel, 1996, 3.2.).

3. When swell travels into sea ice, it can be damped or reflected (Fox and Squire, 1994; Squire, 2007; Vaughan et al., 2009). While low-frequency swell waves travel through sea-ice and are detected in seismic records on the RIS (typical periods of about 15 seconds, Fig. 2.1 shading, Collard et al., 2009; Cathles et al., 2009; Bromirski et al., 2010; MacAyeal et al., 2009), higher frequencies are strongly damped (periods of about 10 seconds and shorter, Kohout et al., 2014; Collins et al., 2015; Ardhuin et al., 2016). It is hypothesized that damping of incident swell energy by sea ice helps to maintain the overall ice shelf stability (Squire et al., 1994/ed; MacAyeal et al., 2006; Robinson and Haskell, 1990; Lipovsky, 2018;

Massom et al., 2018). However, a validated parametric model of sea-ice induced damping does not exist and is therefore not included in our formulation of the model (section 2.5).

The first two processes, wave dispersion and spectral shape, are used to construct our model for the optimization procedure. The model is constrained by prior physical knowledge about the processes that we aim to investigate. If the residual differences between model and data share common features between multiple events, then the misfit can potentially be attributed to physical processes that are not represented in the model, such as the attenuation due to sea ice.

Most ocean swell observations show a superposition of locally and remotely generated waves (Rapizo et al., 2015; O'Reilly et al., 2016). In contrast, the swell spectra observed on the RIS are only due to remotely generated waves because swell generation in the proximity of the ice shelf is suppressed by sea ice. Even in summer, when melting may produce open water areas close to the RIS, any locally-generated waves are shorter than the remotely-generated swell. Wave generation at the observation site is not possible because the observations are made on the ice shelf rather than in the ocean. The fact that RIS data highlight the impacts from remote storm activity in the Southern Ocean makes them unique.

On the other hand, RIS seismic records may be the result of processes that are absent in open ocean observations, such as interactions with sea ice, topography and currents, or the ice shelf itself. The intent of this discussion of the method is to first set these additional complexities aside and, in a second step, assess whether RIS-specific processes can explain the deviation of the observations compared to the model function. This model function represents a physical hypothesis for the evolving ocean wave spectra; however, we do not expect it to apply exactly in each individual case.

2.3 Seismic Observations in the Ross Ice Shelf

The Ross Ice Shelf Vibration Project was a field campaign carried out from October 2014 to December 2016 with the goal of recording the Ross Ice Shelf response to gravity wave impacts for geophysical, glaciological and oceanographic purposes (Wiens et al., 2014). To investigate the RIS response to gravity wave forcing, a network of 28 seismic stations recorded 2 years of continuous vertical and horizontal displacements at each station (Fig. 2.3). The sampling rate was either 100 Hz or 200 Hz depending on the instrument configurations at each station (Bromirski et al., 2015). Data were archived in accordance with IRIS (Incorporated Research Institutions for Seismology, www.iris.edu) standards for seismic data. The 3 stations closest to the front (DR01, DR02 and DR03) recorded the highest amplitude response for swell waves, and are thus used for the analysis presented in this paper, because they are expected to have the largest signal-to-noise ratios for swell waves.

The processing is as follows. First, the 100 Hz or 200 Hz time series are averaged to 1 Hz, because the timescales of interest (waves with frequencies less than 0.1 Hz) are perfectly resolved by 1 Hz sampling, and the much smaller data volume makes processing more efficient.

Second, the recorded time series are corrected for the frequency-dependent response function of the seismometer. The 1 Hz time series is deconvolved with the instrument response function which is a cosine window ($f_1 = 10^{-4}$ Hz, $f_2 = 2 \times 10^{-4}$ Hz, $f_3 = 0.4$ Hz, $f_4 = 0.5$ Hz). The resulting displacement time series are pre-whitened by taking the second derivative in time to generate a time series of acceleration in m s^{-2}. Peaks in the acceleration time series are removed if they deviate from the mean by more than 10 standard deviations; any resulting gaps are filled by linear interpolation. Less than 0.1% of the data are removed from the time series, and the removals have no effect on the model estimate.

After these preliminary adjustments, a spectrogram is calculated at each station using the 1-Hz averaged time series for a shifting window discrete Fourier transformation. To calculate

spectrograms, data are first split into segments of 20 minutes duration, with 50% overlap. Each segment is detrended and fast Fourier transformed to produce periodograms. Spectral estimates are computed at hourly time increments, by averaging periodograms from eleven 20-minute segments centered around 1 hour time steps (i.e. spanning a total time period of 120 minutes), while a Hanning window was applied to each segment. The 20-minute segment length determines the frequency resolution with a lowest frequency of $1/1200$ Hz. The resulting 2-year spectrogram for DR01 is shown in Figure 2.1. (Spectrograms for DR02 and DR03 appear indistinguishable from DR01.)

2.4 Cost function definition

Our next objective is to optimally fit the swell arrivals detected in the spectrograms to a model based on the JONSWAP spectrum by adjusting the free parameters in the model. We do this via a non-linear minimization method performed on a global cost function

$$\Phi = J_d + J_m, \tag{2.4}$$

which is the sum of the data cost function J_d and the model cost function J_m (known as ridge or lasso regularization). The data cost function J_d is the sum of the squared difference between data $\boldsymbol{D}$ and model $\boldsymbol{M}(\boldsymbol{p})$, with $\boldsymbol{p}$ being the model parameter, multiplied by the weight function $\boldsymbol{w}$ at each point

$$J_d = \| (\boldsymbol{D} - \boldsymbol{M})\boldsymbol{w} \|^2 . \tag{2.5}$$

The model cost function J_m is the sum of squares of the normalized parameter values

$$J_m = \left\| \frac{\boldsymbol{p_0} - \boldsymbol{p}}{\boldsymbol{p_\sigma}} \right\|^2, \tag{2.6}$$

where $\boldsymbol{p}$ is a set of function parameters for optimization, $\boldsymbol{p_0}$ represents the initial guesses of the parameter vector, and $\boldsymbol{p_\sigma}$ is the corresponding prior error estimate (Appendix).

The model cost function allows us to optimize function parameters $\boldsymbol{p}$, while taking account of prior estimates of uncertainty in the parameters $\boldsymbol{p}_\sigma$. In order to allow a wider range of parameter values, the prior uncertainty is artificially set to be large. Too small values for $\boldsymbol{p}_\sigma$ result in an overweighting of the costs due to the parameters, resulting in overly conservative model behavior that is more likely to remain close to the initial conditions. The following sections explain the parametric model (section 2.5), and the data preparation and weight function (sec. 2.6).

2.5 Model description

The model $\boldsymbol{M}_S(f,t)$ is compared against the data $\boldsymbol{D}(f,t)$ at each iteration of the minimization procedure. The model has a time component $M_T(t)$ and a spectral component $S(f)$ that are both described here. We assume a separable model $M_s(f,t) = S(f)M_T(t)$.

1. The spectral part of the model $S(f)$ is based on open-ocean swell spectra of a fully developed sea (section 2.2). The JONSWAP spectrum (Hasselmann et al., 1973; Massel, 1996, 3.2.3.2, p. 94, eq. 3.81) is reformulated as

$$S(f) = \hat{\alpha}\,(2\pi f)^{-5} \exp\left[-\chi\left(\frac{f}{f_m}\right)^{-4}\right]\gamma^{\delta}, \tag{2.7}$$

$$\delta = \exp\left[-\frac{1}{2}\left(\frac{f-f_m}{\sigma_0 f_m}\right)^2\right], \tag{2.8}$$

where f is the frequency, $\hat{\alpha}$ the amplitude parameter in units of acceleration squared, χ

the non-dimensional stretching term ($\chi = 5/4$ in the standard JONSWAP model), f_m the position of the peak frequency, γ the measure of the height of the peak function, and σ_0 the width of the peak function. We define an amplitude parameter $\hat{\alpha} = g^2\alpha$ such that the first guess of $\hat{\alpha}$ is of order one, while the initial value of α is inferred from the data (see below). This model reverts to the original PM-spectrum when $\hat{\alpha}$ and χ are set to constant values taken from JONSWAP (Hasselmann et al., 1973).

In total, there are 5 free parameters in (4.3.1) and (2.8): the conventional peak parameter f_m and four more parameters $(\chi, \hat{\alpha}, \gamma, \sigma_0)$ to allow for the additional complexity in the seismic data due to the interaction with sea ice and the RIS (sec. 2.2). Other parameters of the JONSWAP spectrum, such as U_{10} and $\tilde{X}$ are not used directly in the model (4.3.1), but can be inferred using the estimated parameters f_m and $\hat{\alpha}$ in equations (2.1 - 2.3).

2. In the time domain, visual inspection of the spectrogram suggests that swell arrivals generally have a relatively sharp leading edge (Fig. 2.4), while their decay varies (Munk and Snodgrass, 1957). This behavior is approximated by the Γ-distribution

$$M_T(\tilde{t}) = \frac{1}{\sigma_t \Gamma(\tilde{t})} \left(\frac{\tilde{t} - \tilde{t}_{peak}}{\sigma_t} \right)^{b-1} e^{-\tilde{t}}, \tag{2.9}$$

with the Γ-function as

$$\Gamma(\tilde{t}) = \int_0^\infty x^{\tilde{t}-1} e^{-x} dx, \tag{2.10}$$

where $\tilde{t} \equiv (t - t_{start})/(t_{end} - t_{start}) = (t - t_{start})/\Delta t$ is the normalized time, with t_{start} being the lower left and t_{end} the upper right corner of the parallelogram (Fig. 2.4a, described in sec. 2.6.1). The dimensionless parameter σ_t is set to 0.07, so that $M_T(\tilde{t})$ in (4.3.2) has a maximum value of order one, such that the only parameter that determines the amplitude is $\hat{\alpha}$. The term $\tilde{t}_{peak}$ represents the location of the peak in time, and b controls the width of the Γ-distribution; both are used for parameter optimization (section 2.7). Figure 2.5a

illustrates $M_T(\tilde{t})$ for default values of $\tilde{t}_{peak}$ and b and for the maximum and minimum values for b, set as constraints for the optimization (Appendix).

3. The time-evolving peak frequency is expressed as a linear function that is informed by the deep-water dispersion relation:

$$f_{peak}(\tilde{t}) = (\tilde{t} - \tilde{t}_0)\, m_{\tilde{t}}, \tag{2.11}$$

where f_{peak} is the peak frequency, $\tilde{t}_0$ is the center of the non-dimensional normalized time axis, and $m_{\tilde{t}}$ is the rate of change in units of Hz. Note that f_{peak} is different from the maximum peak frequency f_m: f_{peak} is peak frequency at each non-dimensional time $\tilde{t}$, while f_m is the maximum of the peak frequencies, i.e. the peak frequency over the whole event.

The rate of change $m_{\tilde{t}}$ and non-dimensional initial time $\tilde{t}_0$ are directly related to the distance and time estimates (Snodgrass et al., 1966; Munk and Snodgrass, 1957; Barber and Ursell, 1948). The inversion of (2.11) gives a relation for $\tilde{t}_{peak}(f)$, which is inserted into (4.3.2).

The Γ-distribution M_T, the JONSWAP spectrum S, and the linear slope equation (2.11) yield a two-dimensional model of swell arrivals:

$$\boldsymbol{M}_S(f,\tilde{t}) = S(f) M_T(\tilde{t}) \tag{2.12}$$

$$= \hat{\alpha} \frac{2}{0.7(2\pi)^5} \frac{1}{\Gamma(\tilde{t}) f^5} \;\; \gamma^{\delta} \;\; \left[\frac{\tilde{t} - f m_t^{-1} + \tilde{t}_0}{0.07} \right]^{b-1} \exp\left[-\chi \left(\frac{f}{f_m} \right)^{-4} - \tilde{t} \right], \tag{2.13}$$

$$\text{with} \quad \delta = \exp\left[-\frac{1}{2} \left(\frac{f - f_m}{\sigma_0 f_m} \right)^2 \right]. \tag{2.14}$$

Equation 4.3.4 has $N_{var} = 8$ fitting parameters: $\boldsymbol{p} = \left\{ \hat{\alpha}, \chi, f_m, m_f, \tilde{t}_0, b, \gamma, \sigma_0 \right\}^T$. These parameters are the basis for the non-linear optimization procedure described in section 2.7, and the sensitivity of the model (4.3.4) to these parameters is shown in Figure 2.5.

2.6 Pre-handling the data

Achieving optimal agreement between the data and the model function requires selection and preliminary correction of the data. This section explains how events are selected and corrected to facilitate non-linear optimization. First, the shape (sub-section 2.6.1) and amplitude (sub-sections 2.6.2 and 2.6.3) of individual events are used to ensure similar signal-to-noise levels. Subsequently the model is fitted to the adjusted data, given a customized set of initial parameters, but without further individual tuning of the model (sec. 2.7).

2.6.1 Selection procedure and masking

The vertical acceleration spectrograms from Stations DR01 to DR03 show about 250 wave events during the 2-year RIS measurement period. (Fig. 2.1 shows the full record for DR01, and supplementary Figures S2 and S3 show the same for DR02 and DR03.) These events are common features in the spectrograms of other stations across the RIS array (Fig. 2.3). Wave events are strongest near the ice shelf front and decay with distance toward the interior of the shelf (Bromirski et al., 2017).

Each event has a characteristic slope, indicating that low-frequency energy arrives before higher frequencies (sec. 2.2). In this analysis, the slopes are identified using an interactive hand picking procedure. An example of this is shown in Fig. 2.4a, in which the wave event (blue shading) is identified by its low- and high-frequency limits (black dots in Fig. 2.4a) and its estimated time-width (green dot in Fig. 2.4a).

The data mask is a parallelogram defined by three values, as follows (Fig. 2.4a, green perimeter). The upper and lower limits are the corresponding frequencies of the black dots, and the tilted sides are twice the temporal separation between the green point and the black middle line. Initial parameters for slope and intersect (section 2.5) are taken from a line centered between the left boundary and the middle line (Fig. 2.4a, red line).

2.6.2 Data weighting

There is additional prior information about the usefulness of the data within the data mask. High amplitudes close to the mask boundary are typically attributed to noise, while data in the center of the domain are likely associated with the selected event. The geometry derived in the previous section is also used to construct a data weighting function defined as

$$\boldsymbol{w} = (\boldsymbol{w}_G + \boldsymbol{w}_G \boldsymbol{w}_D)/2 + w_{floor}, \tag{2.15}$$

where $\boldsymbol{w}_G$ is a geometrical weight that decays from 1 in the center to 0 at the boundary using a Hanning window (Fig. 2.4a, gray contours), $\boldsymbol{w}_D(f, \tilde{t})$ is the spatially smoothed[1] data divided by its maximum value, such that $\boldsymbol{w}_D$ is a matrix that weights high-amplitude data points more strongly. The minimum is $w_{floor} = 10^{-6}$. The total weight $\boldsymbol{w}$ can vary between w_{floor} and $w_{floor} + 1$ and is constructed such that data points at the boundary, especially of high amplitude, are down-weighted, while data points in the center with high amplitudes are up-weighted. The noise floor value w_{floor} represents the general uncertainty in the data that is estimated from the uncertainty in the spectral estimate. The uncertainty of the spectral estimate is derived from sub-sampling described in section 2.3.

2.6.3 Noise handling

Within the parallelogram-shaped mask used to select data from the spectrogram, higher noise levels often occur at lower frequencies (Fig. 2.4a, below 0.05 Hz and in supplementary Figure S4). Here, noise is accounted for by fitting a noise model prior to fitting the actual model. The noise model follows an exponential decay of the form

$$M_n(f) = \beta_n \ e^{-\tau_n f}, \tag{2.16}$$

[1]The data are smoothed by using a running mean with a width that is 0.2% of the size of the data matrix

where β_n and τ_n are free parameters. The difference between the masked data $\tilde{D}$ and M_n defines the noise cost function

$$||\Phi_n||^2 = \left|\left|\left(\frac{\tilde{\boldsymbol{D}}}{\sigma_{\boldsymbol{D}}} - \boldsymbol{M}_n\right)\boldsymbol{w}_{noise}\right|\right|^2, \tag{2.17}$$

with $\tilde{D}$ as the masked acceleration spectrum, normalized by its standard deviation

$$\sigma_{\boldsymbol{D}} = \left[\frac{1}{N-1}\sum_i^N \left(\tilde{D}_i - \overline{\tilde{D}}\right)^2\right]^{1/2}. \tag{2.18}$$

The model weighting function $\boldsymbol{w}_{noise} = 1 - \boldsymbol{w}_G + w_{floor}$ is the opposite of the geometric weight from (2.15) and down-weights data points with high signal-to-noise ratios, such that (2.16) fits to the background noise rather than the data. The noise cost function (2.17) is minimized for each event individually using the gradient descent methods described in section 2.7. The resulting noise-reduced data matrix

$$\boldsymbol{D} = \frac{\tilde{\boldsymbol{D}}}{\sigma_{\boldsymbol{D}}} - \boldsymbol{M}_n \tag{2.19}$$

is used for the actual model fitting. It contains the noise-corrected and normalized data for each event. The geometric data selection and the constructed weight function focus the non-linear optimization on individual dispersed wave events, while down-weighting neighboring events and the seasonally changing low-frequency noise due to sea-ice (Fig. 2.1). The data selection process generates a collection of 250 similar events that can be well characterized by the model function (sec. 2.4).

2.7 Non-linear fitting

The optimization method changes the parameters $\boldsymbol{p}$ of the model function $\boldsymbol{M}$ to minimize the cost function $\boldsymbol{\Phi}(\boldsymbol{M}(\boldsymbol{p}), \boldsymbol{p})$ eq.(2.6). The smallest value of $\boldsymbol{\Phi}$ that the method finds represents the best fit between model and data and is only dependent on a set of parameters $\boldsymbol{p}$.

2.7.1 Choice of initial values

The initial values of these parameters are either set to a standard value or are informed by the geometrical form of the data mask (Fig. 2.4b). The first guess dispersion slope m_f and non-dimensional initial time $\tilde{t}_0$ are taken from the masking procedure (red line in Fig. 2.4a), and the peak frequency f_m is initially set to the peak frequency of the masked data. The initial f_m is also used to calculate $\hat{\alpha}(\alpha)$ from (2.2) assuming a wind speed of 10 m s^{-1}. Other parameters that modify the spectral shape are initialized from the JONSWAP spectrum standard values (Hasselmann et al., 1973), which are estimated based on open ocean observations.

An overview of the sensitivity to parameter values is shown in Figure 2.5. The initial parameters and their limits are set to physically plausible ranges (see Appendix, Table 2.1 and Massel, 1996), such that they allow a wide range of possible values, and equally importantly, also adjust to the noise level. In high noise cases, the model is often unrealistic and results in a poor fit characterized by a large fractional error (sec. 2.8.1). These cases can be identified and are not considered for further analysis (sec. 2.8.3).

2.7.2 Optimization Method and Estimations of Uncertainty

The non-linear model (eq. 4.3.4) is optimized using a two-stage fitting algorithm to minimize the cost function $\mathbf{\Phi}$ (eq. 2.6). In the first stage, the model is initialized with $\boldsymbol{p}_0$ and then changed using the Levenberg-Marquardt Algorithm (LM, damped least-squares, Newville et al., 2014) to find a local minimum of the cost function. The LM algorithm calculates the local gradient in parameter space and moves its next guess of parameters in the direction of the gradient. The iteration terminates if the change of the cost function is small ($< 10^{-15}$), if the change in the independent variables is small, or if the number of iterations exceeds its limit defined as 100 $(n+1)$ n, with n being the length of $\boldsymbol{D}$. We used a gradient method first, rather than a non-linear search, because of its faster convergence to a (local) minimum for a relatively smooth

cost function.

In the second step, a Parallel Tempering Markov-Chain-Monte-Carlo (PTMCMC, Goodman and Weare, 2010; Foreman-Mackey et al., 2013; Earl and Deem, 2005) method is used to further minimize the cost function and to produce an *a posteriori* error distribution for all variables simultaneously. This process is similar to simulated annealing, where the progress toward an optimal solution can only be seen from the average of many iterations rather than from each single iteration (Kirkpatrick et al., 1983). This is a powerful tool in situations in which multiple optimal solutions could exist, as in this problem: even though one origin per wave event is assumed, the uncertainty estimate from PTMCMC is generally capable of capturing several wave events that arrive at the same time.

Each Markov Chain is initialized with the optimal parameters from the steepest descent method, and its first guess is seeded from a random distribution. This chain, often called a walker, goes through 1000 function evaluations, with two different annealing temperatures, but only every second evaluation from the final 75% of this process contributes to the error distribution (750 function evaluations per walker). This is repeated 1000 times in a Monte Carlo sense to create a distribution with 7.5×10^5 data points in the 8-parameter space.

Figure 2.6 shows two examples of co-distributions of two elements of $\boldsymbol{p}$ for the event in Figure 2.4c. (All distributions are shown in Figure S1.) The distributions have clear maxima, which are the optimal values for each parameter. We use the median (blue lines in Figure 2.6) as the best model fit, while half the difference of the 15.87% and 84.13%-quantiles (dashed lines, the width of one standard deviation in a normal distribution) is taken as a simple measure of uncertainty (Newville et al., 2014). The resulting best (median) model fit is shown in Figure 2.4c.

The parameters are assumed to be uncorrelated (Appendix, Fig. S1), with their width being sensitive to the choice of prior uncertainty values (sec. 2.4 and Appendix). However, the co-distribution of the slope $\tilde{t}_0$ and intersect $m_{\tilde{t}}$ parameters shows a correlated error in all observed

cases (Fig. 2.6 panel a). This distribution is converted from the $\tilde{t}_0$-$m_{\tilde{t}}$ space to initial time

$$t_0 = \tilde{t}_0 \, \Delta T + t_{start}, \tag{2.20}$$

and radial distance

$$r_0 = \frac{g}{4\pi \, \Delta T} \, m_{\tilde{t}}, \tag{2.21}$$

with $\Delta t = t_{end} - t_{start}$ (sec. 2.5) and using the deep water dispersion relations (Barber and Ursell, 1948; Munk and Snodgrass, 1957; Snodgrass et al., 1966). The resulting distribution reveals probabilities of wave event origin in time and radial distance and allows us to create probability maps to quantify the likelihood of a specific origin. Figure 2.7 shows these maps of probability in the time and radial distance space (TR-space). They are direct conversions of the observational scatter captured by the PTMCMC method (sec. 2.7). Smaller patches in the TR-space (Fig. 2.7 bottom) correspond with very certain model estimates of events in the observed spectrogram (Fig. 2.7 top), while larger patches in the TR space correspond with less well defined wave events. This ambiguity between a recent nearby event and a distant event from further back in the past can be reduced by using other dependencies in the model and by drawing on extra information about wind events from atmospheric observations and models. The authors plan to address this in future work.

2.8 Performance of the Optimization

2.8.1 Distribution of Fitting Parameters

To compare the eight model parameters consistently we express them as normalized distance computed relative to the prior (sec. 2.4). Figure 2.8 shows the decomposition of the

model cost J_m (2.6) into the cost introduced by each of the eight parameters for the three front stations. The initial cost of each parameter is zero (green line), while the median model cost of the parameter is indicated by the black line.

The distribution of costs due to the parameter adjustment is similar for all parameters and for all stations, with a clear maximum close to zero. Final parameter values close to the initial value suggest that small changes in the parameters are enough to reduce J_d substantially without introducing costs in J_m. However, there are cases for all parameters where the final value deviates from the initial value more substantially. In these cases, the costs in J_m introduced by large parameter adjustments are small compared to the reduction achieved in J_d such that the overall cost Φ is still minimized. This must be the case because the ratio of model to data cost, J_m/J_d rarely exceeds 20% for all fitted cases (Appendix Figure A1). This suggests that, based on gradients in Φ, an efficient minimization can often be effected via small changes in the model parameters, or sometimes through a few larger changes to a subset of parameters. Since the gradient descent method terminates if the number of iterations exceeds its limit, it is possible that regions of parameter space in the direction of small gradients are never explored. However, these are sampled later by the Monte Carlo method.

Parameters that determine the radial distance and initial time are optimized during the minimization procedure. The position of $\tilde{t}_0$ has, in the median, a larger contribution to J_m than other parameters (Fig. 2.8a). That is, in about 85% of all cases, changes in the modeled position were necessary to achieve minimum cost. In contrast, the model slope parameter m_f also adjusts (Fig. 2.8b), but introduces smaller costs, because the manual selection criteria better define its initial values than the position of the initial time (sec. 2.6.1).

Two parameters of the JONSWAP spectrum (γ and σ_0) also introduce noticeable model costs (Fig. 2.8 c and d). Their initial values were manually adjusted away from the standard JONSWAP values (Appendix Fig. A2), because trials that started with standard JONSWAP values reduced the overall quality of the fit (larger fractional errors). In the end, neither the standard

JONSWAP values nor the chosen initial values (Appendix) are the best choices to capture the shape of the observed swell events well. However, an additional free parameter, χ (Fig. 2.8e), that changes the general shape of the spectrum, often remains close to its initial, theoretically well-constrained value of $5/4$ (eq. 4.3.1), as predicted by Hasselmann et al. (1973).

2.8.2 Comparing fitting performance between front stations

The optimization algorithm found 225 events during the 24-month observational period. They occurred at each of the three "front" stations DR01, DR02 and DR03, each about 2 km away from the ice-shelf edge (blue, orange and red dots in Fig. 2.3); common events at all three stations are identified by similar arrival times.

The seismic stations at the RIS ice shelf front are close together ($\approx$ 80 km separations) compared to the distance traveled by the waves ($\approx$ 1500 km). As a result, the incoming wave angles and amplitudes are assumed to be uniform along the ice shelf front. However, the event amplitudes observed at DR01 are systematically larger than at DR02 and DR03 (Fig 2.9a). The difference in amplitude between the stations may be caused by the structure of the ice shelf, and affected by a major rift that separates DR03 and DR01, near DR02. If the amplitude difference were due to the incoming angle of the waves rather than ice-shelf rheology, one would expect more randomly scattered differences between the stations, because the incident waves are expected to come from a wider range of incident angles.

Comparison of other fitted parameters suggests that the same wave events lead to comparable observations at the three RIS-front stations. For example, peak frequencies of common events vary by about 0.02 Hz or less between the three stations (Fig. 2.9b). Austral summer events, that generally have higher peak frequencies, also have a similar observed frequencies at all three front stations. Differences between them are likely due to independent noise or local shelf structure. Peak frequencies lower than 0.04 Hz are mainly observed at DR01, while the same events at DR02 or DR03 rarely fall below 0.04 Hz. Reasons for this could be systematic

differences in the ice shelf front geometry, or crevasses and rifts in the ice shelf between the stations, which are beyond the scope of this study. Aside from this discrepancy, observations show peak frequencies and spectral shapes similar to those in the open ocean, indicating that the RIS response to incident waves maintains properties from the open ocean waves.

The uncertainty in the radial distance estimate, and therefore also the uncertainty in initial time, can vary between the front stations. Figure 2.9c shows the radial distance uncertainty for all events (defined as half the distance between the 15.87 and 84.13 percentiles of the uncertainty distribution (sec. 2.7.2, Fig. 2.6a black dashed lines). The difference in radial distance uncertainty between the stations is generally larger for larger uncertainties. For many events, DR02 and DR03 have smaller uncertainties than DR01. These events are often, but not always, selected by the criterion of smallest fractional error, which is explained in the the next section (black half dots Fig. 2.9c).

2.8.3 Measures of fit

The performance of the model optimization is assessed quantitatively using the fractional error between data and model

$$e_{frac} = \frac{J_d}{\sum_i^N D_i^2 \, w_i^2}, \tag{2.22}$$

with J_d identifying the cost, D_i the data, and w_i the specific weight for each point. A good model fit, i.e. low fractional errors, means that Φ is small compared to the data. The distributions of e_{frac} for DR01-DR03 are shown in Figure 2.10. Events with a $e_{frac} \leq 0.6$ are defined as successfully fitted (gray area in Fig. 2.10a). This represents between 74% and 84% of all events (varying between stations) considered in this analysis. Values of $e_{frac} > 0.6$ are interpreted as unsuccessful fits and represent between 16% and 26% of all cases considered.

The signal-to-noise ratio is generally the same for all three stations (the median e_{frac} is

0.43 for DR01 and DR03 and 0.37 for DR02), with a large variance between individual events (Fig. 2.10b). For each swell event, the comparison of e_{frac} varies widely between stations, with no systematic preference for one station. Higher values of e_{frac} correspond to a less successful explanation of the data by the model, or higher noise levels.

Most events have a small fractional error at all stations (green area in Figure 2.10b), but there are a number of events in which one station performs substantially better than its neighboring stations (gray areas). To optimize the use of multiple observations, we compile a set of 208 events taken from DR01–03 (88% of all initial events, black half dots) based on events when e_{frac} is smallest. Events with a fractional error larger than 0.6 at all three stations are not considered (upper right area in Figure 2.10b). By considering all three stations, we identify 35 additional events that would not meet our fractional error criterion for DR01 alone. The use of the three stations reduces the mean fractional error from 0.42 to 0.26, with the disadvantage that no common attenuation transfer function can be determined for the events (Fig. 2.10a and Fig. 2.9a).

As shown in Fig. 2.10b, the fractional error for the same swell event varies between the different observation sites, although differences between the three spectrograms are often difficult to distinguish by eye. (Compare Figure 2.1 with Figure S2 and Figure S3 .) The fractional error criterion provides a single metric for evaluating all observed events and when we adopt a conservative threshold for the fractional error, it allows rigorous quality control of the data.

The optimization procedure identified swell arrivals at the RIS based on physical constraints that are parameterized in the model (section 2.5). If data and model are similar, then the fractional error is small, and we conclude that the observed event is indeed related to incident, dispersed swell events. In contrast, a large fractional error suggests a weaker signal-to-noise ratio, implying for example that additional processes have distorted the incident wave events, that more than one storm is contributing to forcing the swell, or that the observed features are not generated by dispersed swell waves.

2.8.4 Observed storm activity and wave spectra

Figure 2.11a shows the radial distance estimate, number of storms per degree latitude, radial uncertainty, and time uncertainty. Events with $e_{frac} \leq 0.6$ are black (Fig. 2.9c, green area), while the remaining events are gray. The vertical lines show one radial-distance standard deviation, inferred from the uncertainty estimate (sec. 2.7.2), while the standard deviation in time is not plotted because it is too small. The distributions of both radial distance and time uncertainty are shown in Fig. 2.11c-d.

The observed RIS events suggest that storm-generated packets of surface waves arrive at the ice shelf more than twice per week (2.3 events per week, all dots in Fig. 2.11a). In total, 208 of these events meet the criterion of a well identified/well fitted event ($e_{frac} < 0.6$, section 2.7). The majority (187 events, 1.8/week) originate from the Southern Ocean, and we see no distinct seasonality in their occurrence rate. The rest (28 events) originate from the sub-tropics or the Northern Hemisphere in boreal winter, and are generated from tropical or extra-tropical cyclones in the North Pacific (Cathles et al., 2009; MacAyeal et al., 2006; Bromirski et al., 2010). The median estimated uncertainty is about 110 km in space and 2 hours in time (Fig. 2.11c and d). These uncertainties are small enough to allow the wave events to be matched to specific high wind speed areas under storms that are often related to fronts or warm conveyor belts (Schemm and Wernli, 2014), as we will explain in future work.

2.9 Summary and conclusions

Ocean swell is commonly observed along coastlines and its origin is a long-standing question in oceanography (Munk, 1947). Swell is known to be generated by strong winds associated with extra-tropical cyclones, but the exact positions of swell generation have not been well characterized. Areas of swell generation are hypothesized to correspond to areas of upper ocean mixing and often of intense air-sea heat exchange. Here, instead of relying on in situ

observations, we have developed a methodology to analyze the remote observation of ocean swell. This can be used to infer characteristics of the swell generation region.

To assess the locations of high surface winds over the Southern Ocean we developed a method that combines spectral analysis from time series of swell arrivals at a single point with a parametric model optimization. The parametric model used here represents a combination of the linearized dispersion relation and the JONSWAP spectrum. These models are based on different descriptions of the wave source: while the inversion of the linear dispersion relation assumes a source that is a delta function in space and time, the JONSWAP spectrum uses a wind speed over a given length or for a given time (Munk, 1947; Hasselmann et al., 1973). Both concepts are approximations to reality, as is their combination (eq. 4.3.4). The resulting 8-parameter model provides a framework to describe the (point) origin and spectra of swell observed by a single point observation.

The systematic comparison of the parametric model with the wave events allows us to quantitatively test models of generation and propagation. It provides a framework for learning about the underlying physical process, rather than letting the machine construct a model of the observations without physical constraints (often referred to as unsupervised machine learning, Nature Geoscience editorial board, 2019).

A two-stage optimization procedure is used to fit the model to the data, by exploring the full 8-parameter space simultaneously. In our procedure, we first apply a gradient descent method and subsequently carry out Monte Carlo sampling to ensure a) that the gradient descent minimum is "annealed" to a globally optimal position in parameter space, and b) that there is a well-sampled uncertainty distribution for each parameter. The uncertainty in the fitting parameters is estimated using a simulated annealing approach (PTMCMC) that is based on the data and the model, with no prior assumptions about the functional form of the distribution of the uncertainty. The methodology exposes differences between events (Fig. A2) that are not obvious to the eye (Fig. 2.1) and also allows quantitative comparison of observations of the same events at three

observation sites (sec. 2.8.2), which can give insight into wave interactions with the ice shelf and into differences in wave propagation to the three sites. We showed that the set of prior model parameters is sufficient to generate well behaved model fits, with fitted model parameters adjusted minimally. Larger parameter adjustments that introduce model costs (lasso regularization) are only introduced for a minimization of the total costs, due to a better fit of the model. Future work could investigate physical reasons for these extreme parameter by reinterpreting the model function.

The method developed here could in principle be used for any data documenting swell arrivals and unmarred by locally-generated noise. Here we apply the approach to three seismic stations on the RIS, which provide a dataset of well resolved swell arrivals close to one of most active cyclone-genesis regions of the globe (Hoskins and Hodges, 2005). These point observations allow us to identify the swell origin in space and time.

For the two years of RIS data available, the optimization method results in a catalog of 208 (self)-similar swell arrivals that can be detected in the ice shelf. In total 187 (90%) of these swell arrivals originate from the Southern Ocean and can be used to improve the understanding of the origin of ocean swell and its interaction with sea ice. The remaining 10% originate from the Northern Hemisphere mid-latitudes during the boreal winter season. This is observational evidence of the distinctly different seasonality in both hemispheres, and establishes the incidence of swell impacts on the Ross Ice Shelf throughout the year. The uncertainties of origin in location and time are correlated and found to be about 110 km or 2 hours, respectively (Fig. 2.11c,d), which allows us to reduce the uncertainty of the wave origins to the scale of atmospheric surface fronts or other features within cyclones, rather than the scales of cyclones themselves (1000 km, 5 days).

A follow-up paper will apply this method to the RIS data to verify Southern Hemisphere storm position in atmospheric reanalysis data. Ice shelf seismic measurements, such as the RIS data, are particularly well suited for detecting swell arrivals, because the general lack of open water

near the seismic stations means that local wind waves are absent in the seismic data, resulting in a relative noise-free set of swell arrivals. In addition, weaker events that might complicate the interpretation of the swell arrivals appear to be largely attenuated when they propagate through sea ice.

Future work could also apply the methodology to a broader network of ice-shelf seismic stations or even to mid-latitude wave buoys, bottom pressure sensors, or even land-based seismic stations, although further tuning would likely be needed to distinguish between locally and remotely generated waves. The methodology is suitable for data records of any duration, ranging from a few days to multiple years, provided that they provide sufficient temporal resolution. The RIS time series are relatively short, and a manual procedure was used to pre-select candidate swell arrivals. If this method were applied to longer observation periods, the manual selection could be replaced with an automated search strategy from the catalog of available machine learning tools (Bergen et al., 2019). Finally, by combining observations at several stations with additional information about ocean currents or sea ice, the method could potentially be further extended to study storm intensity and/or sinuous wave travel paths.

Acknowledgments

MCH and PDB were supported by NSF PLR 1246151, NSF OPP 1744856, and CAL DPR C1670002. BDC gratefully acknowledges support from ONR grants N000141512285 and N000141512598. STG was supported by the National Science Foundation (NSF) grants OCE-1658001 and PLR-1425989, and by NASA award NNX14A078G. AJM was supported by NSF grant OCE-1419306. We thank Guilherme Castelão for advice on data processing. This study could not have been possible without the scientific insight and field work of the Ross Ice Shelf team that includes P. Gerstoft, R. A. Stephen, R. C. Aster, D. A. Wiens, and A. A. Nyblade, whose efforts were instrumental in obtaining the seismic measurements used in this study. Seismic

instruments and on-ice support were provided by the Incorporated Research Institutions for Seismology (IRIS) through the PASSCAL Instrument Center at New Mexico Tech. The RIS seismic data are archived at the IRIS Data Management Center, http://ds.iris.edu/ds/nodes/dmc/, with network code XH. Logistical support from the U.S. Antarctica Program and staff at McMurdo Station were critical, and are much appreciated.

Chapter 2, in full, is a reprint of the material as it appears in Journal of Atmospheric and Oceanic Technology, Hell, M. C., B. D. Cornuelle, S. T. Gille, A. J. Miller, and P. D. Bromirski, AMS, 2019. The dissertation/thesis author was the primary investigator and author of this paper.

Appendices

A Initial parameters and distributions

The parametric model of dispersed swell arrivals is introduced in section 2.5, and the initial values and their prior estimated uncertainties are summarized in Table 2.1. The distribution of the final normalized distance for each parameter as shown in Figure 2.8 is derived by using

$$H^i = \frac{p_0^i - p^i{}_{final}}{p_\sigma^i},$$

where p_0^i is the initial value, $p^i{}_{final}$ the final value, and p_σ^i the prior weight of parameter i. p_0^i and p_σ^i can vary from case to case (sec. 2.7.1). Figure A2 show the distributions all parameters as in Figure 2.8 but for $p^i{}_{final}$ rather then for H^i.

The final model parameters are defined by the median of the Monte Carlo sampling that results in an eight-dimensional uncertainty distribution, shown as joint PDFs for an example case in supplementary Figure S1 and the distribution of the residual between data and model is shown in Figure A3.

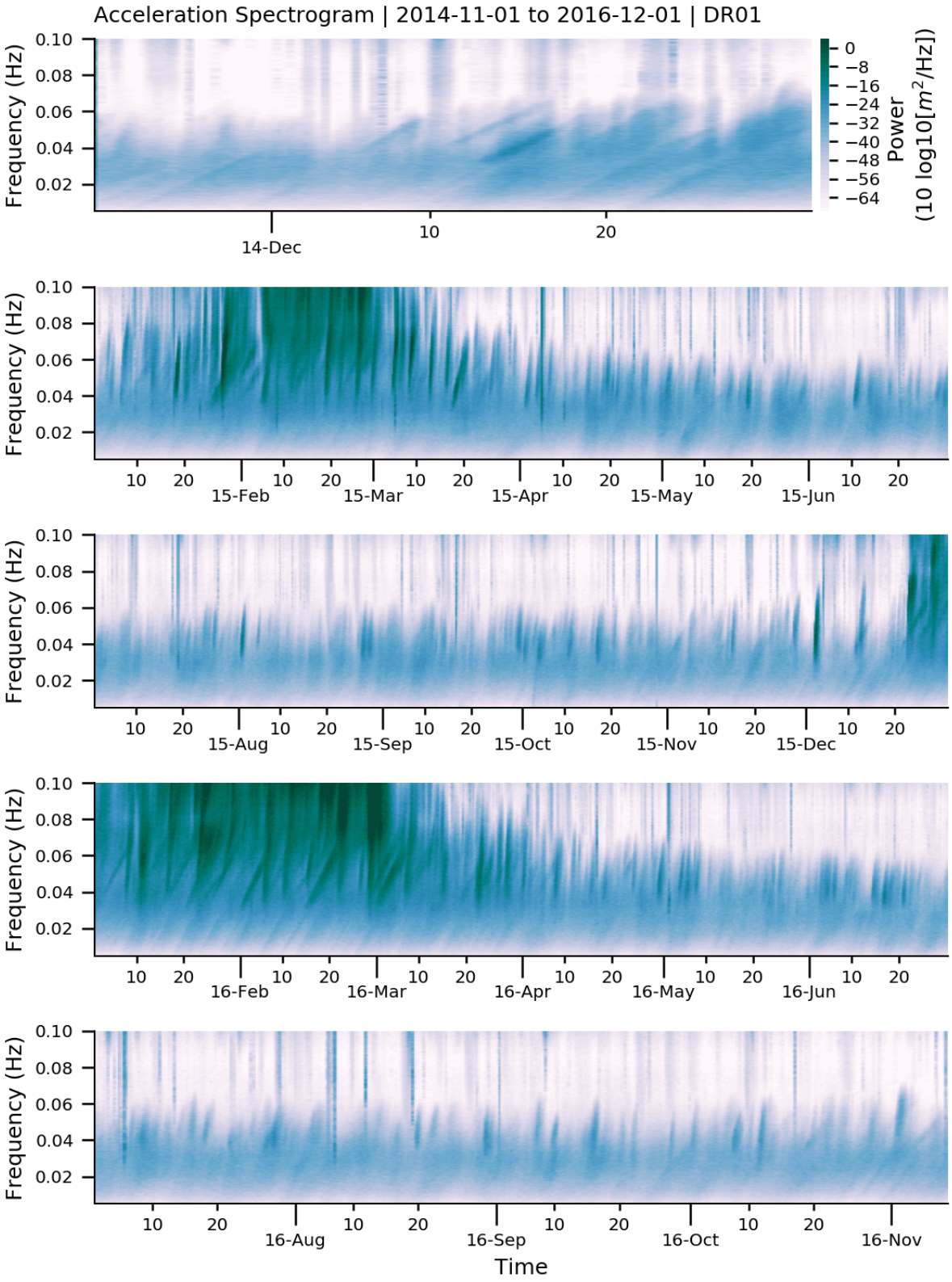

Figure 2.1: Spectrogram of the vertical acceleration in DR01 between November 2014 and December 2016. The spectrogram is expressed as a power spectra with a basic segment length of 20 min. The spectral estimate at each time step is sampled from 12 of these segments.

Table 2.1: Table of model fitting parameters, their initial conditions and priors. An initial value of “adjusted" indicates that the initial value is inferred from the data.

Parameter	initial Value $(\cdot)^0$	Min	Max	prior std $(\cdot)^\sigma$
$\hat{\alpha}$	αg^2	0.01 $\hat{\alpha}^0$	100 $\hat{\alpha}^0$	0.2
f_m	varying	0.04	0.1	0.002
γ	2	1	4	0.4
$\tilde{t}_0$	varying	-0.5	0.2	0.04
σ_0	0.05	0.01	0.1	0.01
m_f	varying	0.5 m_f^0	2.5 m_f^0	0.2
χ	5/4	1	3/2	0.05
b	2.1	1.2	3	0.08

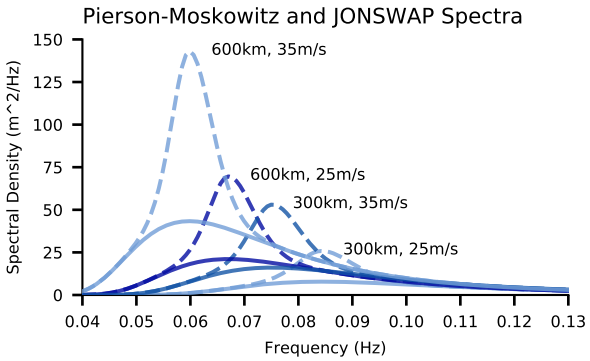

Figure 2.2: Pierson-Moskoviz (solid lines) and JONSWAP spectra (dashed) for a variety of fetches and wind speeds. The fetch length χ and wind speed U_{10} are indicated (see (2.1) and (2.3)).

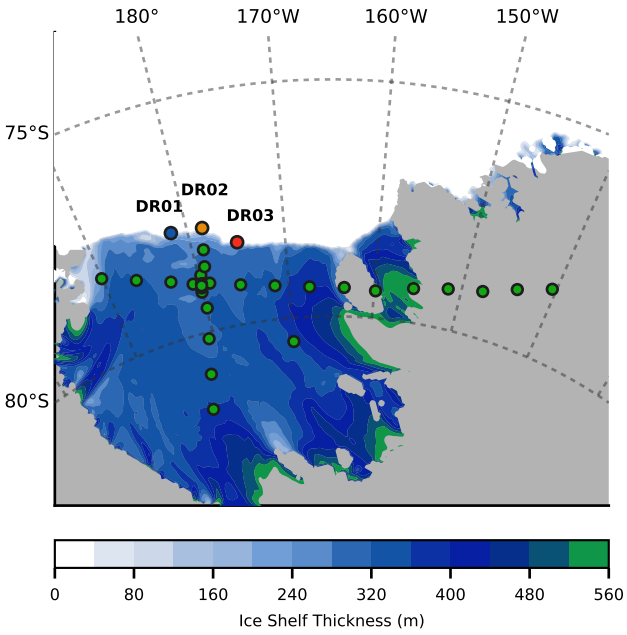

Figure 2.3: Map of the Ross Ice Shelf Vibration Project. The position of the front Stations DR01, DR02, and DR03 are indicated by the blue, orange and red dots. Other seismic stations are shown as green dots. The ice-shelf thickness is shown as shading. The Ice Shelf edge migrated northward since the Ice shelf thickness was derived (Haran, 2005; Haran and Bohlander, 2014). The front stations were about 2 km away from the ice-shelf front when the data was recorded.

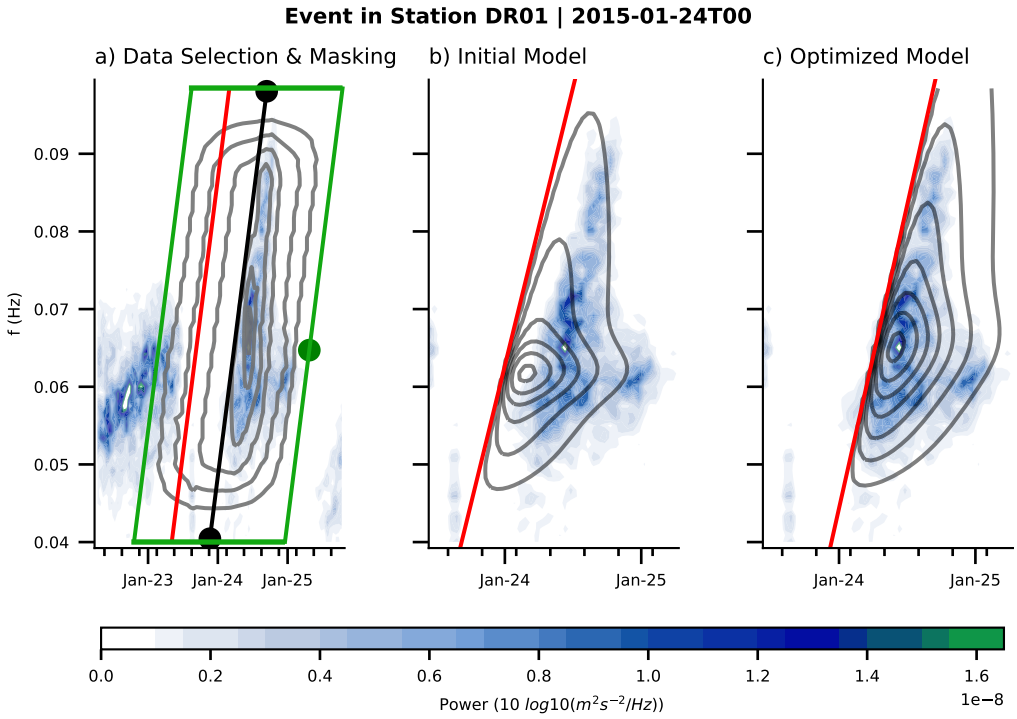

Figure 2.4: Spectrogram of a single swell event in January 2015 with the three stages of the fitting procedure. (a) Derived spectrogram (shading, sec. 2.3). Black and green dots indicate manually identified edge points of the parallelogram-shaped date mask (green line, section 2.6.1). Red lines are used as the model initial condition, and gray contours indicate the data weighting function $\boldsymbol{w}$ (2.15). (b) Masked data (shading, sec. 2.6.1) with initial slope (red) and model (black contours). (c) same as (b) but with the optimized slope and model.

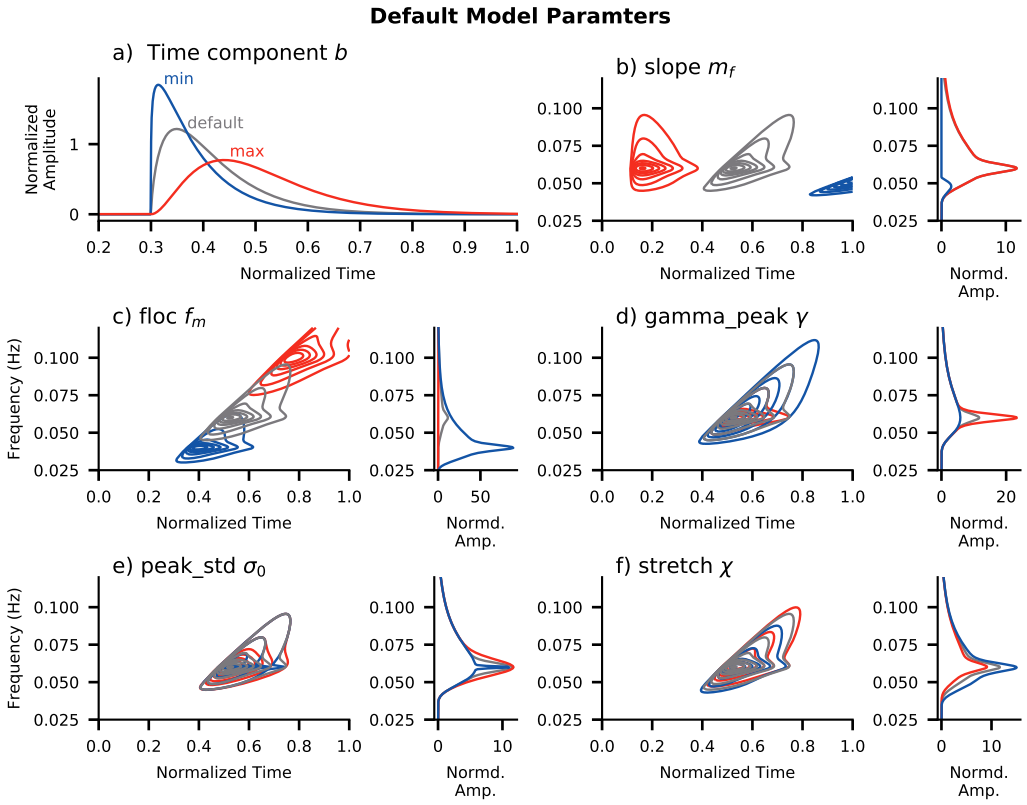

Figure 2.5: Default (gray), minimum (blue) and maximum (red) model parameters with the Γ-distribution for the shape parameter b in (a), the slope parameter m_f in (b), the peak frequency f_m in (c), the peak parameter γ in (d), the peak width σ_0 in (e) and the stretching χ in (f).

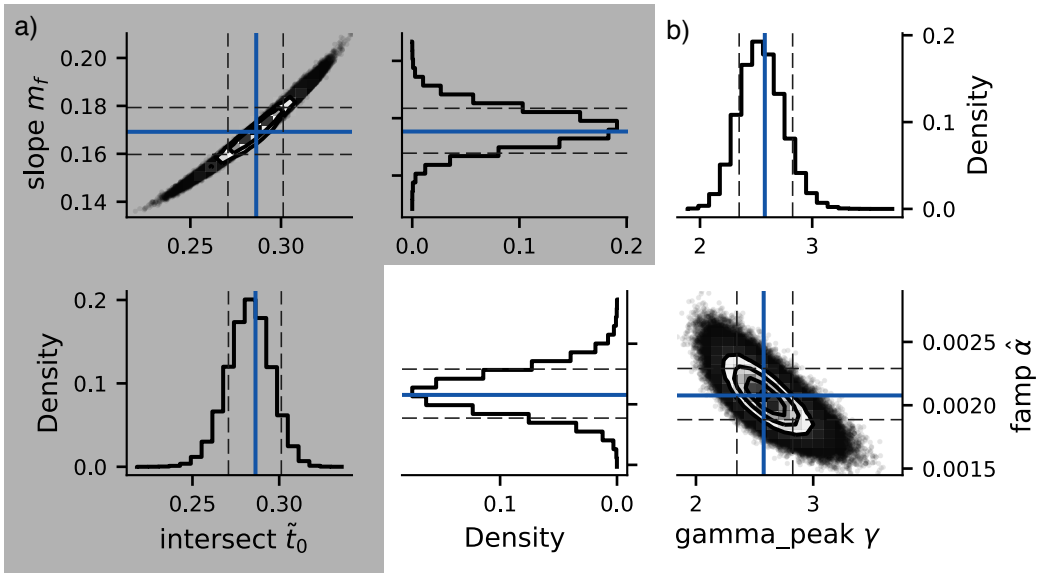

Figure 2.6: PDFs of 4 parameters inferred in an example case using the PTMCMC algorithm. (a) The three panels in the top left show the joint-PDF as well as the single-PDF for the slope parameter m_f and intersect parameter $\tilde{t}_0$. (b) The three panels in the lower right show the joint-PDF and single-PDFs for the peak parameter γ and the amplitude parameter $\hat{\alpha}$. The blue lines indicate the median and the dashed lines the 15.87 and 84.13-percentiles.

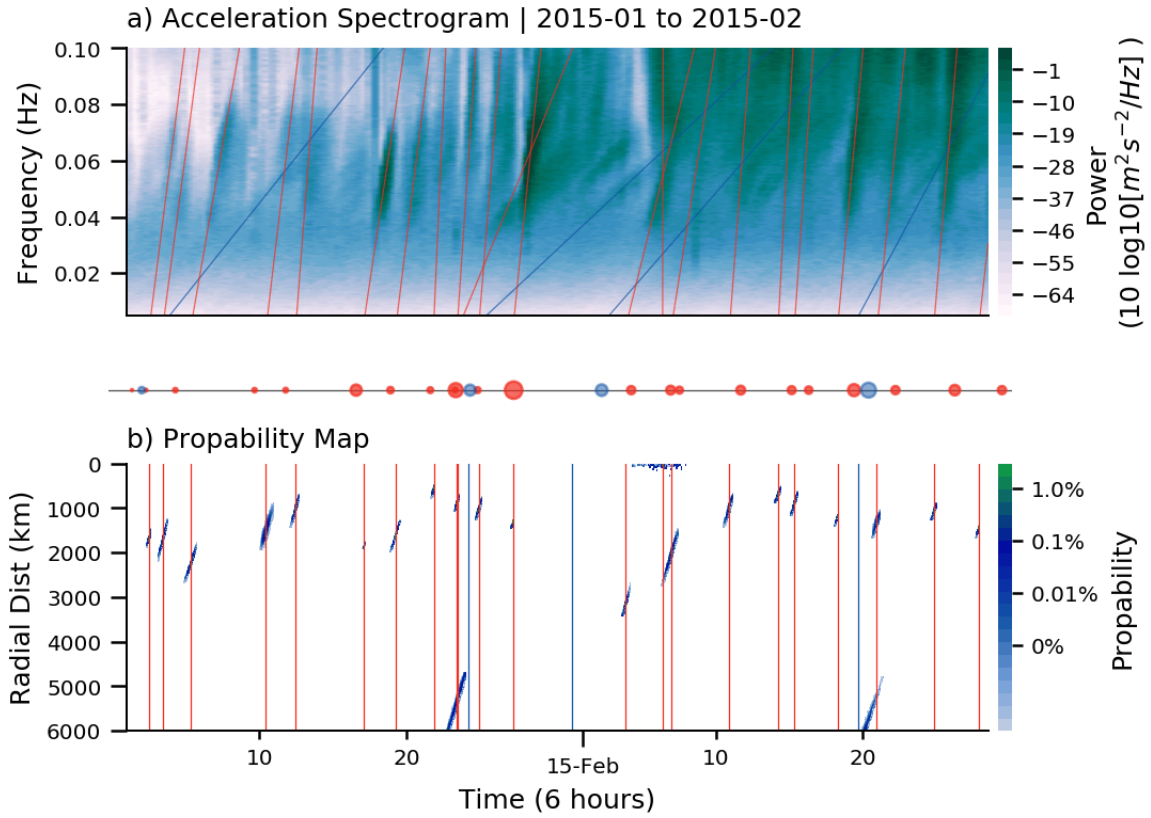

Figure 2.7: Seismic spectrogram in the RIS (as Figure 2.1). The lines show the optimized dispersion slopes for events from the Southern Ocean (red, south of 30°S) or north of it (blue). (b) Probability maps of wave origins in radial distance and time for the same time as (a). The red and blue lines indicate the best guess of the initial time, that is, when the lines in (a) cross the abscissa. Each elliptic pattern in (b) is the probability distribution of the corresponding wave event in (a). The smaller the probability patterns, the more certain the wave event origin is. The red and blue dots between both panels show the amplitude as observed on the RIS but position at there initial time.

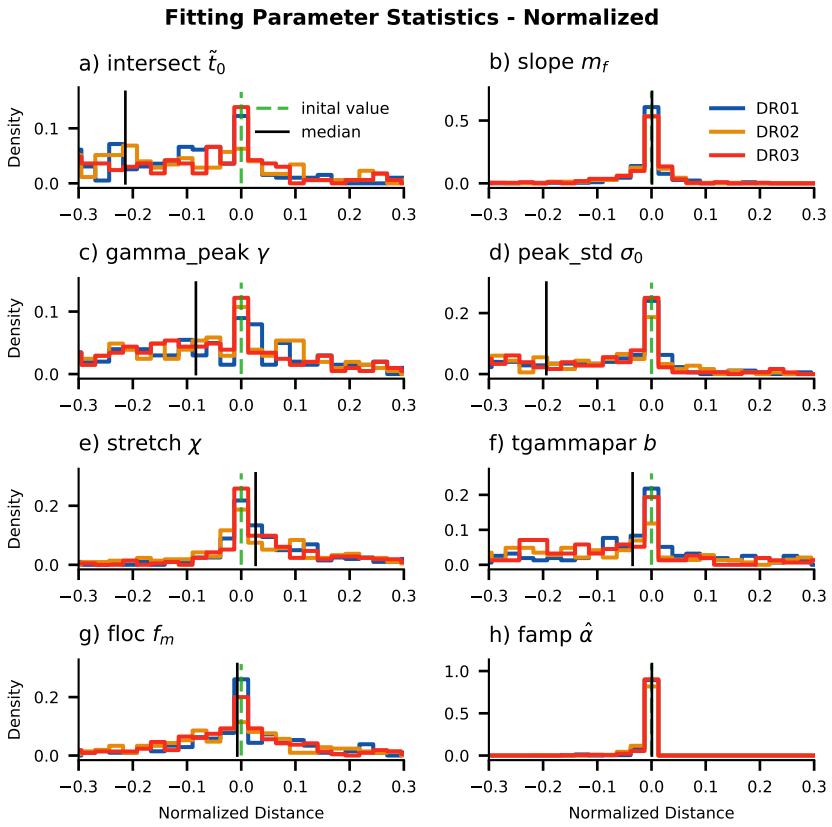

Figure 2.8: PDFs of parameters from the 225 fitted parameters sets in the three front stations DR01 (blue), DR02 (orange) and DR03 (red) expressed as normalized distance to initial value following (2.6). Green dashed lines indicate the normalized initial values of the model and the black lines are the medians of all cases at all stations.

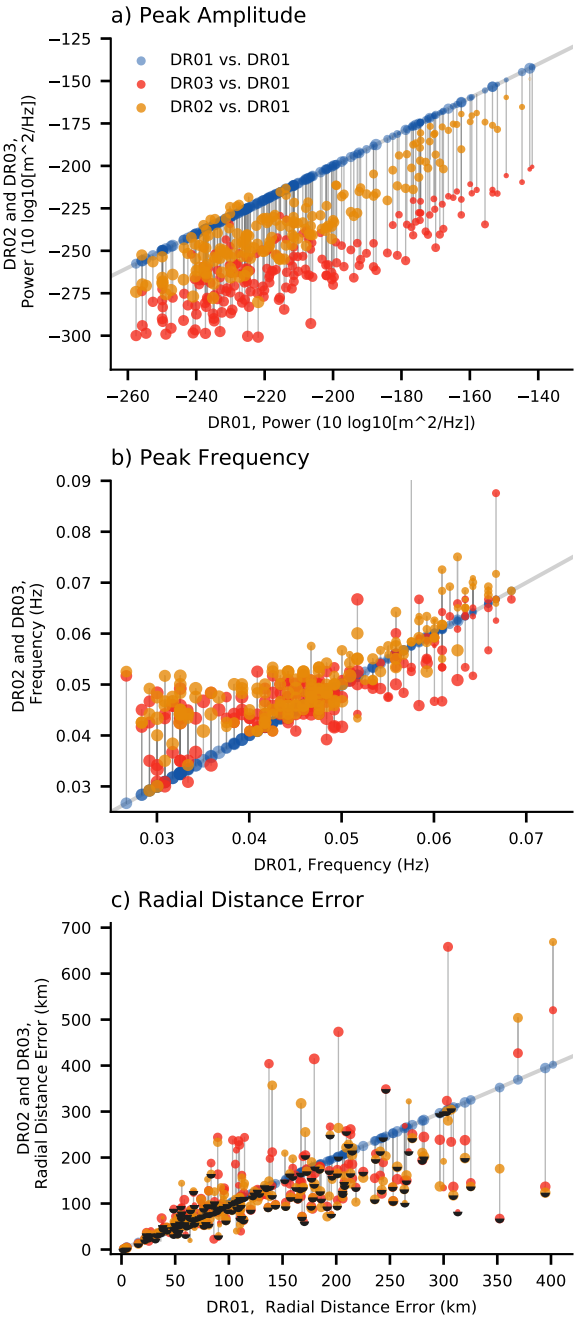

Figure 2.9: (a) Peak amplitude of data under fitted events in DR01 (blue), DR02 (orange) and DR03 (red) against DR01. The dot sizes indicate the event amplitude. The gray lines connect the same event in the three stations. (b) Same as (a) but for the peak frequency. (c) as (a) but for the radial distance error. The half-black circles indicate the station with the minimal fractional error for each case (as in Fig. 2.10b).

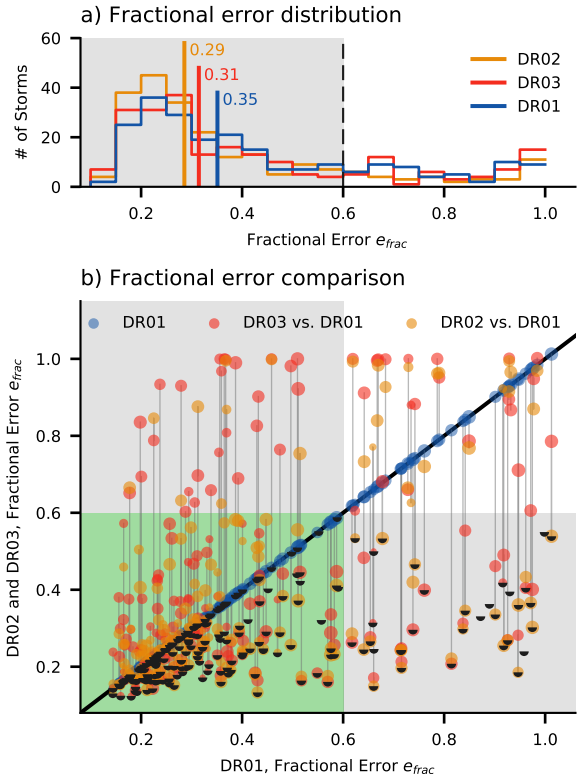

Figure 2.10: Statistics of the fractional error. (a) Histograms of the fractional error for the 225 fitted events in the front stations DR01 (blue), DR02 (orange) and DR03 (red). The colored vertical lines show the median fractional error per station. The vertical dashed line is the threshold chosen to identify good fits ($e_{frac} \leq 0.6$). (b) Fractional error of each event in DR01, DR02 and DR03, compared against DR01. Dot sizes indicate the event amplitude. Gray lines connect the same event in all three stations. For each case, the half-black circles indicate the station with the smallest fractional error. Gray areas correspond to $e_{frac} \leq 0.6$ in DR01, DR02, or DR03 respectively. Dots in the green area indicate with $e_{frac} \leq 0.6$ in DR01 and DR02, or DR01 and DR03.

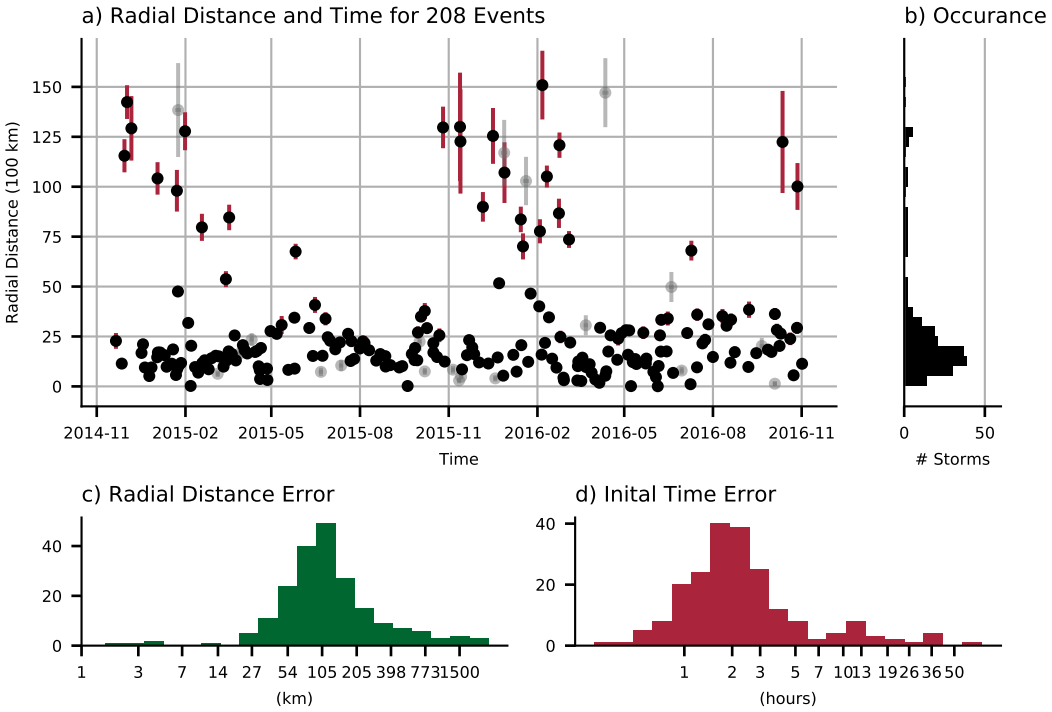

Figure 2.11: (a) Estimated radial distances and initial times for 225 wave events. Black dots are events with a fractional error $e_{frac} <= 0.6$ (208 events), while gray dots correspond to events with $e_{frac} > 0.6$ (17 events). Vertical red lines show the standard deviation of the time inferred from PTMCMC (sec. 2.7.2). (b) Histogram of numbers of storms per radial distance. (c) Histogram of radial distance error and (d) initial time error.

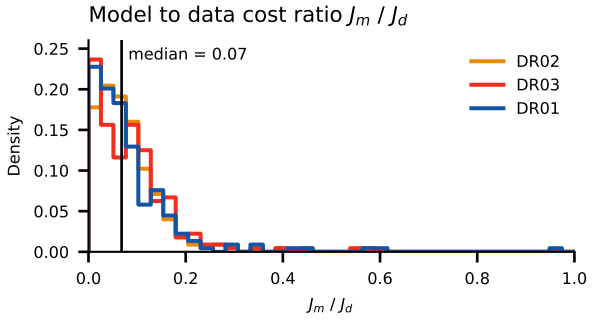

FIG. A1. Distribution of the ratio of model cost function J_m (2.5) to data cost function J_d (2.6) for all events in the three front stations. The median is shown by the black line.

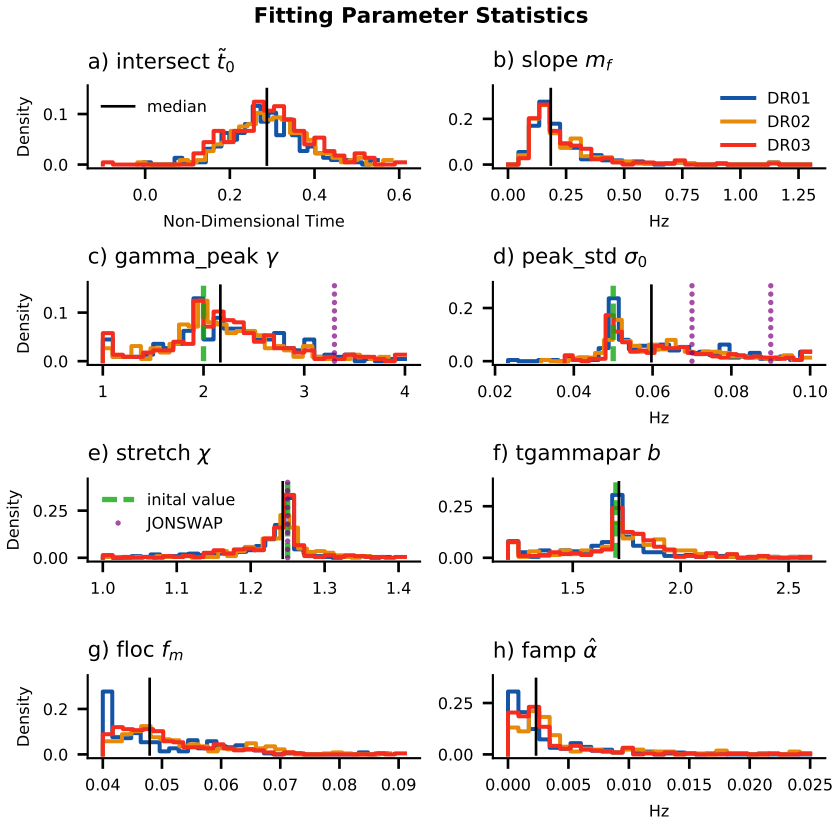

FIG. A2. Same as Figure 2.8, but not normalized by prior uncertainty and initial guesses. Green dashed lines indicate the initial values of the model for cases with independent initial parameters, the black lines are the medians of all cases at all stations, and the purple lines are the standard JONSWAP values if applicable (section 2.5).

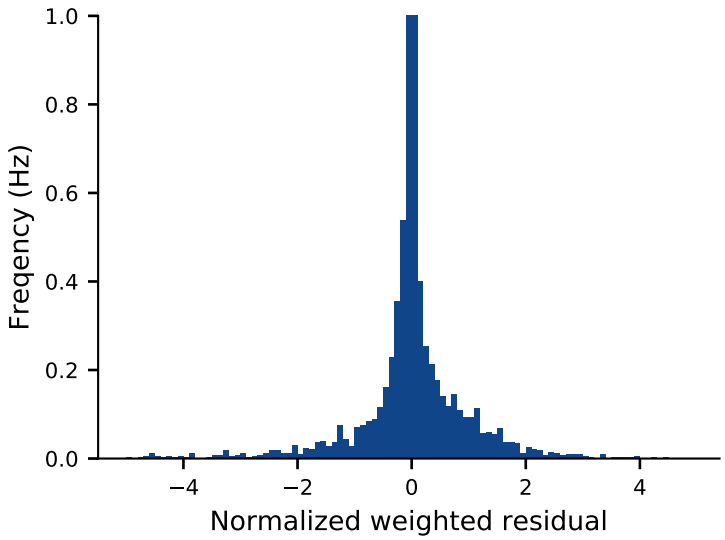

FIG. A3. Distribution of the residual between Data and Model $\boldsymbol{w}$ $(\boldsymbol{D} - \boldsymbol{M})$ for the example case in Figure 2.4 (sec. 7).

Chapter 3

Estimating Southern Ocean storm positions with seismic observations

Abstract

Surface winds from Southern Ocean cyclones generate large waves that travel over long distances (> 1000 km). Wave generation regions are often co-located with enhanced air-sea fluxes and upper ocean mixing. Ocean wave spectra contain information about storm wind speed, fetch size, and intensity at their generation site. Two years of seismic observations from the Ross Ice shelf, combined with modern optimization (machine learning) techniques, are used to trace the origins of wave events in the Southern Ocean with an accuracy of ±110km and ±2h from a hypothetical point source. The observed spectral energy attenuates within sea ice and in the ice shelf, but retains characteristics that can be compared to parametric wave models. Comparison with the MERRA2 and ERA5 reanalyses suggests that less than 45% of ocean swell events can be associated with individual Southern Ocean storms, while the majority of the observed wave events cannot be matched with Southern Ocean high wind events. The reanalysis cyclones and winds are often displaced by about 350 km or 10 hours in MERRA2 and ERA5 compared to the

most likely positions inferred from the seismic data. This high fraction of displaced storms in reanalysis products over the South Pacific can be explained by the limited availability of remote sensing observations, primarily caused by the presence of sea ice. Deviation of wave rays from their great circle path by wave-current interactionplays a minor role.

3.1 Introduction

Southern Hemisphere extra-tropical cyclones are among the strongest cyclones on the planet, with surface wind speeds that can exceed 35 m s^{-1}. They establish a region of variable and high wind speeds in the Southern Ocean storm track (Trenberth, 1991; Simmonds et al., 2003; Hoskins and Hodges, 2005). These high winds are associated with the generation of wave events and the regulation of heat and momentum surface fluxes, as well as biological production in the ocean mixed layer (Miles, 1960; Bourassa et al., 2013; Smith, 2012; Arrigo et al., 2015; Gruber et al., 2019; Carranza et al., 2018). By driving these fluxes, surface winds play an important role in the coupled climate system. In the Southern Ocean, at least three mechanisms govern the response of the ocean, atmosphere, and cryosphere to wind variability.

First, surface winds drive the ocean circulation either via direct surface drag, by regulating freshwater fluxes via sea-ice advection (Abernathey et al., 2016), or by maintaining large atmosphere-ocean temperature gradients at the Antarctic continent (Munk and Palmén, 1951; Johnson and Bryden, 1989; Kwok, 2005; Comiso et al., 2011; Holland and Kwok, 2012; Abernathey et al., 2016; Haumann et al., 2016). In many of these processes, surface winds are assumed to exert a zonal mean force. However, within the storm track, winds are spatially heterogeneous because they are located behind atmospheric fronts, resulting in the forcing being not consistently zonal (Neiman and Shapiro, 1993; Neiman et al., 1993; Beare, 2007).

Second, the upper ocean influences the development of cyclones by moderating the availability of heat and moisture. It regulates production of low-level potential vorticity and

consequently the cyclone life cycle. Evidence suggests that regions of storm generation and decay, as well as storm intensification, are influenced by SST gradients, sea ice, and topography (e.g. Simmonds and Murray, 1999; Hoskins and Hodges, 2005; Lu et al., 2010; Kidston et al., 2011; Ceppi et al., 2017).

Third, precipitation on sea ice and the Antarctic continent is driven by cyclone dynamics. A good estimate of snowfall on the Antarctic continent is needed to understand ice sheet mass balances in order to anticipate their future contribution to sea level rise (Shepherd et al., 2012). In summary, understanding the variability and defining parameters of Southern Ocean cyclones is important for understanding the coupled variability of the Southern Ocean on all time scales, and the associated impacts on Antarctic processes.

The severe weather and difficult access to the region around Antarctica limit in situ observations, making remote sensing techniques essential for observing surface processes. Satellite observations produce spatially well-resolved snapshots of surface winds that allow a detailed view of surface processes. However, the sparseness of in-situ observations in the Southern Ocean impedes the calibration of remote sensing estimates. In particular, a lack of observations of extra-tropical cyclones and severe weather conditions can cause biases to be largest where the winds are strongest (Rascle et al., 2008; Ardhuin et al., 2010; Chawla et al., 2013). These biases correspond to biases in wave climate and surface momentum fluxes (Li et al., 2013; Bourassa et al., 2013; Bidlot et al., 2002; Cavaleri, 2009) and upper ocean mixing (Li et al., 2016). The biases may also have an impact on the assessment of the total energy input by wind (Rascle et al., 2008; Ferrari and Wunsch, 2010)

The lack of in situ surface wind sampling can lead to errors in reanalysis products and wave models. For example, the addition of a single mooring at the Ocean Observatories Initiative site in the southeast Pacific had a significant impact on the regional weather forecast produced by the European Centre for Medium-Range Weather Forecasts (Ogle et al., 2018). Anecdotally this suggests that Southern Hemisphere reanalysis deficiencies in representing synoptic scale variability

could stem from lack of observations. An objective of this study is to provide a quantifiable measure of the accuracy of Southern Ocean storm positions determined from reanalysis products, which will allow refinement of our understanding of Southern Ocean surface processes and improvement of Southern Ocean wind products.

This study takes advantage of two years of continuous seismic observations (Wiens et al., 2014) collected on the Ross Ice Shelf (RIS), using a wave event identification methodology developed for these data by Hell et al. (2019). The methodology uses spectrograms of swell arrivals to estimate the position and time of Southern Ocean high wind events under cyclones (described in section 3.3.1 and 3.3.2). We show here (i) that this method can be used to validate state-of-the-art reanalysis products (sec. 3.4.1) and (ii) that swell from storms travels through the sea ice and impacts the Ross Ice Shelf. The methodology provides a means to verify ocean wave products and to examine both sea ice-wave interactions and the impact of ocean swell on ice shelves (Ren and Leslie, 2014; Massom et al., 2018; Chen et al., 2018).

3.2 Southern Hemisphere Storm Tracking by Forerunners of Swell - A Case Study

Strong wind patterns over the Southern Ocean are generated by extra-tropical cyclones. Each storm undergoes a characteristic life cycle of generation (cyclogenesis), intensification, and decay (cyclolysis). This life cycle is connected to the large-scale baroclinicity and to local surface conditions, such as topography or convection (Neiman and Shapiro, 1993; Simmonds and Murray, 1999; Simmonds and Keay, 2000). Figure 3.1 shows an example of a storm life cycle, in this case for a storm in July/August 2015 (thick black line in Fig. 3.1a). Reanalysis studies suggest that the highest winds are often found on the equatorward side of the cyclone center (Fig. 3.1a, orange dots, Bengtsson et al., 2009; Hodges et al., 2011), so that they move at speeds similar to those of the cyclone centers, about 10-35 m s^{-1}.

Strong winds work on the ocean surface and create wind waves,that lead to the generation of swell waves (Fig. 3.1a, shading shows significant wave height, Hasselmann et al., 1985). Swell properties, such as amplitude and frequency, depend on the “fetch", defined to represent the area over which winds act quasi-stationary, that is with uniform strength and duration (Fig. 3.1a, red outlined area, Pierson and Moskowitz, 1964; Hasselmann, 1963; Barnett, 1968; Kudryavtsev et al., 2015). The mechanisms by which winds generate waves in the fetch area are still an active research question. However, third-generation parametric wave models are able to generate realistic wave spectra using 10-meter or surface winds (gray arrows in Fig. 3.1a, Tolman, 2009; Chawla et al., 2013; Cavaleri, 2009).

If far-field effects are neglected, wind speed and wind duration control the local wave field (Phillips, 1985). Once waves travel out of their generation region, they disperse and dissipate, and can be interpreted as a group of linear gravity waves propagating across the ocean. Wave event spectra have characteristic peak frequencies and amplitudes that are connected to the wind speeds and fetch in the generation region (Pierson and Moskowitz, 1964; Hasselmann, 1963). However, the fetch over the open ocean is often weakly defined, and these semi-empirical models do not consider the wind acting on the ocean in an irregular region that is moving and changing form.

Swell waves generated by storms can travel long distances (Munk and Snodgrass, 1957; Snodgrass et al., 1966), and when they interact with sea ice, higher frequencies are damped, or reflected (Fox and Squire, 1994; Squire, 2007; Vaughan et al., 2009). The remaining low-frequency energy travels through the sea ice and is observed in seismic records from the ice shelves (Fig. 3.1 b, shading, Collard et al., 2009; Cathles et al., 2009; Bromirski et al., 2010; MacAyeal et al., 2009; Hell et al., 2019). These seismic spectrograms show a systematic shift of peak frequency with time (Fig. 3.1b, red line, Bromirski et al., 2010; Barber and Ursell, 1948; Munk, 1947; Snodgrass et al., 1966), which is explained by the deep water dispersion relation of ocean swell

$$\omega^2 = kg, \tag{3.2.1}$$

where $\omega = 2\pi f$, with f being the frequency of the wave, k the wave number, and g the acceleration due to gravity. The group velocity is frequency-dependent, meaning that longer waves travel faster. The group velocity of the wave group is

$$c_g = \frac{\partial \omega}{\partial k} = \frac{1}{2}\sqrt{\frac{g}{k}} = \frac{gT}{4\pi} = \frac{\Delta x}{\Delta t}, \tag{3.2.2}$$

with T as the wave period (Barber and Ursell, 1948; Munk, 1947). For an observed wave with a given frequency, this relates the distance traveled (Δx) and travel time (Δt, Fig. 3.1a, red semi-circular arcs). In other words, if one observes a wave of a given frequency and knows how far it has propagated, then the time of origin can be inferred. Or, if one observes two waves of different frequency and assumes they come from the same source, then both the time of origin and the distance traveled can be estimated.

This principle can be used in combination with spectrograms of ocean waves, mostly from wave buoys, to estimate the travel distance and time of wave generation (Munk, 1947; Barber and Ursell, 1948; Snodgrass et al., 1966; Bromirski and Duennebier, 2002; Gallet and Young, 2014). As explained in detail below, the same phenomenon is observed in spectrograms of seismic observations from ice shelves (Fig. 3.1b, Bromirski et al., 2010; MacAyeal et al., 2009; Cathles et al., 2009). Seismic data from the ice shelf can be used to invert spectrogram slope to estimate propagation time and radial distance to the origin (eq. (3.2.2), Munk, 1947; Munk et al., 1963). Figure 3.1a shows the synoptic situation at the estimated initial time (gray line in Fig. 3.1b), and the red semi-circular arcs provide estimates of the radial distances from the ice shelf seismic station. Both are derived from the red dispersion slope in Figure 3.1b.

A standard assumption is that each wave event is generated at a point source and travels undisturbed along a great circle path. This is a strong simplification (Fig. 3.1a) but works surprisingly well (Snodgrass et al., 1966; Collard et al., 2009). In reality, swell waves are generated by fast moving storms and can be deflected by ocean currents (Munk et al., 1963; Munk

and Snodgrass, 1957; Gallet and Young, 2014; Ardhuin et al., 2017). These impacts will be discussed together with other caveats of these simplifications by utilizing different conceptional models to reveal interactive atmosphere-ocean-ice processes.

3.3 Methods

3.3.1 Seismic Data

The Ross Ice Shelf Vibration Project was a field campaign from October 2014 to December 2016 with the goal of recording the response of the Ross Ice Shelf (RIS) to gravity wave for geophysical, glaciological and oceanographic purposes (Bromirski et al., 2015). A network of 34 seismic stations recorded 2 years of continuous 3-directional displacements at each station. The 3 front stations are used for the analyses in this paper.

Figure 3.2a shows the spectrogram of the vertical displacement at DR01 for about 2 months. The most common features are sloped lines of anomalously high wave activity in the swell band. These are dispersed arrivals of ocean swell at the ice shelf.

3.3.2 Model Optimization

Hell et al. (2019) developed a method to catalog these dispersed swell arrivals (swell events) using a two-stage optimization procedure. Here we give a brief overview of the model function, the optimization method, and the uncertainty estimation.

Model Function

The model function is constructed to mimic the dispersion slope of the swell as well as its characteristic shape in frequency and time. It is chosen because it allows an effective separation of storm-induced signals from those that might be induced by other mechanisms (like iceberg

calving, for example) that are also observed by the RIS seismometers. The model function has six free parameters that determine its shape and two that determine its slope (Fig. 3.1b).

In frequency, the model function employs the JONSWAP spectrum (Hasselmann et al., 1973), which is similar to the Pierson-Moskowitz spectrum for a fully developed sea (Pierson and Moskowitz, 1964). The use of a parametric wave model as a functional form for the swell arrivals has the advantage of potentially reducing the model–data misfit. It incorporates prior physical knowledge in the optimization procedure, which is an advantage compared to other generic “machine learning" approaches.

In the time domain, the model used the Γ-distribution to account for the sharp leading edge of the incident wave events. Both functional forms incorporate a linear trend to account for the change of peak frequency with time (eq. 3.2.2, Fig. 3.1b).

After a preliminary step in which each swell event is isolated, a cost function is constructed as the difference between model and data, weighted by the geometry. In addition, lasso-regularization is used to avoid extremes in the parameter space (Hell et al., 2019).

Optimization Method and Estimations of Uncertainty

The non-linear model is optimized using a two-stage fitting algorithm to minimize the difference between model and data. In the first stage, the model is initialized with an initial set of parameters, which are then refined using the Levenberg-Marquardt Algorithm (LM, damped least-squares, Newville et al., 2014) to find a local minimum of the cost function. The LM algorithm calculates the local cost function gradient in parameter space and moves its next guess of parameters in the direction down the gradient.

In the second step, a Parallel Tempering Markov-Chain-Monte-Carlo (PTMCMC, Goodman and Weare, 2010; Foreman-Mackey et al., 2013; Earl and Deem, 2005) method is used to further minimize the cost function and produce a posterior error distribution for all variables simultaneously. This process is similar to simulated annealing, where the progress toward an

optimal solution can only be seen from the average of many iterations rather than from each single iteration (Kirkpatrick et al., 1983). This is a powerful tool in situations in which multiple optimal solutions could exist. Even though one origin per wave event is assumed, the uncertainty estimate from PTMCMC is generally capable of capturing several wave events that arrive at the same time. The uncertainty in parameter space is inferred by sampling the posterior probability density using the data–model difference (a likelihood function based on an L2-norm) and a prior distribution generated by a random walk process (Foreman-Mackey et al., 2013). The uncertainty distributions of the two slope parameters are converted into a joint probability distribution of radial distance and time. An overview of the resulting initial times and radial distance, as well as the corresponding errors, are shown in Figure 3.3.

Incident wave events are observed at all three stations at the ice shelf front nearly simultaneously, but the quality of the optimization procedure varies between the stations due to independent noise. Hell et al. (2019) selected the best fitted model for each case between the three front stations.Wave arrivals that have a more complex generation history, such as two swell events observed at the same time or swell that is generated by more then one system, they have a larger fitting error and are neglected from the analysis. (See definition of the fractional error in the appendix.) The derived data set contains 182 incident wave events originating from the Southern Ocean. In Fig. 3.3a, each dot represents the estimated radial distance and initial time of an observed and successfully fitted wave event. The red bars indicate radial distance uncertainty, and the dot diameter illustrates the observed amplitude of the events. Most of the events have radial distances that coincide with the Southern Ocean storm track (1-2 $\times 10^3$ km, Fig. 3.3b). The median estimated error is about 110 km in space and 2 hours in time (Fig. 3.3c and d).

3.3.3 Cyclone detection

For cyclone tracking and surface wind fields, we use two reanalysis products: Modern-Era Retrospective analysis for Research and Applications, Version 2 (MERRA2) and ERA5 (Modeling,

2015a,b; Gelaro et al., 2017; European Centre For Medium-Range Weather Forecasts, 2017). These are selected because they provide hourly fields, while many other reanalysis products are released at 6-hour or daily time intervals. The 2 hour and 110 km uncertainties from the optimization method imply that hourly wind fields are needed to compare with observations (Hell et al., 2019). The two reanalysis products rely on similar sets of observations and have comparable overall statistics (Wang et al., 2016). By using two products, we are able to assess cases in which the representation of extra-tropical cyclones differs (Hodges et al., 2011).

In our assessment of reanalysis storm tracks, first, the reanalysis sea level pressure (SLP) is re-gridded to a 50 km equal area grid (Equal-Area Scalable Earth Grid) EASE-Grid in the Southern Hemisphere (Brodzik et al., 2012, 2014), and second, a cyclone detection and tracking procedure is applied to the 1-hourly fields (Crawford and Serreze, 2016, 2017). Our algorithm uses the evolution of SLP rather than the often used 850 hPa vorticity, but the results are expected to be very similar (Simmonds and Keay, 2000; Hoskins and Hodges, 2002; Hodges et al., 2003; Hoskins and Hodges, 2005; Neu et al., 2012; Simmonds and Rudeva, 2014). Compared to vorticity tracking, this algorithm provides a more direct relation to surface winds, smoother fields, and additional analysis fields used to identify wind fetches (next section). In previous studies, storm tracking algorithms have typically been applied to 6-hourly or daily time steps; comparisons on a case-by-case basis generally show good agreement between storm tracks from 1 hour and 6 hour fields of the same reanalysis (Blender and Schubert, 2000).

At each time step the minima of sea level pressure are identified and connected to minima in the previous time step. The resulting cyclone tracks are masked out over land or ice shelves, and rejected if they are in the Indian or Atlantic sectors, or if they have a lifespan shorter than 24 h or a length shorter than 100 km. All remaining cyclone tracks between October 2014 and December 2016 are shown in Figure 3.4a. Each line shows the spatial evolution of a storm track, defined as the time-evolving location of the surface pressure minimum of an extra-tropical cyclone.

Figure 3.4b shows the distribution of storm translational velocities in the Pacific sector of

the SO. The median translational velocity is about 11 m s^{-1}. Based on this, we use 10 m s^{-1} as a simple estimate to convert between spatial distances and time periods (sec. 3.4.1).

3.3.4 Fetch detection

Each storm has areas of strong surface winds. They are often associated with warm or cold fronts (Doyle, 1995; Beare, 2007; Munk, 1947; Neiman and Shapiro, 1993) and found at radial distances from the pressure minima that are roughly aligned with the largest closed contour of sea level pressure around the local pressure minimum (Fig. 3.4c, orange dashed line, Bengtsson et al., 2009; Hodges et al., 2011). These areas of strongest winds under a cyclone are also areas of high surface stress (Adamson et al., 2006; Beare, 2007; Hasselmann et al., 1973), and therefore intensified wave generation. We identified these "fetch areas" using the following procedure:

As indicated in Figure 3.4c, first the cyclone area (solid orange line) is defined as twice the area of the last closed SLP contour (dashed orange line) for each storm track (black thick line) and time step. Second, fetches are identified by searching for patterns that exceed the 90th-percentile of the wind speed distribution under the cyclone area (red outline and black arrows in Fig. 3.4c). As a practical approach to defining fetch area, only patterns larger than 16 grid points (40×10^3 km^2) are kept and used as a practical definition of fetch areas (Fig. 3.4c, red contours). Cyclones can have several fetches at each time step, and fetch centers are generally displaced a few hundred kilometers from the cyclone centers (compare red dots and red cross). This pattern identification allows us to evaluate the evolution of fetch areas under cyclones over time and to draw inferences about reanalysis product performance on the scale of fronts rather than on the scale of cyclones.

3.4 Results

3.4.1 Matching reanalysis storms with observations

To obtain the storm locations in the Southern Ocean from the seismic swell observations, we examine each of the observed events and compare them to the reanalysis storm tracks. The estimated dispersion slopes and uncertainties in observed swell arrivals are converted to 2-dimensional probability density distributions (PDF) of initial time t_0 and radial distance r_0 (Fig. 3.2b, Munk, 1947; Hell et al., 2019). Swell statistics inferred from the seismic data provide direct information about wave origins (compare Fig. 3.2a and b). Smaller patches of high probability density correspond to more certainty in wave origins. Large patches of high probability represent either deficits in the model optimization or just larger possible regions of wave generation. This section explains how a likelihood map of wave origins is used to determine wave generation regions in the Southern Ocean.

To compare the derived likelihood maps with the identified fetches (sec. 3.3.4), storm tracks and fetches are remapped in the same space as the likelihood maps. The remapping is illustrated in Figure 3.5 with black lines showing an individual storm track and orange dots identifying fetch area in latitude-longitude space (Fig. 3.5a,c,e) and radial-distance and time space (Fig. 3.5b,d,f). We calculate the radial distance of each storm position and fetch area to the observation site (blue dots on the RIS in Fig. 5a,c,e) at each time step for all storms and fetches, such that there is one-to-one correspondence between estimated distances and reanalysis winds. This reduces the spatial dimensions to the radial distance between the location of the storm and the observation site on the RIS. Consequently, the red semi-circular arcs in Fig. 3.5a,c,e map to horizontal lines in Fig. 3.5b,d,f and can be used for orientation. In a next step, the orange center points of all tracked fetches under storms are compared to the likelihood maps (black shading in Fig. 3.5b,d,e). Each of these fetch points i is matched with the observation-based probability by

finding

$$p_{match} = \max\left\{p_i \tilde{X}_i\right\} \quad \cap \quad p_i > 0.1\%, \tag{3.4.1}$$

where p_i is the underlying probability of the fetch i at its time and radial distance, and $\tilde{X} = f_m U_{10}/g$ is the non-dimensional fetch as a measure of the wave generation based on the mean wind speed over the area of strom-related high winds from reanalysis (Hasselmann et al., 1973). This is illustrated in Figure 3.5b,d,f for MERRA2 winds (the same events for ERA5 can be found in the Supplementary Material). For this likelihood map, the green dot is the fetch where (3.4.1) is maximized relative to all N fetches and the orange dots also belong to this identified storm track (black line), but occur at timesteps before or after the matched fetch. Only well-identified storm tracks and fetches are shown (see section 3.3.4). Once identified, the time evolution of the identified storm track and fetches can then be displayed in latitude-longitude maps (Fig. 3.5a,c,e) together with estimated radial distances (red lines). Note that (3.4.1) does not require an identified fetch to align with the probability maximum p_{max}. The distance between the most likely origin p_{max} (blue cross) and the matched origin p_{match} (green dot) is shown as a blue line in Figure 3.5b,d,f.

If (3.4.1) is not satisfied, i.e there is no probability > 0.1% assigned to any of the N wind fetches, the fetch with the minimal distance d_i between the highest probability p_{max} and the fetch position is selected using

$$\min\{d_i\}, \tag{3.4.2}$$

with

$$d_i = \left(\left[r_0(p_{max}) \; - \; r_{0,i}\right]^2 + \left[\left(\, t_0(p_{max}) \; - \; t_{0,i}\right) U_c \; \right]^2\right)^{1/2}, \tag{3.4.3}$$

where $U_c = 10$ m s^{-1} is an average cyclone speed estimated from the observed cyclone tracks (sec. 3.3.3, Neu et al., 2012). Cases where condition (3.4.1) is not satisfied will be called *displaced* throughout the paper, and their displacement is estimated by condition (3.4.2). Figure 3.5e,f shows an example of an identified event of this kind. The red star identifies the fetch area using (3.4.2), and the blue line is the calculated distance using (3.4.3). Although there are fetch areas

within the estimated radial distance (Fig. 3.5e and f), they occur at the wrong time to explain the seismic observations (more examples in supplementary material). Similarly, there are fetches that occur at the right time, but not at the appropriate radial distances. This separation between temporal and spatial displacement is only possible because of the correlated uncertainties in radial distance and initial time (Fig. 3.5b,d,f, black contours) that are derived from the uncertainty estimation (sec. 3.3.2). The correlated uncertainty represents the ambiguity between a wave event originating earlier from a distance r_a and a wave event originating later from a distance $r_b < r_a$. A detailed description of the underlying parametric model and the error estimation procedure is given by Hell et al. (2019).

The resulting matches between fetches and likelihood maps are shown in Figure 3.6 for MERRA2 and in Figure S6 for ERA5. The color convention is the same as in Figure 3.5: matched fetch positions are indicated by blue dots, positions of displaced fetches as red stars, and the likelihood maps are in black contours with their maxima emphasized with blue crosses. The distance between the likelihood maximum and the associated fetch is indicated by a red or blue line respectively.

While there is a predominant radial distance from wave origins to seismic stations (about 1500 km), we do not see a systematic difference between matched and displaced events over time, nor do we identify a difference that is associated with larger or smaller likelihood maps. The gray dots in the background show all possible fetches that each observed event was compared to and illustrate that even random pairs of radial distance and initial time might overlap with estimated fetch positions. However, the physical constraints on the optimization model and the uncertainty estimates give us confidence that the likelihood maps describe wave event origins that have more skill than random guesses. The large number of possible point sources as wave origins and the small fraction of observed discrete wave events shows that the concept that waves originate from point sources is oversimplified (Munk, 1947), because many of the identified point sources belong to the same dynamical system, i.e. separate fetches under the same storm can

together do continuous work on the ocean surface and are jointly responsible for swell wave generation by non-linear wave-wave interactions under the storm (Hasselmann et al., 1985). For simplicity, we treat fetches under a storm as independent point sources at each time step, even though we know they are not. However, this assumption of independence allows us to make a leading-order evaluation of the reanalysis surface wind positions.

The sea-ice concentration is also remapped in the same coordinate system and is shown as dashed (20%) and solid black lines (50%) in Figure 3.6. Visual inspection suggests that wave origins in sea ice or near the sea ice edge are more likely to be displaced than open ocean events (see section 3.4.2).

We also note that there are clearly cases with unrealistically distant fetches (Fig. 3.6 at the end of March 2016 and at the end of May 2016). Reasons for this can be multi-fold. The reanalysis winds over land instead of over the ocean would not generate swell, and therefore should be excluded from this analysis, or the actual wind event that generated the swell simply might not exist in the reanalysis product, perhaps because the wave origin is in the region of sea ice.

Because the estimated uncertainties and displacements are small, all cases shown in Figure 3.6 are remapped into a coordinate system centered at the probability maximum p_{max} (Figure 3.7 for fetch derived from MERRA2 and Figure 3.8 for fetch derived from ERA5). Again, dots indicate matched cases ($p > 0.1\%$), i.e. when the fetch identified from reanalysis is consistent with the storm arrival at the seismic station. This includes high probability cases centered at p_{max} and also lower probability cases that align along a 16 m s^{-1} line (fitted orange or green line in Fig. 3.7 and Fig. 3.8). As a result, origins that are shifted by 15 m s^{-1} in space and time from p_{max} are matched, even though they are displaced, due to the correlated uncertainties in t_0 and r_0. Also note that, the estimated average shift of 16 m s^{-1} for matched cases is faster than the assumed storm speed of 10 m s^{-1}. Stars show displaced cases, identified by condition (3.4.2), in which the time and position of the fetch origins are not consistent with the swell arrival at the seismic stations. These cases may be similar to the consistent cases in terms of their distance to p_{max}, but

they are judged to have physically implausible surface wind positions. This distinction between matched and displaced events is justified by the shape of the estimated uncertainties (sec. 3.3.2, Hell et al., 2019). An independent assessment of the spatial and temporal error would lead to a two-dimensional Gaussian-like uncertainty. This independent error assessment would fill a much larger area in the parameter space of Fig. 3.5 or Fig. 3.6 than a correlated error. The combined error assessment used in this analysis provides much finer distinction between physically plausible and implausible cases.

For MERRA2 reanalysis, 76 storm fetches are matched with seismic station swell arrivals with a probability > 0.1%; for ERA5 85 storm fetches match. In total, of the 187 observed and well-fitted swell arrivals, for MERRA2 41% of cases have an identified match and for ERA5 45% of cases (Fig. 3.7 orange dots, Fig. 3.8 green dots). Half of these matched cases are separated from the probability maximum by less than 207 km – or 5 hours – for MERRA2 or less than 170 km – or 5 hours – for ERA5. The other half of the matched cases show larger distances to the storm center, but still are consistent with the observations, because the probabilities are correlated in distance and time (Fig. 3.2 and Fig. 3.5).

For more than half of the events observed at the seismic stations, the position and time cannot be linked to a high-wind area under a cyclone (110 events for MERRA2 and 105 events for ERA5). This represents 59% of the observed events when matched to MERRA2 winds (Fig. 3.7a, red stars) or 55% of the observed events when matched to ERA5 winds (Fig. 3.8a, green stars). The median displacement of the set of displaced storms is about 350 km – or 10 hours – in both observational products (Fig. 3.7b, Fig. 3.8b).

Both reanalysis products have roughly the same number of storms from which waves could originate (3332 tracked storms in MERRA2 and 3118 tracked storms in ERA5, Fig. 3.6, small gray dots). However, the number of storm events observed seismically is less than the total number of south Pacific storms because not every storm generates waves that propagate toward the Ross Sea, not every event is equally well observed, and not every event has long enough waves

to penetrate through sea ice. Only 6% of the storm tracks identified in the reanalyses appear to generate waves that are transmitted to the ice shelf.

Of the 187 total seismic events observed at the ice shelf, 57 (about 30% of all observed) events can be matched to both reanalysis products, 88 (47% of all observed) events cannot be directly associated with either MERRA2 or ERA5, and the remaining 42 observed events (23%) are matched with a fetch in only one of the reanalysis products. We hypothesize that the mismatches and inconsistencies between reanalysis products stem from the paucity of atmospheric observations available to constrain the reanalyses.

3.4.2 Seasonal error dependence and the role of sea ice

A potential reason for displaced winds in the reanalysis products is summarized in Figure 3.9. The seasonal dependence of the median radial distance error d (eq. 3.4.3) is binned in two-month segments (Fig. 3.9a). Distance error estimates are obtained from the distribution of the mean error for each two-month period via bootstrapping using 10^5 repetitions (with replacement). The median of d is highest in late austral winter (September/October) and smallest at the end of summer (March/April, Fig. 3.9, orange and green squares). This seasonal change in the median error is mainly due to displaced events (median of displaced events shown as stars in Fig. 3.9a) and is mainly driven by displacement in radial distance rather than time (Fig. S7).

The seasonal variation in displaced wind events could potentially be attributed either to seasonal change in the performance of the reanalysis products (i.e. seasonal changes in the spatial coverage of in situ or remotely sensed surface wind measurements), or to seasonal changes in the quality of the fitting algorithm. The seasonality in the distribution of d roughly follows the sea ice extent in the Ross Sea (Fig. 3.9b), while there is no seasonal change in the quality of the model fitting (Fig. A1). A comparison of sea-ice concentrations with the identified fetch areas suggests that most events (up to 75%) occur over at least 20% of sea ice when the sea-ice extent is largest (Fig. 3.9c and d).

3.4.3 Available observations at the identified source locations

Displaced wind events in winter more likely originate from locations with sea ice (> 20% sea ice concentration) suggesting that the reanalyses have larger surface wind biases in the presence of sea ice, because the wind retrievals by satellite or in situ observations are impeded by the presence of ice. Figure 3.10 shows the average number of available remote sensing observations per grid point for each of the identified high wind speed areas of matched and displaced wind events (microwave radiometers and scatterometers, taken from Atlas et al., 2011; Wentz et al., 2015). If the reanalyses are constrained by one or more satellite observations per grid point, then the fetch area is at the correct location in about 60% of the cases, but if there are essentially no observations within the fetch area ($N_0 < 0.1$ in Fig. 10), then the reanalysis-derived fetch area only appears to be at the right position and time in about 15% of the matched cases, because they have no direct constraint from remote sensing winds.

In contrast, displaced cases more frequently occur when no winds are available ($23-36$% of cases, see Fig. 3.10b), though they can also occur when at least one observation is available ($34-47$%). Fundamentally, these results suggest that both reanalysis products generate similar, dynamically consistent surface winds that are not accurate enough to explain all of the observed swell events, and that part of the challenge for the reanalysis products stems from the sparsity of satellite observations. If there is at least one wind observation to constrain the reanalysis, then the probability of finding a matched case is about 60% (Fig. 3.10a), though the availability of observational constraints does not preclude the possibility of displaced cases (Fig. 3.10b).

3.4.4 Influences of ray bending and advection by currents

Another hypothesis for why the source location estimates can be displaced from the wind areas identified in reanalyses stems from bending and advection of swell waves due to currents. As we will show in this section, both processes are negligible for this analysis. To assess the

deviations that ray paths might experience due to currents we used 5-day mean surface current fields from a 1/12th degree free model run configured for the Southern Ocean State Estimate (SOSE, Erickson et al., 2016).

Rays were propagated using the ray equations for advecting and bending surface waves (Munk et al., 1963; Gallet and Young, 2014) from the Ross Sea northward for each of the available 488 model time steps (6 years and 8 months). Figure 3.11 top shows the ray positions for several travel path lengths (670 km, 1600 km and 3000 km, 3330 km corresponding to the 10th, 50th, 90th and 95th-percentiles of the estimated distances from the Southern Ocean to the RIS, see Figure 3.3b). The spread of ray positions for fixed ray length grows with the path length, but importantly, this spread in longitude and latitude does not add to the uncertainty in radial distance. It shortens the path length only marginally, even though the latitude-longitude positions can change substantially.

The advection of rays by the currents is also negligible for typical current speeds U of about 0.3 m s^{-1} and even for slow waves (0.1 Hz) with group velocities of about 7.8 m s^{-1} (3.2.2), such that $U \ll c_g$ is true most of the time (Gallet and Young, 2014). Only eddy-scale current speeds (e.g. $U \approx 1.5$ m s^{-1}) can significantly alter the path of shorter waves. However, since Southern Ocean eddies are small, not surprisingly the advective impact on ray paths is small compared to ray bending in this error analysis (Rocha et al., 2015).

The two spatial dimensions are collapsed to a great circle distance by the matching analysis (sec. 3.4.1). The analysis treats all great circle distances equally, regardless of their angle to the station (or latitude-longitude position). Consequently, ray bending can only contribute to the great circle distance uncertainty if it substantially changes the great circle distance for a given path length.

The systematic over-estimation of the great circle distance when assuming great circle paths is expressed as the *radial distance error due to ray bending*. It is defined as the distance of the ray end points from the great circle distance line that has the same path length as the ray

(Fig. 3.11, red line). The median error is proportional to the wave frequency and the ray distance (Fig. 3.11, bottom). For the frequency range in the above analysis (0.02 to 0.1 Hz) the ray bending effect is rather small. Even the shortest waves ($\approx$ 0.1Hz) from the most distant Southern Ocean storms (3300 km) have a *radial distance error due to ray bending* that is smaller than 4 km. This is less than 4% of the typical uncertainty in the great circle distance estimation derived from the RIS observations ($\approx$ 110 km, sec. 3.3.2 and 3.3.2).

3.5 Discussion

We have demonstrated that Southern Ocean storms can be observed by seismic data on the Ross Ice Shelf. Detailed comparisons of the observations with two reanalysis products suggest that slightly less than half of wave events have an origin in the open ocean that is also captured by the reanalysis product (about 41% in MERRA2 and 45% in ERA5). In the majority of cases (59% for MERRA2, 55% for ERA5) the observed wave events have an equivalent high-wind episode in the reanalysis that is displaced by on average about 350 km or 10 hours relative to the seismic observations. The partitioning of the time and distance component of the displaced wind events to these error estimates depends on the choice of the translation velocity of the storm. Here we assume an average velocity of 10 m s^{-1} (sec. 3.3.3, Neu et al., 2012). However, the number of matched storm events does not change with the choice of the translational velocity.

Detailed analysis of biases suggest errors in the representation of Southern Hemisphere cyclones in reanalyses. The direction and timing of cyclone displacement appear to be random (Fig. 3.7 and Fig. 3.8). The displacement length is longer in winter, likely connected to the presence of sea ice (Fig. 3.9a and Fig. 3.6). Generally displaced events are more likely to occur with sea ice close to the wave generation region, while the quality of the fitting model is unaffected by sea ice (Fig. A1).

We suggest that in many cases the inaccuracy of high wind events over the Southern Ocean

is due to lack of available wind observations that can be assimilated in the reanalysis models (sec. 3.4.3). While satellite wind observations over the Southern Ocean are generally sparse, they are effectively non-existent over sea ice, where no winds can be retrieved from remote sensing observations (sec. 3.4.2, Fig. 3.6 and Meissner and Wentz, 2009). The lack of observational constraints over or near sea ice would easily cause the resulting reanalysis to deviate from the (under-observed) true winds.

We showed that the major impact of sea ice in this analysis is that it prohibits wind observations, rather than distorting the observed wave event on its travel path. Sea ice attenuates higher frequency swell (Ardhuin et al., 2016; Bates and Shapiro, 1980; Squire and Allan, 1980; Squire, 2007; Stopa et al., 2018; Hell et al., 2019; Chen et al., 2018), while wave dispersion changes are minor for typical mean sea ice thicknesses of about 1.5 meters in the Southern Ocean Gyres and for periods longer than 15 seconds (Wadhams and Doble, 2009; Williams et al., 2015). This analysis only uses the dispersion of linear deep ocean waves, so the attenuation of waves in sea ice has no effect on the analysis, as long as wave-induced signals are detected by seismometers. This implies that seismic data could be part of an observing system strategy for remote detection of Southern Ocean storms by swell wave dispersion (Fig. 3.6 and Fig. 3.9c and d).

We tested the robustness of the estimated displacements against influence of ray bending due to ocean currents and concluded that the estimated storm location/timing uncertainties are not influenced by ray bending, because the error of the radial distance estimate due ray bending does not exceed 4% of the typical error estimates for the great circle distance.

Additional sources of error are limitations of the cyclone detection and tracking algorithm used here (Crawford and Serreze, 2016, 2017). Although this algorithm's performance is comparable to others (Crawford and Serreze, 2016), its application to 1-hourly data rather than 6-hourly data introduces more noise to the time series of SLP fields. This accentuates errors in cyclone position and especially area, which is sensitive to interference by storms in close proximity (Wernli and Schwierz, 2006). Since our analysis relies on the position of high wind

speed areas close to the cyclone, rather then the cyclone center itself, this is a minor source of error. Additionally, we accounted for the uncertainty in the storm-track position by extending the area used to identify high wind speed fetches beyond the smallest closed SLP contour (sec. 3.3.4). Tests of case studies did not show sensitivity of the high wind speed positions to the chosen cyclone area past a widening factor of 2.

In addition to providing context for evaluating shortcomings in local weather forecast skill, results of this study also have consequences for wave predictions. Wave climates across the Pacific are influenced by remote swell from the Southern Ocean (Bromirski et al., 2013; Villas Bôas et al., 2017), and biases in the position and timing of Southern Ocean swell generation events directly convert to biases of swell in local swell wave forecasts (Bidlot et al., 2002).

We do not include analysis of wave direction in the parametric model (sec. 3.3.2), because the important parameters for estimating the source locations are peak frequency and dispersion, which are invariant along the directional spread (Delpey et al., 2010). We also do not include the reanalysis wind direction in the matching criteria, because it is secondary to the criteria radial distance. If reanalysis winds are biased in their position, they are also biased in direction, such that a wind direction criterion will only further decrease the number of matched cases. In fact, since each high wind event is treated as a point source that radiates waves in all directions, the defined matching criterion (eq. 3.4.1) can find cases of reanalysis winds pointing away from the Ross Ice Shelf. Given the scant number of observed cases, we decided not to further subdivide the analysis. Thus the estimates of matched case (41% to 45%) found here should be understood as an upper bound.

This analysis uses the concept of point sources that generate ocean swell originating from the center of the high wind speed area (Munk, 1947). A wave event observed on the RIS is typically a superposition of several of these point sources (Fig. 3.1 and 3.5). We used a simple point-source conceptual model to identify a single source point as the origin of the wave energy, though we recognize that the waves could have a more complex origin. Although the sparsity

of wind observations is undoubtedly one challenge, a possible further explanation for the high fraction of displaced wind events stems from the shortcomings in the point-source model, which assumes that waves originate from the point in the center of the high winds. This model might be justifiable when seeking a plausible pairing between observed wave events and reanalysis storms, but it falls short in representing all of the complexity involved in the generation of swell by an area of high wind speeds that is moving at speeds similar to the wave group velocities.

Appendices

B Seasonal dependence of the fractional error

The quality of the model fit is assessed by deriving the fractional error of the model fit. The fractional error is defined as

$$e_{frac} = \frac{J_d}{\sum_i^N D_i^2 \, w_i^2}, \tag{B.1}$$

with J_d as a cost function based on the difference between data and model, D_i the data, and w_i the specific weight for each point (see Hell et al., 2019). A good model fit (i.e. low fractional errors) results in a small fractional error, while a bad model fit results in a larger fractional error. In this paper we only use observed events with $e_{frac} < 0.6$. Figure A1 shows the seasonal change of the fractional error and its running mean.

Acknowledgments

MCH and PDB were supported by NSF PLR 1246151, NSF OPP 1744856, and CAL DPR C1670002. BDC gratefully acknowledges support from ONR grants N000141512285 and N000141512598. STG was supported by the National Science Foundation (NSF) grants OCE-1658001 and PLR-1425989, and by NASA awards NNX14A078G and 80NSSC19K0059.

AJM was supported by NSF grant OCE-1419306.

We thank Guilherme Castelão for advice on data processing. This study could not have been possible without the scientific insight and field work of the Ross Ice Shelf team that includes P. Gerstoft, R. A. Stephen, R. C. Aster, D. A. Wiens, and A. A. Nyblade, whose efforts were instrumental in obtaining the seismic measurements used in this study. Seismic instruments and on-ice support were provided by the Incorporated Research Institutions for Seismology (IRIS) through the PASSCAL Instrument Center at New Mexico Tech. The RIS seismic data are archived at the IRIS Data Management Center, http://ds.iris.edu/ds/nodes/dmc/, with network code XH. Logistical support from the U.S. Antarctica Program and staff at McMurdo Station were critical, and are much appreciated. The number of available wind observations were derived from CCMP Version-2.0 vector wind analyses, which are produced by Remote Sensing Systems. Data are available at www.remss.com.

Chapter 3, in full, is a reprint of the material as it appears in Journal of Geophysical Research: Oceans, Hell, M. C., Gille, S. T., Cornuelle, B., Miller, A. J., Bromirski, P. D., Crawford, A. D, Wiley, 2020. The dissertation/thesis author was the primary investigator and author of this paper.

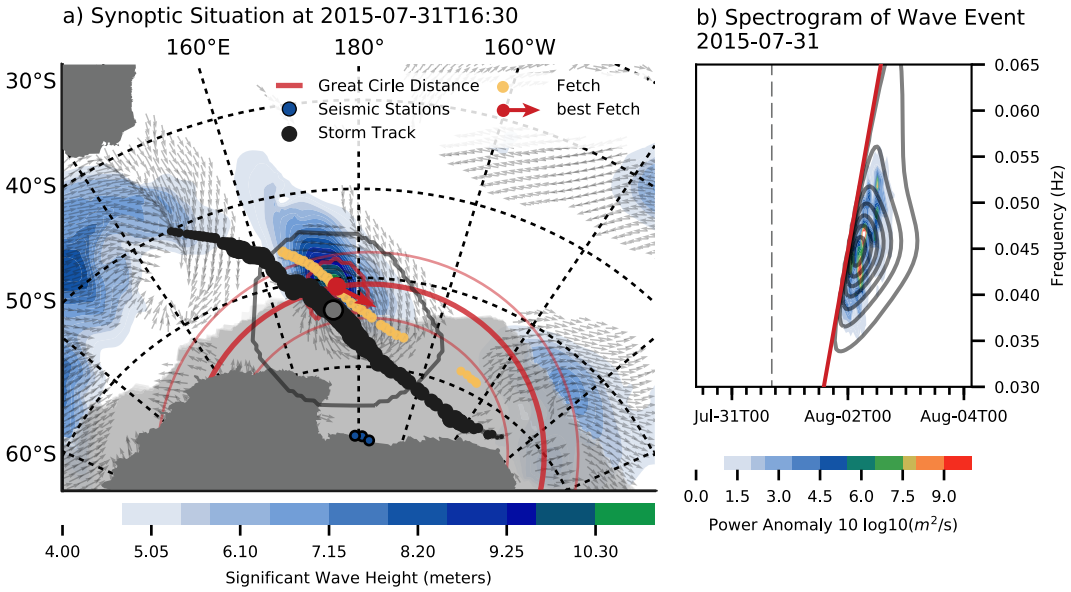

Figure 3.1: Example of a Southern Ocean storm (a) in reanalysis and (b) the spectrograms response at the ice shelf front to the same storm. (a) Synoptic situation at t_0, the time when waves under the storm start to disperse, with the thick black line as the storm track, the gray dot as its intensity maximum, and the single gray contour as the cyclone area. The orange dots indicate fetch centers associated with the storm track (see section 3.3.4) and the red dot is the fetch center at t_0, while the fetch area is the red contour. Small gray arrows indicate surface winds (> 10 m s^{-1}), blue shading shows significant wave heights (>4 m, WW3 with ECMWF winds), the gray area illustrates the sea-ice concentration using ESA Sea Ice CCI products (Toudal Pedersen et al., 2017). The red semi-circle illustrates the estimated radial distance from the seismic stations (dark blue dots) using the slope of the dispersion trend in the seismic observations in (b) and the wave's group velocity (3.2.1) with its 95% confidence interval (thin red semi-circles). (b) Spectrogram of the corresponding wave event in (a) during July 2015. The shading shows the acceleration spectrum from a seismic station at the central dark blue dot in (a), the gray contours are the fitted model (sec. 3.3.2), the red line is the estimated dispersion slope (Hell et al., 2019), and the gray dashed line is the initial time t_0.

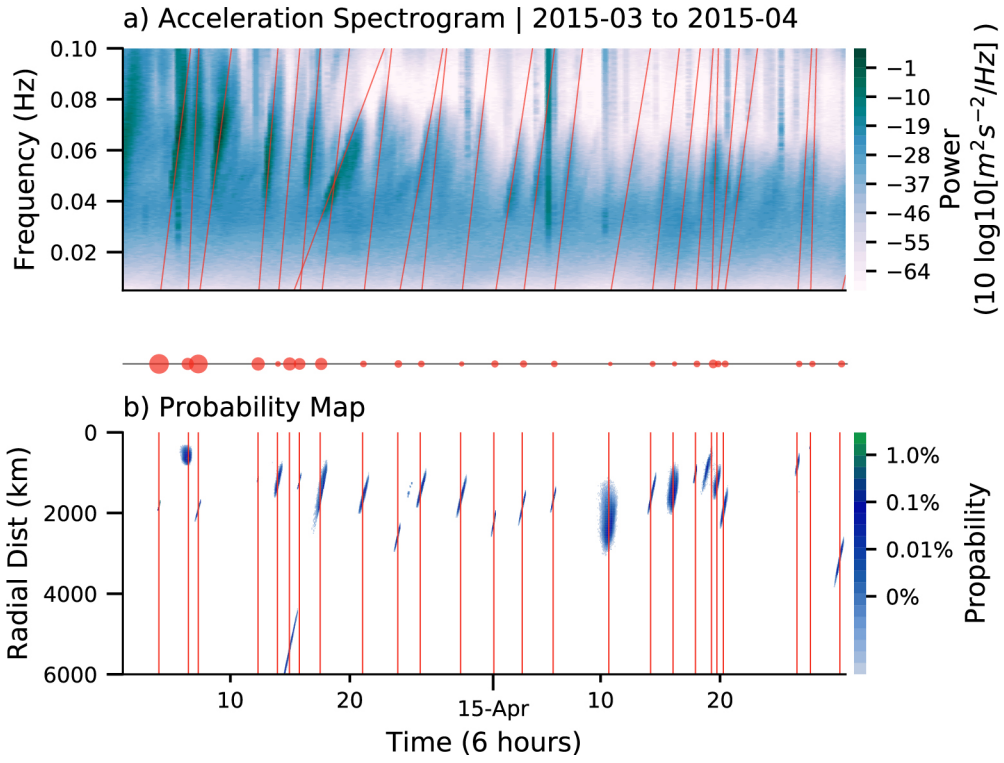

Figure 3.2: (a) Seismic spectrogram of the RIS response to gravity waves. The red lines show the optimized dispersion slopes for events from the Southern Ocean. (b) Probability maps of wave origins in radial distance and time for the same time interval as (a). Here, the red lines indicate the best guess of initial time, that is when the lines in panel (a) are projected to cross the 0 Hz-line. Each elliptic pattern in (b) is the probability distribution of the corresponding wave event in (a). The smaller the probability patterns, the more certain the wave event origin is. The red dots between both plots are proportional to the estimated swell amplitudes for each event at the initial time.

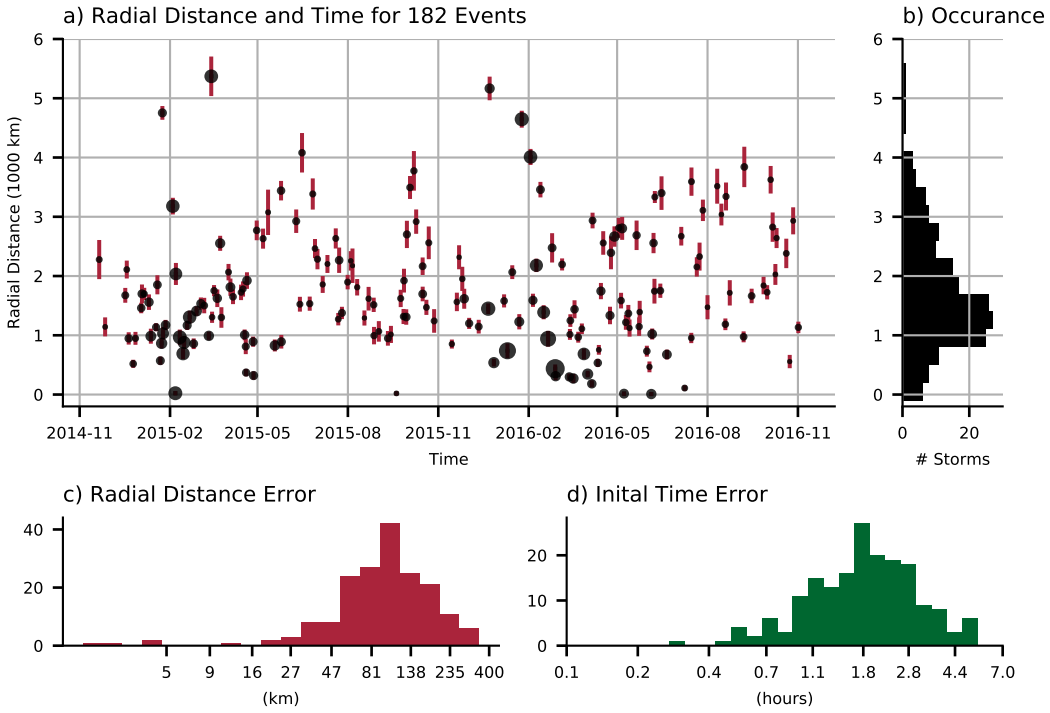

Figure 3.3: (a) Estimated radial distances and initial times for the 182 wave events from Southern Ocean storms. Black dots show the event radial distances and initial times, while their sizes indicate amplitudes. The vertical red lines show two standard deviation of the uncertainty of the initial time inferred from PTMCMC (sec. 3.3.2). (c) Histogram of radial distance error and (d) initial time error.

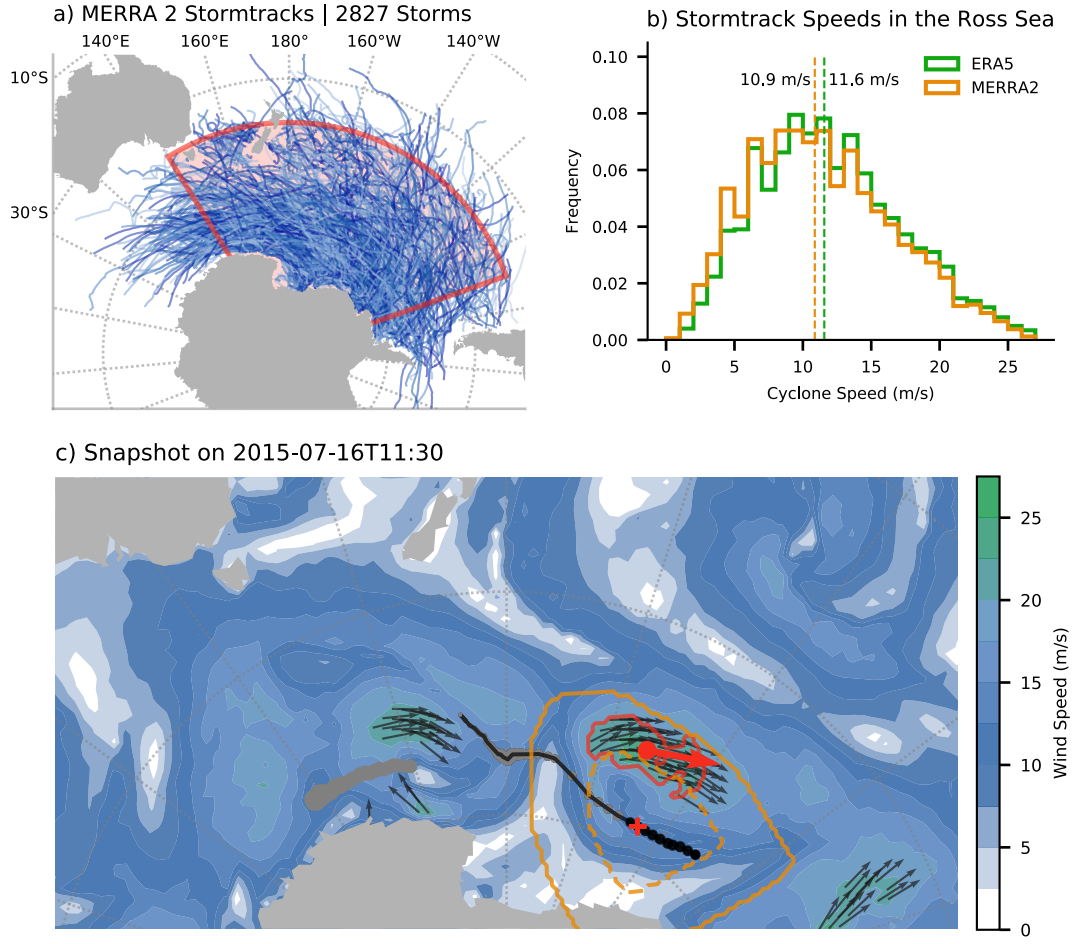

Figure 3.4: a) Storm tracks from MERRA2 between between October 2014 and December 2016 that are longer than 100 km and last longer than 4 hours in the red area. Data points near the coast are excluded. b) Probability density function of cyclone propagation speeds in the Pacific sector of the Southern Ocean derived from ERA5 stormtracks (green) and MERRA2 stormtracks (orange). c) A snapshot of an extratropical cyclone with the black lines indicating individual storm tracks in July 2015. The orange dashed contour is the outer closed sea level pressure contour of the storm track during that highlighted time step and the solid orange contour is the cyclone area, which is the graphically widened closed contour. Patterns of high wind speed that exceed the wind speed 90th-percentile ($\approx$ 16 m s^{-1}) in this area are marked with a red outline, and black arrows indicate the wind direction for these 90th-percentile winds. These are used to define the fetch area. The red dot and arrow show the center and mean wind direction of these patterns, while the red cross indicates the center of the cyclone at the chosen time step. The shading shows the wind speed in m s^{-1}.

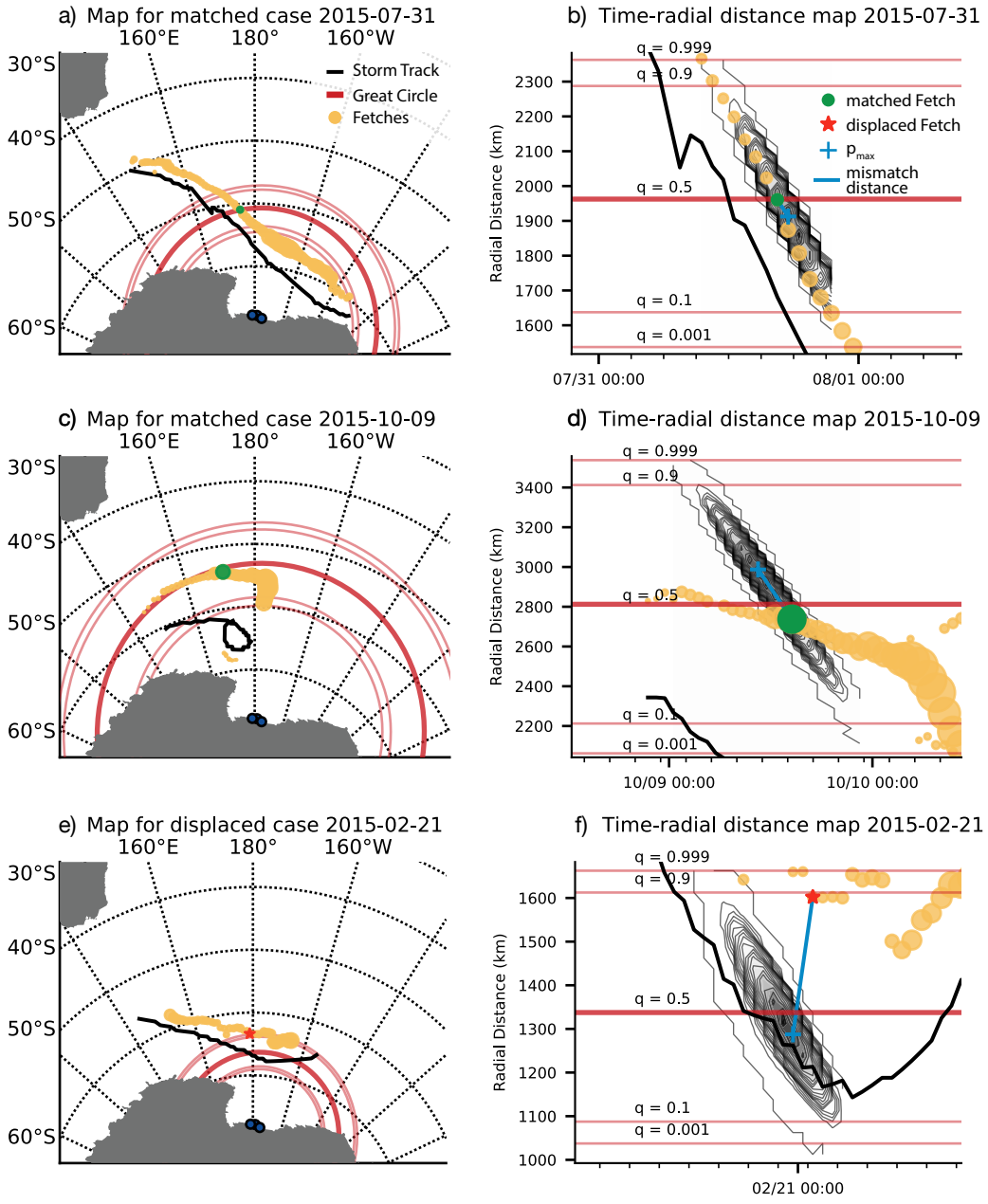

Figure 3.5: Examples of the matching procedure in latitude-longitude space (a, c and e) and associated radial-distance and time (b, d and f) for MERRA2 winds. (a and c) The event's storm track is in black, and associated fetch locations are shown as orange dots, with the dots sizes indicating the non-dimensional fetch size $\tilde{\chi}$ (sec. 3.4.1). The green dot indicates the matched fetch location (3.4.1), as illustrated in b), and the red lines show the 0.1, 10, 50, 90, 99.9%-percentiles of the radial estimate. (b and d) Illustration of the matching procedure with the storm track in black, its fetches in orange, and best identified fetch in green. The distance from the identified fetch (green dot) to the maximum likelihood p_{max} (blue cross) is shown as a blue line. The red lines indicate the same radial distance estimates as in a) and c). Black contours show the likelihood maps generated by Monte Carlo sampling (sec. 3.3.2). e) and f) same as a) and b) but for a case that does not fulfill the matching condition. The best fitted fetch is shown as a red star. Observation positions on the RIS are shown as dark blue dots with black circles in the left panels.

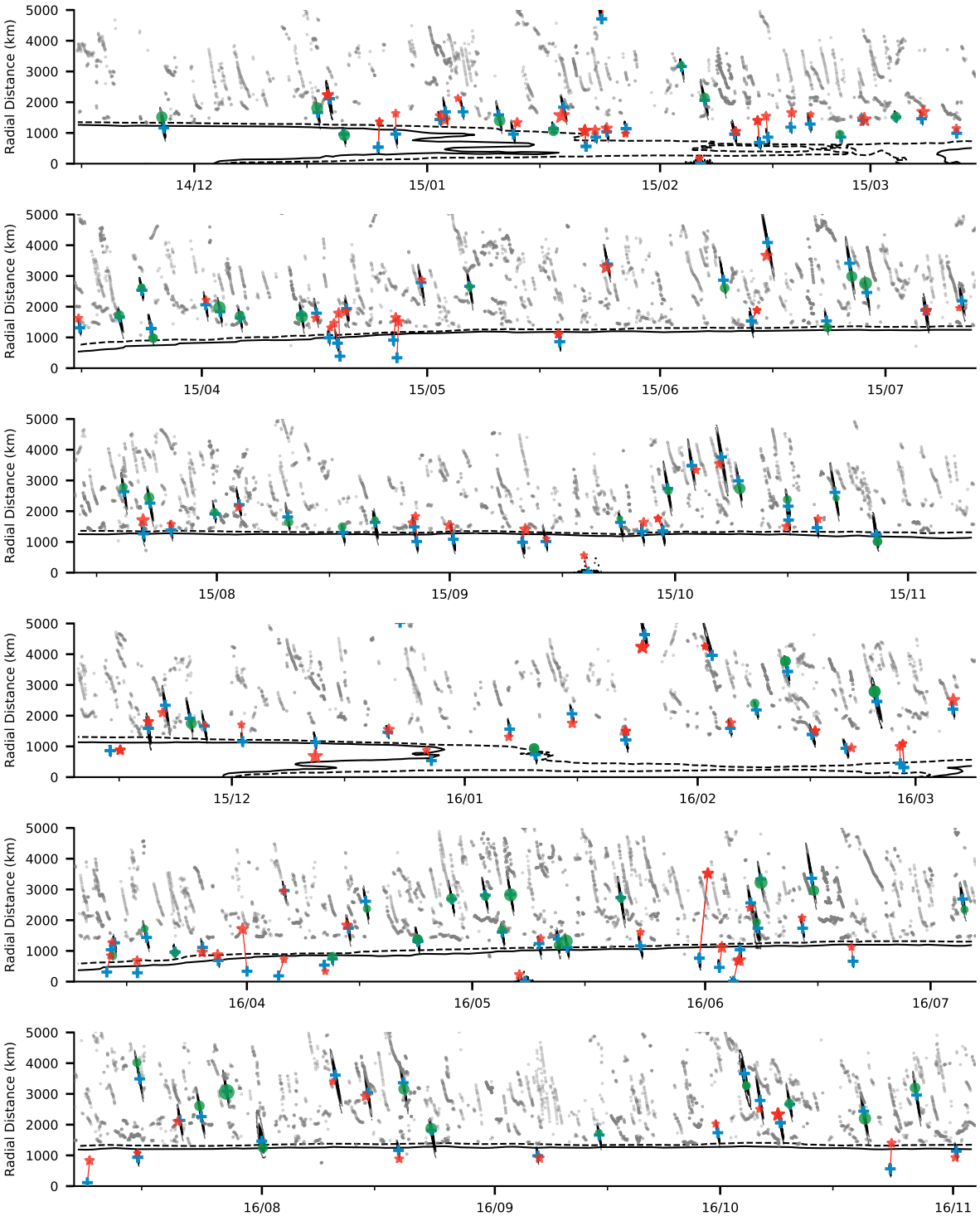

Figure 3.6: All observed wave events remapped in the time and radial distance domain, with each panel spanning about 4 months. Green dots and red stars indicate matched or displaced fetches, respectively, and the green or red lines show the distance (3.4.3) to the probability maximum p_{max} (light blue cross). The black stripes are the likelihood patterns as in Figure 3.5. The black and dashed lines show the 20% and 50% SIC in the same coordinate system (data from Toudal Pedersen et al., 2017), and the gray dots indicate the position of all possible fetches derived from the fetch detection algorithm (sec. 3.3.4).

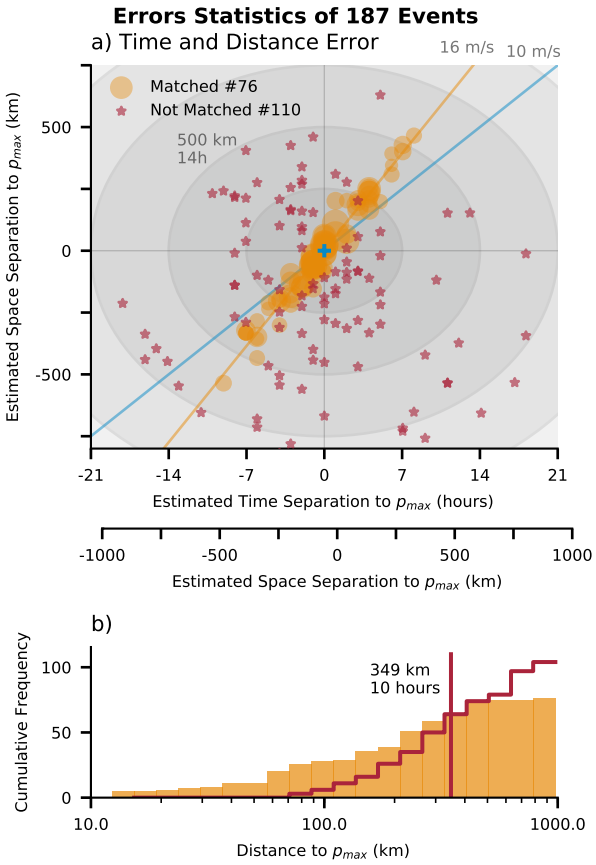

Figure 3.7: (a) Spatial and temporal bias relative to the probability maximum of matched (orange dots) and displaced fetches (red stars). The size of the orange dots indicates the probability from the PTMCMC with which they have been matched, and the orange line shows a least-squared fit to all macthed cases. The gray circles are lines of constant spatial-temporal error in 500 km / 14 hour intervals, because a time difference of 14 hours is converted to a spatial distance of about 500 km using an average cyclone speed of 10 m s^{-1}, indicated by the blue line, while the fitted slope of all matched cases (orange dots) is shown with the orange line (16 m s^{-1}). (b) Cumulative density function of matched (orange) and displaced (red) fetches. The median bias of displaced fetches is about 349 km or ≈10 hours equivalently.

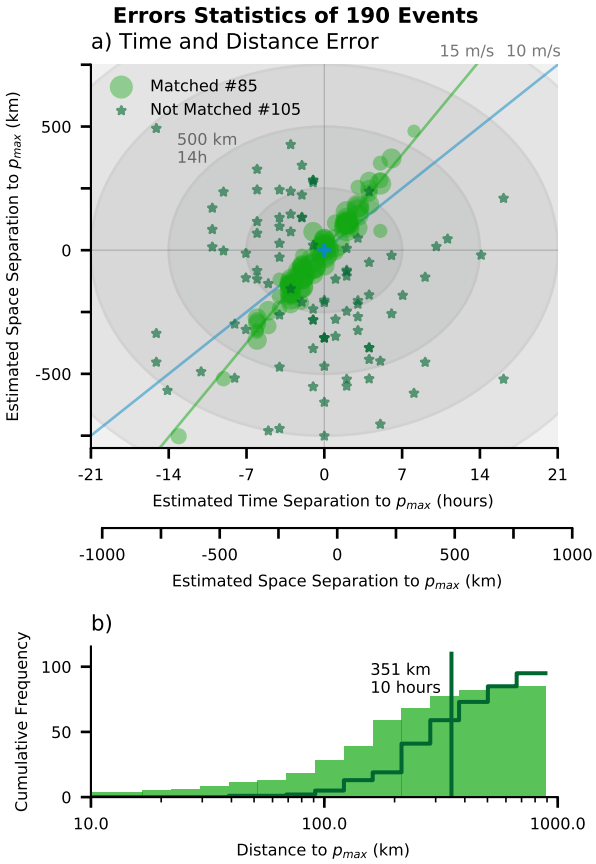

Figure 3.8: Same as Figure 3.7 but for ERA5 with matched cases in light green and displaced cases in dark green.

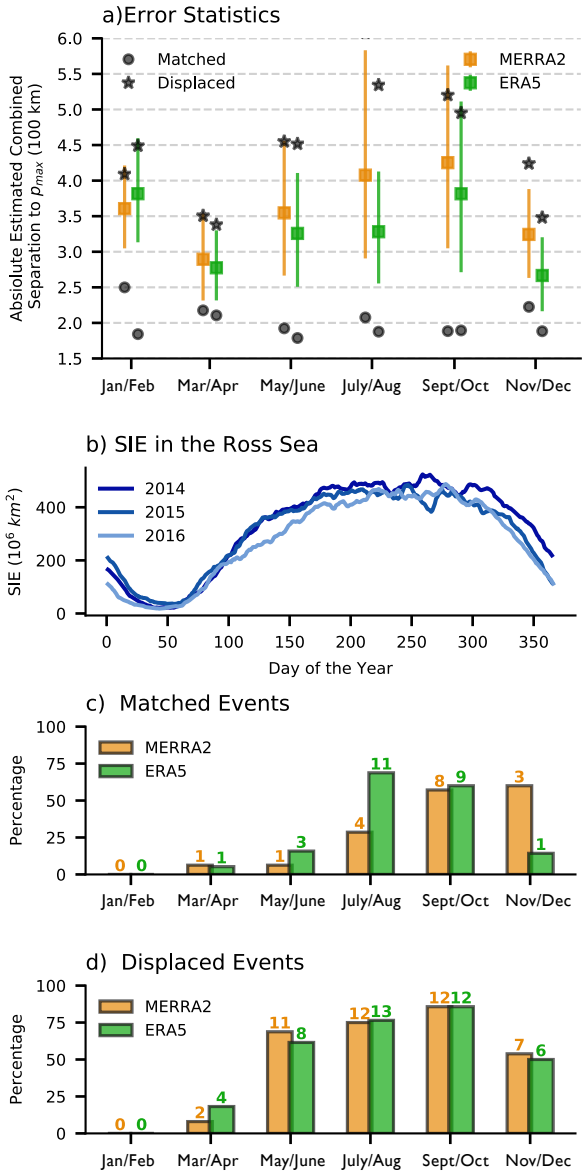

Figure 3.9: (a) Seasonal dependence of the distance to the highest probability p_{max} and the closest fetch in the open ocean (Fig. 3.7a). The orange square is the bootstrapped median of MERRA2 and green represents the bootstrapped median of ERA5, in both cases for matched and unmatched cases combined. The vertical lines indicate the spread of the 5% to 95% percentile of the bootstrapped median distribution. Gray dots are the bootstrapped medians of the matched cases, and gray stars are the bootstrapped median of displaced cases, following the convention in Fig. 3.7 and Fig. 3.8. (b) Sea ice extent in the Ross Sea for 2014 to 2016. (c) Percentages of all matched events in the bi-monthly period with fetches over an area with 20% sea ice concentration or more. The numbers on the bars are the total number of events meeting this criterion, while the vertical axis indicates their percentage. (d) same as (c) but for displaced cases

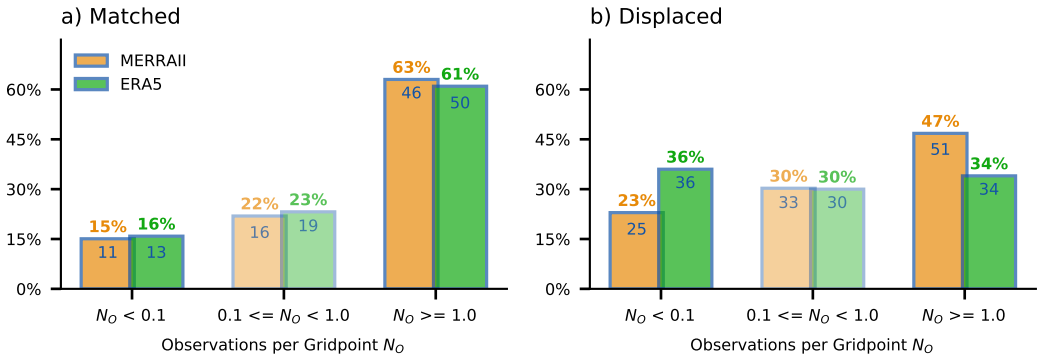

Figure 3.10: Available wind observations at the place and time of the identified fetch areas expressed as observations per grid point N_0. (a) Percentage of matched cases with $N_0 < 0.1$, $0.1 <= N_0 < 1.0$, or $N_0 >= 1.0$ for ERA 5 (green) and MERRA2 (orange). Colored numbers on top indicate the respective percentage, while numbers in the bar indicate the total number of events in each category. (b) same as (a) but for displaced cases.

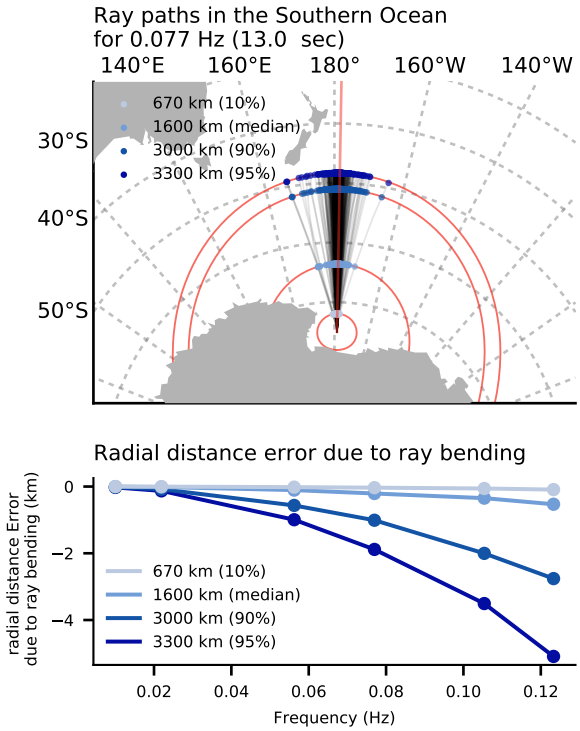

Figure 3.11: (top) Rays paths for waves with a 13 second period (0.077 Hz) that propagated through surface currents. Each ray is propagated from a point near the ice shelf edge through a 5-day mean surface current field obtained from a 1/12th degree SOSE run (Erickson et al., 2016). The blue dots show the end points for a given length (760, 1600, 3000, and 3300 km from the seismic stations at the ice shelf edge), and the red circles are the great circle equivalents. (bottom) Median deviation of the ray's end points to the defined great circle distance.

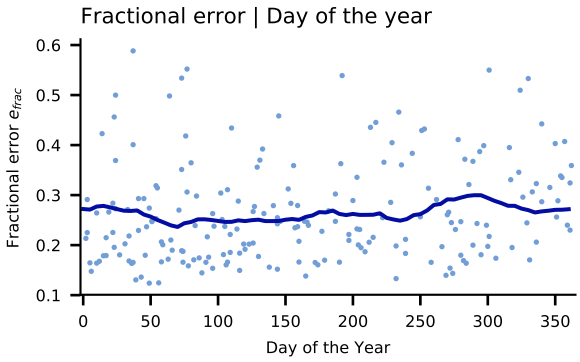

FIG. A1. Fractional error of each observed wave event in the RIS as a function of day of the year (blue dots). The 31-day running mean is shown as blue line.

Chapter 4

A simple model of swell generation under extra-tropical storms

4.1 Abstract

Storm propagate over the ocean at about 10 m s^{-1} for about 4 to 6 days and constantly shift the region of high winds forcing (fetch) over the ocean. Areas of high winds are then co-located with intense air-sea exchange of momentum. This momentum is redistributed between surface waves that interact through linear and nonlinear processes, like wave breaking events, white capping of shorter waves, and enhanced upper-ocean mixing. In sharp contrast, narrowly oriented swell events can emerge in observations at distant locations, suggesting dispersed swell events emanating from a small source location in the open ocean (Munk, 1947; Barber and Ursell, 1948; Snodgrass et al., 1966). In this study, we unify both ideas by outlining the life cycle of open-ocean generated swell in three stages: the generation stage of a non-linear sea state under a moving storm, a transformation stage where the non-linear sea state transforms into linear swell waves, and finally a propagation stage, where the waves travel as linear dispersive waves.

An extended supervised optimization method is used to estimate the displacement of the

swell wave origin compared to the highest wind forcing. The peak period of the non-linear sea state is estimated (Kudryavtsev et al., 2015) from reanalysis winds in the framework of a moving storm, and can reconstruct the observed displacement.

We employ moving fetch models with either constant winds, or temporally- and spatially-varying winds to show how the dependence of trapping and convergence of wave energy under the moving fetch affects the resulting peak wave energy. The spatial wind gradient is the most important for trapping and focusing wave energy in an area much smaller than the wind forcing. A simplified two-dimensional Gaussian model explains why wave energy propagates as coherent swell events across ocean basins.

This simple fetch model connects the large-scale space-time evolution of surface winds under storms to swell generation. It reveals how the structure of surface winds driven by the dynamics of low pressure systems determines the timing and amplitude of swell wave arrivals. It also lays the groundwork for improving long-standing biases in numerical swell forecast models and improved mid-latitude mixed-layer ventilation.

4.2 Introduction

Swell waves are long crested wave systems propagating along a well-defined direction. They are now routinely observed with wave buoys or from satellite measurements (Snodgrass et al., 1966; Ardhuin et al., 2009). Swells impact harbor safety, coastal floating, and beach erosion (Wilson, 1957; Morison and Imberger, 1992; Russell, 1993; Hunt, 1961; Ferreira, SPR 2005; Enríquez et al., 2017), but also modulate the sea surface height signals and affect altimeter measurements (SWOT, Morrow et al., 2019).

Directional swell wave properties can be estimated along coastlines, e.g. the Coastal Data Information Program/National Data Buoy Center (CDIP/NDBC, O'Reilly et al., 2016), or from space by Synthetic Aperture Radar images (SAR, Chapron et al., 2001) and Real Aperture Radar

measurements (Hauser et al., 2020). Methods can then be used to back-track swell to focal points or swell source locations, either by utilizing the deep water dispersion relation and spectrograms observed at a point (Munk, 1947; Barber and Ursell, 1948; Snodgrass et al., 1966; Hell et al., 2019) or by estimating the local convergence of backward trajectories of wave rays derived from SAR-images (Collard et al., 2009; Husson et al., 2012). Both methods assume swells originate from an idealized source point. Clearly, the definition of such a point source is ambiguous, given typical spatial scales O($1000km$) and lifetime O(5 days) of a given storm, whose center can move at about 10 m s^{-1}. Note, self-similar fetch laws, originally suggested by Kitaigorodskii (1962) assume homogeneous wind speeds, constant fetch-length or duration, and do not account for the spatial and temporal variability of the wind forcing ("fetch laws", Hasselmann et al., 1973, 1976; Elfouhaily et al., 1997). Accordingly, it is unclear how a continuously spatio-temporal varying wind field generates a single wave event that seems to stem from a small source region that is at least an order of magnitude smaller than the storm (Munk, 1947; Barber and Ursell, 1948; Hell et al., 2020).

Synoptic-scale storms dominate the mid-latitude atmospheric circulation. Their study is an integral part of synoptic meteorology, and hence there are ambled theories about their dynamics and life cycle (Bjerknes, 1919; Shapiro and Keyser, 1990; Neiman and Shapiro, 1993; Neiman et al., 1993; Schultz et al., 1998; Schemm and Wernli, 2014, review in Schultz et al., 2018). Yet, only a few studies tried to systematically assess the impact of synoptic dynamics on swell generation (Young et al., 1987; Doyle, 1995, 2002). In this study, we will explicitly show how synoptic-scale dynamics can be related to swell-wave generation. This provides means to constrain future wave climate changes and related mixed-layer variability by looking at evolving dynamical properties of synoptic storms, rather than at the air-sea fluxes themselves. In turn, it might allows to use swell observations as a remote tracer of atmospheric synoptic variability.

This study thus aims to reevaluate the conceptual idea from Munk 1947 to demonstrate how swell originates from a relatively small source area generated by a moving storm. We will

first apply a supervised machine learning procedure to estimate a source location and likelihood map from buoy observations (Chapter2 and sec. 4.4) and then estimate the same source location for the associated wind field under the moving storm, following fetch-law constraints recast in a Lagrangian model (Kudryavtsev et al., 2015, sec. 4.5). Based on these findings, we use idealized models of moving constant or continuous wind to characterize the different regime of extra-tropical storms and the resulting waves (sec. 4.6). Finally, we show how swell events are constrained by the scales of the storm (sec. 4.7) and put wave events derived from idealized models in the context of observed storm statistics (sec. 4.8).

4.3 Methods

4.3.1 Focal Point Identification

The swell focal points are derived by estimating the slopes of the peak swell arrivals in multiple wave-buoy stations simultaneously. We extend the algorithm from Chapter 2, originally developed for a single wave event, to multiple stations in order to find the location of their common swell source. In the following, we outline the conceptual idea of the optimization, while Appendix C describes further details.

Data and Model function

Initially, the data in each wave buoy observation are treated independently. Each of the chosen wave buoys (CDIP 166, CDIP 179, CDIP 029, CDIP 067, CDIP 106) samples the directional wave spectrum in 30-minute averages. The wave buoy spectrograms and their directional information are retrieved from the CDIP datawell (Behrens et al., 2019). Local swell maxima are identified in the spectrograms by averaging over the first three frequency bins whose spectral amplitude exceeds e^{-1}. This results in a time series of the amplitude of the longest swell waves that is sensitive to the amplitude and frequency slope of the swell and. This time series is

band-pass filtered for timescales between 18 hours and 7.5 days using a Lanczos filter to retain variability that is mainly related to atmospheric synoptic scales. Examples of the identified swell maxima, also called swell forerunners, are shown in figure 4.1b to e (black dots).

The incident directions of the swell forerunners are used to weight the observed spectrograms. The separately stored directional components of the wave spectrum $D_\theta(\theta, f, t)$ are use to create a weight for the omnidirectional spectral amplitude $D_{amp}(f, t)$ (here, f is the wave frequency and t is time). Frequency bands with wave energy in the same direction as the swell forerunners have a weight of one, while frequency bands that contain energy from a different direction have a weight close to zero. This selects wave energy in a $\pm 15°$-angle around the peak direction of the swell forerunners and filters out secondary swell systems or locally generated higher frequency waves if they come from a different direction.

The second step of the data preparation identifies events and isolates them for the optimization procedure. The initial dispersion slope of each swell event is estimated by the difference between the prior identified local maxima (Fig. 4.1b to e, black dots) and a local maxima on a frequency band that is 0.01Hz higher compared to the prior identified local maximum. This slope between the two local maxima on different frequency bands is used to select and initialize each wave event following Chapter 2.

The pre-identified single wave events are then used to fit a model of swell arrival to each case individual (Chapter 2). The model is defined in frequency f by the standard JONSWAP spectrum

$$\begin{aligned} S(f) &= \frac{\alpha_S\, g^2}{(2\pi f)^5} \exp\left[-\frac{5}{4}\left(\frac{f}{f_m}\right)^{-4}\right] \gamma^\delta, \\ \alpha_S &= 0.076 \left(\frac{f_m\, U}{3.5\, g}\right)^{2/3}, \\ \delta &= \exp\left[-\frac{1}{2}\left(\frac{f - f_m}{\sigma_S\, f_m}\right)^2\right], \end{aligned} \tag{4.3.1}$$

with f_m as the peak frequency of the spectra, $\sigma_S = 0.07$ for $f \leq f_m$ and $\sigma_S = 0.09$ for $f > f_m$, and γ_{par} as the amplitude of the peak-enhancement factor (Hasselmann et al., 1973). In time, the model is defined as a form of a χ^2- or Erlang distribution such that

$$K(\tilde{t}, \tilde{t}_m) = \frac{\tilde{t}_m}{\sigma_K} \, e^{-\tilde{t}_m},$$

$$\tilde{t}_m = \frac{\tilde{t} - \tilde{t}_0 + f \; m_t}{\sigma_K}, \tag{4.3.2}$$

where $\tilde{t}$ is the non-dimensional time, the relative time of the selected data divided by its time span Δt, $\tilde{t}_0$ is the non-dimensional initial time, m_t is the slope of the peak frequency in the spectrogram in units of Hz^{-1}, and σ_K a parameter that controls the width of the distribution (Chapter 2).

The attenuation of the swell along the travel path A is modeled with a simple exponential decay that does not depend on direction (Ardhuin et al., 2009). Since the decay only depends on the distance traveled along a great circle path r_0, it is directly related to the spectral slope m_t (Munk, 1947). Hence, the attenuation model is defined as

$$A(m_t, \mu) = exp\left(-\mu \; \frac{g \; m_t \; \Delta t}{4\pi}\right), \tag{4.3.3}$$

where $\mu \approx 3.7 \; \pm 0.2 \; 10^{-7} \; \mathrm{m}^{-1}$ (Jiang et al., 2016). This simple attenuation model allows the spectral power at the origin to be estimated from the observed swell spectrogram alone, assuming that distortions by other processes are small.

The 2-dimensional model function for the individual events $\boldsymbol{M}^k$ is then defined as

$$\boldsymbol{M}^k(\tilde{t}, f) = A(m_t, \mu) \; K(\tilde{t}, \tilde{t}_0, m_t, \sigma_K) \; S(f, U, f_m, \gamma_{par}), \tag{4.3.4}$$

where $\tilde{K}(\tilde{t}) = K(\tilde{t}) / \max(K)$ is the peak-normalized time component such that the amplitude of

$\boldsymbol{M}^k$ is solely defined by the initial spectral power of S and the attenuation A. The to-be-optimized parameters are summarized as

$$\vec{p}^{\,k} = \{m_t, \mu, \tilde{t}_0, U, f_m, \gamma_{par}, \sigma_t\}. \tag{4.3.5}$$

Those parameters are optimized using a gradient-descent method with a regularized cost function and the uncertainty of the optimization is estimate using a Monte-Carlo method (Newville et al., 2014; Foreman-Mackey et al., 2013). This procedure follows Chapter 2 and the differences described in Appendix C.

The fitting of $\boldsymbol{M}^k$ to the pre-identified swell events at five stations between the year 2014 to 2018 resulted in about 77 successfully fitted wave events per station per year. After quality control, only about 56% of these cases can be bundled to sets of observed events with a common source (Appendix C).

Multiple-stations cost function

The individual model fits provided estimates of the time t_0 when each wave event was generated (sec. 4.3.1). These times were used to pair up wave events between the five stations (Appendix C.2), which resulted in 31 sets of swell events that had a common t_0 from all five stations. Many other events are distorted by noise at the station or the wave ray refraction on their path through the ocean (Gallet and Young, 2014; Villas Bôas and Young, 2020).

The sets of swell event observations were then used to reassess the model parameters by adding the constraint of a common source. Hence, the optimization problem was reformulated in terms of parameters describing a common swell event from a single location

$$\vec{p}_m = \{\lambda, \phi, t\}, \tag{4.3.6}$$

with the longitude λ, latitude ϕ, and time t define the source location. The slope parameter m_t

and attenuation μ at each station k were calculated based on the common source position. Other parameters of the model $\boldsymbol{M}^k$ were set to the five-station mean of the individual fitted parameters and do not vary during the multi-station optimization. This reduces the search space of the optimization procedure and allows for faster optimization. Alternatively, the parameter space $\vec{p}_m$ could have been extended with parameters that describe the spectral shape as well, but the larger parameter space required larger computational efforts. Here we focused on the source location and time, which only requires changes of the dispersion slope, timing, and amplitude.

The parameters for each station $\vec{p}^k(\vec{p}_m)$ are calculated at each function evaluation of the multi-station optimization. The cost function for the multi-station optimization is defined as

$$J_m = \sum_k \frac{w^k_{err}}{\sum_i w^i_{err}} J^k, \tag{4.3.7}$$

where w^k_{err} is a measure of the fit derived from the prior fitting procedure and J^k is the regularized cost function for each individual event k (eq.C.2). A $w^k = 1$ expresses a perfect model fit, while a $w^k = 0$ would describe a complete failure of the optimization at the individual station. The weighting emphasizes station data with a high signal-to-noise ratio rather than uncorrelated noisy data that might appear in some cases. This methodology can be easily extended to incorporate more data from other observations.

The parameters $\vec{p}_m$ are not regularized to allow a more unbiased search of the source location. However, the search space is limited to the North Pacific (20°N-60°N, 140°E-120° W) and ±2 days around the 5-station mean of the individual fits.

The sets of matched observations are used to explore the multi-station cost function with two independent methods. The first method is a brute-force sampling in the 3-dimensional parameter space of $\boldsymbol{p}_m$ and creates a time-varying map of model fit using eq. C.3. This map can be interpreted as a likelihood of wave origin in space and time (sec. 4.4). The second method uses simplicial homology global optimization (SHGO, Endres et al., 2018) followed by the dual

annealing method (DA, Tsallis, 1988; Tsallis and Stariolo, 1996; Xiang et al., 1997). Both methods are developed for fast convergence to the global optimum of the relatively complex cost-function.

4.3.2 Fetch laws in a moving frame of reference

The peak circle frequency ω_p of a wave spectrum that is generated over a certain duration T or distance d by a wind of constant speed u is conventionally described by the so-called spatial or temporal "fetch relations"

$$\omega_p^{\text{space}} \frac{u}{g} = c_\alpha \left(\frac{d\ g}{u^2} \right)^q, \tag{4.3.8}$$

$$\omega_p^{\text{time}} \frac{u}{g} = c_{\alpha t} \left(\frac{T\ g}{u} \right)^{q_t}, \tag{4.3.9}$$

where u is the 10-m wind speed, g is the gravity acceleration, c_α, $c_{\alpha t}$, q, and q_t are constants defined in Appendix D. For the situation of wave growth, self-similar laws relate the resulting wave energy E, significant wave height H_s, or peak period T_p, and read

$$\frac{E\ g^2}{u^4} = \frac{H_s^2\ g^2}{16\ u^4} = c_e \left(\frac{d\ g}{u^2} \right)^p \sim \frac{u\ g^2}{2\ \omega_p^3}, \tag{4.3.10}$$

where c_e is a constant (Kudryavtsev et al., 2015; Hasselmann et al., 1976). The energy of the generated wave field E travels with the group velocity of deep water waves $c_g = \partial_k \omega_p = \sqrt{g/k}/2$, such that the wave fields will travel faster for a longer fetch d or for longer forcing time t.

The wind's movement under the storm must be taken into account to describe waves generated by the wind fetch under the storm. Here we formulate the swell wave generation in a Lagrangian frame of reference, i.e., the frame of a moving fetch (sec. 4.5, Kudryavtsev et al., 2015). We start with the Eulerian wave growth equation from Hasselmann et al. (1976) that

describes the evolution of the spectral peak ω_p of a non-linear sea

$$\frac{\partial \omega_p}{\partial t} + c_g^p \frac{\partial \omega_p}{\partial x} = \left(\frac{g}{u}\right)^2 \phi(\alpha), \tag{4.3.11}$$

with the peak group velocity $c_g^p = g/2\ \omega_p$, the wave age $\alpha = u/c_p^p$, the ratio of the 10-m wind speed u and phase velocity of the spectral peak $c_p^p = g/\omega_p$. The source term is defined as

$$\phi(\alpha) = \frac{1}{2}\ q\ c_\alpha^{1/q} \alpha^{-1/q} \tag{4.3.12}$$

with $10.4 < c_\alpha < 22.7$, and $q \in \{-3/10; -1/4; -3/14\}$ for very young, growing and mature seas respectively.

The wave growth equation (4.3.11) is transformed in a Lagrangian frame of reference – the frame of the storm – that moves with a translational velocity V, such that

$$\partial_t \omega_p + (c_g - V)\ \partial_X \omega_p = \left(\frac{g}{u}\right)^2 \phi(\alpha). \tag{4.3.13}$$

where $X = x - Vt$ is the along-wind coordinate in the moving reference frame. This equation describes the evolution of a growing sea in the moving frame of reference with the coordinates (X,t), while the forcing function $\phi(u, \omega_p)$ is still a function of the local wind speed $u(X,t)$. It is a non-linear 1st-order partial differential equation and is solved using the method of characteristics with various levels of complexity of u (sec. 4.5.1 and 4.6).

4.3.3 Surface wind and storm track data

The 10-meter winds and sea level pressure (SLP) fields are taken from the hourly ERA5 analysis on a 0.25 °-grid (European Centre for Medium-Range Weather Forecasts fifth-generation reanalysis for the global climate and weather , CDS). However, the storm tracks are derived from 6-hourly ERA-interim SLP fields (Dee et al., 2011). They are identified from the SLP data in both

hemispheres using the algorithm detailed in Murray and Simmonds (1991). Only storm tracks are used that last at least 24 hours, travel for a minimum of 300 km, and exceed at least a pressure gradient of two $hPa/\text{Latitude}^2$. The remaining storm track statistics are derived separately for the four seasons and both hemispheres outside of ±10° N/S.

4.4 Observed Swell Origins compared to wind observations

Optimizing the parameters $\boldsymbol{p}_m$ on the cost function J_m is a triangulation for a common source in longitude, latitude, and time. It means that the cost function can be directly interpreted as a likelihood of wave origin in space and time. Figure 4.2 illustrates this for observations between the 4th and 8th of January 2016. Both optimization methods – SHGO/DA and brute-force – suggest a source location south of Ocean Station Papa (CDIP 166) in the early morning of January 4th, 2016 (green hexagon in Fig. 4.2a,b). Both locations are similar, especially compared to the resolution of typical wind data (25 km).

Even though both methods return the same location, they lead to somewhat different interpretations. The global SHGO/DA optimization returns a single glocal optimum, which agrees with the assumption of a common wave source. In contrast, the brute force method can be directly interpreted as a likelihood map of swell origins, which, in principle, can resolve multiple sources. Hence it is less precise then SHGO/DA (compare grey shadings in Fig. 4.2a,b), but it resolves a larger parameter space more effectively.

The brute force method also shows a shift of the most-likely swell origin with time. The black dots in figure 4.2a are the local likelihood maxima at several measurement times: their progression in space is a temporal track of the most likely swell origin.

This is another advantage of the less precise but faster brute force method: Even though the SHGO and brute force methods explore the same cost function, the track of cost function minima from the brute force sampling extends the idea of a single-point source to a progression

of point sources, and hence allows tracking the swell source. It reveals that a single point source location is a too simple model for the swell origin (Munk, 1947) and that the global minimum (Fig. 4.2, green hexagon) may be interpreted as the center of a progression of origin points. This track of origin points comes from an ensemble of similar good fits to a linear inverse model that allows some physical interpretation. Note that a reconstruction of the observed swell arrivals by a superposition of swell source points using fetch laws and Green's functions might be possible, but it will still fall short in describing the non-linear dynamics leading to one coherent swell event (sec. 4.6).

The optimization of the multi-station cost function is difficult due to local wind swell or wave-current interaction distorting the observations at one or more wave buoys. A weak signal-to-noise ratio can lead to no meaningful results and a failure of the model fitting. The individual parametric wave models for this source location are compared to the respective observations in figure 4.2 c to g. The parametric model captures the observed dispersion slopes in four out of five cases. The comparison of the model with CDIP 106 data, close to Hawaii, (Fig. 4.2e and Fig. 4.2b red dot) indicates modeled wave arrival about one day later and further away than the observation. Hence, the observed wave event at Hawaii could (i) result from a closer source than the best model fit suggests or (ii) still be related to the same storm system, but the waves arriving in Hawaii have a different effective fetch than the waves observed further north.

The estimated source locations are compared to reanalysis winds to analyze the occurrence of swell source locations that are neither point sources nor large areas relative to the size of the wind forcing. As an example, figure 4.3 shows the wind speed (shading) and direction (arrows) as well as negative sea-level pressure (SLP) anomalies (purple), at the reanalysis time closest to the time of most likely wave origin for the situation analysed above (Fig. 4.2). As the storm propagates eastward, its associated highest surface winds (fetch) move eastward as well (red area at 45°Nand 150°W); and with it, the most likely wave origin. However, the moving wave origin is systematically ahead of the highest wind speeds (Fig. 4.3a,b,c). This systematic displacement of

the wave origin, estimated from observations (sec. 4.3.1), to the highest wind forcing, estimated from reanalysis, stems from the process of swell generation by a moving fetch. Because the fetch is moving in the same direction as wave energy, wave growth can continue longer than under a stationary fetch, such that frequency dispersion is delayed. This delicate balance between wave growth, storm velocity, propagation speed of wave energy, and onset of wave dispersion is explored in the next sections.

4.5 Swell wave generation by a moving fetch

The systematic displacement between the area of high wind speed (fetch) and the swell origin suggests the following picture of wave growth under a moving storm (Fig. 4.4). A low-pressure system **L** that moves with a translational velocity V has a fetch on its equatorward side, which moves roughly at the same speed as the storm (Fig. 4.4 gray shading). This fetch normally sits behind the cold front of an extra-tropical cyclone and is closely related to the cyclone life-cycle.

The propagation of the fetch (Fig. 4.4 orange arrows) is aligned with its dominant wind direction (Fig. 4.4 blue arrows), and hence, it is also in the same direction as the dominant waves. The source locations estimated in section 4.4 suggests a relatively small area that is situated ahead of the highest wind speeds, close to the storm's cold front (Fig. 4.4 green dot). The backward triangulation method selects this area because it utilizes linear wave dispersion, which means that wave energy radiates away from the source location (Fig. 4.4 gray arrows). In turn, the wave energy must have propagated as a non-linear wave field before it reached the identified source location.

The following subsections explain the processes in the frame of a moving storm (Fig. 4.4) and are based on an idealized storm representation from Kudryavtsev et al. (2015). The discussion will show how the observed source location and observed swell height depend on the parameters

of the storm and explain why the source location is displaced compared to the highest wind forcing.

4.5.1 Computing waves from realistic moving winds

Using reanalysis winds, the observed swell source location can be reconstructed in the Lagrangian frame of the storm. To derive the along-track forcing from the gridded wind product (ERA5), we estimate the path of maximum wave generation from the track of most-likely wave origins (Fig. 4.3 black dots). A least-square line fit to the track of wave origin creates a transect between the points A and B, figure 4.3. This transect is used to derive along- and across-wind observations averaged over a swath width of about $440km$. The time evolution of the along- and across-track velocities between A and B together with the source-location estimates are shown in figure 4.5 a and b.

The area of most likely wave origin can be displaced in space and time compared to the highest wind speeds (Fig. 4.5 green contours). The along-track winds peak around day 2 of the relative time axis, but the most likely origin is at day three and further east than the highest wind speed. It is co-located with the sign change of the across-track winds (Fig. 4.5b). Hence, stationary fetch laws that relate the local wind duration or fetch length to the created wave field do not explain this observation. Instead, this displacement between the wind energy input and the triangulated wave source location suggests some spatial and temporal delay between both processes.

The observed wind data are transformed into the moving frame of reference to understand wave generation under a moving storm. In a first step, the translational speed V is estimated from the along-track velocity data using a least-square fit (Fig. 4.5 a black line). In a second step, the estimated translational velocity $V = 14.1\text{m s}^{-1}$ is used to shift the wind data such that it shows the along-track winds in a moving frame of reference (Fig. 4.6a). The same transformation is applied to the estimated source locations (Fig. 4.6a, green contours).

In the moving frame of reference, the estimated swell source position is at a similar position to that at the highest wind speed, but it is delayed by about one day Fig. 4.6a). This delay can be explained by solving the evolution equation of the peak frequency for a growing sea in the moving frame of reference (eq.4.3.13). It is forced with the transformed Lagrangian wind field and solved numerically using the method of characteristics (Appendix D). They are initialized from a sea at rest ($T_p \approx 0.1$ sec), where the local winds are zero ($u = 0$). The resulting characteristic curves are paths of wave energy that propagate in the moving frame of reference (Fig. 4.6b). Their energy increases as they propagate because ω_p decreases (indicated by the line thickness).

The waves are small at first, which means ω_p will be large. A large peak frequency suggests a slow group velocity $c_g = \partial_k \omega_p$ likely smaller than the fetch's translational velocity V. The initially generated wave energy at any position in the wind fetch travels backward in the reference frame of the storm (Fig. 4.6c, black contours). Some wave energy eventually will leave the storm in the rear even though it travels in the same direction as the storm (Fig. 4.6b black contours on the left). However, most of the wave energy will remain under the storm and continue to grow. The peak frequency will then decrease over time, which leads to a faster propagation of the wave energy and a gradual reduction of the difference between V and c_g. It results in an upward bending of the ray-paths in the moving framework (Fig. 4.6b, black curves).

If the winds are strong enough and/or the moving fetch is sufficiently large, wave growth continues to accelerate the propagation speed under the storm until the group velocity equals the storm's translational speed ($c_g = V$). In this situation, wave energy propagated at the same speed as its forcing, such that the wave energy remain (*trapped*) under the storm (sec.4.6.1). Because the wind continues to supply energy to wave growth, the wave's energy will eventually be faster than the moving fetch ($c_g > V$). Now, the wave energy propagates to the front of the moving fetch.

This process of wave growth and acceleration of the group velocity ends when the wind forcing decreases or wave creation at high frequencies ($\omega > \omega_p$) no longer drives non-linear

wave-wave interactions (Hasselmann and Hasselmann, 1985). When the non-linear wave-wave interactions decay, the wave energies in each frequency band of the wave spectrum start to propagate at their own group speed $c_g(\omega)$. While active wind forcing prevents the wave energy from dispersing due to maintenance of a non-linear sea-state, the lack of wind forcing let the energy flux from wave-wave interactions decay. So, the wave's energy begins to propagate as linear waves. As we show and discuss below, the area where the wave-wave interaction decays and become insignificant is the source location identified by the triangulation (sec. 4.4).

4.6 Simple models of swell generation

To help understand the growth of wave energy spectra under a moving fetch and the observed source location of swell, we compare moving fetch models of different complexity. This analysis reveals how the parameters of the storm are related to wave event energy and shape.

4.6.1 Constant, finite moving wind models

The simplest model that describes wave growth in a moving frame is to consider constant wind u under a storm of length L, steadily moving with constant translational velocity V, during a forcing time T. Constant winds mean a constant forcing $\phi(u, \omega_p)$ (eq. 4.3.13), such that one can seek an analytic solution for ω_p (Appendix D). Figure 4.7 shows the characteristic curves of wave energy derived from eq. (4.3.13) with constant forcing. The characteristic curves $X(t)$ describe the growing wave energy position as it passes through the forcing field. The slopes of characteristics are related to the relative speed of peak wave frequency in the moving frame of reference by

$$\frac{\partial}{\partial t} X \propto (c_g - V).$$

The initial wave energy is small and slow, and propagates backward in the moving frame of reference (Fig. 4.7a day 0 to 1). Even though these young seas propagate slower than the storm,

their energy continues to grow. The peak frequency decreases, so the group velocity of the peak wave energy increases eq. (4.3.10). Eventually, the peak wave energy travels at the same speed as the storm ($V = c_g$, Fig. 4.7, dashed back lines). The time since the onset of the wind and the distance the storm has moved until $c_g = V$ are given by

$$\tau_{crit} = \frac{c_t^T}{g}\, u^{-q}\, V^{1+\frac{1}{q}}, \tag{4.6.1}$$

$$X_{crit} = \frac{q c_t^T}{g}\, u^2 \left(\frac{u}{V}\right)^{\frac{1}{q}}, \tag{4.6.2}$$

where $c_t^T = 2.7 \times 10^5$ and $q < 0$ are constants that describe the efficiency of wave growth and depends on the sea state (Appendix D). The timescale τ_{crit} and length scale X_{crit} are necessary conditions for the growth of large waves, corresponding to the lower limits to trap wave energy under the storm. Both scales also mark a region in the rear of the storm in which waves are generated but left behind. In this region the trapping condition is not fulfilled (Fig. 4.7, light blue characteristics near the origin).

Comparing different storm scales shows that the trapping conditions τ_{crit} and X_{crit} depend on the characteristic scales of the storm (Fig. 4.7a to c). On the one hand, stronger winds decrease τ_{crit} (Fig. 4.7a,b, dashed black line) and X_{crit} (Fig. 4.7a,b black axes), while on the other hand faster propagating storms increase both scales (eq. 4.6.1 and eq. 4.6.2).

Since the trapping conditions depend on the wind forcing and the storm's velocity, both also influence the location and amplitude of the largest wave energy. Trapped wave energy will continue to grow under the storm and will eventually travel faster than the moving fetch ($c_g > V$). This leads to wave energy that propagates forward from the rear of the storm to the front (Fig. 4.7, dark blue curves t_{crit}). It further accelerate and gain wave energy, until reaching the edge of the moving wind fetch.

The longest path is the path that gains the most wave energy and is determined by the storm's scales (Fig. 4.7, dark blue lines). For constant forcing over a finite length and time, the

largest resulting wave energies can be either limited by the storm's length-scale ("fetch-limited", Fig. 4.7a), or by the storm's timescale ("time-limited", Fig. 4.7b). Hence, the location where the largest wave-energy should occur is either where the wave energy propagates out of the wind forcing at the front of the storm (Fig. 4.7a, green dot), or where the wind forcing stops before the path of longest wave forcing reaches the storms front (Fig. 4.7b, green dot). In both cases, there is more than one characteristic curve that generates the largest possible wave energy. Either because there is more than one curve that can describe the longest path (time-limited, Fig. 4.7b), or because the duration of the wind forcing is long enough such that the wave generation under the storm is in equilibrium with the constant forcing (fetch-limited, Fig. 4.7a and c, Appendix D.3). Note, equilibrium fetch conditions are often observed for tropical cyclones (Fig. 4.7c, Kudryavtsev et al., 2015) where the resulting group-velocity of the emitted wave field can be calculated by solving eq. (4.3.13) for c_g assuming a constant peak frequency (eq. D.3).

The effect of changes in the length, speed, and wind forcing on the largest generated group velocity is shown in figure 4.8. For the observed ranges of wind speeds and scales of extra-tropical storms, the fetches can be either time or length limited (Fig. 4.8c), while there is a sharp transition between both types (Fig. 4.8a, black line). This constant-wind model is thus able to outline the general dynamics of swell generation under a moving fetch, but fails to explain why there is an observed single origin of waves rather than a line of origins with the same amplitude (Fig. 4.7a,b). In the next section, we relax the requirement of constant winds to account for the fact that real wind forcing smoothly varies over space and time.

4.6.2 Gaussian moving wind model

To model varying winds $u(X,t)$, the time and spatially varying properties are described by a double-Gaussian that mimics the life cycle of the storm. This model will be shown to explain how the storm's wave energy is focused at a location significantly smaller than the fetch (Fig. 4.6, green shading).

The double-Gaussian wind model is defined by a wind speed maximum in the center of the fetch u_{max}, a 95%-width, and a 95%-duration. These measures correspond to the 95%-extent of a Gaussian curve, which is about ±2 times the standard deviation. Solutions of eq. (4.3.13) for two extra-tropical storms with Gaussian winds are shown in figure 4.9 a and d. A storm with a 95%-fetch-width of 1000 km, a 95%-duration of 3.6 days and u_{max} = 10 m s^{-1}shows characteristic curves similar to the fetch-limited case of constant winds (Fig. 4.9a, Fig. 4.7a). The major difference compared to the constant wind case is that the curves converge and cross near the storm's leading edge at the end of the storm's lifecycle (Fig. 4.9a, day 2.5-3). The convergence of characteristic curves in a focus area appears due to spatial gradients in the Gaussian wind-forcing. It does not appear with constant wind forcing by a Heaviside function (sec. 4.6.1). Hence, any fetch that is continuous but has a local wind maximum will have spatial gradients and will focus characteristic curves from different parts of the moving fetch.

The convergence of the characteristic curves indicates a focusing of wave energy, with the superposition of wave trains and the formation of a caustic. The method of characteristics provides separate solutions to the PDE on each curve. However, it does not capture the convergence or crossing of wave energy and subsequent sea state responses. Hence, the appearance of a caustic can be interpreted in the following way: The convergence and crossing of curves indicate that sea states with different generation histories (different paths of integration) propagate to the focal area and locally enhance the wave energy spectrum. Enhanced wave energy will lead to increased dissipation and more active non-linear wave-wave interactions (Phillips, 1958; Hasselmann and Hasselmann, 1985), i.e. the convergence of wave energy can add as another forcing term to eq. (4.3.13). Hence, the largest estimated wave energies on the characteristic curves (Fig. 4.9b, light blue to red curves) are likely lower estimates, because independent curve solutions do not cover the expected enhanced dissipation and non-linear wave-wave interactions due to wave energy convergence. Further analysis of this critical situation for swell generation remains for further studies. Nevertheless, the proposed model is sufficient to explain the governing relations between

the fetch scales and the moving storm, although it might have a systematic bias to lower wave energies or higher peak wave frequencies.

This convergence of wave energy, or focal points, is directly sensitive to gradients of the wind field. In the Gaussian wind model, spatial gradients are proportional to the ratio of u_{max} and the 95%-width. Figure 4.9d shows a moving fetch with the same parameters as in figure 4.9a, but for a weaker peak wind speed and hence a weaker spatial gradient. Compared to strong wind conditions, the location where the characteristic curves cross under weak winds is more delayed (Fig. 4.9d,a). Also, the resulting group velocities are lower for a lower peak wind speed because the trapping condition $c_g = V$ is reached later compared to the strong wind case (Fig. 4.9d, e). This is one example of how the storm's parameters can impact the generated peak period. The impact of other parameters is described in section 4.7.

The largest generated wave group velocity c_g depends on the wave energy's integration path under the moving forcing field. This is especially important during the storm's decay, where the sea state is mature while the wind forcing is relatively weak (Fig. 4.9 after day 2). Old seas are normally identified by the wave age ($\alpha = 2\ c_g/u_{10}$), and figure 4.9 c and f shows the wave age for the chosen characteristic curves in panels a and d. The wave age remains small ("young") as long as the wind forcing increases inline with the wave energy. However, once the wave energy passes the location of the peak wind speed, the wave age rapidly increases. Wage age can capture the difference between a growing and established sea, but in this simple model it fails to describe the advancing sea state during wave growth, because the winds and sea state increase simultaneously (Fig. 4.9 c,f day 0 to 2, or 2.5).

The Gaussian moving wind model reconstructs the observed focal point for the case study used in section 4.4. By matching the scales of the observed Lagrangian wind field (V = 14.1m s^{-1}, u_{max} = 22m s^{-1}, a 95%-duration of 4 days and 95%-width of 2800km), the largest generated wave energy along a characteristic curve appears at a similar and location as the observed focal point (compare Fig. 4.10 with Fig. 4.6 green dot and area). This shows that a Gaussian moving

fetch is a simple but useful model of swell generation.

4.7 Characteristic scales of extra-tropical Storms shape wave events

Here we describe how changes in the scales of extra-tropical cyclone can shift the focal point of wave energy convergence, create different peak group speeds c_g, and be related to wave energies. As before, we calculate characteristic curves using eq. (4.3.13), but now for various combinations of storm sizes, duration, speeds, and wind forcing. For each set of boundary conditions, we take the largest resulting group velocities to test the sensitivity of c_g on the storm scales. Because the characteristic curves overlap, and their wave energies merge (sec. 4.6.2), the largest c_g from a single curve is likely an underestimation of the actual c_g. However, it is still a good tracer to show changes in the dynamic regime.

Comparisons of the peak velocity u_{max} and translation velocity V for typical scales of extra-tropical cyclones are shown in figure 4.11a (95%-width and -duration are $1000km$ and 3.5 days, Eady, 1949, see below). The two cases from 4.9 are indicated by black triangles and illustrate how changes in the peak wind speed lead to different peak wave energies. Higher peak velocities or faster-moving storms lead to higher group velocities (Fig. 4.11a green shading). However, if the storms move too fast, wave growth is limited because trapping of wave energy is weaker or does not appear at all (Kudryavtsev et al., 2015, Fig. 4.11a, to right of the dashed black line). No trapping appears for fast storms with relatively weak winds, which is probably uncommon for the observed characteristic storm scales (sec. 4.8).

The fetch and duration also affect the wave energy generation (Fig. 4.11b). For typical but constant translation velocities and peak wind speeds, the wave energy increases when the storm is larger or lasts longer. However, more persistent storms are more effective at creating larger wave energies than larger storms. For example, changing in the storm size by 20% to about 1200 km

has a weaker effect than changing the storm's duration by one day. The importance of the storm's duration is again due to the trapping condition (sec. 4.6.1) because trapping will always occur if the storm lasts long enough.

4.8 Storm track variability drives changes in wave events

Here we relate the wave energies from Gaussian wind models to statistics of the storm track speeds and lifetime (Fig. 4.12). The wave energies are described in terms of the largest generated peak period. The peak period is proportional to the energy of the generated wave event, as it would be observed at a wave buoy (eq. 4.3.10).

Northern Hemisphere (NH) storms are generally smaller in area and faster in winter than in summer (Fig. 4.12a,b blue and red contours). Changes in both these parameters only result in a difference of 0.5 m s^{-1}or a given peak velocity and scale of u_{max} = 10 m s^{-1}, and 1000 km (Fig. 4.12a red and blue dot). Changes in storm's speeds and sizes are thus not enough to explain the observed seasonal difference in peak periods for North Pacific, or North Atlantic storms. Observed differences likely stem from seasonal changes in peak wind velocities u_{max} (Fig. 4.12b). Changes in the peak velocity u_{max} have indeed a larger effect on the peak period than the storm's size since more intense wave growth leads to earlier wave energy trapping (compare Fig. 4.12a and b, Fig. 4.11b, sec. 4.6.1). Hence, the peak velocity is an important parameter for the generation of large waves.

The Southern Hemisphere (SH) shows larger variability of the storm's lifetime than the NH (Fig. 4.12c and d). Austral summer storms appear to last between 3 and 5 days and propagate between 8 and 10 m s^{-1} (Fig. 4.12c red contours and dot). In contrast, austral winter storms are generally more variable, faster, and shorter living (Fig. 4.12c blue contours and red dot). This results in a seasonal difference of 1.3 sec for the typical peak periods, which is more than double the NH difference. It means that even if there is no change in the storm's peak velocity, austral

summer storms will generate larger wave events than austral winter storms. However, since the wind variability and peak velocities over the SO are mainly driven by the Southern Annular mode (SAM, Chapter 5), changes in the peak wind speeds might have a larger effect on the variability of the generated wave events than the storm's size or speed.

4.9 Summary: A life-cycle of a swell wave

Swell waves are the residual of intense wave generation under tropical and extra-tropical storms. Here we have used standard wave buoy observations of ocean swell in the eastern Pacific to identify the storm system that generated wave events. We have used a 2-dimensional parametric swell propagation model that is a combination of standard swell spectra, a prescribed time decay, and the deep water wave dispersion (sec.4.3.1). This model is optimized on data from five wave buoy stations simultaneously to triangulate a source location using two different optimization methods. While a search for a global minimum provides a single source location as the inversion the linearly dispersed swell arrivals suggests, a brute-force sampling of the cost function returns a progression of likely origin points in space and time (Fig. 4.2). This progression – or track – of estimated wave origins is used to sample the wind forcing field along its major axis (Fig. 4.2). This along-track wind forcing is transformed to the frame of reference of the moving storm, and we showed that the estimated swell source location is systematically displaced compared to the strongest winds.

This displacement of the most likely wave origin can be explained by solving the evolution equation of wave growth in the frame of the moving storm (Hasselmann et al., 1976; Kudryavtsev et al., 2015). The swell origin is displaced because wave energy in the different frequency bands is coupled through non-linear wave-wave interaction during wave growth, prohibiting frequency dispersion. Frequency dispersion starts once the wind forcing and the wave-wave interaction decay. Hence the swell life-cycle can be described in three stages:

- **Stage 1: Wave growth under a moving fetch**

  Starting from a sea at rest, wind forcing creates short waves that drive wave-wave interaction and wave growth. The wave-wave interactions lead to a continuous decrease of the peak frequency ω_p, while the total wave's energy (H_s) increases. An actively growing wave field means that the wave energies in different frequency bands are strongly coupled through wave-wave interactions, and this coupling prohibits frequency dispersion. The energy of the non-linear sea state travels with the group velocity of ω_p, such that a reduction of ω_p leads to an acceleration of the non-linear sea.

  Because the wave energy and the wind forcing propagate and move, wave generation over the open ocean must be understood in the reference frame of the storm (Fig. 4.4, Kudryavtsev et al., 2015). The initial peak group velocity is slower than the velocity of the moving storm, such that that the wave energy propagates to the rear of the storm. However, as the wave energy continues to grow, its peak frequency decreases, accelerating the associated group velocity. Eventually, the wave energy will propagate with the same speed as the wind forcing, such that the wave energy is trapped under the storm (sec. 4.6.1). The wave growth will only decay if the wave energy leaves the storm at the leading edge or when then wind forcing reduces (fetch- or time-limited, Fig. 4.7). The trapping condition generally depends on the ratio of the wind speed and the translation velocity, such that wave energy is more easily trapped if the translation velocity of the storm is small or the forcing wind speed is high (sec. 4.6.1, eq. 4.6.2).

- **Stage 2: Decay of non-linear Terms**

  Once the wind forcing decays, the steep non-linear sea decays as well. Less wind forcing leads to weaker and eventuelly negligible wave-wave interaction, and a transformation to a more linear sea. The timescale on which the non-linear terms in the wave-action

equation decay is about three hours (eq.F.1, Zakharov and Badulin, 2011; Zakharov et al., 2019). During this time, the wave field transforms from a non-linear sea state (steep wave spectrum) to a dominantly linear sea state (flatter wave spectrum). However, because the wave field still propagates during this relaxation time, the location where the wave spectrum is dominantly linear is different from the location where the wind was acting on growing waves. This relaxation time largely explains the displacement between the detected origin of swell and the wind forcing (Fig. 4.6).

Note that the non-linear terms decay faster for higher frequencies than for lower frequencies. Compared to longer waves, shorter waves are earlier dominantly linear, which implies that they also disperse earlier. This frequency dependence explains the identified track of wave origins (Fig. 4.3).

- **Stage 3: Linear Propagation**

  Once the wave field is linear, the wave energy in each frequency band propagates following deep water waves' dispersion relation. From this point on, the travel distance and energy attenuation are proportional to the amount of dispersion, which in turn is the difference in the arrival time between waves of different frequencies (Barber and Ursell, 1948; Munk, 1947). Hence radial distance and attenuation can be estimated by the dispersion slope eq.(4.3.3).

4.10 Discussion and Conclusion

Swell wave generation from extra-tropical storms is a long-standing problem of oceanography (Munk, 1947). Here, we have represented a comprehensive explanation of why swell seem to originate from a location that is not the same as the wind forcing. Ocean swell systems result

from a three-stage process of wave growth, relaxation of the non-linear terms, and linear swell propagation (sec. 4.9). The transition between the growth and decay of waves is the reason for the displacement of an observable swell-source location and the area of the strongest wind energy input (Fig. 4.4). During wave growth, spectral wave energy fluxes prohibit frequency dispersion. Once the wind forcing decays, the wave-energy flux decays as well, and the individual waves become linear. The wave energy in the different frequency bands is now uncoupled and can travel as dispersive linear deep water waves.

We employed a double-Gaussian model of wind forcing by a moving storm. The model assumes that the storm and its cold sector travel with a constant translation velocity. This simplifies the problem but can still capture the main life-cycle of an extra-tropical cyclone (Neiman and Shapiro, 1993; Neiman et al., 1993). In reality, the storm's speed or the speed of the fetch might also change with time. However, for our demonstrative purpose, a double-Gaussian model of constant speed is a sufficient minimal model to reproduce the observed source location (Fig. 4.10). This analysis then provides original means to connect observed swell events to dynamically parameters of storms. It confirms that swell can be used as a remote observation of storms over the open ocean. Furthermore, because areas of intense swell generation under storms are areas of intense heat fluxes (Schulz et al., 2012; Ogle et al., 2018; Tamsitt et al., 2020), swell is also a marker of intense air-sea interaction.

The Gaussian wind model is used to explain how observed swell events (Fig. 4.1) are related to the scale of the moving fetch (Fig. 4.11 and Fig. 4.12). Four parameters characterize the moving fetch; its translation velocity V, its length-scale along the peak wind direction (95%-width), its lifetime (95%-duration), and its peak wind speed u_{max}. All of them are determined by synoptic dynamics. Processes that influence the cyclone's intensity may also influence the shape, amplitude, and peak period of the observed swell events (Fig. 4.12). This links the current and future swell wave climate to common diagnostics of extra-tropical storms (Schultz et al., 2018; Hoskins et al., 1985; Schemm and Wernli, 2014) and their statistics (Charney, 1947; Eady, 1949; Andrews and

McIntyre, 1976; Bengtsson et al., 2006; Mbengue and Schneider, 2016; Shaw et al., 2016, and others)

The idealized model of a moving fetch suggests that wave events are most sensitive to the peak wind speed u_{max} because wind speed determines the spatial gradient of the wind forcing and hence the scales for trapping wave energy (sec. 4.6.1, Fig. 4.11 and Fig. 4.12). A stronger spatial wind gradient leads to more efficient trapping of the wave energy, which leads to larger swell waves. At the leading edge of the moving frame, the spatial wind gradient is related to the complex dynamics at the storm's cold front. The Gaussian wind model (sec. 4.6.2) may not capture this small-scale wind gradient near the cold front well, but it can be easily extended by introducing non-Gaussian corrections to the spatial wind distribution.

A moving fetch with any non-constant winds will have spatial wind gradients leading to convergence of wave energy (sec. 4.6.2). A convergence of the characteristic curves from different regions of the moving fetch can create a focal area, indicated by crossing characteristics (Fig. 4.9). Even though we did not analyze these hot-spots in detail, we conclude that they must correspond to intense non-linear sea states. The convergence of wave energy may lead to additional dissipation and/or additional wave-wave interaction, which intensifies swell wave growth and peak frequency down-shifts. The convergence of additional wave energy might act as an additional forcing term (eq. 4.3.13), to which the equilibrium range can adjust rather quickly. This means that these locations also correspond to enhanced breaking regions over which part of the wave energy is dissipated in the upper ocean, and hence is where the storm fetch excites the largest stress on the ocean. Accordingly, we can speculate that the location of the strongest winds may not necessarily be the place of largest momentum transfers nor the observable origin of swell (see above).

Reanalysis products have known biases in their representation of wind extremes (Gille, 2005; Hell et al., submitted to Jclim). Wind extremes in the mid-latitudes occur under storms and are represented in the Gaussian model as the peak wind speed. The sensitivity of the resulting swell peak period to the peak wind speed (sec. 4.7) indicates that biases in wind extremes likely

cause biases in wave models by altering the processes of wave growth. Errors in the peak wind speed of a few meters per second change the spatial wind gradients, alter the location of the highest energy convergence, and the location where the swell energy starts to travel as linear waves. It would mean that wave models can be improved by proving mid-latitude surface wind distributions in reanalysis.

Air-sea fluxes of heat, momentum, and CO_2 are parameterized by the standard bulk flux formula (Fairall et al., 2003; Edson et al., 2013). The wave field contribution to these fluxes is often described by wave age $\alpha = 2u/c_g^p$. Our analysis suggests that wave age at many locations under a moving storm cannot be explained by local parameters alone (Fig. 4.9, c, f). Because the local wave energy results from the moving wind fetch, its group velocity c_g^p is constrained by the wind forcing the wave energy was exposed to before. It introduces a non-local condition on the momentum transfer between the atmosphere and ocean. This means that feedbacks between the wave spectrum and the turbulent spectrum of the atmosphere (Ayet et al., 2020; Zou et al., 2020), often parametrized by wave-age (Edson et al., 2013), can only capture this non-local condition when the wave spectra are simulated rather than assumed. Or, alternatively, the wave spectrum should be characterized by metrics additional to wave age.

Appendices

C Optimization Procedure

C.1 Initial optimization

The model function $\boldsymbol{M}^k$ eq. (4.3.4) depends on 7 parameters

$$\vec{p} = \{m_t, \tilde{t}_0, U, f_{peak}, \gamma_{par}, \sigma_t, \mu\}^T, \tag{C.1}$$

that are optimized to find the best fit of the model to the data $\boldsymbol{D^k}$. The cost function for a single wave event at station k is adapted from (Chapter 2) such that

$$J^k = \left\| \left(\boldsymbol{D}^k - \boldsymbol{M}^k\right)\boldsymbol{w}^k \right\|^2 + \left\| \frac{\boldsymbol{p_0} - \boldsymbol{p}}{\boldsymbol{p_\sigma}} \right\|^2, \tag{C.2}$$

where $\boldsymbol{p_0}$ is the initial guess of the parameters derived from the data, and $\boldsymbol{p_\sigma}$ is the priors of the model parameters taken from (Chapter 2). The data weighting function $\boldsymbol{w}^k$ describes double-Gaussian weight around the center of the event such that noise at the corner of the data is excluded (Fig. 4.2 dark shading in b to f, section.2.6.d).

The cost function is optimized with three-stage optimization procedure. An initial semi-random 'basinhopping' search finds the minimal cost varying only m_f and $\tilde{t}_0$ to determine the best model slope that goes through the pre-identified forerunner point (Wales and Doye, 1997). In a second step, the cost function is minimized by varying all parameters using the Levenberg-Marquardt Algorithm (Newville et al., 2014, LM, damped least-squares,) and finally, a *posteriori* error distribution is derived with a Parallel Tempering Markov-Chain-Monte-Carlo (PTMCMC, Goodman and Weare, 2010; Foreman-Mackey et al., 2013; Earl and Deem, 2005).

C.2 Identifying and optimizing common swell source

To derive the initial swell spectra and common source location we combine the identified and fitted wave event in all five wave buoys. The initial time estimates and their uncertainty estimates for the year 2016 are shown in Figure 4.13. Blue lines are two-standard deviation uncertainty ranges around estimated initial times that pass a quality criterion of good model fit (Chapter 2), while light green lines show the initial time uncertainties that do not pass this criterion. Red blocks indicate time ranges where two or more initial time estimates overlap. These events are used to triangulate the source locations in the north pacific (longitude and latitude) from the radial distance estimates of the identified overlapping subset. Figure 4.2 illustrates that

by far not all initial time estimates are good enough and the not all initial time estimates coincide. To account for this, the triangulated location and time from the identified subset of wave buoys are used to re-select data from the not identified wave buoys by forward propagating the model M and estimating the slope and model shape at the buoy location. The the now selected data in the additional wave buoys is fed in to the parameter estimation described in Appendix C.1. This results in five data array from each wave buoy that likely contain observations from the same swell event.

Using this procedure, only about 7.5 events per year are well observed at 2 ot more wave buoys, while about 50-70 event per year are identified in each wave buoy. That low matching rate is a) due to an insufficient initial detection algorithm based on the forerunners of swell (sec. 4.3.1), b) noise by local wind swell at buoy locations, c) deflection of waves by currents, and finally d) the fact that not all wave events cover the north pacific such that they are detected by multiple wave buoys.

The multi-station cost function is than defined as the sum of the individual costfunctions (4.3.7) weighted by the fit of the prior individual fits. The weight for each station k is defined as

$$w_{err}^{k} = 1 - \frac{\left\| \left(\boldsymbol{D}^{k} - \boldsymbol{M}^{k}\right)\boldsymbol{w}^{k} \right\|^{2}}{\left\| \boldsymbol{D}^{k}\boldsymbol{w}^{k} \right\|^{2}}, \tag{C.3}$$

where $\boldsymbol{w}$ is again the geometric weight of the event (Fig. 4.2 dark shading in b to f, (section 2.6.d). This allows emphasis data at stations with clear wave arrivals versus stations with more noise. The fractional error e_f, as a measure of misfit between the data and model, is defined as

$$e_f = \frac{J_m}{\sum_i^N (D^i\ w^i)^2}. \tag{C.4}$$

D Solution of the advection equation in the (X,t) plane

D.1 Stationary solution

In the following, we solve the advection equation (eq. 4.3.13, Kudryavtsev et al., 2015), for stationary winds u_l and a constant advection speed V along a characteristic line $(t(s), X(s), c_g(s))$, with initial conditions $t_0, X(t_0)$ and $c_g(t_0))$ at $s = 0$. The set of equations to be solved is

$$\frac{dt}{ds} = 1 \tag{D.1}$$

$$\frac{d\omega_p}{ds} = \left(\frac{g}{u}\right)^2 \phi(\alpha) \tag{D.2}$$

$$\frac{dX}{ds} = c_g - V, \tag{D.3}$$

where the peak period ω_p is related to the peak group velocity via the deep water dispersion relation

$$c_g = \frac{1}{2}\frac{g}{\omega_p}.$$

Equation (D.1) reduces to $s = t - t_0$ and hence gives the characteristic coordinate as a function of time. Equation (D.2) is the temporal fetch relation, as mentioned in Kudryavtsev et al. (2015), which reads in dimensional coordinates

$$\omega_p(t) = c_{\alpha t}\frac{g}{u}\left(\frac{g}{u}\right)^{q_t}(t - t_0)^{q_t} + C_\omega, \tag{D.4}$$

where

$$q_t = q/(1+q), \;\; c_{\alpha t} = \left[c_\alpha^{1/q}\frac{1+q}{2}\right]^{q/(1+q)}, \tag{D.5}$$

and C_ω is an integration constant. Note that, for the values of q following (Kudryavtsev et al., 2015), q_t is negative and is respectively $-3/7$, $-1/3$, $-3/11$.

Equation (D.2) can also be solved for the group velocity c_g, and yields

$$c_g(t) = (c_t^T)^{q_t} u \left(\frac{g}{u}\right)^{-q_t} (t - t_0)^{-q_t} + c_g(t_0). \tag{D.6}$$

with $c_t^T = 2^{1+q-1/q} c_\alpha^{-1/q} (1+q)^{-2-q} (-q)^{1+q} = 2.7 \times 10^5$.

Finally, the position X along the characteristic reads, from equation D.3

$$X(t) = \frac{1}{-q_t + 1} (c_t^T)^{q_t} u \left(\frac{g}{u}\right)^{-q_t} (t - t_0)^{-q_t+1} + (t - t_0)[c_g(t_0) - V] + X(t_0). \tag{D.7}$$

D.2 Trajectory of waves generated at the beginning of the storm

Waves that are generated at the beginning of the storm ($t_0 = 0$) follow characteristic curves with initial conditions $X(0) = X_0$ and $c_g(0) = 0$. This assumes there is no prior significant background sea.

For those waves, it is interesting to find X_{crit}, the initial position of waves below which they escape the cyclone. The time t_{crit} at which their group velocity matches the speed of the cyclone is computed from equation (D.6) as

$$V = (c_t^T)^{q_t} u \left(\frac{g}{u}\right)^{-q_t} t_{crit}^{-q_t}, \tag{D.8}$$

which yields

$$t_{crit} = c_t^T \left(\frac{u}{V}\right)^{1/q_t} \frac{u}{g}, \tag{D.9}$$

$$t_{crit} = \frac{c_t^T}{g} u^{-q} V^{1+\frac{1}{q}}. \tag{D.10}$$

At t_{crit}, waves that have started at X_{crit} should be exactly at the rear boundary of the storm, i.e. at

$X = 0$. From equation (D.7), this then yields

$$X_{crit} = \frac{-1}{-q_t + 1} (c_t^T)^{q_t} u \left(\frac{g}{u}\right)^{-q_t} t_{crit}^{-q_t+1} + t_{crit}\, V, \tag{D.11}$$

$$X_{crit} = \frac{c_t^T}{g}\, u^{1+\frac{1}{q_t}}\, V^{1-\frac{1}{q_t}} \left[\frac{q_t}{1-q_t}\right], \tag{D.12}$$

$$X_{crit} = \frac{c_t^T\, q}{g}\, u^2 \left(\frac{u}{V}\right)^{\frac{1}{q}}. \tag{D.13}$$

Waves such that $X_0 > X_{crit}$ will eventually move faster than the storm (trapped waves) and have all the same group velocity at a given time t, following the temporal fetch law eq. (D.6).

D.3 Waves generated after t_{crit}

After t_{crit} is reached, the waves start to propagate to the front of the storm. The characteristic X_{crit} is the dominant characteristic that starts at the rear of the storm and propagates forward, because it's speed is faster than the storm translation velocity V. For times $t > t_{crit}$ the dominant characteristic X_{crit} non-stationary processes occur and the sea continues to grow, but this time with a significantly developed background sea (which is left behind by the dominant waves as they propagate to the upwind edge of the storm). Similarly to before, within the time t_{crit}, some waves are going to be left behind the storm, and others are going to remain under the storm and move forward. Waves need to reach the translation velocity V to be trapped and continue to grow.

A simplified view of this process is to assume that this region is described by characteristics starting in the rear of the storm ($X(t_0) = 0$) at times $t_0 > t_{crit}$ with an initial group velocity matching that of the storm $c_g(t_0) = V$. This assumption only considers the fastest waves at the rear of the storm.

In this region ($t > t_{crit}$ and $X < X(t|X_{crit}, 0, 0)$, all waves are generated at $X = 0$ with the group velocity $c_g = V$. With a stationary wind forcing, all waves at a given X are the same.

Eq.(4.3.11) can be written as time invariant such that

$$\frac{\partial \omega_p}{\partial t} + c_g^p \frac{\partial \omega_p}{\partial x} = \left(\frac{g}{u}\right)^2 \phi(\alpha), \tag{D.14}$$

or in the moving framework with eq. (4.3.13)

$$(c_g - V)\partial_X \omega_p = \left(\frac{g}{u}\right)^2 \phi(\alpha), \tag{D.15}$$

which is the case considered in appendix A2 (equation A13) in Kudryavtsev et al. (2015). This equation can be solved for c_g with the boundary conditions $c_g(0) = V$ and yields

$$\left(\frac{u}{2c_g}\right)^{1/q} \left[1 + q - \frac{V}{c_g}\right] - q\left(\frac{u}{2V}\right)^{1/q} = (1+q)c_\alpha^{1/q}\frac{Xg}{u^2}. \tag{D.16}$$

E Non-linear energy flux in a wind sea

We consider deep water waves of wavenumber k and angular frequency $\omega = \sqrt{gk}$. Longuet-Higgins (1976) computed simplified expressions of the rate of change of energy density due to wave-wave interactions assuming that the non-linear interactions occur for neigbouring wavenumbers. He considered the simplified situations of a narrow spectrum

$$S(k_1, k_2) = S_0 \exp\{-k_p^2[(1/2)P(k_p - k_1)^2 + Qk_2^2]\}.$$

Longuet-Higgins (1976) found that the contributions are concentrated around the wavenumber k_p and are independent of its shape

$$\frac{\partial \phi(k_p, 0)}{\partial t} = -34\omega_p k_p^6 S_0^3 \Delta k_1 \Delta k_2, \tag{E.1}$$

and $S_0 \Delta k_1 \Delta k_2 \propto msa$ (where msa is the mean square wave amplitude).

F Non-linear relaxation timescale

When the moving fetch edge is reached, the non-linear terms in the wave action equation start to decay. The characteristic time scale for the decay and for the wave spectrum travel linear wave is

$$T_c \simeq \frac{1}{\omega_p \mu^4} = \frac{T_p}{2\pi\ k_p^4\ E(\omega_p, u)^2} = \frac{g}{E(\omega_p, u)^2\ \omega_p^9}, \tag{F.1}$$

with $\mu^2 = E\ \omega_p^4/g^2 = E\ k^2$ is the average wave steepness, and E the total spectral power (like the total variance of the data), estimated using JONSWAP parameters (Zakharov et al., 2019; Zakharov, 2010).

Acknowledgments

I thank Alex Ayet and Bertrand Chapron for the intense discussion that lead to this manuscript. It is planned to develop it further to a publication. I also thank Bruce Cornuelle and Sarah Gille for discussing topics related to this chapter.

Chapter 4, in part, is currently being prepared for submission for publication of the material: A simple model of swell generation under extra-tropical storms, Hell, M. C., Ayet, A, Chapron, B. The dissertation/thesis author was the primary investigator and author of this material.

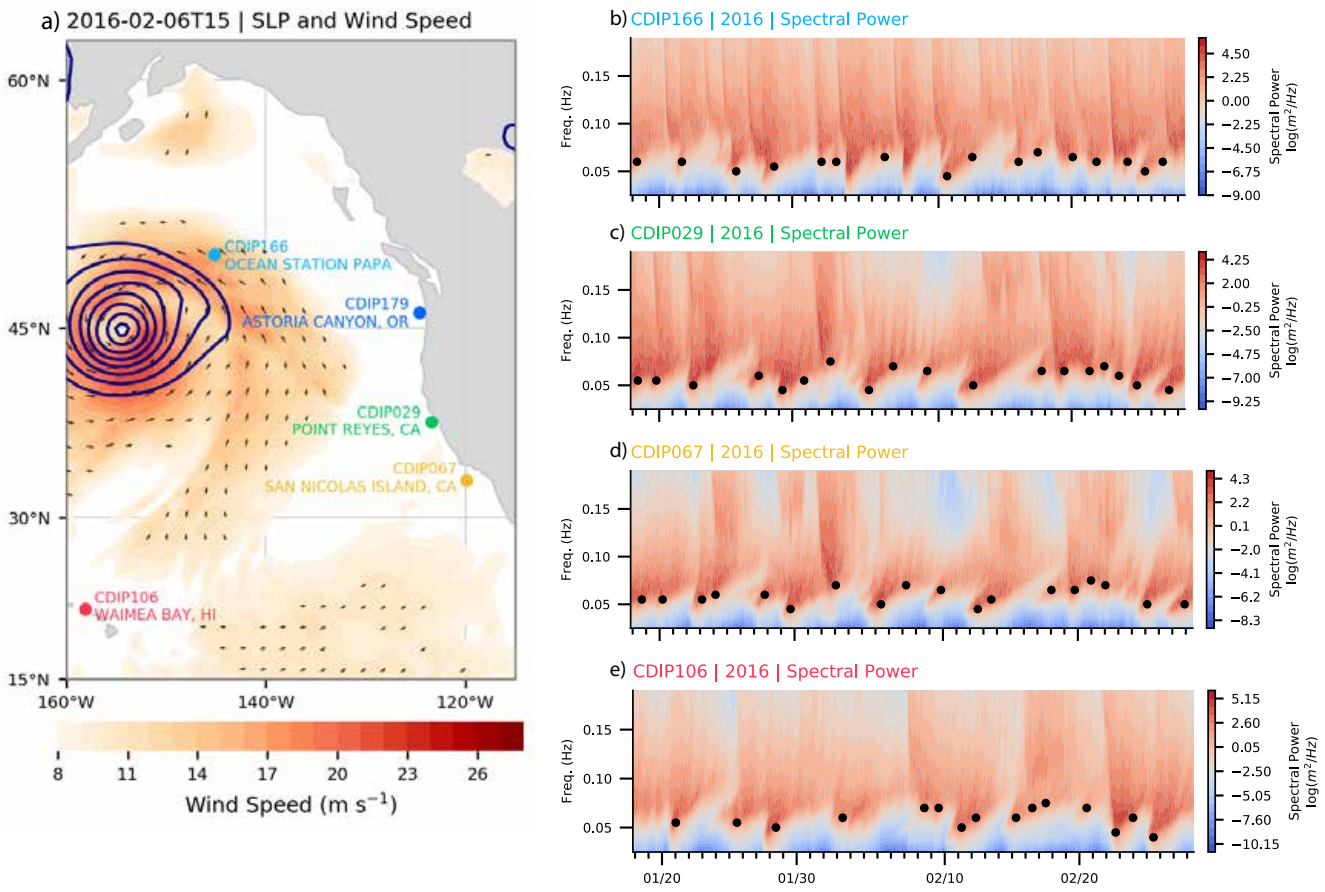

Figure 4.1: a) Example synoptic situation on February 2nd, 2016 with the surface wind speed (shading) and native anomalies of SLP in dark blue with 5hPa increments. The arrows in indicate the surface wind direction and intensity. The position of the used CDIP wave buoy stations (CDIP029, CDIP067, CDIP106, CDIP166) are shown as colored dots. Their observed spectrograms between mid January and mid February 2016 are shown in panel b to e.

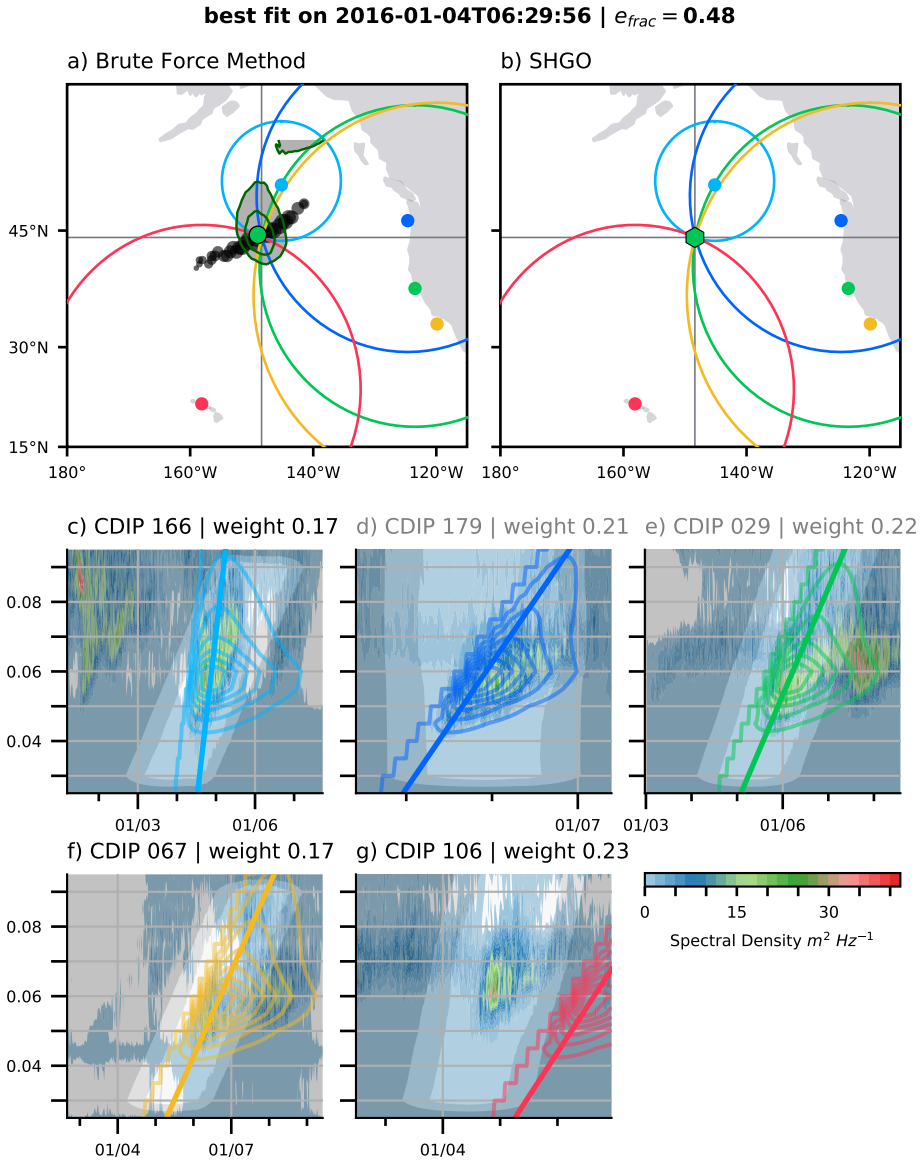

Figure 4.2: Fitting results for the case study in January 2016. (a) Synoptic situation for the time of minimal cost (January 4th 2016) for the same station as in Fig. 4.1. The colored circles show the best fitted great-circle distanced for the respective stations. They correspond to the sloped lines in panel c to g. The green dot shows the position of the minimal cost between the five station on January 4th 2016 at 06:00 UTC using eq. 4.3.7 and the brute-force method (sec. 4.3.1). The black dots show the minimal costs for time steps prior or after the identified minimal cost time-step. The gray shading shows the regions indicates an fractional error $e_f \leq 0.4$. (b) Same as (a) but for the global minimal cost using the SHGO/DA method. The fitted parametric models $\boldsymbol{M}^k$ are compared to the station data $\boldsymbol{D}^k$ in panel (c) to (g), while the colors indicate the different stations. The gray shadings in panel (c) to (g) illustrate the weighting $\boldsymbol{w}^k$ on the data.

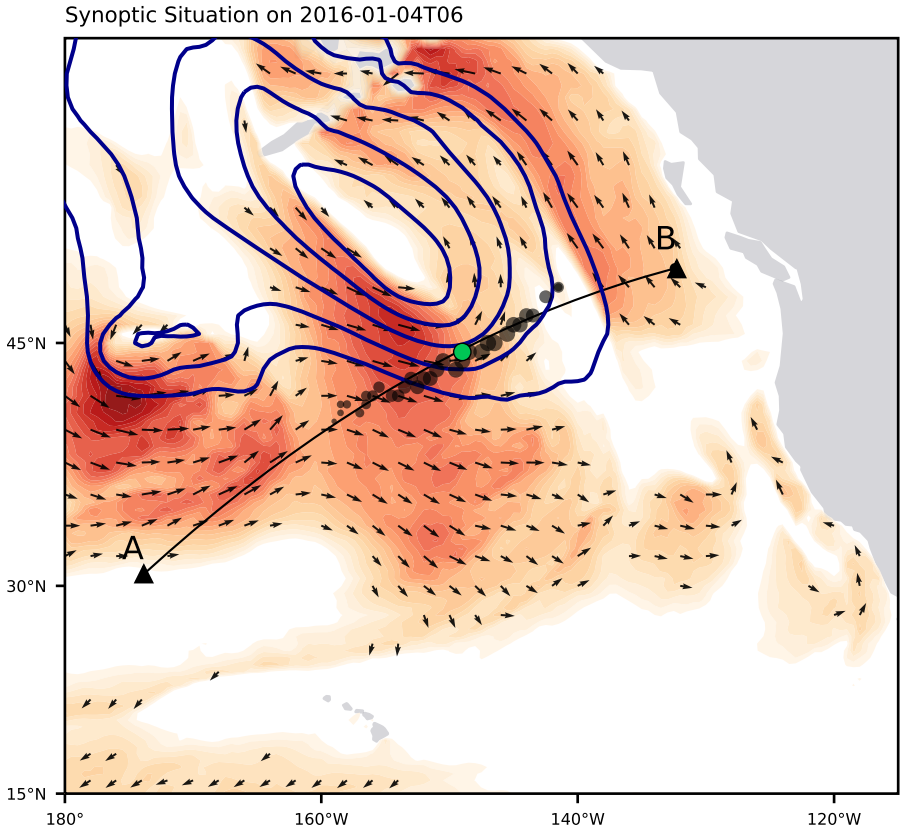

Figure 4.3: Same as Figure 4.2 a but now compared to the reanalysis winds. (red shading and black arrows). The color intervals are the same as in figure 4.1). The dark blue lines indicate negative SLP anomalies in 5 hPa intervals. The black dots are most likely wave origin for each timestep, and the green dot is the most likely origin point of all time steps. The black line between the points A and B is the least-square fit to the black dots and is used to transect the wind data.

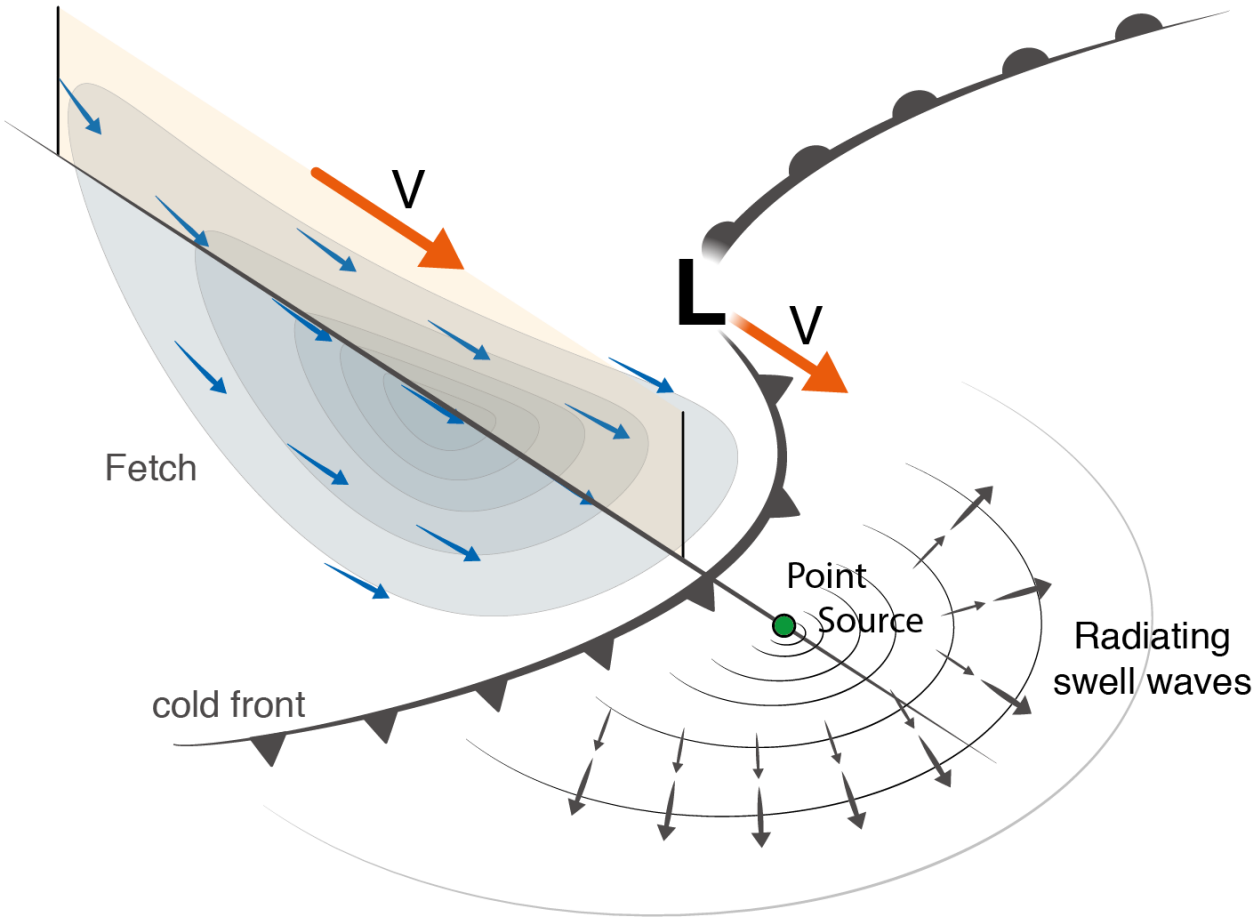

Figure 4.4: A moving fetch embedded in an Northern Hemisphere extra-tropical cycle. The cyclones center **L** is adjacent by a warm and cold front (thick gray lines with half circles or triangles). The moving fetch is located behind the cold front (gray shading with blue arrows) and moves with the same translational velocity **V** as the cyclone center **L** (orange arrows) to the bottom right. The green dot indicated the source location of swell as it can be triangulated from wave-buoy observations. Swell waves radiate away from this theoretical source location (small gray arrows).

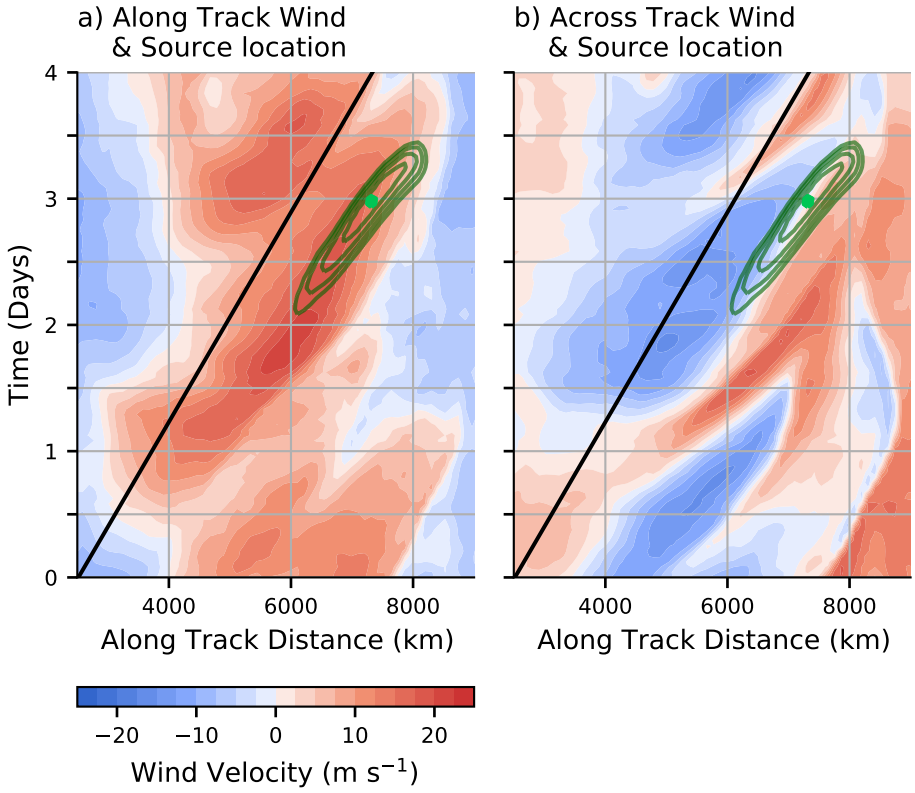

Figure 4.5: Transect along the track of most likely origins between the points A and B in figure 4.3. a) Along-track winds (red-blue shading), areas of $e_f \leq 0.4$ (green contours), most likely origin (green dot). The estimated translational velocity along the transect is shown as black line. b) same as a) but for the across track velocity.

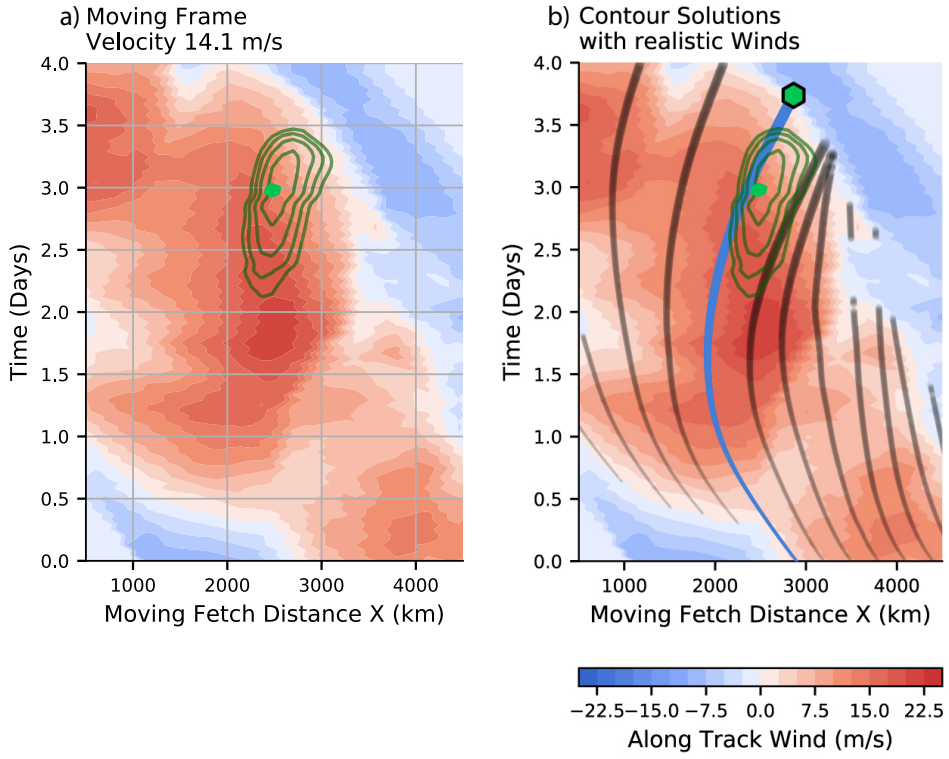

Figure 4.6: Transect between point A and B in the moving frame of reference. a) Same as figure 4.5a but in the moving frame of reference. The black line Fig. 4.5 is a vertical line at in the moving frame of reference. b) Same as a) but with characteristic curves of ω_p using eq. 4.3.13 and the method of characteristics.

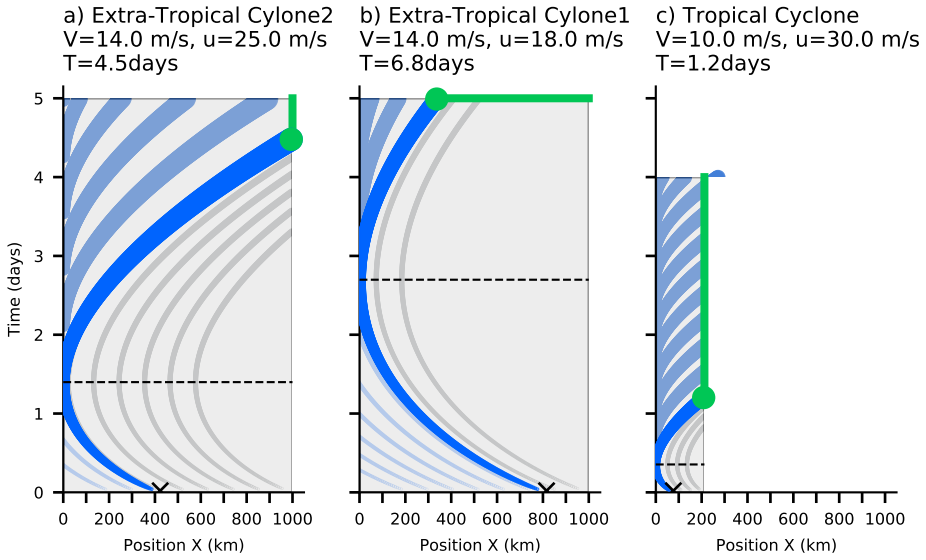

Figure 4.7: Idealized models of constant wind under a moving fetch. a) characteristics for typical scales of an extra tropical cyclone (V= 14 m s^{-1}, u= 25 m s^{-1}, duration T= 5 days, length-scale = 1000 km). The characteristic with lowest ω_p and the highest wave energy (longest characteristic) is in dark blue with its exit location marked as green dot. The green line indicates exit locations that have the same ω_p value as the green dot. Gray-blue line show characteristics that develop after τ_{crit} (dashed black line) but result in smaller wave energy than the longest characteristic. Gray lines indicate characteristics that start at t_0 but don't grow as long as the longest characteristic and also result in smaller wave energy. The thickness of the characteristic curves is proportional to ω_p^{-1}. b) Same as a) but for a fetch with u= 18 m s^{-1}. c) Same as a) but for typical scales of a tropical cyclone (V= 10 m s^{-1}, u= 30 m s^{-1}, duration T= 1.2 days, length scale = 200 km, same parameters as in Kudryavtsev et al. (2015)).

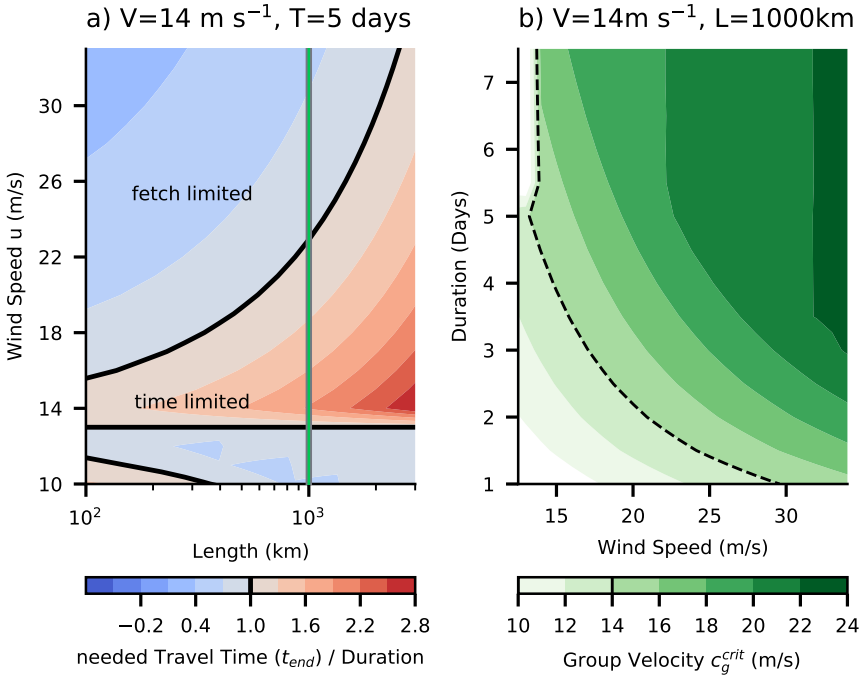

Figure 4.8: a) Travel time of the longest characteristic divided by the fetch duration of 5 days for constant moving winds with V= 14 m s^{-1}. Time-limited fetches are in red shading, length-limited fetches are with blue shading. The black line shows parameters where the travel time is equal the duration and the green line indicates the parameter space in b). b) Group velocity of the longest characteristic for a fetches length of L= 1000 km and a translational speed of V= 14 m s^{-1}. The trapping condition ($c_g = V$) is shown as dashed black line.

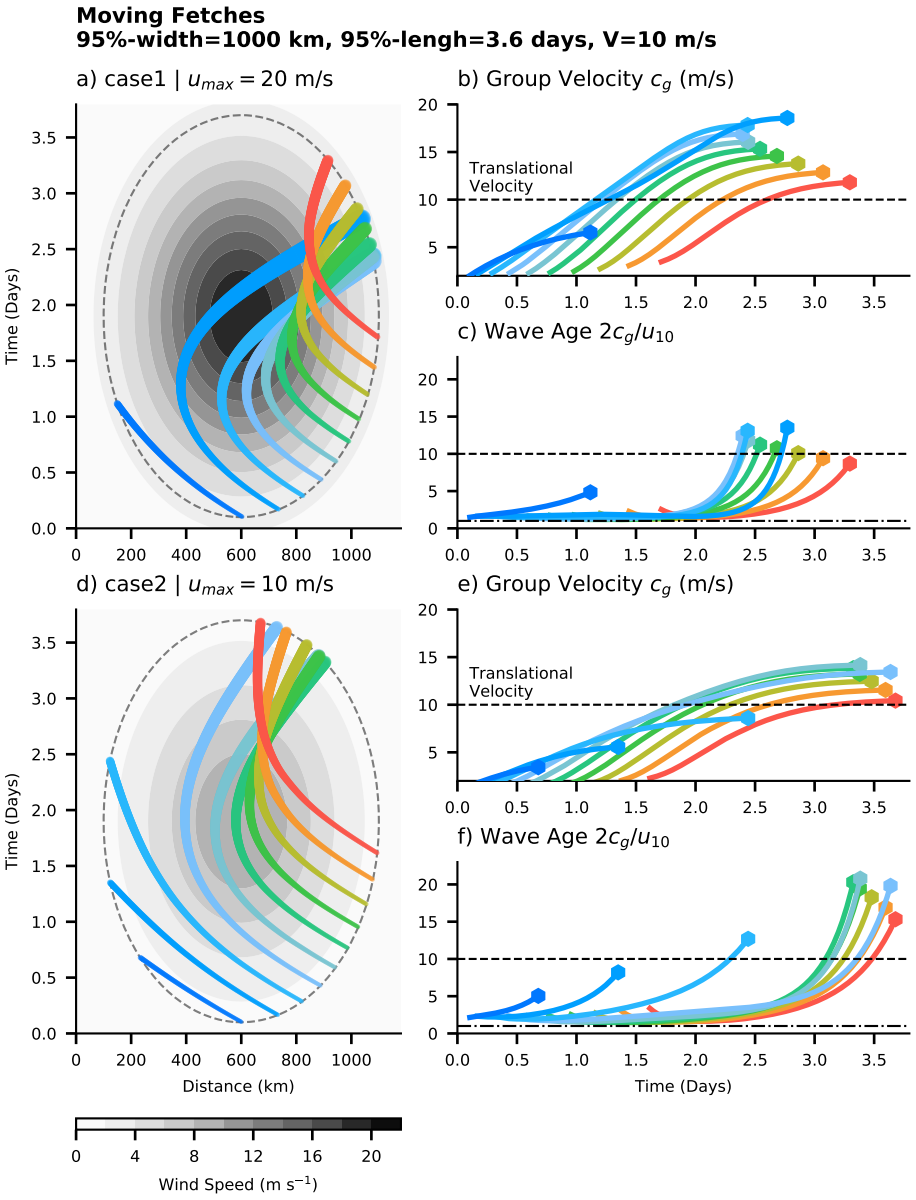

Figure 4.9: Characteristics from double-Gaussian winds in the moving frame of reference. a) double-Gaussian wind forcing (gray shading) with characteristic curves (colored lines). The wind forcing is defined by a 95%-width of 1000 km, a 95%-duration of 3.6 days, a translational velocity V= 10 m s^{-1}nd peak wind speed. u_{max}= 20m s^{-1}. The dashed black line is the 95%-extension of the wind field. b) Group velocity along the characteristics (colors same as in a). The translational velocity V= 10 m s^{-1}s shown as black dashed line. c) Same as in b) but for wave age $\alpha = 2c_g/u_{10}$. The dashed-dotted and dashed line indicate α=1 or 10 respectively. d) to f) as as a) to c) but for peak wind speed u_{max}=10 m s^{-1}.

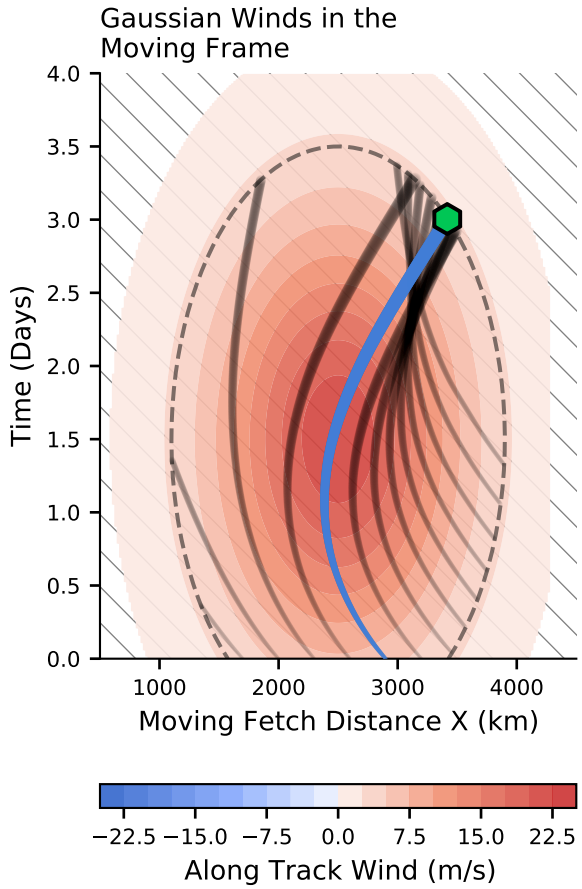

Figure 4.10: Same as figure 4.9 a but for the scale estimated in figure 4.6 (95%-width = 2800 km, 95%-duration = 4 days, u_{max}= 22 m s^{-1}, and V= 14.1 m s^{-1}.) The characteristic with the highest wave energy is marked as blue line with green hexagon indicating its final location. The dashed black line is the 95%-boundary of the forcing field.

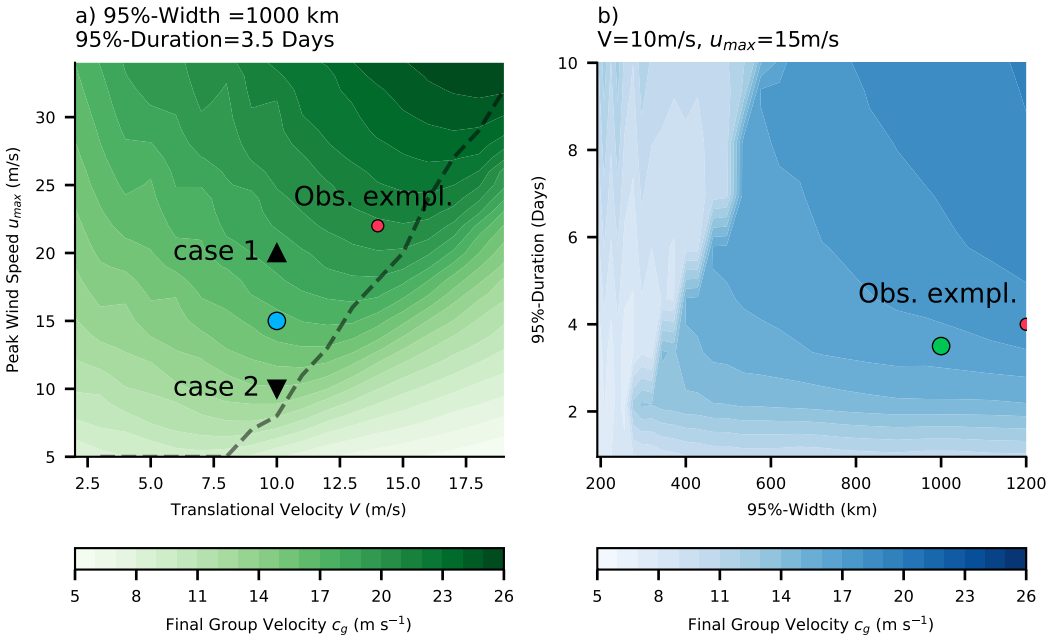

Figure 4.11: Largest final group velocity of a characteristic in the double-Gaussian model. a) Group velocities for varying translational velocity V and peak wind speed u_{max}. The local maximum group velocity (dashed black line) separates fetch- and time-limited cases. Case 1 and 2 from figure 4.9 are shown as upward- and downward pointing triangles and the observational case from sec. 4.4 (Fig. 4.10) is shown as red dot. The cases shown in panel b) are here represented as blue dot. b) Same as a) but for changes in the 95%-width and 95%-duration. Here the parameter space from a) is indicated as green dot and the observational case from section 4.4 as red dot.

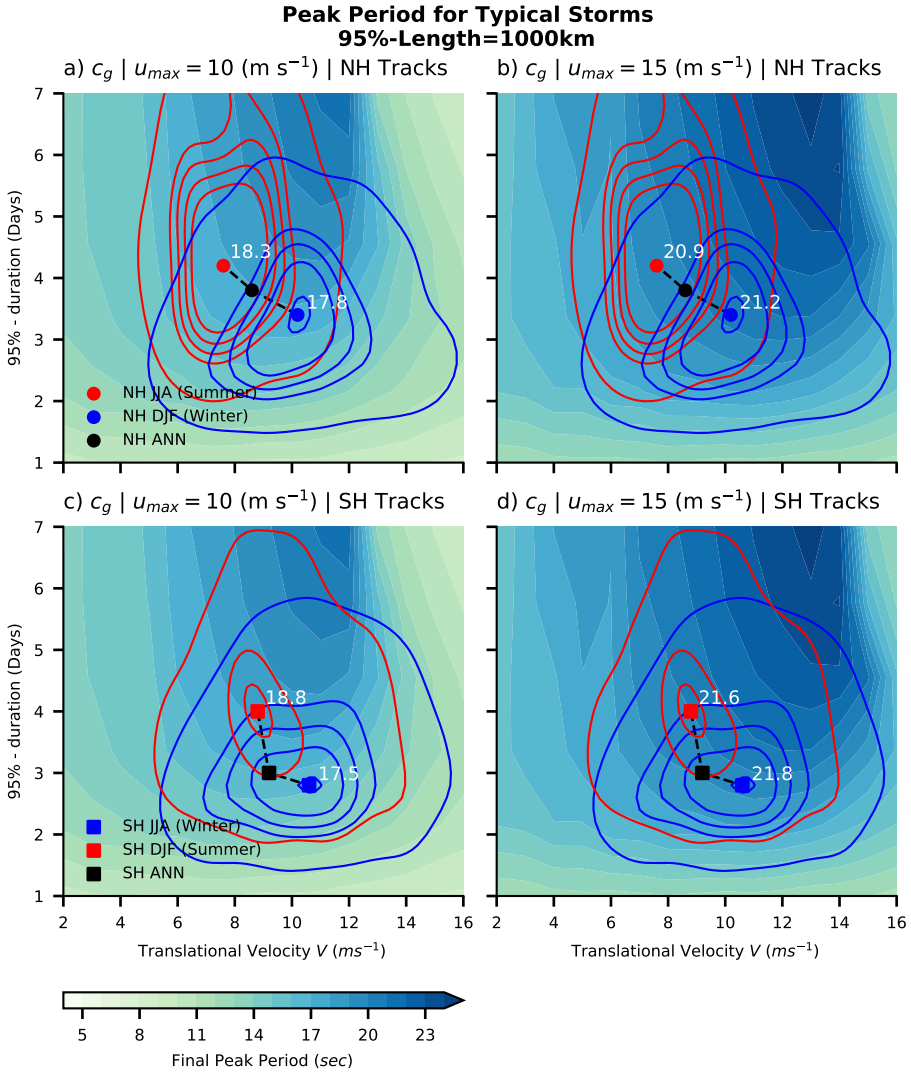

Figure 4.12: Largest occurring peak period T_{peak} for double-Gaussian winds of different velocity V and duration given a peak wind speed u_{max}= 10 m s^{-1}a and c) or u_{max}= 15 m s^{-1}b and d) and a 95%-width of 1000 km. The joint distributions of storm track speeds and lifetime are shown for summer (red) and winter (blue) for the NH (a,b) and SH (c,d). The distributions maximums are shown as red (summer), blue (winter) and black (annual mean) dots.

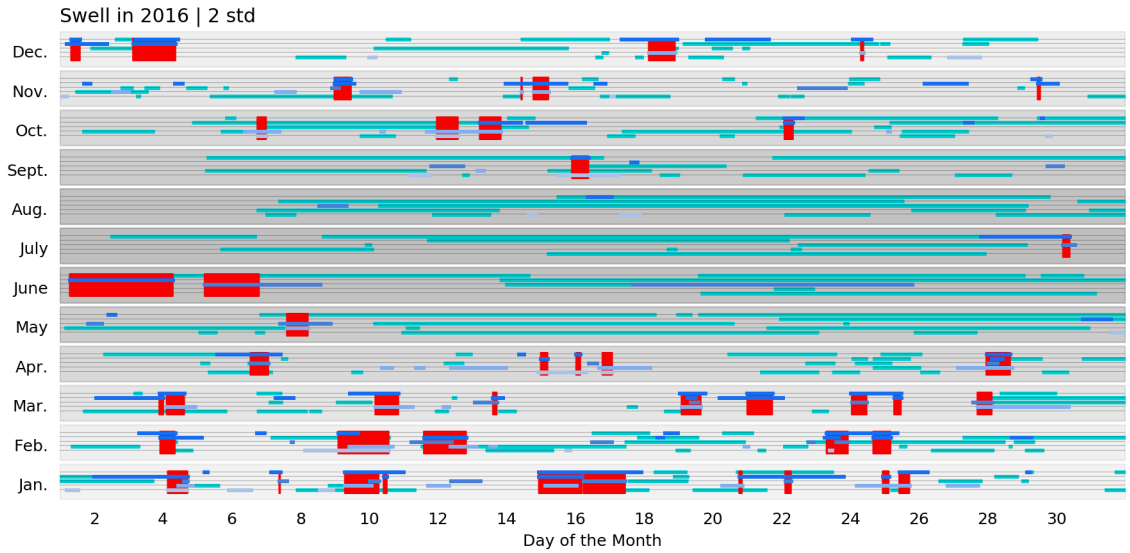

Figure 4.13: Simplified time series for one year of fitted initial times uncertainty estimates. Each green or dark blue line shows $t_0 \pm 2\,\sigma_{t_0}$ for events identified at one of the stations. Green bars indicate events that have fractional error $e_f < 0.4$, while blue bars are events with $e_f \geq 0.4$. The red areas show time spans where at least 3 or more events have overlapping estimated initial times.

Chapter 5

Time-varying empirical probability densities of Southern Ocean surface winds: Leading modes linked to SAM, the annual cycle, and product biases

Abstract

Southern Ocean (SO) surface winds are essential for ventilating the upper ocean by bringing heat and CO_2 to the ocean interior. Observations demonstrate that the SO is primarily ventilated during short, but extreme events that drive intense turbulent atmosphere-ocean fluxes. SO surface winds are related to the Southern Annular Mode (SAM), but the SAM's impact on short-term wind events that drive upper-ocean mixing remains unclear.

In this study, observed time-varying 5-day probability density functions (PDFs) of ERA5 surface winds and stress over the SO are used in a singular value decomposition to derive a linearly independent set of empirical basis functions. The leading order modes of wind and stress

(72% of the total variance) are highly correlated with a standard SAM index ($r = 0.82$) and show how SAM drives cyclone intensity and, in turn, extreme winds. This suggests that southerly and less westerly winds are more frequent during short and distinct negative SAM phases and that strong westerly winds during positive SAM are likely insufficient to drive mixed-layer ventilation. The second mode describes seasonal changes in the wind variance (16% of the total variance) that are uncorrelated with the first mode. The analysis produces similar results when repeated using 5-day PDFs from a suite of scatterometer products. Differences between wind product PDFs resemble the leading order variability of the PDFs. Together, these results demonstrate the strong link between surface stress and the leading modes of atmospheric variability, suggesting that empirical modes can serve as a novel pathway for understanding biases and variability of surface stress PDFs.

5.1 Introduction

The Southern Ocean (SO) governs the global ocean uptake of anthropogenic heat and CO_2 (Gnanadesikan, 1999; Gruber et al., 2019; Swart et al., 2018), and projections of future climate change depend on our of understanding SO ventilation (Sabine et al., 2004; Soloviev and Lukas, 2013; Boé et al., 2009; Flato et al., 2014; Kuhlbrodt and Gregory, 2012), trends in water mass transformation (Roemmich et al., 2015; Haumann et al., 2016), and mode water formation (Hanawa and Talley, 2001; Naveira Garabato et al., 2009; Holte et al., 2012; Gao et al., 2018; Cerovečki et al., 2019). Changes in the SO mixed layer are largely driven by a combination of surface stresses and atmosphere-ocean heat fluxes that together ventilate the upper ocean through stirring and mixing, with the ventilation being largest where surface winds and associated fluxes of momentum and heat are strongest.

The strong link between surface winds and ventilation of the SO mixed layer (ML) suggests that the Southern Annular Mode (SAM), as the leading-order mode of the Southern Hemisphere

atmospheric variability (Thompson and Wallace, 2000), impacts long-term mixed-layer changes (Meijers et al., 2019; Cerovečki et al., 2019). However, it remains unclear how large-scale month-to-month atmospheric variability drives short-term intense wind events under storms (Risien and Chelton, 2008; Lin et al., 2018). This paper explores how short-term wind and stress variability relate to SAM, how they vary in time, and how well they are represented in observational products.

SO flux buoy observations suggest that only a few episodic wind extremes per year are responsible for most ventilation and deepening of the mixed layer (Schulz et al., 2012; Ogle et al., 2018; Tamsitt et al., 2020), and similar intermittent effects emerge in other regions as well (Giglio et al., 2017). The strength of mixing is also sensitive to the ocean mixed-layer stratification, but intense mixing will nearly always require strong surface winds that persist over multiple hours, and therefore that correspond to storms extending over hundreds of kilometers (except in deep water formation regions where buoyancy forcing plays a central role). For most of the mid-latitude oceans, rare high-wind (or high-stress) events initiate highly non-linear processes that transfer energy from the wind-generated waves to the upper ocean (Phillips, 1985) and eventually to the large-scale flow through near-inertial oscillations, the Ekman spiral, and currents (Cavaleri et al., 2012).

Extremes in Southern Ocean surface winds are difficult to observe. The severe weather and lack of access to the region around Antarctica limit in-situ observations and make remote sensing the dominant technique to record surface winds. Satellite scatterometers observe surface capillary waves (cm-scale surface roughness) that are used to estimate the local 10-meter surface winds (Atlas et al., 2011). However, the sparseness of in-situ SO observations has impeded the calibration of remote sensing estimates for high wind speeds (Bourassa et al., 2019). In particular, a lack of observations of extreme winds under cyclones and gaps in our knowledge of air-sea coupling under severe conditions make biases potentially largest where the winds are strongest (Rascle et al., 2008; Ardhuin et al., 2010; Chawla et al., 2013). These biases might correspond

to differences between assimilated atmospheric reanalysis models (Wen et al., 2019; Ramon et al., 2019; McDonald and Cairns, 2020), or between estimates of heat and momentum fluxes to the ocean (Li et al., 2013; Bourassa et al., 2013; Bidlot et al., 2002; Cavaleri, 2009; Yagi and Kutsuwada, 2020) and subsequent biases in ocean forcing or upper-ocean mixing (Li et al., 2016; Taboada et al., 2019). All of these processes affect the assessment of the total wind energy input to the ocean (Rascle et al., 2008; Ferrari and Wunsch, 2010).

Given the difficulties in observing surface winds, how certain can we be about surface stresses? Momentum transfer to the upper ocean relies on a variety of non-linear processes that are driven by instabilities (surface wave growth, wave-wave interaction, conversion of near-inertial waves) and often involve turbulence (e.g. Phillips, 1957; Miles, 1960; Hasselmann and Hasselmann, 1985; Asselin and Young, 2020). A common way to parameterize the transfer of wind energy to the ocean is by calculating a surface stress vector $\boldsymbol{\tau}$ using the standard drag formula

$$\boldsymbol{\tau} = \rho_a \, C_d \, |\mathbf{u}_{10}| \, \mathbf{u}_{10}, \tag{5.1.1}$$

where ρ_a is the density of air, and $\mathbf{u}_{10}$ is the 10-meter wind speed. The drag coefficient C_d depends on wind speed $|\mathbf{u}_{10}|$, the ocean's sea state (surface wave spectrum), and the stratification of the atmospheric boundary layer (Fairall et al., 2003; Edson et al., 2013). Independent of the complex physics included in C_d, the surface stress has at least a quadratic dependence on the wind speed magnitude $|\mathbf{u}_{10}|$.

The goal of this study is to characterize the surface wind and stress over the SO in light of the complex relations between the surface stress and wind vector. We will use the time-varying probability density functions (PDFs) of surface stress and wind to understand their relation without assuming particular shapes.

Surface winds on typical atmosphere model scales (daily timescales and O(100 km) length scales) are often characterized entirely by their mean and standard deviation. Hence, they are

approximated as Gaussian distributions that represent averaged quantities of the model output which are used as ocean forcing. Gaussian-distributed wind components are then used to derive a Weibull distribution (a family of distributions that includes the Rayleigh distribution) for the surface wind speed, which is commonly used to model subsequent air-sea fluxes (Wentz et al., 1984; Wanninkhof, 1992, 2014; Monahan, 2006a). However, a number of studies have shown that surface stress depends on more than just the mean surface wind vector and its standard deviation (e.g. Monahan, 2006a; Ponte and Rosen, 2004; Monahan, 2008). These studies showed that higher order moments of the joint surface wind *PDF* must be known to derive a joint *PDF* of surface stress. Hence, the question arises of how to account for the deviations from Gaussian distributed winds, especially over the Southern Ocean, where winds regularly violate the Gaussian assumption (Wanninkhof et al., 2002; Tuller and Brett, 1984; Pavia and O'Brien, 1986).

With the need for improved seasonal and climate predictions and more available computational power, the spatial and temporal resolution of weather and climate models continues to increase (Delworth et al., 2012; Small et al., 2014; Haarsma et al., 2016; Mizuta et al., 2017). As computational capabilities improve, models explicitly resolve more non-linear surface processes and enhance the non-Gaussianity of surface variables, such that they have begun to advance beyond the assumption of Gaussian distributed surface variables (Blein et al., 2020, and references therein). Unsurprisingly, atmosphere-ocean interaction and related model biases have been identified as one of the biggest challenges in long-range weather forecast and climate models (White et al., 2017; Huang et al., 2020; Lin et al., 2020). In order to better represent highly non-linear fluxes, parametrizations of bulk air-sea fluxes need to account for the non-Gaussianity of variables at high spatial resolution (Wanninkhof, 1992; Wanninkhof et al., 2002; Edson et al., 2013).

In this paper, we represent surface wind variability as a probability density function (PDF) to understand its physical drivers on timescales longer than five days. We also use time-varying PDFs to learn about SO surface wind biases and the occurrence of extreme surface stress. First,

we derive time-varying PDFs from reanalysis and scatterometer data (sec. 5.2.1) and than apply a Principal Component Analysis (PCA, sec. 5.2.3) to decompose the PDFs into their leading modes. Second, we show the close relation of the leading modes in zonal wind and stress to the SAM (sec. 5.3). Third, we represent the zonal and meridional co-variability in the surface wind and stress as the superposition of a few patterns that are driven by changes in the strength of extratropical cyclones, their frontal structure and the seasonal cycle (sec. 5.4). Fourth, we show how the leading modes map into the climatological wind biases (sec. 5.5) and how surface wind extremes can be understood with respect to these climatological biases (sec. 5.6). Although correlation is not causation, we discuss how correlation analysis can be used to understand non-linear surface processes and their drivers in the broader context of the SO surface climate (sec. 5.7.1).

5.2 Methods

5.2.1 Time-varying PDFs of Southern Ocean wind and stress

The 10-meter surface winds (u_{10} and v_{10}) and surface stresses (τ_x and τ_y) from the ERA5 reanalysis (European Centre for Medium-Range Weather Forecasts fifth generation reanalysis for the global climate and weather, , CDS) between 55°S and 63°S are used to derive robust, empirical time-evolving probability densities functions (PDFs) in the Southern Hemisphere (SH) between 1979 and 2017. The latitude limits are chosen such that the wind patterns and fronts over the ocean are solely driven by extra-tropical storms, rather than by flow around topography or sub-tropical dynamics (Fig. 5.1a,b). The same analysis for a broader latitude range leads to similar results, albeit with increased noise levels (Appendix A, Gille, 2005).

Without any prior averaging, the hourly and 0.25° data are divided into 5-day chunks starting on 1 January each year. (Leap years have a 6-day chunk at the end of February.) Five-day chunks are selected in order to capture the characteristic time scale of baroclinic wave activity

(Blackmon, 1976; Wallace et al., 1988; Randel and Held, 1991). The 5.4×10^6 data points in each block (1440 longitudes $\times$ 31 latitudes $\times$ 120 hours) are used to derive joint histograms of winds and stresses ($\mathbf{u}$ and $\boldsymbol{\tau}$) in the zonal and meridional directions for every 5-day period between 1979 and 2018 (see example PDFs in Fig. 5.2). Histograms of only the zonal or meridional components are derived from the joint histograms by summing in the respective orthogonal direction. All histograms are then represented as probability density functions (PDFs) $D(\mathbf{u},t)$ by dividing by the bin width and the total number of data points used in the respective 5-day mean.

Figure 5.3 shows the resulting time-varying PDFs for 5-day increments of zonal wind and stress. For the SO, zonal wind PDFs have a non-zero mean, with a long tail on the negative side of the PDF that can be diagnosed from negative skewness (Fig. 5.3a). The variability of the zonal wind variability is echoed by similar variability patterns in the zonal wind stress (Fig. 5.3b). Increases in the mean zonal wind are associated with extreme zonal stresses, and weak zonal winds coincide with exceptionally weak zonal stress (September and December in Fig. 5.3). This co-varying behavior will be further analyzed in sections 5.3 and 5.4.

We also derive surface wind PDFs using three additional Southern Ocean surface wind products. The CCMPv2 (Cross-Calibrated Multi-Platform version 2.0) winds provide 6-hourly fields on a 0.25°-grid. They blend ERA-Interim winds with all available wind observations to produce a gridded product: observational gaps between scatterometer swaths are filled with winds from ERA-Interim (Wentz et al., 2015). For this study, data points between these swaths are ignored, and CCMPv2 data are used only if they are informed by one or more observation.

In addition to the blended winds, we also analyze two Level 3 (L3) wind products that are based on the Advanced Scatterometer (ASCAT) aboard the European Meteorological Operational Satellites (METOP), METOP-A, METOP-B, and METOP-C. Remote Sensing Systems (RSS) provides ASCAT winds on a 0.25° grid for ascending and descending swaths. We treat these as quasi-twice-daily observations (Ricciardulli and Wentz, Apri, 2016). Similarly, Global Ocean L3 METOP-A winds from CMEMS (Copernicus Marine Environment Monitoring Service) are

also provided twice-daily at 0.25° grid spacing (based on the Royal Netherlands Meteorological Institute, KNMI, Driesenaar et al., 2019). Time-evolving PDFs for 5-day bins are derived for the three scatterometer wind products in the same way as for ERA5. CCMPv2, RSS ASCAT and METOP-A ASCAT each provide $4-13\%$ as many data points as provided by ERA5, with large seasonal variability due to sea ice cover (Satellite products have a spatial coverage $50-85\%$ per 5-days compared to ERA5, Appendix B, Fig. B1).

5.2.2 Effective Degrees of Freedom

The data from ERA5 and scatterometer products are spatially and temporally correlated, such that the effective degrees of freedom (DOF) are much less than the number of data points used to establish each 5-day-distribution. This effect is illustrated in Fig. 5.2, where we compare ERA5 PDFs derived from a single time step (1 hour, dashed black lines), five days (solid black lines) and the climatology (gray shading). We see that the 5-day PDFs are smooth compared to the 1-day PDFs. The effective DOF is calculated by estimating the spatial and temporal decorrelation scales in ERA5 (Appendix B). The effective DOF for the zonal wind u_{10} is 175 and for the meridional wind v_{10} 1070. The e-folding scales are 2.4 days, 1100 km in the zonal and 40 km in the meridional direction for u_{10} and 1.4 days, 130 km in the zonal and 40km in the meridional direction for v_{10} (Fig. B1). These characteristic scales suggest that we can assume each 5-day PDF to be a robust estimate, which implies that differences between successive PDFs are due to changes in physical drivers, rather than uncertainties in the estimate of the PDF.

The 5-day joint PDFs have more noise than their meridional or zonal projections because the same number of effective DOF as in the one-dimensional PDFs is now spread over the squared number of spatial data points (Fig. 5.2c).

5.2.3 Principal Component Analysis of time-varying PDFs

To derive the covariance between the time-varying PDFs, the PDFs of zonal wind $\boldsymbol{D}(u_{10}, t)$ and stress $\boldsymbol{D}(\tau_x, t)$ for ERA5, CCMPv2, RSS ASCAT and METOP-A ASCAT are decomposed into their leading-order modes using singular value decomposition ($\boldsymbol{D} = \boldsymbol{U}\boldsymbol{\Sigma}\boldsymbol{E}^T$). The probability variation patterns $\boldsymbol{E}$ (empirical orthogonal functions, EOFs) are multiplied by the singular values from $\boldsymbol{\Sigma}$, so that they have units of probability density. The columns of $\boldsymbol{U}$ (principal components, PCs) are unit vectors that specify the time variability of the EOF.

The PDFs of wind and stress are either decomposed from their one dimensional PDFs in the zonal or meridional direction, or from their joint PDFs. The following analysis focuses on the leading modes in the zonal direction as well as the leading modes from the joint PDFs, because the other decompositions mainly express the same variability (Fig. 5.4). The cross-correlation between PCs of all decompositions can be found in the supplementary material.

The first three EOFs of the zonal and meridional wind PDFs are very similar for all four wind products (Fig. 5.5, higher modes are in the supplementary material). The first three EOFs explain similar fractions of the total variance, and in these cases the fraction of variance explained exceeds a null-hypothesis threshold defined by decomposing Gaussian noise, implying that the EOF has more structure than we would expect to see if the signal were simply Gaussian white noise (Fig. 5.5g, h; Preisendorfer N-test, Preisendorfer and Mobley, 1988; von Storch and Zwiers, 1999, chap. 13).

Note that relative to ERA5, the spatial coverage and amount of data vary between the scatterometer wind products from a minimum of 30% for METOP-A ASCAT in austral winter to about 85% in austral summer in CCMPv2, and the effective DOF of the scatterometer winds are substantially less than for ERA5 (Appendix B). Despite the varying effective DOF, the decomposition of all scatterometer wind products appears to be robust, even for the joint PDFs which have a weaker signal-to-noise ratio (Fig. 5.2c and sec. 5.2.1). Hence, the analysis in section 5.3 and 5.4 focuses on ERA5 because it provides a complete dataset of surface winds and

stresses with the highest signal-to-noise ratio. Equivalent statements can also be derived from the scatterometer data, although the climatologies of the scatterometer fields differ relative to ERA5, as outlined in section 5.5.

5.3 Zonal Wind and Stress Co-Variability and its Relation to SAM

In this section we show that the leading modes of surface stresses, and therefore the ocean's forcing, are tightly linked to the leading modes in the zonal wind. In particular, the first two PCs of wind and stress are nearly identical, and explain 90% of the variance of each variable.

Figure 5.6a,b compares the first three EOFs of the zonal wind and zonal stress from ERA5 with the climatological PDFs. The 1st zonal wind EOF (u_{10} EOF1, 72% of variance) is asymmetric around the median of the PDF. Positive values of the PC1 time series are associated with less frequent weak zonal winds (around zero) and more frequent zonal wind speeds exceeding 10 m s^{-1}(Fig. 5.6a, dark blue line). Since the zonal wind PDFs are in general skewed, the range over which the 1st EOF reduces the zonal wind PDF (-10 to 5 m s^{-1} is larger than the range over which the EOF enhances winds (5 to 15 m s^{-1} Fig. 5.6a). This asymmetry is even more pronounced in the 1st EOF of zonal stress (τ_x EOF1 in Fig. 5.6b, correlation coefficient r(u_{10} PC1, τ_x PC1)= 0.94). A positive value of the stress PC1 reduces the stress PDF's peak (positive, but close to zero), increases the likelihood of extreme eastward stresses, but decreases the likelihood of westward stresses. Hence, the leading EOFs can be interpreted as shifting the center of the zonal wind PDF, accompanied by asymmetric flattening of the double exponential zonal stress PDF.

The 2nd EOFs of the zonal wind and stress are both symmetric around the median of the PDF (Fig. 5.6a and b, dotted gray lines), indicating fluctuations in wind or stress variance. This mode shows that increases in the likelihood of winds being concentrated near the PDF's center

are accompanied by a symmetric reduction in the likelihood of winds occurring in the tails of the PDF, and vice versa. The PCs of the second EOFs are also well correlated between wind and wind stress (correlation coefficient r=0.92, Fig. 5.6d) but only explain about 18% of the overall variance in probability density. The PCs of 3rd EOFs explain even less variance in probability density (< 5%) and are close to the noise level (sec. 5.2).

Figure 5.6c,d shows the PCs of the leading two EOFs in the zonal wind and zonal stress for 15 years. The similarity between the wind and stress PCs suggests that the zonal stress variability can be solely explained by zonal wind. The first two PCs of τ_x together explain 92% of the variance and are explained by the first two PCs of u_{10}. This is surprising since stress depends not only on zonal winds but also on meridional winds and non-linear boundary layer processes that are represented through the drag coefficient (eq. 5.1.1). The role of the meridional wind component is further explored in section 5.4. In Fig. 5.6a,b, a shift of the zonal wind maximum by 5 m s^{-1} (+1 u_{10} PC1) leads to a 30% reduction in the likelihood of wind stresses around ±2 hPa around the peak and a 50% increase in the likelihood of stresses larger than 10 hPa (green dashed line in Fig. 5.6b, eq. 5.1.1). The close relationship between the 1st PCs of u_{10} and τ_x also appears in their power spectra (Fig. 5.7a, blue and red line): the leading PCs of zonal wind and stress are indistinguishable on timescales between 250 days and one month, with a distinct peak at the semi-annual cycle.

The first PCs of wind and stress exhibit strong year-to-year variability, but extreme zonal stresses are more frequent during short events in austral winter (March to October) and less frequent in austral summer (December and January). This variability is coherent with the SAM with zero phase lag on all scales between four years and a month except on the seasonal and semi-seasonal cycle (Fig. 5.7b,c, the correlation coefficient of u_{10} PC1 and SAM = 0.82). This coherence extends to significant poleward trends in u_{10} PC1 and τ_x PC1 similar to the observed poleward trends for SAM (about 0.054 ± 10^{-5} PC1/decade, p-value = 0.001, in line with Thompson et al. (2000); Thompson and Solomon (2002); Lin et al. (2018)). Here, SAM is defined as the

leading-order mode of the 5-day-mean zonal-mean zonal wind in the SH extra-tropics (Thompson and Wallace, 2000; Thompson and Woodworth, 2013). Hence, long-term trends in the surface stress PDFs are related to trends in the zonal mean wind. The coherence between PC1 and SAM implies a relationship between local wind probabilities (represented by the PDFs) and larger-scale zonal mean winds (represented by SAM). The weaker coherence at the semi-annual and annual frequencies is an artifact of the conventional definition of SAM, which removes annual-cycle variability before the SVD decomposition (Appendix C).

The 2nd PC of the u_{10} and τ_x PDFs show regular seasonal cycles, which are, by construction, linearly independent of the variability in the 1st PCs (Fig. 5.6d, and a Fig. 5.7a, dashed blue and dashed red line). The seasonal cycle is the variance mode (EOF2 in Fig. 5.6a,b) , which implies that the seasonal atmospheric circulation is weaker than its month-to-month or year-to-year variability (Trenberth, 1991). In other words, in the latitude band of the Drake Passage, the seasonal cycle affects the variance of the winds more than it affects the mean of the zonal winds.

5.4 Synoptic Variability in the Joint Wind and Stress Decompositions

In this section, we extend the analysis of the zonal wind and stress co-variability to include the meridional component. This allows us to represent a significant fraction of variance with a small number of functions, which also reveals the synoptic-scale drivers of the variance. Figure 5.8 shows the first two EOFs of the joint surface winds ($\mathbf{u}$ EOF1 and $\mathbf{u}$ EOF2 in c and d) and the joint surface stress ($\boldsymbol{\tau}$ EOF1 and $\boldsymbol{\tau}$ EOF2 in f and g), as well as the projected means in the meridional and zonal directions (a,b,e,h,i and j). The first two modes of the joint surface winds show the same patterns as the one-dimensional decomposition, but they explain less variance (together 58% of the total variance). A smaller fraction of explained variance is not surprising since the joint decompositions have to represent the variance for the square of the number of grid

points compared to the one-dimensional decomposition.

The 1st joint wind mode ($\mathbf{u}$ EOF1) combines the variability of the u_{10} EOF1 and v_{10} EOF2 (41% variance explained, r($\boldsymbol{\tau}$ PC1, u_{10} PC1)=0.99, r($\boldsymbol{\tau}$ PC1, v_{10} PC2)=0.68). The zonal and meridional means show the same patterns as the related one-dimensional decompositions. This similarity in patterns suggests that wind shifts in the zonal direction dominate the joint PDF, meaning that SAM variability also dominates the joint PDF.

In addition to enhancing zonal winds, the SAM mode of the joint EOF corresponds to a poleward shift of the meridional wind maximum (v_{10} EOF2, compare Fig. 5.8a with Fig. 5.5a, and Fig. 5.8e and Fig. 5.5d). This co-variability of both wind components is a representation of the structure and variability of extra-tropical cyclones. Since the joint PDFs are a reduced representation of the maps of surface winds (Fig. 5.1), the PDF shape and variability also represent the synoptic variability of surface wind or even sea level pressure. The joint PDF measures the intensity of the cyclone fronts, and hence the intensity of the cyclones themselves. This is possible because extra-tropical storms are inherently asymmetric, and their dynamics are linked to their frontal systems (Shapiro and Keyser, 1990; Neiman and Shapiro, 1993; Schemm and Wernli, 2014).

The cyclones' imprint on the surface winds is characterized by intensified winds in the cyclone cold sectors that shift the PDF maximum toward more frequent stronger westerlies (Fig. 5.9, horizontal red arrows). The stronger westerlies are accompanied by intense, but narrow southward flow ahead of the cold front (low-level jet, Fig. 5.9 curved red arrow). These cold-front winds add the southward inclination of the dipole pattern of the joint PDF (Fig. 5.8c, green dot). The surface winds on both sides of the cold front imprint on the 1st EOFs for both wind and stress. While the joint wind PDF's maximum shifts along a diagonal through the PDF's median (Fig. 5.8c black dot), the joint wind stress PDF weakens at the peak and is enhanced mainly in the southeastward direction (Fig. 5.8f and g, orange and green dots, note the non-linear color-scale). At times when the 1st principal component is positive, the EOFs indicate less equatorward flow

and less weak zonal wind regimes, as typically appears in the wake of an eastward propagating storm (weakening of the blue arrows in Fig. 5.9 correspond to orange dot in Fig. 5.8c).

The leading mode of the joint PDF can be understood as a measure of the cyclone activity in the latitude limits of Drake Passage. Cyclone activity is highly coherent with SAM (Fig. 5.7b blue line, power spectra of **u** PC1 and u_{10} PC1 are indistinguishable, see supplementary material). A positive SAM with anomalously intense extra-tropical storms (Fig. 5.9, red arrows) projects onto the leading mode of the joint wind and the joint stress PDF (Fig. 5.8f, note the non-linear color scale, corr(**u** PC1, $\boldsymbol{\tau}$ PC1)=0.81). In contrast, a negative SAM leads to anomalously weak cyclone activity and enhanced equatorward flow (Fig. 5.9, blue arrows). Since the latitude limits of Drake Passage capture the southward, barotropic shift of the tropospheric zonal mean zonal winds, the leading wind PDF mode can also be interpreted as a shift of the storm track around its climatological position (Lorenz and Hartmann, 2001).

The 2nd joint wind mode has a more circular structure and captures changes in the width of the joint PDF (Fig. 5.8, explained variance 16%). The projections of the **u** EOF2 on the zonal and meridional axes are similar to the u_{10} EOF2 and v_{10} EOF1 (Fig. 5.5b,c, r(**u** PC2, u_{10} PC2)=0.73, r(**u** PC2, v_{10} PC1)=0.81), though they contain variance due to processes other than storm intensity driven by SAM.

The 2nd mode of the joint wind PDF also leads to a dipole in the joint stress PDF (r($\boldsymbol{\tau}$ PC2, **u** PC2)=0.84). The dipole structure arises because the 2nd joint wind EOF is not precisely symmetric. Nevertheless, the 2nd joint stress mode is confined around ±3 hPa, which illustrates again how changes in the wind variance alone are not responsible for extreme surface stresses. Higher-order modes are not judged to be statistically different from what we would expect to find by computing EOFs of Gaussian noise and are not explored here (Fig. 5.10).

5.5 Biases in Reanalysis and scatterometer products

The leading order modes of the surface wind PDFs provide a framework for interpreting differences between surface wind products. Figure 5.11 shows climatologies of meridional and zonal wind PDFs derived from ERA5 (1979 to 2017), CCMPv2 (1978 to 2017), RSS ASCAT (2007 to 2016) and METOP-A ASCAT (2007 to 2016). The log-scaling exposes velocity differences of up to 30% at a probability density level (for $|u| > 20$m s^{-1} Fig. 5.11a,b). Alternatively, this is expressed as a probability density change for a given velocity compared to ERA5 (Fig. 5.11c,d). While ERA5 and METOP-A ASCAT have narrower tails that rarely exceed 30 m s^{-1}in the zonal direction and 25 m s^{-1}in the meridional direction, CCMPv2 and RSS ASCAT estimate velocities up to 40 m s^{-1}in the zonal direction and 33 m s^{-1}in the meridional direction for a probability density level of 10^{-7}. (In the Drake Passage latitude band, a density level of 10^{-7} corresponds to an area of about two km^2 having a particular wind value.) That is, CCMPv2 and RSS ASCAT exceed extremes winds of 25 m s^{-1}30 to 100 times more often than does ERA5 (Fig. 5.11c,d).

Biases near the PDF centers fall into two simple patterns that approximately match the leading EOFs for the PDFs of u_{10} and v_{10} (compare Fig. 5.11e,f with Fig. 5.5a,b). Here we show the difference of METOP-A ASCAT, CCMPv2, and RSS ASCAT to ERA5 to emphasize these anomaly patterns. For the zonal wind, three scatterometer products have PDFs that are higher around 10 m s^{-1}and lower around zero compared to ERA5. Since the node point of this dipole sits at the median of the ERA5 PDF (Fig. 5.11e, dashed gray line), this pattern is associated with a shift in the maxima of the PDFs (sec. 5.3) and leads to a difference in the PDF means, medians, and standard deviations (Fig. 5.12a).

A different behavior appears in the meridional direction (Fig. 5.11b,d,f). The scatterometer PDFs show a symmetric difference relative to ERA5 and CCMPv2, with fewer winds around zero and more winds at about ± 10 m s^{-1}. This widening of the PDF implies a difference in variance (sec. 5.3). However, these biases are not well captured by the variance metric because biases in

the center may be partly compensated by biases in the tails such that changes in variances are rather small (Fig. 5.12b dashed lines). As an alternative to the metrics provided by mean and variance, the climatological bias pattern in Fig. 5.11f is better understood as resembling the v_{10} PC1 (Fig. 5.5b). This approach works well for both ASCAT products – despite the spikes around zero for RSS ASCAT – but less well for CCMPv2 (Fig. 5.11f). This analysis shows that differences between scatterometer-based products and model-based winds (ERA5) are systematic and similar to the signatures of SAM-related wind variability (sec. 5.3 and 5.4) and suggests that biases reveal differences in the assumptions made in the dynamical model (ERA5) and assumptions made to derive the scatterometer winds.

5.6 Leading modes of extreme winds

Informed by the differences between PDFs for different wind products, we can now investigate the leading modes for extremes of the u_{10} and v_{10} wind PDFs. Figure 5.13 shows the leading zonal and meridional EOFs as in Figure 5.5, but now added to their respective climatology (gray shading for ERA5 and METOP-A ASCAT, blue shading for CCMPv2 and RSS ASCAT). To emphasize the changes in the PDF tails, in Fig. 5.13a,b we show only values outside ±20 m s^{-1}on a log scale. In this scaling, anomalies relative to the climatology are not area equivalent, and negative deviations appear larger than positive deviations.

The 1st u_{10} EOFs extend to extreme wind conditions. An increase in u_{10} PC1 corresponds to a shift in the u_{10} EOF1 maximum, which co-varies with an increase in the extreme zonal winds (compare Fig. 5.6a and Fig. 5.13a). This correlation is generally stronger for ASCAT-based wind products than for ERA5 or CCMPv2, such that an increase in PC1 by one standard deviation means a doubling in the likelihood of extreme wind velocities in the 1st EOF from RSS ASCAT, but less in other products (Fig. 5.13a).

The 1st v_{10} EOF is more consistent for all of the wind products. A typical narrowing of

the v_{10} PDF leads to a reduction by a factor of 3 to 5 in the occurrence of velocities in the tails (Fig. 5.5b and Fig. 5.13b). However, extremes in the 2nd and higher EOFS of v_{10} or u_{10} are not as coherent as the 1st EOFs and are not further analyzed here.

We note that here the SVD decomposes the covariances of very different scales and must be treated with caution. The SVD is an axis rotation along the most common mode of variability in the covariance matrix and these axes (EOFs) are mainly defined by fluctuations in the PDF centers ($O(10^{-2})$), while small fluctuations in the tails ($O(10^{-6})$) only marginally contribute to the modes of the covariance matrix.

To test the robustness of the modal decomposition, we re-derive the SVD for the log-PDFs $\log[D(u,t)]$. Use of the log enhances the variability of the tail compared to fluctuations in the center. The overall shape of the leading-order modes remains robust under a log-weighting for all wind products but with less explained variance for the first modes (supplementary material). The enhancement of extreme winds in the u_{10} EOF1, as observed in Fig. 5.13, also remains robust, while changes in the v_{10} EOF1 are not.

5.7 Discussion

5.7.1 Large-scale circulation establishes surface winds and stress PDFs

As we showed in section 5.3, the first two modes of both the one-dimensional and joint surface wind PDFs resemble the leading modes in surface stress (Fig. 5.4 and 5.6). These two modes trace changes in the conversion of excess atmospheric angular momentum to surface momentum fluxes, without explicitly resolving the cascade of processes involved in converting atmospheric momentum to stress.

The first mode is mainly an eastward shift of the zonal wind probability maximum that leads to more frequent extreme zonal stresses (Fig. 5.6a,b). This shift in the PDF is more complex than a shift of a Gaussian distribution. Southern Ocean zonal surface winds are negatively skewed

and limited in their extremes due to the non-linear relation of surface drag (eq. 5.1.1), and this shift in the PDF maximum does not imply a proportional increase in the PDF's extreme quantile. Instead, the higher-order dependence of surface stress on wind leads to changes in the mean, skewness, and kurtosis; this is captured in the 1st EOF (PC1 u_{10} and PC1 $\boldsymbol{\tau}$ in Fig. 5.14). Changes in the variance, however, are mainly captured in the 2nd EOF (PC2 u_{10} in Fig. 5.14).

The EOF decomposition of the time-varying joint PDF adds a meridional component to dominantly zonal wind and stress variability. As the zonal wind maximum increases in the leading order mode, the meridional component shifts southward (Fig. 5.8c,e). This joint mode is highly coherent with SAM (Thompson and Woodworth, 2013; Thompson and Barnes, 2014) and is created by changes in the storm activity in the latitudes of Drake Passage, which are equivalent to a shift in the storm track position over the SO (Lorenz and Hartmann, 2001). One explanation for the appearance of the meridional wind component in EOF1 is because its associated Coriolis acceleration balances the effect of friction on the zonal surface wind (Limpasuvan and Hartmann, 2000).

This analysis underscores the fact that SAM and zonal statistics of storm activity have similar variability on timescales between five days and four years. While SAM describes the variability of angular momentum-flux convergence in the mid-latitude upper troposphere, extra-tropical cyclones are the dominant mechanism to remove angular momentum from these latitudes (sec. 5.3; Lorenz, 1967; Hartmann and Lo, 1998; Schneider, 2006). Hence, there is a direct dynamical link between upper level wave breaking and the surface stress PDF that is shaped by storms (sec. 5.3 and 5.4). The steady-state leading-order atmospheric zonal momentum balance in mid-latitudes can be written as

$$\partial_y \int_0^\infty \widetilde{[u^* v^*]}\, dz = [\tilde{F}], \tag{5.7.1}$$

where $[u^* v^*]$ is the zonal-mean eddy-momentum flux in the atmosphere, $[F]$ is the zonal mean

surface drag, and $\tilde{(\cdot)}$ indicates the average over a 5-day interval (see e.g. Chapter 11 of Peixoto and Oort, 1992; Edmon et al., 1980). This illustrates that the zonal mean zonal surface drag in the latitude limits of Drake Passage is the result of the atmospheric zonal momentum balance, and, as we showed in section 5.3, the zonal mean surface drag in each 5-day interval can be written as

$$[\tilde{F}] \simeq \bar{\tau}_x + PC1_{\tau_x}(t) \sum_{i=-\infty}^{\infty} \tau_x(i)\, EOF1_{\tau_x}(i),$$

which implies that

$$\partial_y \int_0^{\infty} \widetilde{[u^* v^*]}\, dz \;\simeq\; \bar{\tau}_x + PC1_{\tau_x}(t) \int_{-\infty}^{\infty} EOF1_{\tau_x}\, d\tau_x, \tag{5.7.2}$$

where $\bar{\tau}_x$ is the climatological zonal surface stress and $\tau_x(i)$ is the surface stress for bin-index i of the PDF. Equation 5.7.2 describes how the vertical integral of the momentum-flux convergence in mid-latitudes is balanced by the climatological eastward stress and its 1st EOF. Since the momentum flux convergence is the result of irreversible Rossby wave breaking, its short-term variability is mainly balanced by adjusting the amplitude of the 1st EOF of the zonal surface stress PDF. Changes in the momentum flux convergence are captured by SAM, and hence SAM can be described as rescaled variability of the 1st PC of zonal stress and wind (section 5.3). Since the zonal momentum equation on a rotating sphere essentially describes the conservation of angular momentum, an exact version of (5.7.2) would follow the form of a Fokker-Plank equation (Risken, 1996) and describe a closed balance between the atmospheric angular momentum and the zonal surface stress PDFs. In addition, τ in equation (5.7.2) depends on C_d in equation (5.1.1), which indicates the critical role of C_d in shaping the surface wind and stress PDF (Fairall et al., 2003, and references therein) as well as the relation of the eddy-driven jet to surface drag (Mbengue and Woollings, 2019).

The strong coherence between SAM and the leading mode of surface stress and wind reveals how SAM relates to extreme winds within synoptic-scale systems (Claud et al., 2009;

Booth et al., 2010). A positive SAM increases the probability of wind patterns that are associated with fronts under storms (Fig. 5.9, red arrows). Extreme zonal winds and stresses behind and stronger southward stress ahead of the cold front lead to the southeastward shift of the maximum in $\mathbf{u}$ EOF1 and $\boldsymbol{\tau}$ EOF1 (Fig. 5.6a,b and Fig. 5.8c,f). In turn, a negative SAM is associated with fewer extreme westerly winds (or even no predominant westerly winds) and instead enhanced equatorward winds and stresses from the southwest, due to a shift of the cyclone centers into or out of Drake Passage latitudes. This SAM-mode alters the wind and stress PDFs following an EOF pattern that also extends to the tails of the PDF (sec. 5.6, Sampe and Xie, 2007; Lin et al., 2018).

The second mode of variability is linearly independent of the first mode by construction. It describes symmetric widening and contraction of the PDF, indicating a periodic change of variance without changing the mean (Fig. 5.5b, Fig. 5.6, Fig. 5.14). This mode explains about 18% of the zonal and 53% of the meridional wind variability, mainly due to annual and semi-annual changes in the PDF variance (Fig. 5.7a, Fig. 5.14). This mode is concentrated around the PDF's center with little or no influence on extreme winds and only mild impact on extreme stresses (Fig. 5.8d,g).

We have shown that SAM variability and trend represent more complex changes of the atmospheric forcing than just changes in the mean winds and stress. This provides a new perspective on the observed increase of eddy activity in the SO that is accompanied by only weak changes in the SO zonal transport ("eddy saturation", e.g. Hallberg and Gnanadesikan, 2006; Meredith and Hogg, 2006; Böning et al., 2008). While changes in the mean zonal wind stress, i.e. a trend in SAM, may change the larger-scale SO baroclinicity and subsequent mesoscale eddy activity (Thompson and Solomon, 2002; Meredith et al., 2012), section 5.3 and 5.6 show that trends in SAM also have a significant impact on extreme stress statistics. Extreme, localized wind stress under storms (sec.5.4 and 5.75.7.2) can imply stronger wind-stress curls leading to localized strengthened Ekman pumping (e.g. O'Neill et al., 2003, 2005), which then interact with

the mesoscale eddy field. In addition, extreme winds under storms also enhance near-inertial oscillations in the upper ocean (Pollard, 1980; Thomson and Huggett, 1981; Gill, 1984; D'Asaro et al., 1995) and can possibly provide energy for the mesoscale eddy field (Xie and Vanneste, 2015; Asselin and Young, 2020). Hence, we speculate that a positive SAM trend could increase upper-ocean mesoscale activity by increasing wind extremes, in addition to increasing the mean wind speed and subsequent balances of the larger-scale baroclinicity.

5.7.2 Interpreting the leading-order mode as a dominant mode of SO atmosphere-ocean interaction

The empirical decomposition of surface wind and stress into two leading modes leads us to ask which mode is responsible for strong air-sea heat and property fluxes associated with SO mixed-layer ventilation events (Schulz et al., 2012; Ogle et al., 2018; Tamsitt et al., 2020) and marine cold-air outbreaks (Bracegirdle and Kolstad, 2010; Papritz et al., 2015; Fletcher et al., 2016). While SO mixed-layer ventilation is observed to be driven by extreme turbulent heat fluxes that often coincide with equatorward winds advecting cold air from the south (Tamsitt et al., 2020; Ogawa and Spengler, 2019; Song, 2020), the same process, described as a marine cold-air outbreak, leads to atmospheric boundary layer deepening (Grossman and Betts, 1990; Brümmer, 1996; Renfrew and Moore, 1999) and affects the synoptic scale circulation (Papritz and Pfahl, 2016).

Equatorward winds occur during a negative SAM mode (Fig. 5.8c,e, and Fig. 5.5d) and also during a negative variance mode (increasing variance, Fig. 5.8d,e, and Fig. 5.5b). Both modes, or their superposition, could capture events that create strong air-sea fluxes associated with mixed-layer ventilation and marine cold-air outbreaks. While the variance mode has a dominant seasonal cycle, as observed in the mixed-layer ventilation (dashed orange-red line in Fig. 5.7, Tamsitt et al., 2020), SAM explains 67% of the wind variance (Fig. 5.4) and 33% of stress variance (not shown).

We suggest that SO mixed-layer ventilation is a result of the superposition of SAM and oceanographic preconditions such that enhanced equatorward winds during negative SAM are likely to be conducive to increased turbulent heat fluxes by winter cold air advection (sec. 5.4, Fig. 5.9). This mechanism is plausible even when taking into account observed long-term trends of SO ventilation and heat content (Gille, 2008; Sallée et al., 2010), SAM-like variations in SO mixed-layer depths (Cerovečki et al., 2019; Meijers et al., 2019), and the long-term trend to a more positive SAM with more westerly wind extremes in the Drake Passage latitudes (Thompson et al., 2000; Thompson and Solomon, 2002; Lin et al., 2018). Because mixed-layer ventilation relies on additional limiting factors like seasonal changes in the meridional surface temperature gradient, local insolation, and mixed-layer stratification, it is likely that the northward advection of cold polar air during negative SAM modes is more effective in winter when thermodynamic preconditioning favors mixed-layer ventilation. This is in agreement with observed mixed-layer ventilation and marine cold-air outbreak events that occur preferentially in austral winter (Papritz et al., 2015; Fletcher et al., 2016; Tamsitt et al., 2020): even if SAM has no dominant seasonality (Fig. 5.7a) and a small, long-term trend to more positive values, its negative phase is likely the important contributor to trends in highly non-linear atmosphere-ocean interaction. We hypothesize that exceptionally strong westerly winds (positive SAM) are not enough to drive deep mixed-layer ventilation, because they are not the only factor in determining ocean ventilation and they are also not observed as the dominant mechanism to perturb the atmospheric boundary layer.

Even though we do not explicitly analyze atmosphere-ocean heat fluxes in this study, the oceanic and atmospheric processes outlined above suggest that equatorward winds are important for the evolution of both boundary layers and for the exchange of heat and CO_2. SAM controls the statistics of equatorward winds, but it can only control the statistics of intensified atmosphere-ocean fluxes if the ocean stratification is responsive to the atmospheric forcing.

5.7.3 Dynamic drivers of climatological biases

The leading modes of zonal and meridional winds resemble climatological biases between ERA5, CCMPv2, RSS ASCAT and METOP-A ASCAT (sec. 5.5). These biases also extend to the PDF's extremes (Fig. 5.11, Gille, 2005). The probability of velocities larger than ± 20 m s^{-1}s about 100 times higher for CCMPv2 and RSS ASCAT than for ERA5 and METOP-A ASCAT.

These climatological biases also appear in the extremes of the leading EOFs (sec. 5.6). We found more extreme wind events during positive SAM in RSS ASCAT products than in ERA5 or METOP-A ASCAT climatology. However, SVD results from the PDF tails must be treated with caution because extreme values are the least certain portion of a PDF given the rarity of extreme events, and the covariance is largely determined by the PDF's centers (sec. 5.6 and Appendix B).

These results agree with recent central-moment-based (Monahan, 2006a) validations of reanalysis surface winds in which ERA5 winds show systematic biases compared to ASCAT and wave-buoy observations (Yagi and Kutsuwada, 2020; Rivas et al., 2019). Additionally, the analysis in section 5.5 hints at reasons why reanalysis surface winds differ (Taboada et al., 2019; Wen et al., 2019; McDonald and Cairns, 2020): since biases in surface wind PDFs resemble the leading mode of atmospheric angular-momentum flux convergence (sec. 5.7.1), differences between wind products, whether from reanalyses or scatterometers, might arise from errors in the parametrization of boundary layer turbulence or wind retrieval algorithms, errors in representing mesoscale processes associated with cold fronts (Blein et al., 2020), or large-scale biases in the reanalysis momentum budget (Pithan et al., 2016).

The high correlation of the large-scale flow and surface wind biases can potentially improve surface wind products and subsequently surface wave models (Wentz et al., 2015; Ribal and Young, 2019; Trindade et al., 2020; Allen et al., 2020). Spectral wave models rely on accurate surface winds and are particularly sensitive to surface wind extremes (Cavaleri, 1994; Cardone et al., 1996; Ponce and Ocampo-Torres, 1998; Feng et al., 2006; Durrant et al., 2013; Stopa and Cheung, 2014; Janssen and Bidlot, 2018; Osinski and Radtke, 2020). Due to the biases described

above and deficits in the momentum balance of Atmospheric Circulations Models (Pithan et al., 2016), wave hindcast models are commonly tuned to wave buoy observations by adjusting high surface wind speeds. This practice cannot be applied in "free-running" surface wave models as part of a coupled climate model (Li et al., 2016; Bourassa et al., 2019), because biases in the model mean state of other model components hinder direct validation with in-situ observations. At the same time including surface wave models in a coupled model framework might improve estimates of C_d, which plays a critical role in shaping the surface stress PDF (sec. 5.7.1 and Edson et al., 2013) and the large-scale atmospheric flow (Mbengue and Woollings, 2019).

5.8 Conclusion

Southern Ocean surface winds play an important role in ventilating the upper ocean, mainly due to short, extreme events of atmosphere-ocean interaction. This study has investigated a statistical representation of surface wind and stress PDFs that connects large-scale modes of atmospheric variability with short-term processes at the atmosphere-ocean interface.

We have derived leading modes of variability of PDFs of surface winds and stresses between 55°S and 63°S using four wind products (ERA5, CCMPv2, RSS ASCAT, METOP-A ASCAT). After calculating time-varying PDFs from all available data points in longitude and latitude in 5-day chunks, we use an SVD of the zonal, meridional, or joint PDF. The first two modes of the zonal or meridional wind together explain 90% to 92% of the total variance, while the first three modes of the joint wind SVD explain about 65% of the total variance. These decompositions are robust between the wind products, despite differences in their degrees of freedom (sec. 5.2.3 and Appendix B).

The first two PCs of the surface stress PDFs explain an equivalent or greater fraction of variance than the first two PCs of the wind PDFs (Fig. 5.6 and Fig. 5.10) and the temporal variability of the leading wind stress modes (PC1 and PC2) is nearly identical (sec. 5.3). This

surprising co-variability occurs despite the different noise levels in their SVDs (Fig. 5.6). They appear because the variance of the joint stress PDFs is the square of the variance of the joint surface wind PDFs.

We would like to put the result in the broader context of atmosphere-ocean coupling:

- PDFs, used in place of mean quantities, are a cornerstone of stochastic climate modeling (Hasselmann, 1976). Here we have expanded on this idea, but, instead of creating PDFs for large ensembles (Kay et al., 2015; Maher et al., 2019; Deser et al., 2020; Reimann and von Storch, 2020), we have assumed that the governing processes are ergodic in the latitudes of Drake Passage and over short time-periods. This has allowed us to derive a time-evolving PDF from a single realization of the winds (here ERA5 reanalysis or direct scatterometer winds). The leading order variability of the wind PDFs can then be analyzed using an SVD and compared to other models or wind-products. We choose a standard SVD in order to reduce the complexity of the PDF variability to a set of linearly independent lower-dimensional EOFs, although other forms of modal decomposition might be similarly illuminating. We have shown that EOFs of surface variables offer an efficient way of capturing larger-scale modes of atmospheric variability (SAM) that can be described as stochastic processes ("zonal index", Robinson, 2000; Vallis et al., 2004)).

- We showed that assuming Gaussian distributions as a basis for surface wind is insufficient (also shown by Monahan, 2008). This assumption is usually made when wind speed is modeled as a Weibull distribution, which can be derived from independent Gaussian distributions in u and v, with a non-zero mean wind (Hennessey, 1977; Justus et al., 1978; Monahan, 2007). Deviation from the Weibull distribution can be captured by higher-order moments (Monahan, 2006b), but their relations require many degrees of freedom to be well constrained. The SVD of time-varying PDFs used here needs fewer degrees of freedom per time interval to constrain the PDF tails (Fig. 5.13 and sec. 5.2.2), and the superposition of a few modes explains most of the variance, even when the variance is

non-stationary and non-symmetric. These leading modes also suggest physical drivers of the PDF shape (eq. 5.7.2). Tracing these physical drivers using just the time-varying mean or variance is often possible, but central moment estimates mix several signals and hinder the interpretation of physical mechanisms (Fig. 5.14).

- SVDs of surface wind PDFs connect scales of upper-level Rossby wave breaking (SAM, O(10^6 m)) with surface winds on the O(10^4 m) scales resolved through scatterometer retrievals. This means that scatterometer observations over the SO can be directly related to the large-scale flow of the atmospheric interior (as shown for a two-layer model in George et al., 2019). In addition to validating cyclone intensities in general circulation models and reanalysis, scatterometer winds provide an independent constraint on the atmospheric angular momentum balance on short timescales.

- SVDs of the surface stress PDFs often show a higher signal-to-noise ratio (S/N) then surface winds because they have a steeper decay in the eigenvalues (for example, Fig. 5.10). Given that the leading modes of wind and stress capture the same underlying process, the S/N ratio in the commonly analyzed surface winds is likely weaker than in surface stress because of their square relationship (5.1.1). Since scatterometers observe surface capillary waves, which are more closely related to surface stress than to surface winds, we would expect that capillary wave roughness has an even higher S/N than found in this analysis. The initial S/N from capillary wave roughness is reduced when converting to 10-meter winds, and only partly recovered again when 10-meter winds are converted to stress, due to assumptions about the lower 10 meters of the atmosphere, surface waves, and temporal or spatial averaging.

We demonstrated that retaining the full PDFs of variables, rather than reducing them to the moments of the PDF, can be a useful tool to understand the physical processes likely to govern wind variability. This approach is especially relevant when observing variables near the surface

because they are often the result of non-linear processes that create non-Gaussian distributions. Any kind of spatial or temporal averaging will tend to reduce the number of fluctuations in the PDF tails. Because averaging involves summing multiple independent values, through the central limit theorem, it leads to more Gaussian-like distributions. Even the hourly, 0.25° wind and stress data used here are an approximation to the PDF that would arise from instantaneous point observations. The time and spatial scales that would be required for a sufficient PDF are related to the scales at which momentum is transferred to the ocean. This scale is described by the adjustment timescale of the equilibrium range of the surface wave spectrum (Phillips, 1985).

Acknowledgments

MCH and STG were supported by the NASA Ocean Vector Winds Science Team (NASA award 80NSSC19K0059). BDC and STG also received support from the NASA Surface Water and Ocean Topography Science Team (NASA awards NNX16AH67G and 80NSSC20K1136).

Chapter 5, in full, has been submitted for publication of the material as it may appear in Journal of Climate, Hell, M. C., Cornuelle, B. D., Gille, S. T., Lutsko, N. J., AMS, 2020. The dissertation/thesis author was the primary investigator and author of this paper.

Appendices

G Analysis of the larger SO

In order to test the robustness of the Drake Passage PDFs, the joint PDFs of surface wind and stress are rederived for 25°S to 65°S to cover the larger SO. Figure A1 compares the EOFs derived for the latitudes of Drake Passage (55°S to 63°S, black) with EOFs from the SO (red). The figure also shows the EOF decomposition for CCMPv2 winds for the larger SO latitude range.

The first PCs for the larger SO 5-day records explain less variance than do PCs for the Drake Passage latitude band, but the leading order EOFs have the same shapes in both cases (Fig. A1). A higher noise level and hence less explained variance leads to weaker EOF amplitudes that are less well separated (Fig. A1d). The PCs of the leading modes derived for the SO correlate well with the PCs of the leading modes derived for Drake Passage when the SVDs are performed in one direction only (Fig. A2). The joint PDFs correlate less well, due to the different noise levels and more subtropical wind regimes and/or coastal winds in the large SO case. The larger SO includes additional processes and result in more Gaussian like primary modes (Fig. A2 right panels).

H Effective sample size

The effective sample size is estimated by calculating the e-folding scales in longitude, latitude and time from zonal and meridional winds in the latitudes of Drake Passage (55°S to 63°S). The ERA5 data are provided on an hourly 0.25°-grid such that the autocorrelation function ρ_{dim} in the zonal and time directions can be robustly estimated using a fast Fourier transform. In the meridional direction, we use lagged autocorrelation (Fig. B1a-c). After deriving ρ_{dim} for u_{10} and v_{10} separately in all three dimensions, the effective number of degrees of freedom N_{eff} is calculated by correcting the number of grid points per 5-day period $N = 5,356,800$ with

$$N_{eff} = N \;\; \gamma(\rho_{u_{10}})\; \gamma(\rho_{v_{10}}) \;\; \gamma(\rho_{time}), \tag{H.1}$$

with

$$\gamma(\rho_{dim}) = \frac{N}{1 + 2\ \text{median}[\sum_1^{n-1} \left(1 - \frac{k}{n}\right) \rho_{dim}(k), n]}, \tag{H.2}$$

where k is the lag of the auto-correlation function (von Storch and Zwiers, 1999, Chapter 6). We take the median of the PDF of all possible auto-correlation lengths n to have an estimate that is

less dependent on the truncation of ρ_{dim}.

The number of data points differs between the products because the spatial coverage and time steps differ. To calculate N_{eff} for CCMPv2, RSS A-SCAT, and METOP-A ASCAT, we adjust N and $\rho_{time}(k)$. The auto-correlation ρ_{time} is adjusted by a factor of $1/6$ for the 6-hourly CCMPv2 data and by a factor of $1/12$ for the twice-daily RSS A-SCAT and METOP-A ASCAT data. Fig. B1d shows the effective DOF for u_{10} and v_{10} as well as their spatial coverage as a function of time for all four data products (ERA5 is assumed to provide 100% coverage. The u_{10} and v_{10} DOF have a fixed ratio of about 6.)

I Southern Annular Mode

The Southern Annular Mode (SAM) is derived from hourly zonal mean ERA5 zonal wind data that are averaged to 5-day-means (, CDS). We closely follow Thompson and Woodworth (2013) by first deriving the seasonal anomalies for each 5-day period between 1000 hPa and 50 hPa from 1979 to 2017 at each gridpoint. The seasonal anomalies are weighted by the square root of the cosine of latitude and by mass, while the latter is estimated from the pressure levels prior to performing the SVD (Thompson and Wallace, 2000). Figure C1 shows the results of the SVD of the zonally averaged zonal wind. The leading-order mode of this decomposition is defined as the Southern Annular Mode (SAM) in this study. SAM derived from geopotential heights rather from zonal winds leads to a nearly identical mode of of variability, and for this study we chose to use zonal wind, because of its direct relation to the zonal momentum equation.

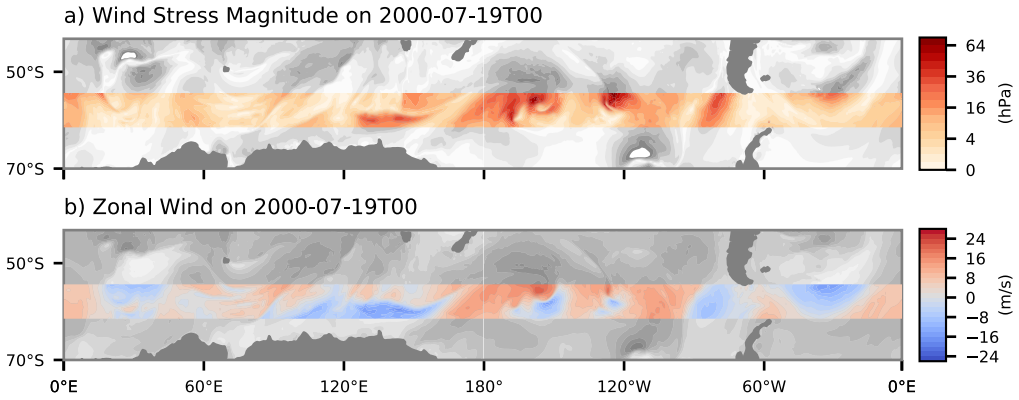

Figure 5.1: (a) Surface wind stress magnitude over the Southern Ocean on 19 July 2000. Data from the Drake Passage range are in red shading. (b) Zonal surface winds (u_{10}) for the same date as in (a).

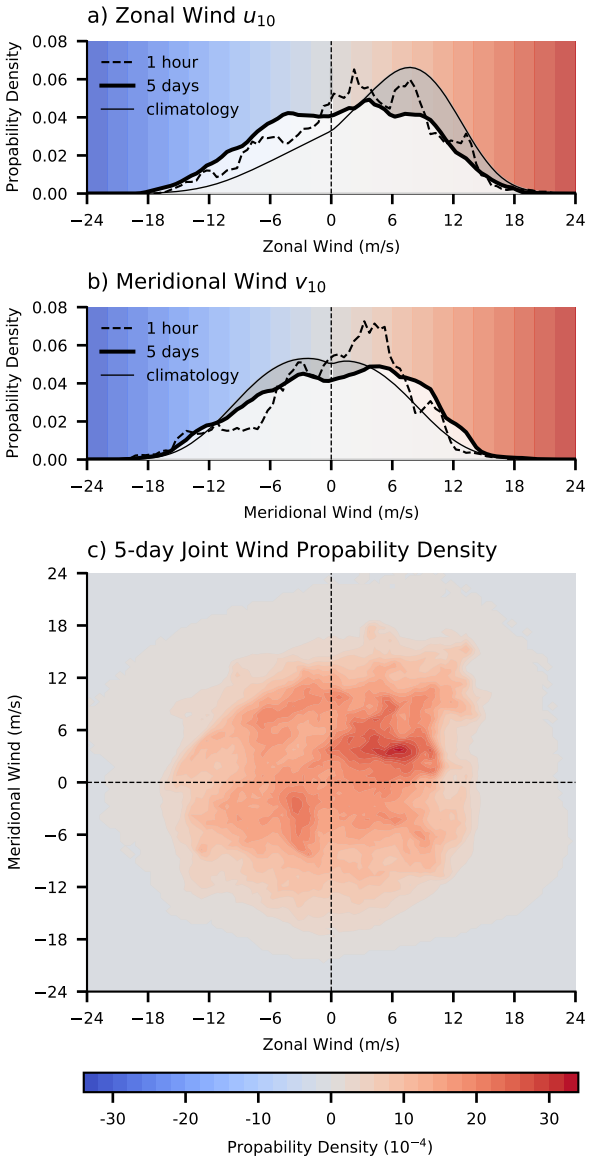

Figure 5.2: (a) Zonal wind PDFs for the 1-hour time step shown in Figure 5.1b (dashed black line), 5-days including this time step (thin black line with filled gray area), and the climatology (thick black line, white shading). The background coloring corresponds to the color scale in Figure 5.1b. (b) Same as (a) but for the meridional wind component. (c) The corresponding joint wind PDFs for a 5-day timestep.

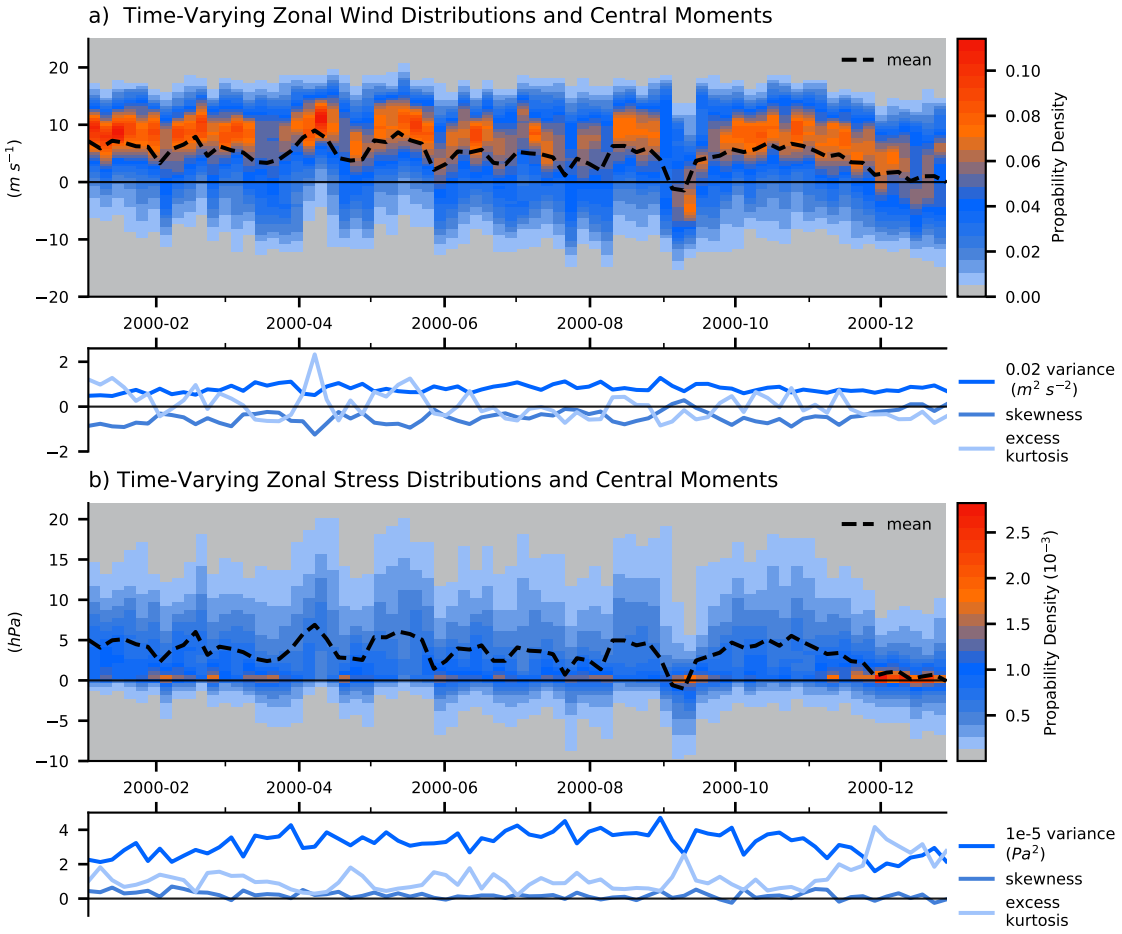

Figure 5.3: (a) One year of time-varying zonal wind PDFs. Each pixel indicates the probability of wind occurring in a 0.5 m s^{-1}-wind interval within 5 days. The black dashed lines indicate the PDF mean. The blue lines in the sub-panel show the higher moments of the PDF: variance ($m^2 s^{-2}$), skewness (unitless) and excess kurtosis (unitless). The variance is rescaled by a factor of 0.02. (b) same as (a) but for zonal stress. In this case the variance (Pa^2) is re-scaled by 10^{-5} .

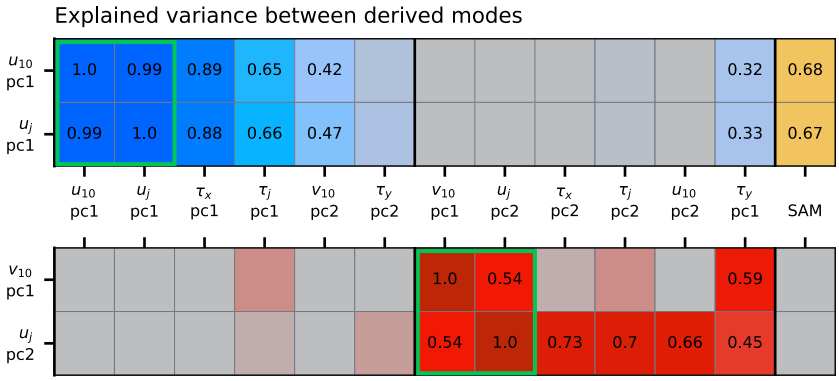

Figure 5.4: Squared correlations (explained variances) between leading PCs and the Southern Annular Mode (SAM). Modes in the green boxes are used in sections 5.3 and 5.4, namely the 1st PCs of the u_{10} decomposition (u_{10} PC1), the joint wind decomposition (**u** PC1), the u_{10} decomposition (v_{10} PC1) and the 2nd PC of the joint wind decomposition (**u** PC2). Modes where most of the variance is explained by u_{10} PC1 are marked with blue (upper half) and modes where most of the variance is explained by v_{10} PC1 are in red (lower half). The explained variance shared with SAM is shown in orange in the most right column. Only explained variances larger than 0.5 are indicated.

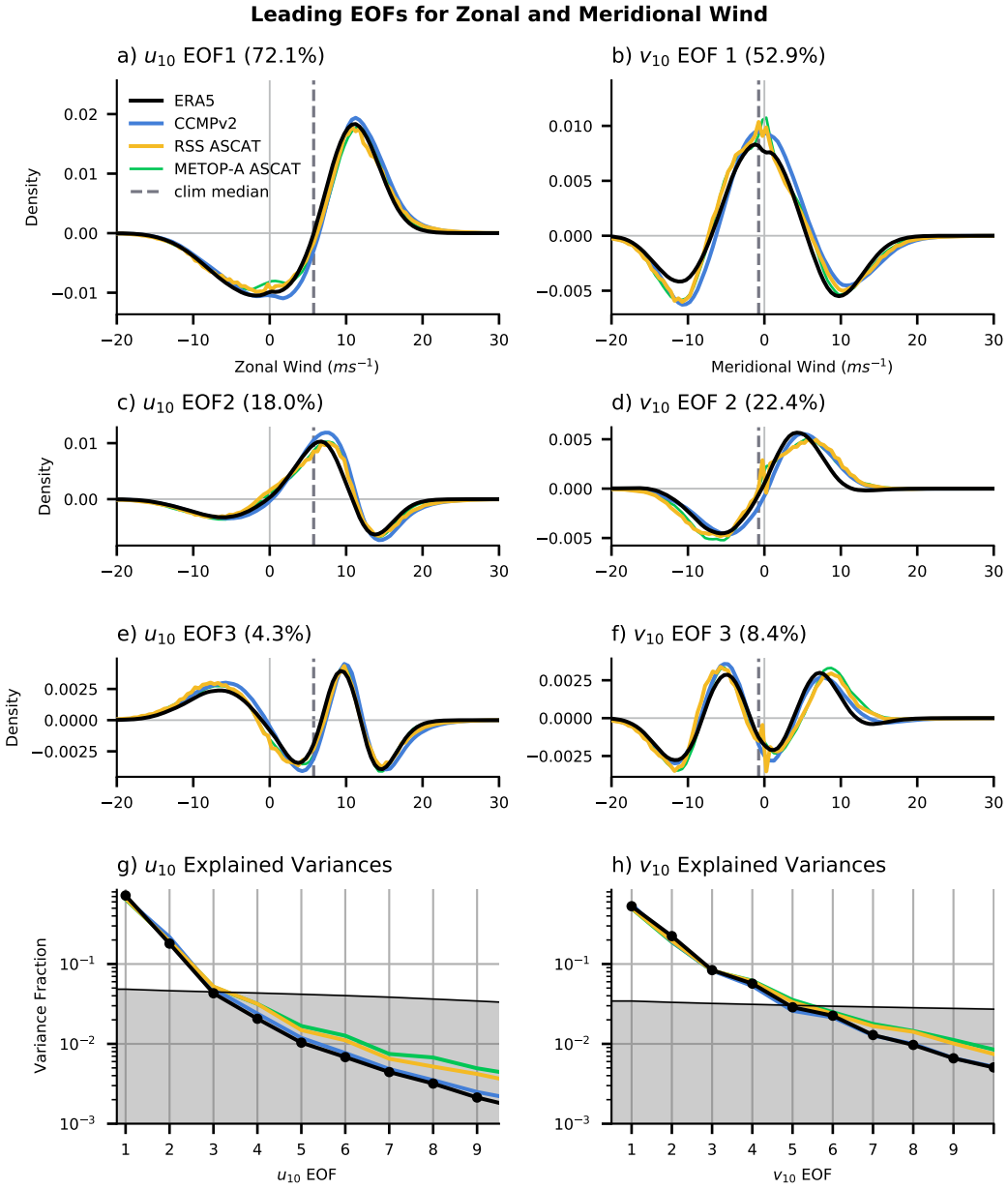

Figure 5.5: First three leading EOFs of zonal wind (a,c,e) and meridional wind (b,d,f) for ERA5 (black), CCMPv2 (blue), RSS ASCAT (orange) and METOP-A ASCAT (green) with their fraction of explained variance in the title. Explained variance for the first 10 modes in log-scale for the zonal wind (g) and meridional wind (h). Gray shading indicates the fraction of variance explained by a decomposition of Gaussian noise (Preisendorfer N-test).

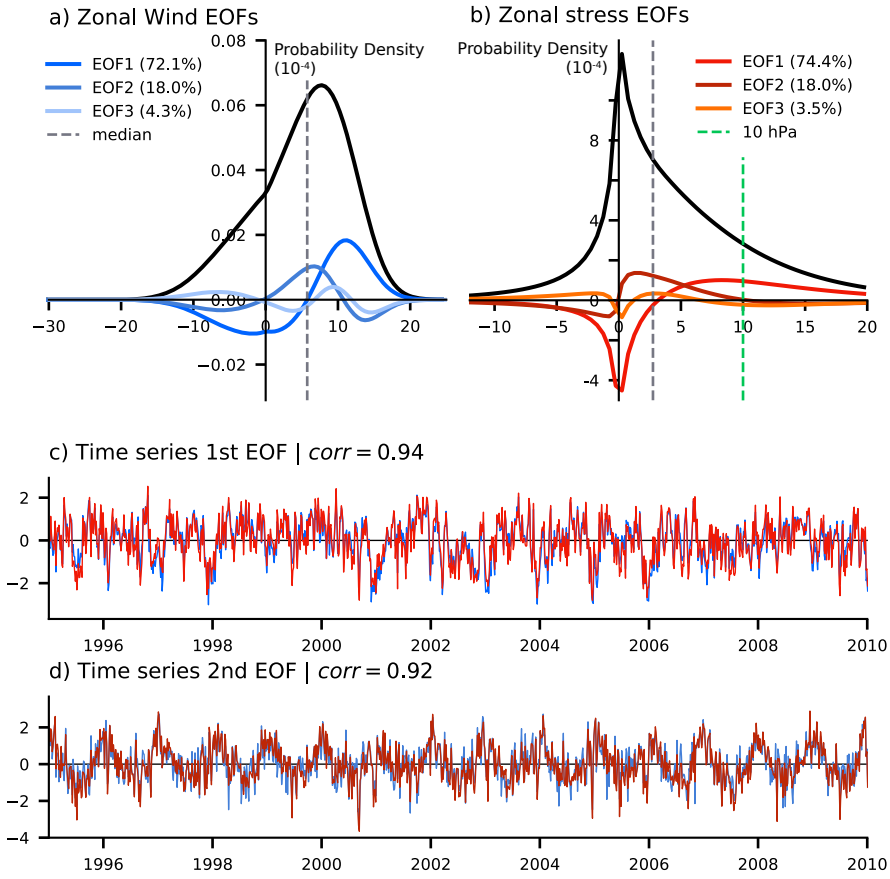

Figure 5.6: Leading EOFs for (a) zonal wind and (b) stress. The climatology is indicated in black, the median with dashed gray lines, and the 10 hPa line as green dashed line. (c) PCs of the 1st mode of zonal wind (u_{10} PC1, blue) and the 1st mode of zonal stress (τ_x PC1, red). (d) Same as (c) but for the 2nd mode (u_{10} PC2 and τ_x PC2).

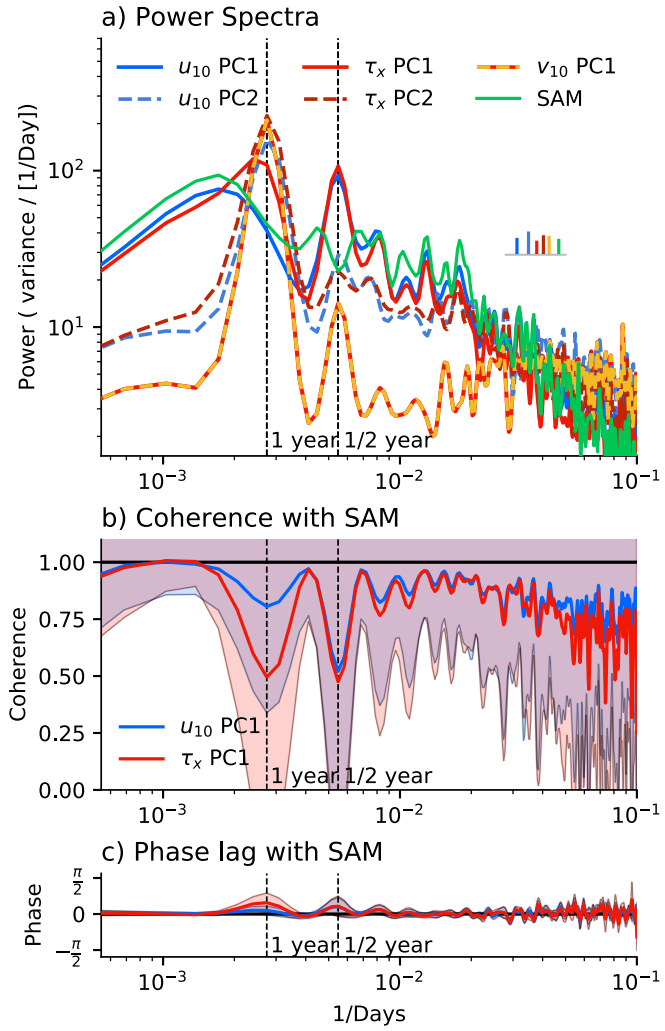

Figure 5.7: (a) Power spectra of u_{10} PC1 (blue), u_{10} PC2 (dashed blue), τ_x PC1 (red), τ_x PC2 (dashed dark red), v_{10} PC1 (orange-red dashed), and SAM (green). (b) Coherence of u_{10} PC1 (blue) and τ_x PC1 (red) with SAM as defined in Appendix C. (c) Coherence phase of u_{10} PC1 and τ_x PC1 with SAM. Shadings in (b) and (c) indicate ± 1 standard deviation of the estimated coherence or phase respectively (Bendat and Piersol, 2010). Power spectra and co-spectra are estimated using a Welch's overlapping segment method with a segment length of 8 years (584 data points) with a Hanning window on the detrended data. The resulting lines are smoothed with a Lanczos filter of 2×10^{-3} days^{-1} window length.

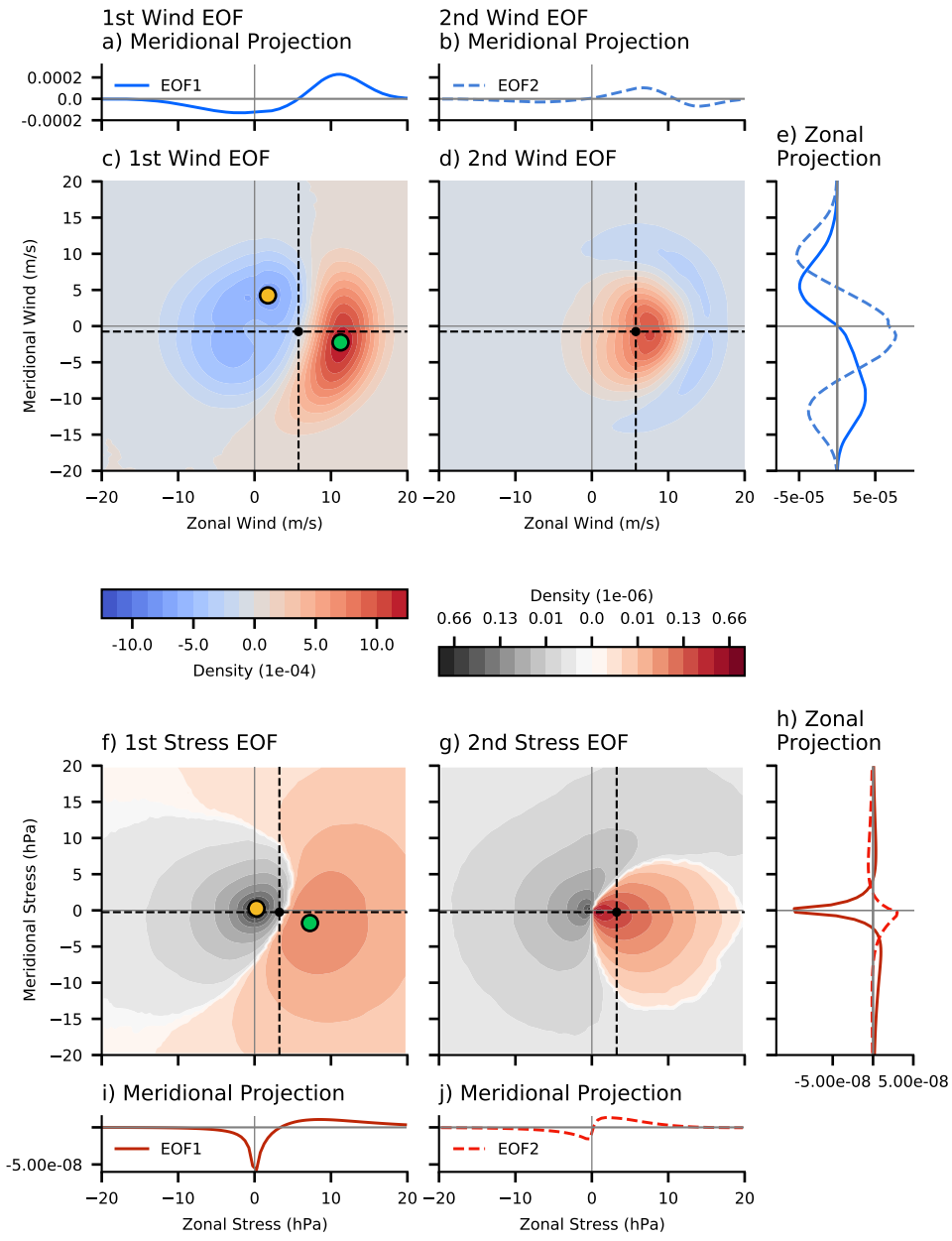

Figure 5.8: First two EOFs of the joint PDFs of wind (c and d) and stress (f and g) and their projections. (a and b) Meridional mean of the 1st (blue) and 2nd (blue dashed) joint wind EOFs. (e) Zonal mean of the 1st and 2nd joint wind EOFs. (h) Zonal mean of the 1st (red) and 2nd (red dashed) joint stress EOFs. (i and j) Meridional mean of the 1st and 2nd joint stress EOFs. The orange and green dots in (c) and (f) indicate the maximum and minimum of the respective EOF. The shading for stress modes is adjusted following a $(\cdot)^{1/4}$-scale.

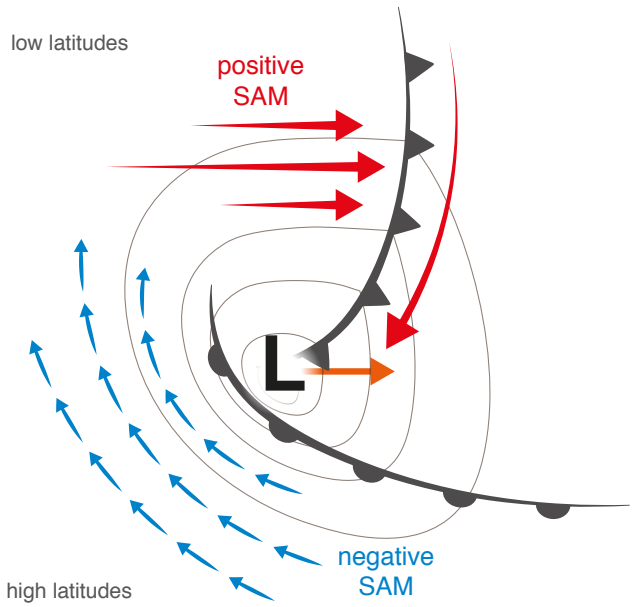

Figure 5.9: Schematic of SH surface winds in the moving frame of an extra-tropical cyclone. Strong westerly winds behind the cold front and along-front winds ahead of the cold front (in red) are enhanced during positive SAM phase. Southeasterly winds not associated with the cold front (in blue) are enhanced during negative SAM. Light gray lines show idealized sea level pressure lines, and the orange arrow indicates the average travel direction of the cyclone.

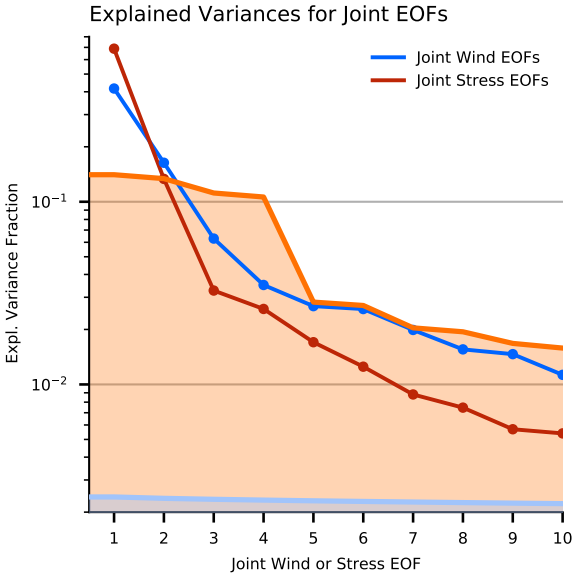

Figure 5.10: Explained variances for the joint wind PDF in (blue) and the joint stress PDF in (red) on a log scale. The orange and light blue lines show the 95% levels for the joint stress and wind estimated from the Preisendorfer and Mobley (1988) N-test after 1000 repetitions.

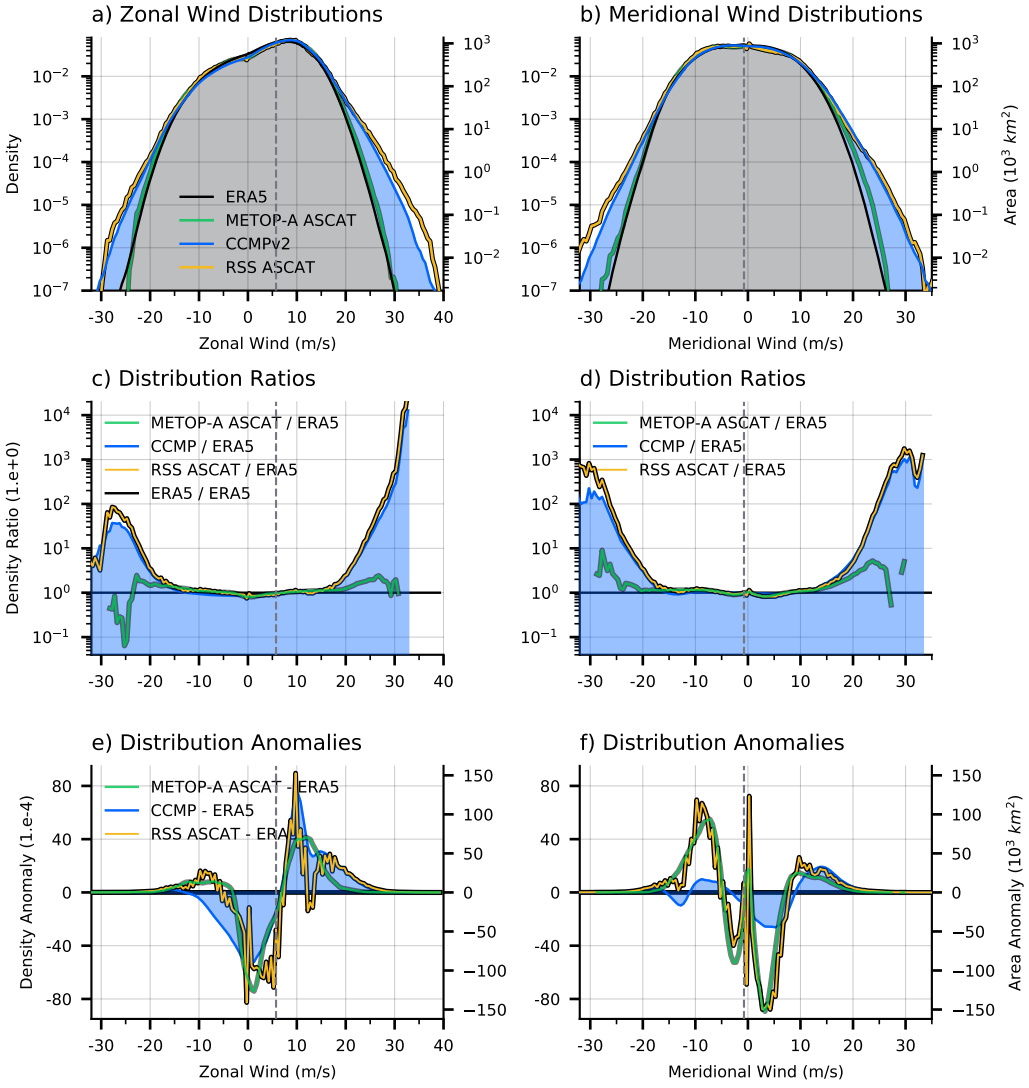

Figure 5.11: PDFs of (a) zonal and (b) meridional wind between 55°S and 63°S derived from ERA5 reanalysis (black), observationally constrained CCMPv2 winds (blue), METOP-A ASCAT (green), and RSS ASCAT scatterometer winds (orange) with log scaling. The scaling on the right ordinate is the area equivalent for a given probability density in 10^3 km^2. (c) and (d), same as (a) and (b) but shown as ratio compared to the ERA5 PDF. (e) and (f) same as (a) and (b) but shown as difference to the ERA5 PDF for zonal and meridional wind respectively.

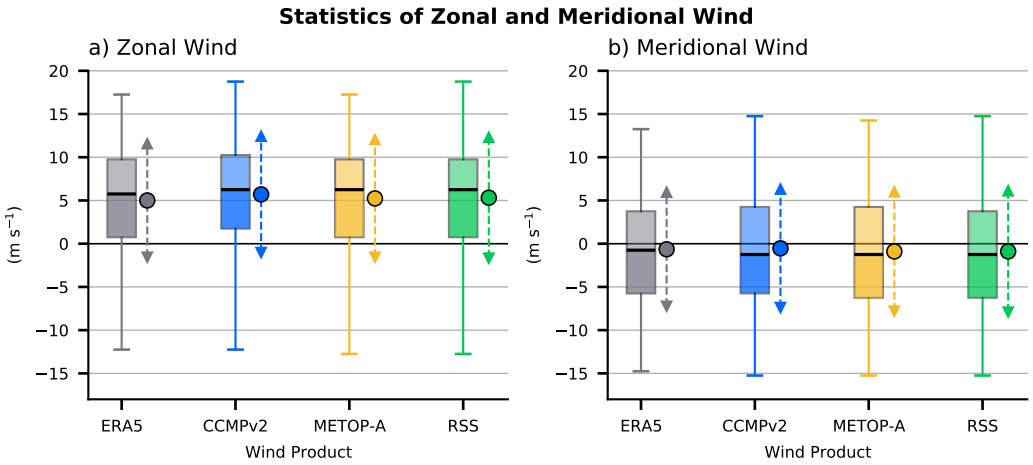

Figure 5.12: Zonal wind (a) and meridional wind (b) statistics as box-and-whisker plot for ERA5 (gray), CCMPv2 (blue), METOP-A ASCAT (orange), and RSS ASCAT (green). The boxes indicate the limits of the 1st and 3rd quartile surrounding the medians (horizontal black lines), and the whiskers indicate the 1% and 99% quantiles. The colored dots are the mean centered between the range of ± 1 standard deviation (dashed lines between triangles).

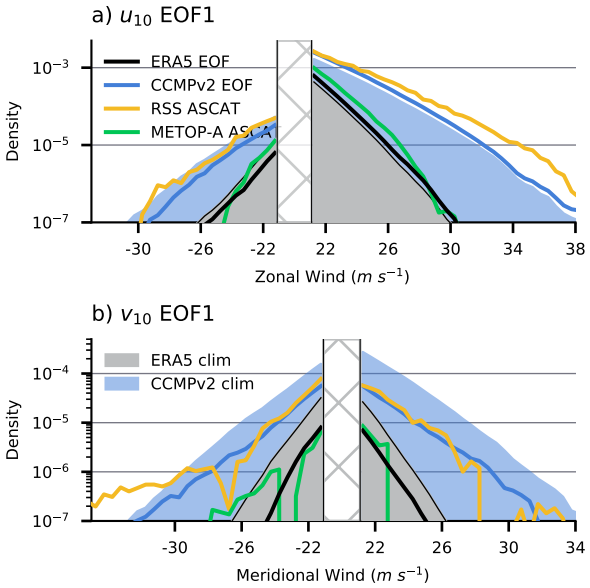

Figure 5.13: First EOFs of the zonal (a) and meridional wind (b) added to their climatology and shown on a log scale. Data between ±21 m s^{-1} are masked out to emphasize the variability in the tails.

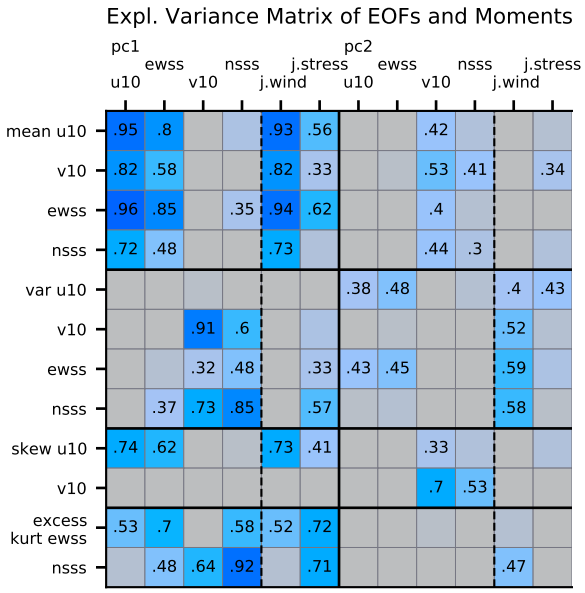

Figure 5.14: Explained variances between PCs from the SVDs of directional wind and stress and first four moments of the PDF.

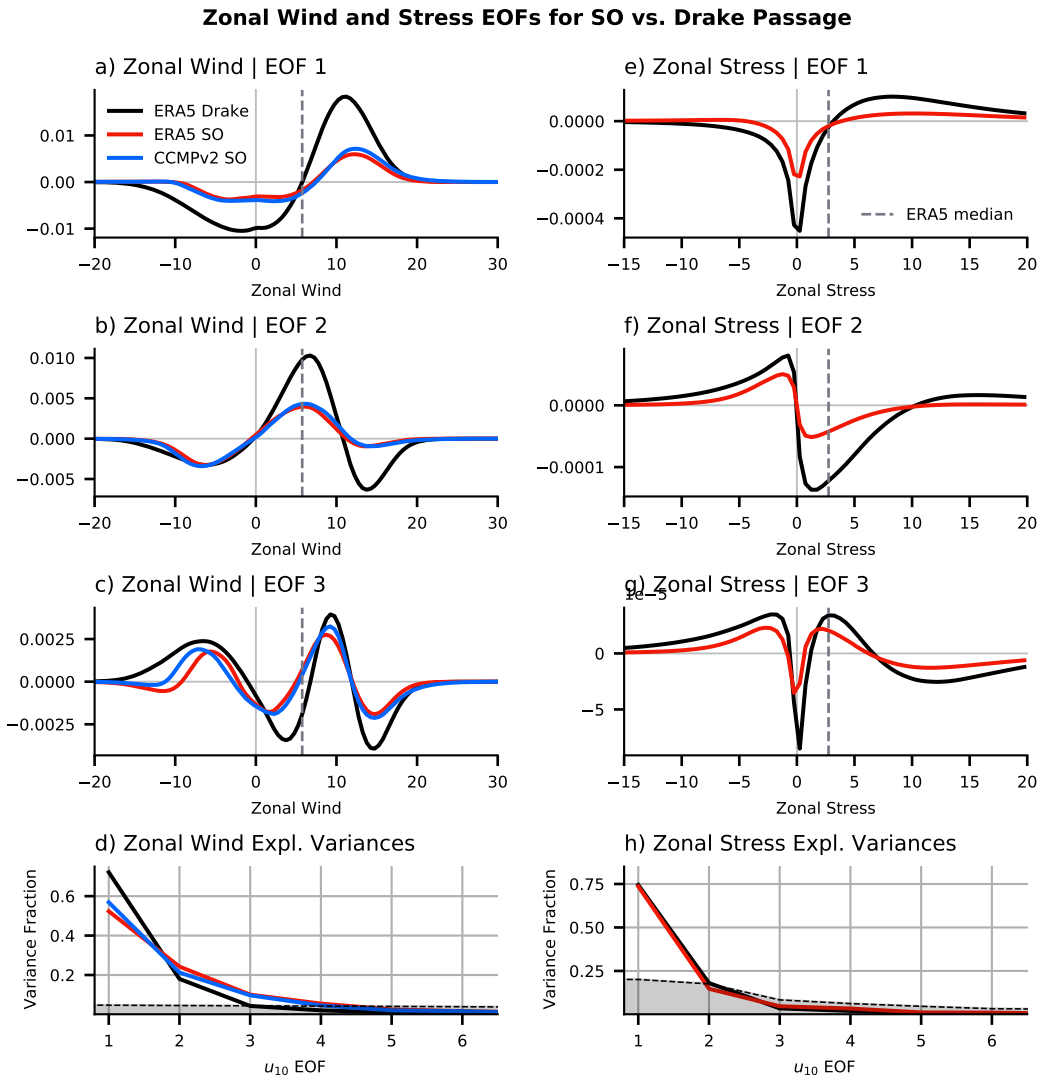

Figure 5.15: (a to f) Leading three EOFs of zonal surface wind and stress derived from data in the latitude range of Drake Passage (55°S and 63°S) using ERA5 (black) and for the SO (25°S and 65°S, red for ERA5 and blue for CCMPv2). (g,h) Explained variances for surface wind and stress with the significance levels derived as in Figure 5.5.

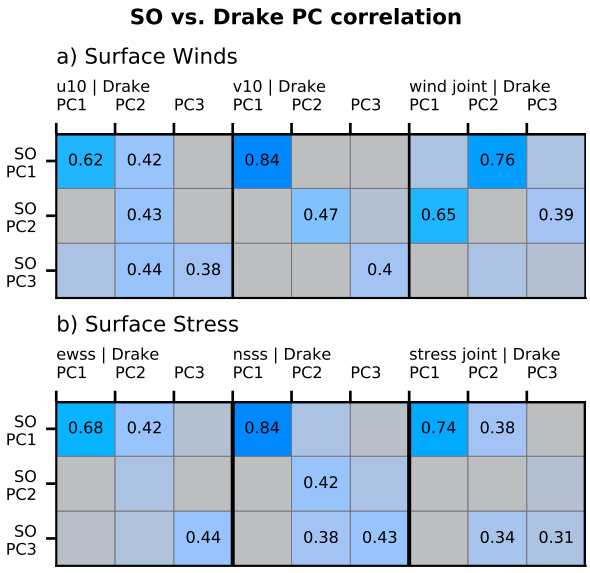

Figure 5.16: Correlation of the three leading modes of the zonal winds u_{10}, meridional v_{10} and joint wind **u** decompositions from Drake Passage PDFs with the corresponding leading three modes from larger SO PDFs. (b) Same as (a) but for zonal τ_x, meridional τ_y, and joint wind $\boldsymbol{\tau}$.

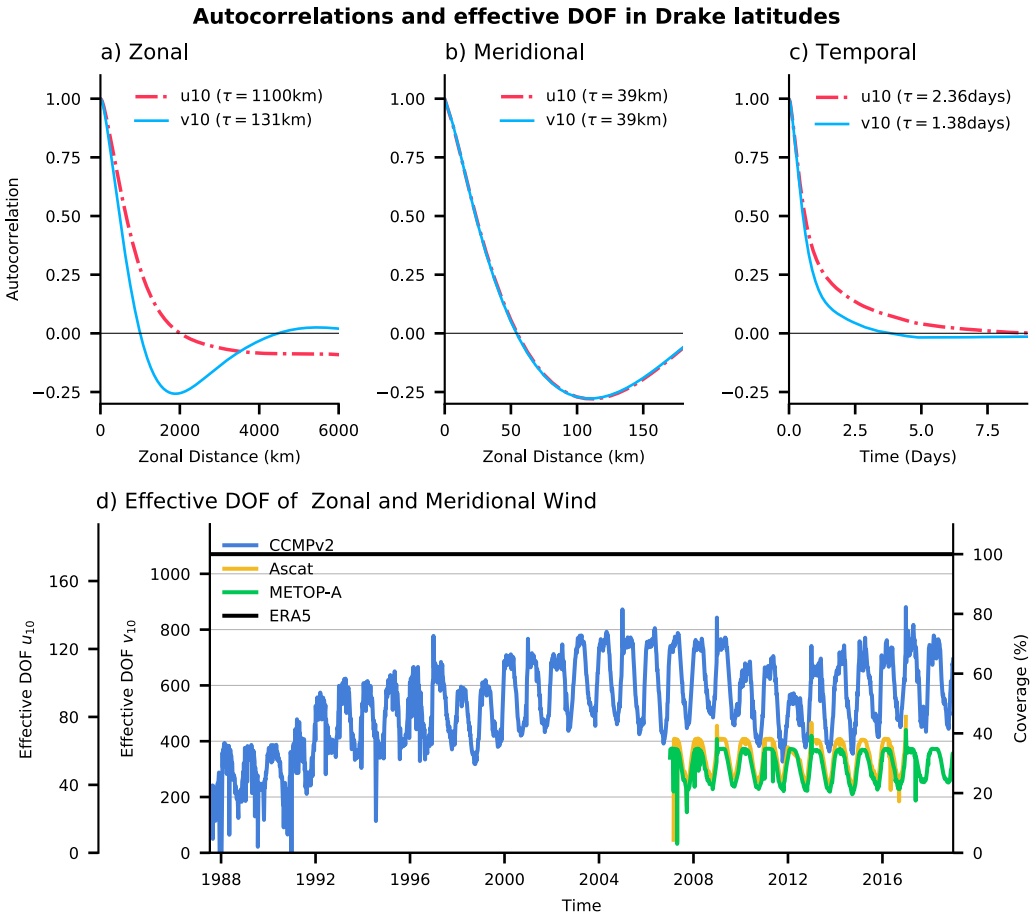

Figure 5.17: Auto-correlations and time-scales for zonal (red dashed dotted) and meridional wind (light blue) in (a) zonal and (b) meridional direction, as well as (c) time. (d) Effective degrees of freedom (DOF) and coverage for ERA5 (black), CCMPv2 (blue), ASCAT (red) and METOP-A ASCAT (orange).

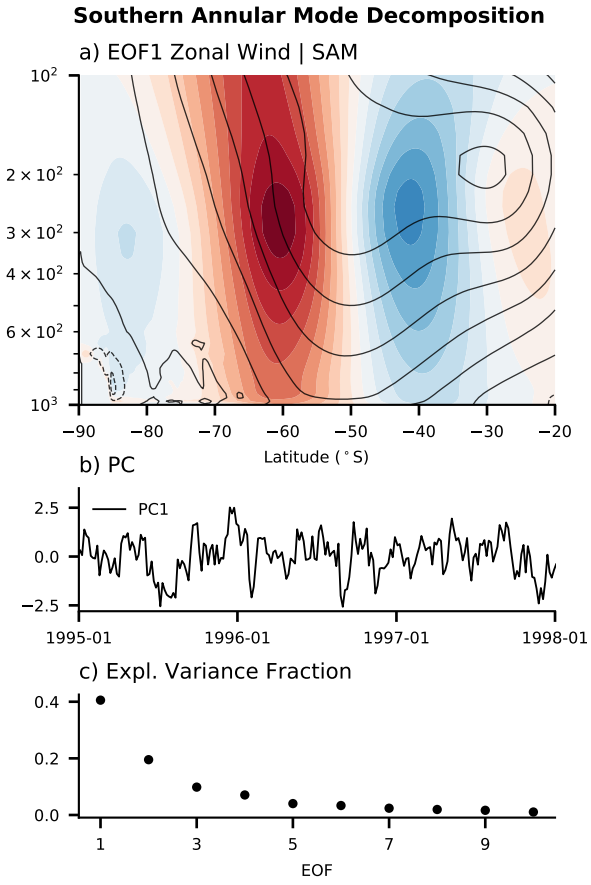

Figure 5.18: Southern Annular Mode decomposition. (a) 1st EOF of the zonal mean zonal wind between 20°S to 90°S in the troposphere. (b) Example of the corresponding 1st PC, (c) explained variance for each mode.

Bibliography

Ryan P. Abernathey, Ivana Cerovecki, Paul R. Holland, Emily Newsom, Matt Mazloff, and Lynne D. Talley. Water-mass transformation by sea ice in the upper branch of the Southern Ocean overturning. *Nat. Geosci.*, 9:596–601, August 2016. ISSN 1752-0894, 1752-0908. doi: 10.1038/ngeo2749.

D. S. Adamson, S. E. Belcher, B. J. Hoskins, and R. S. Plant. Boundary-layer friction in midlatitude cyclones. *Q.J.R. Meteorol. Soc.*, 132:101–124, January 2006. ISSN 1477-870X. doi: 10.1256/qj.04.145.

Michael A. Alexander, Ileana Bladé, Matthew Newman, John R. Lanzante, Ngar-Cheung Lau, and James D. Scott. The Atmospheric Bridge: The influence of ENSO teleconnections on air–sea interaction over the global oceans. *J. Climate*, 15:2205–2231, August 2002. ISSN 0894-8755. doi: 10.1175/1520-0442(2002)015<2205:TABTIO>2.0.CO;2.

S. Allen, C. a. T. Ferro, and F. Kwasniok. Recalibrating wind-speed forecasts using regime-dependent ensemble model output statistics. *Q. J. R. Meteorol. Soc.*, pages 1–21, April 2020. ISSN 1477-870X. doi: 10.1002/qj.3806.

D. G. Andrews and M. E. McIntyre. Planetary waves in horizontal and vertical shear: The generalized Eliassen-Palm relation and the mean zonal acceleration. *J. Atmos. Sci.*, 33: 2031–2048, November 1976. ISSN 0022-4928. doi: 10.1175/1520-0469(1976)033<2031: PWIHAV>2.0.CO;2.

D. G. Andrews and M. E. McIntyre. Generalized Eliassen-Palm and Charney-Drazin Theorems for Waves oin Axismmetric Mean Flows in Compressible Atmospheres. *J. Atmos. Sci.*, 35:175–185, February 1978. ISSN 0022-4928. doi: 10.1175/1520-0469(1978)035<0175: GEPACD>2.0.CO;2.

David G. Andrews, James R. Holton, and Conway B. Leovy. *Middle Atmosphere Dynamics*. Academic Press, 1987. ISBN 978-0-12-058576-2.

Fabrice Ardhuin, Bertrand Chapron, and Fabrice Collard. Observation of swell dissipation across oceans. *Geophys. Res. Lett.*, 36:L06607, March 2009. ISSN 1944-8007. doi: 10.1029/2008GL037030.

Fabrice Ardhuin, Erick Rogers, Alexander V. Babanin, Jean-François Filipot, Rudy Magne, Aaron Roland, Andre van der Westhuysen, Pierre Queffeulou, Jean-Michel Lefevre, Lotfi Aouf, and Fabrice Collard. Semiempirical dissipation source functions for ocean waves. Part I: definition, calibration, and validation. *J. Phys. Oceanogr.*, 40:1917–1941, April 2010. ISSN 0022-3670. doi: 10.1175/2010JPO4324.1.

Fabrice Ardhuin, Peter Sutherland, Martin Doble, and Peter Wadhams. Ocean waves across the Arctic: Attenuation due to dissipation dominates over scattering for periods longer than 19 s. *Geophys. Res. Lett.*, 43:5775–5783, June 2016. ISSN 1944-8007. doi: 10.1002/2016GL068204.

Fabrice Ardhuin, Sarah T. Gille, Dimitris Menemenlis, Cesar B. Rocha, Nicolas Rascle, Bertrand Chapron, Jonathan Gula, and Jeroen Molemaker. Small-scale open ocean currents have large effects on wind wave heights. *J. Geophys. Res. Oceans*, 122:4500–4517, 2017. ISSN 2169-9291. doi: 10.1002/2016JC012413.

Kevin R. Arrigo, Gert L. van Dijken, and Aaron L. Strong. Environmental controls of marine productivity hot spots around Antarctica. *Journal of Geophysical Research: Oceans*, 120: 5545–5565, June 2015. ISSN 2169-9275. doi: 10.1002/2015JC010888.

Olivier Asselin and William R. Young. Penetration of Wind-Generated Near-Inertial Waves into a Turbulent Ocean. *J. Phys. Oceanogr.*, 50:1699–1716, June 2020. ISSN 0022-3670, 1520-0485. doi: 10.1175/JPO-D-19-0319.1.

Robert Atlas, Ross N. Hoffman, Joseph Ardizzone, S. Mark Leidner, Juan Carlos Jusem, Deborah K. Smith, and Daniel Gombos. A Cross-calibrated, Multiplatform Ocean Surface Wind Velocity Product for Meteorological and Oceanographic Applications. *Bull. Amer. Meteor. Soc.*, 92: 157–174, February 2011. ISSN 0003-0007, 1520-0477. doi: 10.1175/2010BAMS2946.1.

A. Ayet, B. Chapron, J. L. Redelsperger, G. Lapeyre, and L. Marié. On the Impact of Long Wind-Waves on Near-Surface Turbulence and Momentum Fluxes. *Bound.-Layer Meteorol.*, 174:465–491, March 2020. ISSN 0006-8314, 1573-1472. doi: 10.1007/s10546-019-00492-x.

N. F. Barber and F. Ursell. The generation and propagation of ocean waves and swell. I. Wave periods and velocities. *Phil. Trans. R. Soc. Lond. A*, 240:527–560, February 1948. ISSN 0080-4614, 2054-0272. doi: 10.1098/rsta.1948.0005.

Elizabeth A. Barnes and Lorenzo Polvani. Response of the Midlatitude Jets, and of Their Variability, to Increased Greenhouse Gases in the CMIP5 Models. *J. Clim.*, 26:7117–7135, September 2013. ISSN 0894-8755, 1520-0442. doi: 10.1175/JCLI-D-12-00536.1.

Elizabeth A. Barnes and Lorenzo M. Polvani. CMIP5 Projections of Arctic Amplification, of the North American/North Atlantic Circulation, and of Their Relationship. *J. Climate*, 28: 5254–5271, April 2015. ISSN 0894-8755. doi: 10.1175/JCLI-D-14-00589.1.

T. P. Barnett. On the generation, dissipation, and prediction of ocean wind waves. *J. Geophys. Res.*, 73:513–529, January 1968. ISSN 2156-2202. doi: 10.1029/JB073i002p00513.

Howard F. Bates and Lewis H. Shapiro. Long-period gravity waves in ice-covered sea. *J. Geophys. Res.*, 85:1095–1100, February 1980. ISSN 2156-2202. doi: 10.1029/JC085iC02p01095.

Robert J. Beare. Boundary layer mechanisms in extratropical cyclones. *Q.J.R. Meteorol. Soc.*, 133:503–515, January 2007. ISSN 1477-870X. doi: 10.1002/qj.30.

James Behrens, Julie Thomas, Eric Terrill, and Robert Jensen. CDIP: Maintaining a Robust and Reliable Ocean Observing Buoy Network. In *2019 IEEE/OES Twelfth Current, Waves and Turbulence Measurement (CWTM)*, pages 1–5, San Diego, CA, USA, March 2019. IEEE. ISBN 978-1-5386-5485-9. doi: 10.1109/CWTM43797.2019.8955166.

Julius S. Bendat and Allan G. Piersol. *Random Data: Analysis and Measurement Procedures*. Wiley, New York, NY, USA, 2010. ISBN ISBN: 978-0-470-24877-5.

Lennart Bengtsson, Kevin I. Hodges, and Erich Roeckner. Storm Tracks and Climate Change. *J. Climate*, 19:3518–3543, August 2006. ISSN 0894-8755. doi: 10.1175/JCLI3815.1.

Lennart Bengtsson, Kevin I. Hodges, and Noel Keenlyside. Will Extratropical Storms Intensify in a Warmer Climate? *J. Climate*, 22:2276–2301, May 2009. ISSN 0894-8755. doi: 10.1175/2008JCLI2678.1.

Karianne J. Bergen, Paul A. Johnson, Maarten V. de Hoop, and Gregory C. Beroza. Machine learning for data-driven discovery in solid Earth geoscience. *Science*, 363:eaau0323, March 2019. ISSN 0036-8075, 1095-9203. doi: 10.1126/science.aau0323.

Vidhi Bharti, Christopher W. Fairall, Byron W. Blomquist, Yi Huang, Alain Protat, Peter P. Sullivan, Steven T. Siems, and Michael J. Manton. Air-Sea Heat and Momentum Fluxes in the Southern Ocean. *J. Geophys. Res. Atmospheres*, 124:12426–12443, 2019. ISSN 2169-8996. doi: 10.1029/2018JD029761.

Jean-Raymond Bidlot, Damian J. Holmes, Paul A. Wittmann, Roop Lalbeharry, and Hsuan S. Chen. Intercomparison of the Performance of Operational Ocean Wave Forecasting Systems with Buoy Data. *Wea. Forecasting*, 17:287–310, April 2002. ISSN 0882-8156. doi: 10.1175/1520-0434(2002)017<0287:IOTPOO>2.0.CO;2.

J. Bjerknes. On the structure of moving cyclones. *Mon. Wea. Rev.*, 47:95–99, February 1919. ISSN 0027-0644. doi: 10.1175/1520-0493(1919)47<95:OTSOMC>2.0.CO;2.

Jakob Bjerknes and Halvor Skappel Solberg. Meteorological conditions for the formation of rain. *Geofys. Publ.*, 2:1–61, 1921.

Jakob Bjerknes and Halvor Skappel Solberg. Life cycle of cyclones and the polar front theory of atmospheric circulation. *Geofys. Publ.*, 3:3–18, 1922.

Maurice L. Blackmon. A Climatological Spectral Study of the 500 mb Geopotential Height of the Northern Hemisphere. *J. Atmos. Sci.*, 33:1607–1623, August 1976. ISSN 0022-4928. doi: 10.1175/1520-0469(1976)033<1607:ACSSOT>2.0.CO;2.

Sébastien Blein, Romain Roehrig, Aurore Voldoire, and Ghislain Faure. Meso-scale contribution to air–sea turbulent fluxes at GCM scale. *Q. J. R. Meteorol. Soc.*, n/a:1–30, 2020. ISSN 1477-870X. doi: 10.1002/qj.3804.

R. Blender and M. Schubert. Cyclone Tracking in Different Spatial and Temporal Resolutions. *Mon. Weather Rev.*, 128:377, 2000. ISSN 0027-0644, 1520-0493. doi: 10.1175/1520-0493(2000)128<0377:CTIDSA>2.0.CO;2.

J. Boé, A. Hall, and X. Qu. Deep ocean heat uptake as a major source of spread in transient climate change simulations. *Geophys. Res. Lett.*, 36, 2009. ISSN 1944-8007. doi: 10.1029/2009GL040845.

C. W. Böning, A. Dispert, M. Visbeck, S. R. Rintoul, and F. U. Schwarzkopf. The response of the Antarctic Circumpolar Current to recent climate change. *Nature Geosci*, 1:864–869, December 2008. ISSN 1752-0894. doi: 10.1038/ngeo362.

James F. Booth, Lu Anne Thompson, Jérôme Patoux, Kathryn A. Kelly, and Suzanne Dickinson. The Signature of the Midlatitude Tropospheric Storm Tracks in the Surface Winds. *J. Climate*, 23:1160–1174, March 2010. ISSN 0894-8755. doi: 10.1175/2009JCLI3064.1.

Mark A. Bourassa, Sarah T. Gille, Cecilia Bitz, David Carlson, Ivana Cerovecki, Carol Anne Clayson, Meghan F. Cronin, Will M. Drennan, Chris W. Fairall, Ross N. Hoffman, Gudrun Magnusdottir, Rachel T. Pinker, Ian A. Renfrew, Mark Serreze, Kevin Speer, Lynne D. Talley, and Gary A. Wick. High-Latitude Ocean and Sea Ice Surface Fluxes: Challenges for Climate Research. *Bull. Amer. Meteor. Soc.*, 94:403–423, March 2013. ISSN 0003-0007. doi: 10.1175/BAMS-D-11-00244.1.

Mark A. Bourassa, Thomas Meissner, Ivana Cerovecki, Paul S. Chang, Xiaolong Dong, Giovanna De Chiara, Craig Donlon, Dmitry S. Dukhovskoy, Jocelyn Elya, Alexander Fore, Melanie R. Fewings, Ralph C. Foster, Sarah T. Gille, Brian K. Haus, Svetla Hristova-Veleva, Heather M. Holbach, Zorana Jelenak, John A. Knaff, Sven A. Kranz, Andrew Manaster, Matthew Mazloff, Carl Mears, Alexis Mouche, Marcos Portabella, Nicolas Reul, Lucrezia Ricciardulli, Ernesto Rodriguez, Charles Sampson, Daniel Solis, Ad Stoffelen, Michael R. Stukel, Bryan Stiles, David Weissman, and Frank Wentz. Remotely Sensed Winds and Wind Stresses for Marine Forecasting and Ocean Modeling. *Front. Mar. Sci.*, 6, 2019. ISSN 2296-7745. doi: 10.3389/fmars.2019.00443.

Thomas J. Bracegirdle and Erik W. Kolstad. Climatology and variability of Southern Hemisphere marine cold-air outbreaks. *Tellus Dyn. Meteorol. Oceanogr.*, 62:202–208, January 2010. ISSN null. doi: 10.1111/j.1600-0870.2009.00431.x.

Mary Brodzik, Brendan Billingsley, Terry Haran, Bruce Raup, and Matthew Savoie. Correction: Brodzik, M.J., et al. EASE-Grid 2.0: Incremental but Significant Improvements for Earth-Gridded Data Sets. ISPRS International Journal of Geo-Information 2012, 1, 32–45. *ISPRS Int. J. Geo-Inf.*, 3:1154–1156, September 2014. ISSN 2220-9964. doi: 10.3390/ijgi3031154.

Mary J. Brodzik, Brendan Billingsley, Terry Haran, Bruce Raup, and Matthew H. Savoie. EASE-Grid 2.0: Incremental but Significant Improvements for Earth-Gridded Data Sets. *ISPRS Int. J. Geo-Inf.*, 1:32–45, March 2012. ISSN 2220-9964. doi: 10.3390/ijgi1010032.

P. D. Bromirski, A. Diez, P. Gerstoft, R. A. Stephen, T. Bolmer, D. A. Wiens, R. C. Aster, and A. Nyblade. Ross ice shelf vibrations. *Geophys. Res. Lett.*, 42:7589–7597, September 2015. ISSN 1944-8007. doi: 10.1002/2015GL065284.

P. D. Bromirski, Z. Chen, R. A. Stephen, P. Gerstoft, D. Arcas, A. Diez, R. C. Aster, D. A. Wiens, and A. Nyblade. Tsunami and infragravity waves impacting Antarctic ice shelves. *J. Geophys. Res. Oceans*, 122:5786–5801, July 2017. ISSN 2169-9291. doi: 10.1002/2017JC012913.

Peter D. Bromirski and Fred K. Duennebier. The near-coastal microseism spectrum: Spatial and temporal wave climate relationships. *J. Geophys. Res. Solid Earth*, 107:ESE 5–1–ESE 5–20, August 2002. ISSN 2156-2202. doi: 10.1029/2001JB000265.

Peter D. Bromirski, Reinhard E. Flick, and Nicholas Graham. Ocean wave height determined from inland seismometer data: Implications for investigating wave climate changes in the NE Pacific. *J. Geophys. Res.*, 104:20753–20766, September 1999. ISSN 2156-2202. doi: 10.1029/1999JC900156.

Peter D. Bromirski, Olga V. Sergienko, and Douglas R. MacAyeal. Transoceanic infragravity waves impacting Antarctic ice shelves. *Geophys. Res. Lett.*, 37, January 2010. ISSN 00948276. doi: 10.1029/2009GL041488.

Peter D. Bromirski, Daniel R. Cayan, John Helly, and Paul Wittmann. Wave power variability and trends across the North Pacific. *J. Geophys. Res. Oceans*, 118:6329–6348, 2013. ISSN 2169-9291. doi: 10.1002/2013JC009189.

Burghard Brümmer. Boundary-layer modification in wintertime cold-air outbreaks from the Arctic sea ice. *Boundary-Layer Meteorol*, 80:109–125, July 1996. ISSN 1573-1472. doi: 10.1007/BF00119014.

V. J. Cardone, R. E. Jensen, D. T. Resio, V. R. Swail, and A. T. Cox. Evaluation of Contemporary Ocean Wave Models in Rare Extreme Events: The "Halloween Storm" of October 1991 and the "Storm of the Century" of March 1993. *J. Atmos. Oceanic Technol.*, 13:198–230, February 1996. ISSN 0739-0572. doi: 10.1175/1520-0426(1996)013<0198:EOCOWM>2.0.CO;2.

Magdalena M. Carranza, Sarah T. Gille, Peter J. S. Franks, Kenneth S. Johnson, Robert Pinkel, and James B. Girton. When Mixed Layers Are Not Mixed. Storm-Driven Mixing and Bio-optical Vertical Gradients in Mixed Layers of the Southern Ocean. *J. Geophys. Res. Oceans*, 123: 7264–7289, October 2018. ISSN 2169-9275, 2169-9291. doi: 10.1029/2018JC014416.

L. M. Cathles, Emile A. Okal, and Douglas R. MacAyeal. Seismic observations of sea swell on the floating Ross Ice Shelf, Antarctica. *J. Geophys. Res.*, 114:F02015, June 2009. ISSN 2156-2202. doi: 10.1029/2007JF000934.

L. Cavaleri. Applications to wave hindcasting and forecasting; Chapter IV. In *Dynamics and Modeling of Ocean Waves*, page 532. Cambridge University Press, USA, 1994.

L. Cavaleri, B. Fox-Kemper, and M. Hemer. Wind Waves in the Coupled Climate System. *Bull. Am. Meteorol. Soc.*, 93:1651–1661, November 2012. ISSN 0003-0007, 1520-0477. doi: 10.1175/BAMS-D-11-00170.1.

Luigi Cavaleri. Wave Modeling-Missing the Peaks. *J. Phys. Oceanogr.*, 39:2757–2778, November 2009. ISSN 0022-3670. doi: 10.1175/2009JPO4067.1.

Copernicus Climate Change Service Climate Data Store (CDS). Copernicus Climate Change Service (C3S) (2017): ERA5: Fifth generation of ECMWF atmospheric reanalyses of the global climate, June 2017.

Paulo Ceppi, Giuseppe Zappa, Theodore G. Shepherd, and Jonathan M. Gregory. Fast and Slow Components of the Extratropical Atmospheric Circulation Response to CO2 Forcing. *J. Climate*, 31:1091–1105, September 2017. ISSN 0894-8755. doi: 10.1175/JCLI-D-17-0323.1.

Ivana Cerovečki, Andrew J. S. Meijers, Matthew R. Mazloff, Sarah T. Gille, Veronica M. Tamsitt, and Paul R. Holland. The Effects of Enhanced Sea Ice Export from the Ross Sea on Recent Cooling and Freshening of the Southeast Pacific. *J. Climate*, 32:2013–2035, February 2019. ISSN 0894-8755. doi: 10.1175/JCLI-D-18-0205.1.

Edmund K. M. Chang, Yanjuan Guo, and Xiaoming Xia. CMIP5 multimodel ensemble projection of storm track change under global warming. *Journal of Geophysical Research: Atmospheres*, 117, December 2012. ISSN 0148-0227. doi: 10.1029/2012JD018578.

B. Chapron, H. Johnsen, and R. Garello. Wave and wind retrieval from sar images of the ocean. *Ann. Télécommun.*, 56:682–699, November 2001. ISSN 1958-9395. doi: 10.1007/BF02995562.

J. G. Charney and M. E. Stern. On the Stability of Internal Baroclinic Jets in a Rotating Atmosphere. *J. Atmos. Sci.*, 19:159–172, March 1962. ISSN 0022-4928. doi: 10.1175/1520-0469(1962)019<0159:OTSOIB>2.0.CO;2.

Jg Charney. The Dynamics of Long Waves in a Baroclinic Westerly Current. *J. Meteorol.*, 4: 135–162, 1947.

Arun Chawla, Deanna M. Spindler, and Hendrik L. Tolman. Validation of a thirty year wave hindcast using the Climate Forecast System Reanalysis winds. *Ocean Modelling*, 70:189–206, October 2013. ISSN 1463-5003. doi: 10.1016/j.ocemod.2012.07.005.

Zhao Chen, Peter D. Bromirski, Peter Gerstoft, Ralph A. Stephen, Douglas A. Wiens, Richard C. Aster, and Andrew A. Nyblade. Ocean-excited plate waves in the Ross and Pine Island Glacier ice shelves. *J. Glaciol.*, 64:730–744, October 2018. ISSN 0022-1430, 1727-5652. doi: 10.1017/jog.2018.66.

C. Claud, A. M. Carleton, B. Duchiron, and P. Terray. Southern hemisphere winter cold-air mesocyclones: Climatic environments and associations with teleconnections. *Clim Dyn*, 33: 383–408, August 2009. ISSN 1432-0894. doi: 10.1007/s00382-008-0468-5.

Fabrice Collard, Fabrice Ardhuin, and Bertrand Chapron. Monitoring and analysis of ocean swell fields from space: New methods for routine observations. *J. Geophys. Res. Oceans*, 114, 2009. ISSN 2156-2202. doi: 10.1029/2008JC005215.

Clarence O. Collins, W. Erick Rogers, Aleksey Marchenko, and Alexander V. Babanin. In situ measurements of an energetic wave event in the Arctic marginal ice zone. *Geophys. Res. Lett.*, 42:1863–1870, March 2015. ISSN 1944-8007. doi: 10.1002/2015GL063063.

Josefino C. Comiso, Ronald Kwok, Seelye Martin, and Arnold L. Gordon. Variability and trends in sea ice extent and ice production in the Ross Sea. *J. Geophys. Res.*, 116:C04021, April 2011. ISSN 2156-2202. doi: 10.1029/2010JC006391.

National Research Council. Carbon Dioxide and Climate: A Scientific Assessment: Report of an Ad Hoc Study Group on Carbon Dioxide and Climate to the Climate Research Board, Assembly of Mathematical and Physical Sciences, National Research Council. Technical report, National Academies, Woods Hole, Massachusetts, July 1979.

Alex D. Crawford and Mark C. Serreze. Does the summer Arctic frontal zone influence Arctic ocean cyclone activity? *J. Climate*, 29:4977–4993, April 2016. ISSN 0894-8755. doi: 10.1175/JCLI-D-15-0755.1.

Alex D. Crawford and Mark C. Serreze. Projected changes in the Arctic frontal zone and summer Arctic cyclone activity in the CESM Large Ensemble. *J. Climate*, September 2017. ISSN 0894-8755. doi: 10.1175/JCLI-D-17-0296.1.

Eric A. D'Asaro, Charles C. Eriksen, Murray D. Levine, Clayton A. Paulson, Peter Niiler, and Pim Van Meurs. Upper-Ocean Inertial Currents Forced by a Strong Storm. Part I: Data and Comparisons with Linear Theory. *J. Phys. Oceanogr.*, 25:2909–2936, November 1995. ISSN 0022-3670. doi: 10.1175/1520-0485(1995)025<2909:UOICFB>2.0.CO;2.

D. P. Dee, S. M. Uppala, A. J. Simmons, P. Berrisford, P. Poli, S. Kobayashi, U. Andrae, M. A. Balmaseda, G. Balsamo, P. Bauer, P. Bechtold, A. C. M. Beljaars, L. van de Berg, J. Bidlot, N. Bormann, C. Delsol, R. Dragani, M. Fuentes, A. J. Geer, L. Haimberger, S. B. Healy, H. Hersbach, E. V. Hólm, L. Isaksen, P. Kållberg, M. Köhler, M. Matricardi, A. P. McNally, B. M. Monge-Sanz, J.-J. Morcrette, B.-K. Park, C. Peubey, P. de Rosnay, C. Tavolato, J.-N. Thépaut, and F. Vitart. The ERA-Interim reanalysis: Configuration and performance of the data assimilation system. *Q. J. R. Meteorol. Soc.*, 137:553–597, April 2011. ISSN 00359009. doi: 10.1002/qj.828.

Matthias T. Delpey, Fabrice Ardhuin, Fabrice Collard, and Bertrand Chapron. Space-time structure of long ocean swell fields. *J. Geophys. Res.*, 115:C12037, December 2010. ISSN 2156-2202. doi: 10.1029/2009JC005885.

Thomas L. Delworth, Anthony Rosati, Whit Anderson, Alistair J. Adcroft, V. Balaji, Rusty Benson, Keith Dixon, Stephen M. Griffies, Hyun-Chul Lee, Ronald C. Pacanowski, Gabriel A. Vecchi, Andrew T. Wittenberg, Fanrong Zeng, and Rong Zhang. Simulated Climate and Climate Change in the GFDL CM2.5 High-Resolution Coupled Climate Model. *J. Clim.*, 25:2755–2781, April 2012. ISSN 0894-8755. doi: 10.1175/JCLI-D-11-00316.1.

C. Deser, F. Lehner, K. B. Rodgers, T. Ault, T. L. Delworth, P. N. DiNezio, A. Fiore, C. Frankignoul, J. C. Fyfe, D. E. Horton, J. E. Kay, R. Knutti, N. S. Lovenduski, J. Marotzke, K. A. McKinnon, S. Minobe, J. Randerson, J. A. Screen, I. R. Simpson, and M. Ting. Insights from Earth system model initial-condition large ensembles and future prospects. *Nat. Clim. Change*, 10:277–286, April 2020. ISSN 1758-6798. doi: 10.1038/s41558-020-0731-2.

James D. Doyle. Coupled ocean wave/atmosphere mesoscale model simulations of cyclogenesis. *Tellus A*, 47:766–778, October 1995. ISSN 1600-0870. doi: 10.1034/j.1600-0870.1995.00119.x.

James D. Doyle. Coupled Atmosphere–Ocean Wave Simulations under High Wind Conditions. *Mon. Wea. Rev.*, 130:3087–3099, December 2002. ISSN 0027-0644. doi: 10.1175/1520-0493(2002)130<3087:CAOWSU>2.0.CO;2.

Tilly Driesenaar, Abderrahim Bentamy, Jos de Kloe, and Maria Belmonte Rivas. Quality Information Dosument For the Global Ocean Wind Products, December 2019.

Tom H. Durrant, Diana J. M. Greenslade, and Ian Simmonds. The effect of statistical wind corrections on global wave forecasts. *Ocean Modelling*, 70:116–131, October 2013. ISSN 1463-5003. doi: 10.1016/j.ocemod.2012.10.006.

E. T. Eady. Long Waves and Cyclone Waves. *Tellus*, 1:33–52, January 1949. ISSN 0040-2826. doi: 10.3402/tellusa.v1i3.8507.

David J. Earl and Michael W. Deem. Parallel tempering: Theory, applications, and new perspectives. *Phys. Chem. Chem. Phys.*, 7:3910–3916, November 2005. ISSN 1463-9084. doi: 10.1039/B509983H.

H. J. Edmon, B. J. Hoskins, and M. E. McIntyre. Eliassen-Palm Cross Sections for the Troposphere. *J. Atmos. Sci.*, 37:2600–2616, December 1980. ISSN 0022-4928. doi: 10.1175/1520-0469(1980)037<2600:EPCSFT>2.0.CO;2.

James B. Edson, Venkata Jampana, Robert A. Weller, Sebastien P. Bigorre, Albert J. Plueddemann, Christopher W. Fairall, Scott D. Miller, Larry Mahrt, Dean Vickers, and Hans Hersbach. On the Exchange of Momentum over the Open Ocean. *J. Phys. Oceanogr.*, 43:1589–1610, May 2013. ISSN 0022-3670. doi: 10.1175/JPO-D-12-0173.1.

T. Elfouhaily, B. Chapron, K. Katsaros, and D. Vandemark. A unified directional spectrum for long and short wind-driven waves. *J. Geophys. Res.*, 102:15781–15796, July 1997. ISSN 2156-2202. doi: 10.1029/97JC00467.

Stefan C. Endres, Carl Sandrock, and Walter W. Focke. A simplicial homology algorithm for Lipschitz optimisation. *J Glob Optim*, 72:181–217, October 2018. ISSN 1573-2916. doi: 10.1007/s10898-018-0645-y.

Alejandra R. Enríquez, Marta Marcos, Amaya Álvarez-Ellacuría, Alejandro Orfila, and Damià Gomis. Changes in beach shoreline due to sea level rise and waves under climate change scenarios: Application to the Balearic Islands (western Mediterranean). *Nat. Hazards Earth Syst. Sci.*, 17:1075–1089, July 2017. ISSN 1561-8633. doi: 10.5194/nhess-17-1075-2017.

Zachary K. Erickson, Andrew F. Thompson, Nicolas Cassar, Janet Sprintall, and Matthew R. Mazloff. An advective mechanism for deep chlorophyll maxima formation in southern Drake Passage. *Geophys. Res. Lett.*, 43:10,846–10,855, October 2016. ISSN 1944-8007. doi: 10.1002/2016GL070565.

European Centre For Medium-Range Weather Forecasts. ERA5 Reanalysis, 2017.

C. W. Fairall, E. F. Bradley, J. E. Hare, A. A. Grachev, and J. B. Edson. Bulk Parameterization of Air–Sea Fluxes: Updates and Verification for the COARE Algorithm. *J. Climate*, 16: 571–591, February 2003. ISSN 0894-8755. doi: 10.1175/1520-0442(2003)016<0571: BPOASF>2.0.CO;2.

Hui Feng, Doug Vandemark, Yves Quilfen, Bertrand Chapron, and Brian Beckley. Assessment of wind-forcing impact on a global wind-wave model using the TOPEX altimeter. *Ocean Engineering*, 33:1431–1461, August 2006. ISSN 0029-8018. doi: 10.1016/j.oceaneng.2005.10.015.

Raffaele Ferrari and Carl Wunsch. Ocean Circulation Kinetic Energy: Reservoirs, Sources, and Sinks. *Annu. Rev. Fluid Mech.*, 41:253–282, December 2008. ISSN 0066-4189. doi: 10.1146/annurev.fluid.40.111406.102139.

Raffaele Ferrari and Carl Wunsch. The distribution of eddy kinetic and potential energies in the global ocean. *Tellus Dyn. Meteorol. Oceanogr.*, 62:92–108, January 2010. ISSN null. doi: 10.1111/j.1600-0870.2009.00432.x.

O. Ferreira. Storm groups versus extreme single storms: Predicted erosion and management consequences. *J. Coast. Res.*, pages 221–227, SPR 2005. ISSN 0749-0208.

Gregory Flato, Jochem Marotzke, Babatunde Abiodun, Pascale Braconnot, Sin Chan Chou, William Collins, Peter Cox, Fatima Driouech, Seita Emori, Veronika Eyring, Chris Forest, Peter Gleckler, Eric Guilyardi, Christian Jakob, Vladimir Kattsov, Chris Reason, Markku Rummukainen, Krishna AchutaRao, Alessandro Anav, Timothy Andrews, Johanna Baehr, Nathaniel L. Bindoff, Alejandro Bodas-Salcedo, Jennifer Catto, Don Chambers, Ping Chang, Aiguo Dai, Clara Deser, Francisco Doblas-Reyes, Paul J. Durack, Michael Eby, Ramon de Elia, Thierry Fichefet, Piers Forster, David Frame, John Fyfe, Emiola Gbobaniyi, Nathan Gillett, Jesus Fidel Gonzalez-Rouco, Clare Goodess, Stephen Griffies, Alex Hall, Sandy Harrison, Andreas Hense, Elizabeth Hunke, Tatiana Ilyina, Detelina Ivanova, Gregory Johnson, Masa Kageyama,

Viatcheslav Kharin, Stephen A. Klein, Jeff Knight, Reto Knutti, Felix Landerer, Tong Lee, Hongmei Li, Natalie Mahowald, Carl Mears, Gerald Meehl, Colin Morice, Rym Msadek, Gunnar Myhre, J. David Neelin, Jeff Painter, Tatiana Pavlova, Judith Perlwitz, Jean-Yves Peterschmitt, Jouni Raisanen, Florian Rauser, Jeffrey Reid, Mark Rodwell, Benjamin Santer, Adam A. Scaife, Joerg Schulz, John Scinocca, David Sexton, Drew Shindell, Hideo Shiogama, Jana Sillmann, Adrian Simmons, Kenneth Sperber, David Stephenson, Bjorn Stevens, Peter Stott, Rowan Sutton, Peter W. Thorne, Geert Jan van Oldenborgh, Gabriel Vecchi, Mark Webb, Keith Williams, Tim Woollings, Shang-Ping Xie, and Jianglong Zhang. Climate Change 2013: The Physical Science Basis. Contribution of Working Group I to the Fifth Assess- ment Report of the Intergovernmental Panel on Climate Change, Chapter 9. In T. F. Stocker, D. Qin, G. K. Plattner, M. M. B. Tignor, S. K. Allen, J. Boschung, A. Nauels, Y. Xia, V. Bex, and P. M. Midgley, editors, *Evaluation of Climate Models*, pages 741–853. Cambridge Univ Press, Cambridge, 2014.

Jennifer Fletcher, Shannon Mason, and Christian Jakob. The Climatology, Meteorology, and Boundary Layer Structure of Marine Cold Air Outbreaks in Both Hemispheres. *J. Climate*, 29: 1999–2014, March 2016. ISSN 0894-8755. doi: 10.1175/JCLI-D-15-0268.1.

Daniel Foreman-Mackey, David W. Hogg, Dustin Lang, and Jonathan Goodman. Emcee: The MCMC Hammer. *Publ. Astron. Soc. Pac.*, 125:306–312, March 2013. ISSN 00046280, 15383873. doi: 10.1086/670067.

Colin Fox and Vernon A. Squire. On the Oblique Reflexion and Transmission of Ocean Waves at Shore Fast Sea Ice. *Philos. Trans. R. Soc. Lond. Math. Phys. Eng. Sci.*, 347:185–218, April 1994. ISSN 1364-503X, 1471-2962. doi: 10.1098/rsta.1994.0044.

Basile Gallet and William R. Young. Refraction of swell by surface currents. *J. Mar. Res.*, 72: 105–126, 2014. doi: info:doi/10.1357/002224014813758959.

Libao Gao, Stephen R. Rintoul, and Weidong Yu. Recent wind-driven change in Subantarctic Mode Water and its impact on ocean heat storage. *Nature Clim Change*, 8:58–63, January 2018. ISSN 1758-6798. doi: 10.1038/s41558-017-0022-8.

J. R. Garratt. The atmospheric boundary layer, Cambridge atmospheric and space science series. *Camb. Univ. Press Camb.*, 416:444, 1992.

Ronald Gelaro, Will McCarty, Max J. Suárez, Ricardo Todling, Andrea Molod, Lawrence Takacs, Cynthia A. Randles, Anton Darmenov, Michael G. Bosilovich, Rolf Reichle, Krzysztof Wargan, Lawrence Coy, Richard Cullather, Clara Draper, Santha Akella, Virginie Buchard, Austin Conaty, Arlindo M. da Silva, Wei Gu, Gi-Kong Kim, Randal Koster, Robert Lucchesi, Dagmar Merkova, Jon Eric Nielsen, Gary Partyka, Steven Pawson, William Putman, Michele Rienecker, Siegfried D. Schubert, Meta Sienkiewicz, and Bin Zhao. The Modern-Era Retrospective Analysis for Research and Applications, Version 2 (MERRA-2). *J. Clim.*, 30:5419–5454, July 2017. ISSN 0894-8755, 1520-0442. doi: 10.1175/JCLI-D-16-0758.1.

Tom George, Georgy Manucharyan, and Andrew Thompson. Deep learning to infer eddy heat fluxes from sea surface height patterns of mesoscale turbulence. Technical report, EarthArXiv, November 2019.

Donata Giglio, Sarah T. Gille, Aneesh C. Subramanian, and San Nguyen. The role of wind gusts in upper ocean diurnal variability: DIURNAL SST AND WIND GUSTS. *J. Geophys. Res. Oceans*, 122:7751–7764, September 2017. ISSN 21699275. doi: 10.1002/2017JC012794.

A. E. Gill. On the Behavior of Internal Waves in the Wakes of Storms. *J. Phys. Oceanogr.*, 14:1129–1151, July 1984. ISSN 0022-3670. doi: 10.1175/1520-0485(1984)014<1129:OTBOIW>2.0.CO;2.

Adrian E Gill. *Atmosphere-Ocean Dynamics*, volume 30. Academic Press, New York, first edition, 1982. ISBN 978-0-12-283522-3 978-0-12-283520-9.

Sarah T. Gille. Statistical Characterization of Zonal and Meridional Ocean Wind Stress. *J. Atmospheric Ocean. Technol.*, 22:1353–1372, September 2005. ISSN 0739-0572, 1520-0426. doi: 10.1175/JTECH1789.1.

Sarah T. Gille. Decadal-Scale Temperature Trends in the Southern Hemisphere Ocean. *J. Climate*, 21:4749–4765, September 2008. ISSN 0894-8755. doi: 10.1175/2008JCLI2131.1.

Anand Gnanadesikan. A Simple Predictive Model for the Structure of the Oceanic Pycnocline. *Science*, 283:2077–2079, March 1999. ISSN 0036-8075, 1095-9203. doi: 10.1126/science.283.5410.2077.

Jonathan Goodman and Jonathan Weare. Ensemble samplers with affine invariance. *Commun. Appl. Math. Comput. Sci.*, 5:65–80, January 2010. ISSN 2157-5452. doi: 10.2140/camcos.2010.5.65.

Robert L. Grossman and Alan K. Betts. Air–Sea Interaction during an Extreme Cold Air Outbreak from the Eastern Coast of the United States. *Mon. Wea. Rev.*, 118:324–342, February 1990. ISSN 0027-0644. doi: 10.1175/1520-0493(1990)118<0324:AIDAEC>2.0.CO;2.

Nicolas Gruber, Dominic Clement, Brendan R. Carter, Richard A. Feely, Steven van Heuven, Mario Hoppema, Masao Ishii, Robert M. Key, Alex Kozyr, Siv K. Lauvset, Claire Lo Monaco, Jeremy T. Mathis, Akihiko Murata, Are Olsen, Fiz F. Perez, Christopher L. Sabine, Toste Tanhua, and Rik Wanninkhof. The oceanic sink for anthropogenic CO2 from 1994 to 2007. *Science*, 363:1193–1199, March 2019. ISSN 0036-8075, 1095-9203. doi: 10.1126/science.aau5153.

Reindert J. Haarsma, Malcolm J. Roberts, Pier Luigi Vidale, Catherine A. Senior, Alessio Bellucci, Qing Bao, Ping Chang, Susanna Corti, Neven S. Fuckar, Virginie Guemas, Jost von Hardenberg, Wilco Hazeleger, Chihiro Kodama, Torben Koenigk, L. Ruby Leung, Jian Lu, Jing-Jia Luo, Jiafu Mao, Matthew S. Mizielinski, Ryo Mizuta, Paulo Nobre, Masaki Satoh, Enrico Scoccimarro, Tido Semmler, Justin Small, and Jin-Song von Storch. High Resolution Model Intercomparison Project (HighResMIP v1.0) for CMIP6. *Geosci. Model Dev.*, 9:4185–4208, November 2016. ISSN 1991-959X. doi: 10.5194/gmd-9-4185-2016.

Robert Hallberg and Anand Gnanadesikan. The Role of Eddies in Determining the Structure and Response of the Wind-Driven Southern Hemisphere Overturning: Results from the Modeling Eddies in the Southern Ocean (MESO) Project. *J. Phys. Oceanogr.*, 36:2232–2252, December 2006. ISSN 0022-3670. doi: 10.1175/JPO2980.1.

Kimio Hanawa and Lynne D. Talley. Mode waters. *Int. Geophys. Ser.*, 77:373–386, 2001.

T. Haran. MODIS Mosaic of Antarctica 2003-2004 (MOA2004), 2005.

Terry Haran and Jennifer Bohlander. MODIS Mosaic of Antarctica 2008-2009 (MOA2009) Image Map, 2014.

Dennis L. Hartmann and Fiona Lo. Wave-Driven Zonal Flow Vacillation in the Southern Hemisphere. *J. Atmos. Sci.*, 55:1303–1315, April 1998. ISSN 0022-4928. doi: 10.1175/1520-0469(1998)055<1303:WDZFVI>2.0.CO;2.

K. Hasselmann. A statistical analysis of the generation of microseisms. *Rev. Geophys.*, 1:177–210, May 1963. ISSN 1944-9208. doi: 10.1029/RG001i002p00177.

K. Hasselmann. Stochastic climate models Part I. Theory. *Tellus*, 28:473–485, January 1976. ISSN 0040-2826. doi: 10.3402/tellusa.v28i6.11316.

K. Hasselmann, T. P. Barnett, E. Bouws, H. Carlson, D. E. Cartwright, K. Enke, J. A. Ewing, H. Gienapp, D. E. Hasselmann, P. Kruseman, A. Meerburg, P. Müller, D. J. Olbers, K. Richter, W. Sell, and H. Walden. Measurements of wind-wave growth and swell decay during the Joint North Sea Wave Project (JONSWAP). *Ergänzungsheft 8-12*, 1973.

K. Hasselmann, W. Sell, D. B. Ross, and P. Müller. A Parametric Wave Prediction Model. *J. Phys. Oceanogr.*, 6:200–228, March 1976. ISSN 0022-3670. doi: 10.1175/1520-0485(1976)006<0200:APWPM>2.0.CO;2.

Klaus Hasselmann. On the spectral dissipation of ocean waves due to white capping. *Boundary-Layer Meteorol*, 6:107–127, March 1974. ISSN 0006-8314, 1573-1472. doi: 10.1007/BF00232479.

S. Hasselmann and K. Hasselmann. Computations and Parameterizations of the Nonlinear Energy Transfer in a Gravity-Wave Spectrum. Part I: A New Method for Efficient Computations of the Exact Nonlinear Transfer Integral. *J. Phys. Oceanogr.*, 15:1369–1377, November 1985. ISSN 0022-3670. doi: 10.1175/1520-0485(1985)015<1369:CAPOTN>2.0.CO;2.

S. Hasselmann, K. Hasselmann, J. H. Allender, and T. P. Barnett. Computations and Parameterizations of the Nonlinear Energy Transfer in a Gravity-Wave Specturm. Part II: Parameterizations of the Nonlinear Energy Transfer for Application in Wave Models. *J. Phys. Oceanogr.*, 15:1378–1391, November 1985. ISSN 0022-3670. doi: 10.1175/1520-0485(1985)015<1378:CAPOTN>2.0.CO;2.

F. Alexander Haumann, Nicolas Gruber, Matthias Münnich, Ivy Frenger, and Stefan Kern. Sea-ice transport driving Southern Ocean salinity and its recent trends. *Nature*, 537:89–92, September 2016. ISSN 1476-4687. doi: 10.1038/nature19101.

D. Hauser, C. Tourain, L. Hermozo, D. Alraddawi, L. Aouf, B. Chapron, A. Dalphinet, L. Delaye, M. Dalila, E. Dormy, F. Gouillon, V. Gressani, A. Grouazel, G. Guitton, R. Husson, A. Mironov, A. Mouche, A. Ollivier, L. Oruba, F. Piras, R. R. Suquet, P. Schippers, C. Tison, and N. Tran. New Observations From the SWIM Radar On-Board CFOSAT: Instrument Validation and Ocean Wave Measurement Assessment. *IEEE Trans. Geosci. Remote Sens.*, pages 1–22, 2020. ISSN 1558-0644. doi: 10.1109/TGRS.2020.2994372.

Isaac M. Held and Brian J. Soden. Robust Responses of the Hydrological Cycle to Global Warming. *J. Climate*, 19:5686–5699, November 2006. ISSN 0894-8755. doi: 10.1175/JCLI3990.1.

Momme C. Hell, Bruce D. Cornuelle, Sarah T. Gille, Arthur J. Miller, and Peter D. Bromirski. Identifying Ocean Swell Generation Events from Ross Ice Shelf Seismic Data. *J. Atmos. Oceanic Technol.*, 36:2171–2189, October 2019. ISSN 0739-0572. doi: 10.1175/JTECH-D-19-0093.1.

Momme C. Hell, Sarah T. Gille, Bruce D. Cornuelle, Arthur J. Miller, Peter D. Bromirski, and Alex D. Crawford. Estimating Southern Ocean Storm Positions With Seismic Observations. *J. Geophys. Res. Oceans*, 125:e2019JC015898, 2020. ISSN 2169-9291. doi: 10.1029/2019JC015898.

Momme C. Hell, Bruce D. Cornuelle, S. T. Gille, Sarah T., and Nick J. Lutsko. Time-varying empirical probability densities of Southern Ocean surface winds: Leading modes linked to SAM, the annual cycle, and product biases. submitted to Jclim.

Joseph P. Hennessey. Some Aspects of Wind Power Statistics. *J. Appl. Meteor.*, 16:119–128, February 1977. ISSN 0021-8952. doi: 10.1175/1520-0450(1977)016<0119:SAOWPS>2.0.CO;2.

K. I. Hodges, B. J. Hoskins, J. Boyle, and C. Thorncroft. A Comparison of Recent Reanalysis Datasets Using Objective Feature Tracking: Storm Tracks and Tropical Easterly Waves. *Mon. Wea. Rev.*, 131:2012–2037, September 2003. ISSN 0027-0644. doi: 10.1175/1520-0493(2003)131<2012:ACORRD>2.0.CO;2.

K. I. Hodges, R. W. Lee, and L. Bengtsson. A Comparison of Extratropical Cyclones in Recent Reanalyses ERA-Interim, NASA MERRA, NCEP CFSR, and JRA-25. *J. Climate*, 24:4888–4906, April 2011. ISSN 0894-8755. doi: 10.1175/2011JCLI4097.1.

Paul R. Holland and Ron Kwok. Wind-driven trends in Antarctic sea-ice drift. *Nature Geosci*, 5:872–875, December 2012. ISSN 1752-0894. doi: 10.1038/ngeo1627.

James W. Holte, Lynne D. Talley, Teresa K. Chereskin, and Bernadette M. Sloyan. The role of air-sea fluxes in Subantarctic Mode Water formation. *J. Geophys. Res. Oceans*, 117, 2012. ISSN 2156-2202. doi: 10.1029/2011JC007798.

B. J. Hoskins and K. I. Hodges. A New Perspective on Southern Hemisphere Storm Tracks. *J. Climate*, 18:4108–4129, October 2005. ISSN 0894-8755. doi: 10.1175/JCLI3570.1.

B. J. Hoskins, M. E. McIntyre, and A. W. Robertson. On the use and significance of isentropic potential vorticity maps. *Q.J.R. Meteorol. Soc.*, 111:877–946, 1985. ISSN 1477-870X. doi: 10.1002/qj.49711147002.

Brian J. Hoskins and Kevin I. Hodges. New perspectives on the Northern Hemisphere winter storm tracks. *J. Atmospheric Sci.*, 59:1041–1061, 2002.

Fang Huang, Zhongfeng Xu, and Weidong Guo. The linkage between CMIP5 climate models' abilities to simulate precipitation and vector winds. *Clim Dyn*, April 2020. ISSN 1432-0894. doi: 10.1007/s00382-020-05259-6.

Ira A. Hunt. Design of Sea-Walls and Breakwaters. *Trans. Am. Soc. Civ. Eng.*, 126:542–570, 1961.

R. Husson, F. Ardhuin, F. Collard, B. Chapron, and A. Balanche. Revealing forerunners on Envisat's wave mode ASAR using the Global Seismic Network. *Geophys. Res. Lett.*, 39, August 2012. ISSN 00948276. doi: 10.1029/2012GL052334.

Peter Janssen. *The Interaction of Ocean Waves and Wind*. Cambridge University Press, Cambridge, 2004. ISBN 978-0-511-52501-8. doi: 10.1017/CBO9780511525018.

Peter A.E.M. Janssen and Jean-Raymond Bidlot. Progress in Operational Wave Forecasting. *Procedia IUTAM*, 26:14–29, 2018. ISSN 22109838. doi: 10.1016/j.piutam.2018.03.003.

Haoyu Jiang, Justin E. Stopa, He Wang, Romain Husson, Alexis Mouche, Bertrand Chapron, and Ge Chen. Tracking the attenuation and nonbreaking dissipation of swells using altimeters. *J. Geophys. Res. Oceans*, 121:1446–1458, 2016. ISSN 2169-9291. doi: 10.1002/2015JC011536.

Gregory C. Johnson and Harry L. Bryden. On the size of the Antarctic Circumpolar Current. *Deep Sea Research Part A. Oceanographic Research Papers*, 36:39–53, January 1989. ISSN 0198-0149. doi: 10.1016/0198-0149(89)90017-4.

C. G. Justus, W. R. Hargraves, Amir Mikhail, and Denise Graber. Methods for Estimating Wind Speed Frequency Distributions. *J. Appl. Meteor.*, 17:350–353, March 1978. ISSN 0021-8952. doi: 10.1175/1520-0450(1978)017<0350:MFEWSF>2.0.CO;2.

Theodor von Kármán. Mechanical similitude and turbulence. *NACA Tech*, 1931.

J. E. Kay, C. Deser, A. Phillips, A. Mai, C. Hannay, G. Strand, J. M. Arblaster, S. C. Bates, G. Danabasoglu, J. Edwards, M. Holland, P. Kushner, J.-F. Lamarque, D. Lawrence, K. Lindsay, A. Middleton, E. Munoz, R. Neale, K. Oleson, L. Polvani, and M. Vertenstein. The Community Earth System Model (CESM) Large Ensemble Project: A Community Resource for Studying Climate Change in the Presence of Internal Climate Variability. *Bull. Amer. Meteor. Soc.*, 96: 1333–1349, August 2015. ISSN 0003-0007. doi: 10.1175/BAMS-D-13-00255.1.

Ralph F. Keeling and Charles D. Keeling. Atmospheric Monthly In Situ CO2 Data - Mauna Loa Observatory, Hawaii. In Scripps CO2 Program Data, 2017.

J. Kidston, A. S. Taschetto, D. W. J. Thompson, and M. H. England. The influence of Southern Hemisphere sea-ice extent on the latitude of the mid-latitude jet stream. *Geophys. Res. Lett.*, 38:L15804, August 2011. ISSN 1944-8007. doi: 10.1029/2011GL048056.

Blair Kinsman. *Wind Waves:Their Generation And Propagation On The Ocean Surface*. prentice hall,inc, November 2013.

S. Kirkpatrick, C. D. Gelatt, and M. P. Vecchi. Optimization by Simulated Annealing. *Science*, 220:671–680, May 1983. ISSN 0036-8075, 1095-9203. doi: 10.1126/science.220.4598.671.

Reto Knutti and Jan Sedláček. Robustness and uncertainties in the new CMIP5 climate model projections. *Nature Clim. Change*, 3:369–373, April 2013. ISSN 1758-678X. doi: 10.1038/nclimate1716.

A. L. Kohout, M. J. M. Williams, S. M. Dean, and M. H. Meylan. Storm-induced sea-ice breakup and the implications for ice extent. *Nature*, 509:604–607, May 2014. ISSN 0028-0836. doi: 10.1038/nature13262.

Vladimir Kudryavtsev, Pavel Golubkin, and Bertrand Chapron. A simplified wave enhancement criterion for moving extreme events. *J. Geophys. Res. Oceans*, 120:7538–7558, 2015. ISSN 2169-9291. doi: 10.1002/2015JC011284.

T. Kuhlbrodt and J. M. Gregory. Ocean heat uptake and its consequences for the magnitude of sea level rise and climate change. *Geophys. Res. Lett.*, 39, 2012. ISSN 1944-8007. doi: 10.1029/2012GL052952.

R. Kwok. Ross Sea Ice Motion, Area Flux, and Deformation. *J. Climate*, 18:3759–3776, September 2005. ISSN 0894-8755. doi: 10.1175/JCLI3507.1.

Ming Li, Jiping Liu, Zhenzhan Wang, Hui Wang, Zhanhai Zhang, Lin Zhang, and Qinghua Yang. Assessment of Sea Surface Wind from NWP Reanalyses and Satellites in the Southern Ocean. *J. Atmos. Oceanic Technol.*, 30:1842–1853, May 2013. ISSN 0739-0572. doi: 10.1175/JTECH-D-12-00240.1.

Qing Li, Adrean Webb, Baylor Fox-Kemper, Anthony Craig, Gokhan Danabasoglu, William G. Large, and Mariana Vertenstein. Langmuir mixing effects on global climate: WAVEWATCH III in CESM. *Ocean Model.*, 103:145–160, July 2016. ISSN 14635003. doi: 10.1016/j.ocemod.2015.07.020.

Varavut Limpasuvan and Dennis L. Hartmann. Wave-Maintained Annular Modes of Climate Variability. *J. Climate*, 13:4414–4429, December 2000. ISSN 0894-8755. doi: 10.1175/1520-0442(2000)013<4414:WMAMOC>2.0.CO;2.

Xia Lin, Xiaoming Zhai, Zhaomin Wang, and David R. Munday. Mean, Variability, and Trend of Southern Ocean Wind Stress: Role of Wind Fluctuations. *J. Climate*, 31:3557–3573, February 2018. ISSN 0894-8755. doi: 10.1175/JCLI-D-17-0481.1.

Xia Lin, Xiaoming Zhai, Zhaomin Wang, and David R. Munday. Southern Ocean Wind Stress in CMIP5 Models: Role of Wind Fluctuations. *J. Climate*, 33:1209–1226, January 2020. ISSN 0894-8755. doi: 10.1175/JCLI-D-19-0466.1.

Bradley Paul Lipovsky. Ice Shelf Rift Propagation and the Mechanics of Wave-Induced Fracture. *J. Geophys. Res. Oceans*, 123:4014–4033, June 2018. ISSN 2169-9291. doi: 10.1029/2017JC013664.

Michael Selwyn Longuet-Higgins. On the nonlinear transfer of energy in the peak of a gravity-wave spectrum: A simplified model. *Proceedings of the Royal Society of London. A. Mathematical and Physical Sciences*, 347:311–328, January 1976. doi: 10.1098/rspa.1976.0003.

David J. Lorenz and Dennis L. Hartmann. Eddy–Zonal Flow Feedback in the Southern Hemisphere. *J. Atmos. Sci.*, 58:3312–3327, November 2001. ISSN 0022-4928. doi: 10.1175/1520-0469(2001)058<3312:EZFFIT>2.0.CO;2.

E. N. Lorenz. *The Nature and Theory of the General Circulation of the Atmosphere*. World Meteorological Organization, Geneva, 1967.

Edward N. Lorenz. Available Potential Energy and the Maintenance of the General Circulation. *Tellus*, 7:157–167, January 1955. ISSN 0040-2826. doi: 10.3402/tellusa.v7i2.8796.

Edward N. Lorenz. Deterministic Nonperiodic Flow. *J. Atmos. Sci.*, 20:130–141, March 1963. ISSN 0022-4928. doi: 10.1175/1520-0469(1963)020<0130:DNF>2.0.CO;2.

Edward N. Lorenz. The predictability of a flow which possesses many scales of motion. *Tellus*, 21:289–307, June 1969. ISSN 2153-3490. doi: 10.1111/j.2153-3490.1969.tb00444.x.

Jian Lu, Gang Chen, and Dargan M. W. Frierson. The Position of the Midlatitude Storm Track and Eddy-Driven Westerlies in Aquaplanet AGCMs. *J. Atmos. Sci.*, 67:3984–4000, September 2010. ISSN 0022-4928. doi: 10.1175/2010JAS3477.1.

Douglas R. MacAyeal, Emile A. Okal, Richard C. Aster, Jeremy N. Bassis, Kelly M. Brunt, L. Mac. Cathles, Robert Drucker, Helen A. Fricker, Young-Jin Kim, Seelye Martin, Marianne H. Okal, Olga V. Sergienko, Mark P. Sponsler, and Jonathan E. Thom. Transoceanic wave propagation links iceberg calving margins of Antarctica with storms in tropics and Northern Hemisphere. *Geophys. Res. Lett.*, 33:L17502, September 2006. ISSN 1944-8007. doi: 10.1029/2006GL027235.

Douglas R. MacAyeal, Emile A. Okal, Richard C. Aster, and Jeremy N. Bassis. Seismic observations of glaciogenic ocean waves (micro-tsunamis) on icebergs and ice shelves. *Journal of Glaciology*, 55:193–206, April 2009. doi: 10.3189/002214309788608679.

Nicola Maher, Sebastian Milinski, Laura Suarez-Gutierrez, Michael Botzet, Mikhail Dobrynin, Luis Kornblueh, Jürgen Kröger, Yohei Takano, Rohit Ghosh, Christopher Hedemann, Chao Li, Hongmei Li, Elisa Manzini, Dirk Notz, Dian Putrasahan, Lena Boysen, Martin Claussen, Tatiana Ilyina, Dirk Olonscheck, Thomas Raddatz, Bjorn Stevens, and Jochem Marotzke. The Max Planck Institute Grand Ensemble: Enabling the Exploration of Climate System Variability. *J. Adv. Model. Earth Syst.*, 11:2050–2069, 2019. ISSN 1942-2466. doi: 10.1029/2019MS001639.

Chris Marone. Training machines in Earthly ways. *Nat. Geosci.*, 11:301–302, May 2018. ISSN 1752-0908. doi: 10.1038/s41561-018-0117-5.

David P. Marshall, David R. Munday, Lesley C. Allison, Russell J. Hay, and Helen L. Johnson. Gill's model of the Antarctic Circumpolar Current, revisited: The role of latitudinal variations in wind stress. *Ocean Modelling*, 97:37–51, January 2016. ISSN 1463-5003. doi: 10.1016/j.ocemod.2015.11.010.

Giacomo Masato, Brian J. Hoskins, and Tim Woollings. Winter and Summer Northern Hemisphere Blocking in CMIP5 Models. *J. Climate*, 26:7044–7059, March 2013. ISSN 0894-8755. doi: 10.1175/JCLI-D-12-00466.1.

Stanislaw R. Massel. *Ocean Surface Waves: Their Physics and Prediction*. Advanced Series on Ocean Engineering. World Scientific, Singapore ; River Edge, NJ, 1996. ISBN 978-981-02-1686-3 978-981-02-2109-6.

Robert A. Massom, Theodore A. Scambos, Luke G. Bennetts, Phillip Reid, Vernon A. Squire, and Sharon E. Stammerjohn. Antarctic ice shelf disintegration triggered by sea ice loss and ocean swell. *Nature*, 558:383–389, June 2018. ISSN 1476-4687. doi: 10.1038/s41586-018-0212-1.

Cheikh Mbengue and Tapio Schneider. Storm-Track Shifts under Climate Change: Toward a Mechanistic Understanding Using Baroclinic Mean Available Potential Energy. *J. Atmos. Sci.*, 74:93–110, October 2016. ISSN 0022-4928. doi: 10.1175/JAS-D-15-0267.1.

Cheikh O. Mbengue and Tim Woollings. The Eddy-Driven Jet and Storm-Track Responses to Boundary Layer Drag: Insights from an Idealized Dry GCM Study. *J. Atmos. Sci.*, 76:1055–1076, April 2019. ISSN 0022-4928. doi: 10.1175/JAS-D-18-0086.1.

Adrian J. McDonald and Luke H. Cairns. A New Method to Evaluate Reanalyses Using Synoptic Patterns: An Example Application in the Ross Sea/Ross Ice Shelf Region. *Earth Space Sci.*, 7:UNSP e2019EA000794, January 2020. doi: 10.1029/2019EA000794.

A. J. S. Meijers, I. Cerovečki, B. A. King, and V. Tamsitt. A See-Saw in Pacific Subantarctic Mode Water Formation Driven by Atmospheric Modes. *Geophys. Res. Lett.*, 46:13152–13160, 2019. ISSN 1944-8007. doi: 10.1029/2019GL085280.

T. Meissner and F. J. Wentz. Wind-Vector Retrievals Under Rain With Passive Satellite Microwave Radiometers. *IEEE Trans. Geosci. Remote Sens.*, 47:3065–3083, September 2009. doi: 10.1109/TGRS.2009.2027012.

Michael P. Meredith and Andrew M. Hogg. Circumpolar response of Southern Ocean eddy activity to a change in the Southern Annular Mode. *Geophys. Res. Lett.*, 33, 2006. ISSN 0094-8276. doi: 10.1029/2006GL026499.

Michael P. Meredith, Alberto C. Naveira Garabato, Andrew McC. Hogg, and Riccardo Farneti. Sensitivity of the Overturning Circulation in the Southern Ocean to Decadal Changes in Wind Forcing. *J. Clim.*, 25:99–110, January 2012. ISSN 0894-8755, 1520-0442. doi: 10.1175/2011JCLI4204.1.

John W. Miles. On the generation of surface waves by shear flows. *J. Fluid Mech.*, 3:185–204, November 1957. ISSN 1469-7645, 0022-1120. doi: 10.1017/S0022112057000567.

John W. Miles. On the generation of surface waves by turbulent shear flows. *J. Fluid Mech.*, 7: 469–478, March 1960. ISSN 1469-7645, 0022-1120. doi: 10.1017/S0022112060000220.

J. F. B. Mitchell, C. A. Wilson, and W. M. Cunnington. On Co2 climate sensitivity and model dependence of results. *Q. J. R. Meteorol. Soc.*, 113:293–322, 1987. ISSN 1477-870X. doi: 10.1002/qj.49711347517.

Ryo Mizuta, Akihiko Murata, Masayoshi Ishii, Hideo Shiogama, Kenshi Hibino, Nobuhito Mori, Osamu Arakawa, Yukiko Imada, Kohei Yoshida, Toshinori Aoyagi, Hiroaki Kawase, Masato Mori, Yasuko Okada, Tomoya Shimura, Toshiharu Nagatomo, Mikiko Ikeda, Hirokazu Endo, Masaya Nosaka, Miki Arai, Chiharu Takahashi, Kenji Tanaka, Tetsuya Takemi, Yasuto Tachikawa, Khujanazarov Temur, Youichi Kamae, Masahiro Watanabe, Hidetaka Sasaki, Akio Kitoh, Izuru Takayabu, Eiichi Nakakita, and Masahide Kimoto. Over 5,000 Years of Ensemble Future Climate Simulations by 60-Km Global and 20-Km Regional Atmospheric Models. *Bull. Amer. Meteorol. Soc.*, 98:1383–1398, July 2017. ISSN 0003-0007. doi: 10.1175/BAMS-D-16-0099.1.

Global Modeling. MERRA-2 tavg1_2d_slv_Nx: 2d,1-Hourly,Time-Averaged,Single-Level,Assimilation,Single-Level Diagnostics V5.12.4, 2015a.

Global Modeling. MERRA-2 const_2d_asm_Nx: 2d, constants, 2015b.

Adam H. Monahan. Probability distribution of sea surface wind stresses. *Geophys. Res. Lett.*, 35, 2008. ISSN 1944-8007. doi: 10.1029/2007GL032268.

Adam Hugh Monahan. The Probability Distribution of Sea Surface Wind Speeds. Part I: Theory and SeaWinds Observations. *J. Climate*, 19:497–520, February 2006a. ISSN 0894-8755. doi: 10.1175/JCLI3640.1.

Adam Hugh Monahan. The Probability Distribution of Sea Surface Wind Speeds. Part II: Dataset Intercomparison and Seasonal Variability. *J. Climate*, 19:521–534, February 2006b. ISSN 0894-8755. doi: 10.1175/JCLI3641.1.

Adam Hugh Monahan. Empirical Models of the Probability Distribution of Sea Surface Wind Speeds. *J. Climate*, 20:5798–5814, December 2007. ISSN 0894-8755. doi: 10.1175/2007JCLI1609.1.

A S Monin and A M Obukhov. Basic laws of turbulent mixing in the surface layer of the atmosphere. *Tr Akad Nauk SSSR Geophiz Inst*, 24:163–187, 1954.

Michael L. Morison and Jörg Imberger. Water-Level Oscillations in Esperance Harbour. *J. Waterw. Port Coast. Ocean Eng.*, 118:352–367, July 1992. ISSN 0733-950X. doi: 10.1061/(ASCE)0733-950X(1992)118:4(352).

Rosemary Morrow, Lee-Lueng Fu, Fabrice Ardhuin, Mounir Benkiran, Bertrand Chapron, Emmanuel Cosme, Francesco d'Ovidio, J. Thomas Farrar, Sarah T. Gille, Guillaume Lapeyre, Pierre-Yves Le Traon, Ananda Pascual, Aurélien Ponte, Bo Qiu, Nicolas Rascle, Clement Ubelmann, Jinbo Wang, and Edward D. Zaron. Global Observations of Fine-Scale Ocean Surface Topography With the Surface Water and Ocean Topography (SWOT) Mission. *Front. Mar. Sci.*, 6, 2019. ISSN 2296-7745. doi: 10.3389/fmars.2019.00232.

D. R. Munday and X. Zhai. The impact of atmospheric storminess on the sensitivity of Southern Ocean circulation to wind stress changes. *Ocean Modelling*, 115:14–26, July 2017. ISSN 1463-5003. doi: 10.1016/j.ocemod.2017.05.005.

W. H. Munk and E. Palmén. Note on the Dynamics of the Antarctic Circumpolar Current1. *Tellus*, 3:53–55, February 1951. ISSN 2153-3490. doi: 10.1111/j.2153-3490.1951.tb00776.x.

W. H. Munk and F. E. Snodgrass. Measurements of southern swell at Guadalupe Island. *Deep Sea Research (1953)*, 4:272–286, January 1957. ISSN 0146-6313. doi: 10.1016/0146-6313(56)90061-2.

W. H. Munk, G. R. Miller, F. E. Snodgrass, and N. F. Barber. Directional recording of swell from distant storms. *Phil. Trans. R. Soc. Lond. A*, 255:505–584, April 1963. ISSN 0080-4614, 2054-0272. doi: 10.1098/rsta.1963.0011.

Walter H. Munk. Tracking storms by forerunners of swell. *J. Meteor.*, 4:45–57, April 1947. ISSN 0095-9634. doi: 10.1175/1520-0469(1947)004<0045:TSBFOS>2.0.CO;2.

Ross J. Murray and Ian Simmonds. A numerical scheme for tracking cyclone centres from digital data. Part I: Development and operation of the scheme. *Aust Meteor Mag*, 39:155–166, 1991.

Jerome Namias. The Use of Isentropic Analysis in Short Term Forecasting. *J. Aeronaut. Sci.*, 6:295–298, May 1939. doi: 10.2514/8.860.

Nature Geoscience editorial board. Use machines to tame big data. *Nat. Geosci.*, 12:1–1, January 2019. ISSN 1752-0894. doi: 10.1038/s41561-018-0290-6.

Alberto C. Naveira Garabato, Loïc Jullion, David P. Stevens, Karen J. Heywood, and Brian A. King. Variability of Subantarctic Mode Water and Antarctic Intermediate Water in the Drake Passage during the Late-Twentieth and Early-Twenty-First Centuries. *J. Climate*, 22:3661–3688, July 2009. ISSN 0894-8755. doi: 10.1175/2009JCLI2621.1.

Paul J. Neiman and M. A. Shapiro. The Life Cycle of an Extratropical Marine Cyclone. Part I: Frontal-Cyclone Evolution and Thermodynamic Air-Sea Interaction. *Mon. Wea. Rev.*, 121:2153–2176, August 1993. ISSN 0027-0644. doi: 10.1175/1520-0493(1993)121<2153:TLCOAE>2.0.CO;2.

Paul J. Neiman, M. A. Shapiro, and L. S. Fedor. The Life Cycle of an Extratropical Marine Cyclone. Part II: Mesoscale Structure and Diagnostics. *Mon. Wea. Rev.*, 121:2177–2199, August 1993. ISSN 0027-0644. doi: 10.1175/1520-0493(1993)121<2177:TLCOAE>2.0.CO;2.

Urs Neu, Mirseid G. Akperov, Nina Bellenbaum, Rasmus Benestad, Richard Blender, Rodrigo Caballero, Angela Cocozza, Helen F. Dacre, Yang Feng, Klaus Fraedrich, Jens Grieger, Sergey Gulev, John Hanley, Tim Hewson, Masaru Inatsu, Kevin Keay, Sarah F. Kew, Ina Kindem, Gregor C. Leckebusch, Margarida L. R. Liberato, Piero Lionello, Igor I. Mokhov, Joaquim G. Pinto, Christoph C. Raible, Marco Reale, Irina Rudeva, Mareike Schuster, Ian Simmonds, Mark Sinclair, Michael Sprenger, Natalia D. Tilinina, Isabel F. Trigo, Sven Ulbrich, Uwe Ulbrich, Xiaolan L. Wang, and Heini Wernli. IMILAST: A Community Effort to Intercompare Extratropical Cyclone Detection and Tracking Algorithms. *Bull. Amer. Meteor. Soc.*, 94: 529–547, September 2012. ISSN 0003-0007. doi: 10.1175/BAMS-D-11-00154.1.

Matthew Newville, Till Stensitzki, Daniel B. Allen, and Antonino Ingargiola. LMFIT: Non-Linear Least-Square Minimization and Curve-Fitting for Python. Zenodo, September 2014.

Fumiaki Ogawa and Thomas Spengler. Prevailing Surface Wind Direction during Air–Sea Heat Exchange. *J. Climate*, 32:5601–5617, September 2019. ISSN 0894-8755. doi: 10.1175/JCLI-D-18-0752.1.

S. E. Ogle, V. Tamsitt, S. A. Josey, S. T. Gille, I. Cerovečki, L. D. Talley, and R. A. Weller. Episodic Southern Ocean Heat Loss and Its Mixed Layer Impacts Revealed by the Farthest South Multiyear Surface Flux Mooring. *Geophys. Res. Lett.*, 45:5002–5010, May 2018. ISSN 1944-8007. doi: 10.1029/2017GL076909.

Larry W. O'Neill, Dudley B. Chelton, and Steven K. Esbensen. Observations of SST-Induced Perturbations of the Wind Stress Field over the Southern Ocean on Seasonal Timescales. *J. Climate*, 16:2340–2354, July 2003. ISSN 0894-8755. doi: 10.1175/2780.1.

Larry W. O'Neill, Dudley B. Chelton, Steven K. Esbensen, and Frank J. Wentz. High-Resolution Satellite Measurements of the Atmospheric Boundary Layer Response to SST Variations along the Agulhas Return Current. *J. Climate*, 18:2706–2723, July 2005. ISSN 0894-8755. doi: 10.1175/JCLI3415.1.

W. C. O'Reilly, Corey B. Olfe, Julianna Thomas, R. J. Seymour, and R. T. Guza. The California coastal wave monitoring and prediction system. *Coastal Engineering*, 116:118–132, October 2016. ISSN 0378-3839. doi: 10.1016/j.coastaleng.2016.06.005.

Robert Daniel Osinski and Hagen Radtke. Ensemble hindcasting of wind and wave conditions with WRF and WAVEWATCH III® driven by ERA5. *Ocean Sci.*, 16:355–371, March 2020. ISSN 1812-0784. doi: 10.5194/os-16-355-2020.

Lukas Papritz and Stephan Pfahl. Importance of Latent Heating in Mesocyclones for the Decay of Cold Air Outbreaks: A Numerical Process Study from the Pacific Sector of the Southern Ocean. *Mon. Wea. Rev.*, 144:315–336, January 2016. ISSN 0027-0644. doi: 10.1175/MWR-D-15-0268.1.

Lukas Papritz, Stephan Pfahl, Harald Sodemann, and Heini Wernli. A Climatology of Cold Air Outbreaks and Their Impact on Air–Sea Heat Fluxes in the High-Latitude South Pacific. *J. Climate*, 28:342–364, January 2015. ISSN 0894-8755. doi: 10.1175/JCLI-D-14-00482.1.

Edgar G. Pavia and James J. O'Brien. Weibull Statistics of Wind Speed over the Ocean. *J. Climate Appl. Meteor.*, 25:1324–1332, October 1986. ISSN 0733-3021. doi: 10.1175/1520-0450(1986)025<1324:WSOWSO>2.0.CO;2.

Jose P. Peixoto and Abraham H. Oort. *Physics of Climate*. AIP-Press, 1992. ISBN 978-0-88318-712-8.

Norman A. Phillips. Energy Transformations and Meridional Circulations associated with simple Baroclinic Waves in a two-level, Quasi-geostrophic Model. *Tellus*, 6:274–286, January 1954. ISSN 0040-2826. doi: 10.3402/tellusa.v6i3.8734.

O. M. Phillips. On the generation of waves by turbulent wind. *J. Fluid Mech.*, 2:417–445, July 1957. ISSN 1469-7645, 0022-1120. doi: 10.1017/S0022112057000233.

O. M. Phillips. The equilibrium range in the spectrum of wind-generated waves. *J. Fluid Mech.*, 4:426–434, August 1958. ISSN 1469-7645, 0022-1120. doi: 10.1017/S0022112058000550.

O. M. Phillips. Spectral and statistical properties of the equilibrium range in wind-generated gravity waves. *J. Fluid Mech.*, 156:505–531, July 1985. ISSN 1469-7645, 0022-1120. doi: 10.1017/S0022112085002221.

Willard J. Pierson and Lionel Moskowitz. A proposed spectral form for fully developed wind seas based on the similarity theory of S. A. Kitaigorodskii. *J. Geophys. Res.*, 69:5181–5190, December 1964. ISSN 2156-2202. doi: 10.1029/JZ069i024p05181.

Felix Pithan, Theodore G. Shepherd, Giuseppe Zappa, and Irina Sandu. Climate model biases in jet streams, blocking and storm tracks resulting from missing orographic drag. *Geophys. Res. Lett.*, 43:7231–7240, July 2016. ISSN 1944-8007. doi: 10.1002/2016GL069551.

R. T. Pollard. Properties of Near-Surface Inertial Oscillations. *J. Phys. Oceanogr.*, 10:385–398, March 1980. ISSN 0022-3670. doi: 10.1175/1520-0485(1980)010<0385:PONSIO>2.0.CO;2.

Sonia Ponce and Francisco J. Ocampo-Torres. Sensitivity of a wave model to wind variability. *J. Geophys. Res. Oceans*, 103:3179–3201, 1998. ISSN 2156-2202. doi: 10.1029/97JC02328.

Rui M. Ponte and Richard D. Rosen. Nonlinear Effects of Variable Winds on Ocean Stress Climatologies. *J. Climate*, 17:1283–1293, March 2004. ISSN 0894-8755. doi: 10.1175/1520-0442(2004)017<1283:NEOVWO>2.0.CO;2.

Rudolph W Preisendorfer and Curtis D Mobley. *Principal Component Analysis in Meteorology and Oceanography*. Elsevier, Amsterdam; New York; New York, NY, U.S.A., 1988. ISBN 978-0-444-43014-4 978-0-444-41710-7.

Jaume Ramon, Llorenç Lledó, Verónica Torralba, Albert Soret, and Francisco J. Doblas-Reyes. What global reanalysis best represents near-surface winds? *Q. J. R. Meteorol. Soc.*, 145: 3236–3251, 2019. ISSN 1477-870X. doi: 10.1002/qj.3616.

William J. Randel and Isaac M. Held. Phase Speed Spectra of Transient Eddy Fluxes and Critical Layer Absorption. *J. Atmos. Sci.*, 48:688–697, March 1991. ISSN 0022-4928. doi: 10.1175/1520-0469(1991)048<0688:PSSOTE>2.0.CO;2.

Henrique Rapizo, Alexander V. Babanin, Eric Schulz, Mark A. Hemer, and Tom H. Durrant. Observation of wind-waves from a moored buoy in the Southern Ocean. *Ocean Dyn.*, 65: 1275–1288, September 2015. ISSN 1616-7341, 1616-7228. doi: 10.1007/s10236-015-0873-3.

Nicolas Rascle, Fabrice Ardhuin, Pierre Queffeulou, and Denis Croizé-Fillon. A global wave parameter database for geophysical applications. Part 1: Wave-current–turbulence interaction parameters for the open ocean based on traditional parameterizations. *Ocean Model.*, 25: 154–171, January 2008. ISSN 14635003. doi: 10.1016/j.ocemod.2008.07.006.

Lucas Reimann and Jin-Song von Storch. A phase-space consideration of changing climate-PDF. *Clim Dyn*, 54:2633–2662, March 2020. ISSN 1432-0894. doi: 10.1007/s00382-020-05130-8.

Diandong Ren and Lance M. Leslie. Effects of Waves on Tabular Ice-Shelf Calving. *Earth Interact.*, 18:1–28, July 2014. ISSN 1087-3562. doi: 10.1175/EI-D-14-0005.1.

Ian A. Renfrew and G. W. K. Moore. An Extreme Cold-Air Outbreak over the Labrador Sea: Roll Vortices and Air–Sea Interaction. *Mon. Wea. Rev.*, 127:2379–2394, October 1999. ISSN 0027-0644. doi: 10.1175/1520-0493(1999)127<2379:AECAOO>2.0.CO;2.

Agustinus Ribal and Ian R. Young. Calibration and Cross Validation of Global Ocean Wind Speed Based on Scatterometer Observations. *J. Atmos. Oceanic Technol.*, 37:279–297, December 2019. ISSN 0739-0572. doi: 10.1175/JTECH-D-19-0119.1.

Lucrezia Ricciardulli and F. J. Wentz. Remote Sensing Systems ASCAT C-2015 Daily Ocean Vector Winds on 0.25 deg grid, Version 02.1. Santa Rosa, CA: Remote Sensing Systems. Available at www.remss.com/missions/ascat. Accessed [02-02-2020]., Apri, 2016.

Stephen R. Rintoul. The global influence of localized dynamics in the Southern Ocean. *Nature*, 558:209–218, June 2018. ISSN 1476-4687. doi: 10.1038/s41586-018-0182-3.

Craig M. Risien and Dudley B. Chelton. A Global Climatology of Surface Wind and Wind Stress Fields from Eight Years of QuikSCAT Scatterometer Data. *J. Phys. Oceanogr.*, 38:2379–2413, November 2008. ISSN 0022-3670. doi: 10.1175/2008JPO3881.1.

Hannes Risken. Fokker-Planck Equation. In Hannes Risken, editor, *The Fokker-Planck Equation: Methods of Solution and Applications*, Springer Series in Synergetics, pages 63–95. Springer, Berlin, Heidelberg, 1996. ISBN 978-3-642-61544-3. doi: 10.1007/978-3-642-61544-3_4.

Maria Belmonte Rivas, this link will open in a new window Link to external site, Ad Stoffelen, and this link will open in a new window Link to external site. Characterizing ERA-Interim and ERA5 surface wind biases using ASCAT. *Ocean Sci. Katlenburg-Lindau*, 15:831–852, 2019. ISSN 18120784. doi: http://dx.doi.org/10.5194/os-15-831-2019.

W. Robinson and T. G. Haskell. Calving of Erebus Glacier tongue. *Nature*, 346:615–616, August 1990. ISSN 0028-0836, 1476-4687. doi: 10.1038/346615b0.

Walter A. Robinson. A Baroclinic Mechanism for the Eddy Feedback on the Zonal Index. *J. Atmos. Sci.*, 57:415–422, February 2000. ISSN 0022-4928. doi: 10.1175/1520-0469(2000)057<0415:ABMFTE>2.0.CO;2.

Cesar B. Rocha, Teresa K. Chereskin, Sarah T. Gille, and Dimitris Menemenlis. Mesoscale to Submesoscale Wavenumber Spectra in Drake Passage. *J. Phys. Oceanogr.*, 46:601–620, December 2015. ISSN 0022-3670. doi: 10.1175/JPO-D-15-0087.1.

Dean Roemmich, John Church, John Gilson, Didier Monselesan, Philip Sutton, and Susan Wijffels. Unabated planetary warming and its ocean structure since 2006. *Nature Clim Change*, 5: 240–245, March 2015. ISSN 1758-6798. doi: 10.1038/nclimate2513.

Paul E. Russell. Mechanisms for beach erosion during storms. *Continental Shelf Research*, 13: 1243–1265, November 1993. ISSN 0278-4343. doi: 10.1016/0278-4343(93)90051-X.

Christopher L. Sabine, Richard A. Feely, Nicolas Gruber, Robert M. Key, Kitack Lee, John L. Bullister, Rik Wanninkhof, C. S. Wong, Douglas W. R. Wallace, Bronte Tilbrook, Frank J. Millero, Tsung-Hung Peng, Alexander Kozyr, Tsueno Ono, and Aida F. Rios. The Oceanic Sink for Anthropogenic CO2. *Science*, 305:367–371, July 2004. ISSN 0036-8075, 1095-9203. doi: 10.1126/science.1097403.

J. B. Sallée, K. G. Speer, and S. R. Rintoul. Zonally asymmetric response of the Southern Ocean mixed-layer depth to the Southern Annular Mode. *Nature Geosci*, 3:273–279, April 2010. ISSN 1752-0908. doi: 10.1038/ngeo812.

Takeaki Sampe and Shang-Ping Xie. Mapping High Sea Winds from Space: A Global Climatology. *Bull. Amer. Meteor. Soc.*, 88:1965–1978, December 2007. ISSN 0003-0007. doi: 10.1175/BAMS-88-12-1965.

Sebastian Schemm and Heini Wernli. The linkage between the warm and the cold conveyor belts in an idealized extratropical cyclone. *J. Atmospheric Sci.*, 71:1443–1459, 2014.

Tapio Schneider. The general circulation of the atmosphere. *Annu Rev Earth Planet Sci*, 34: 655–688, 2006.

David M. Schultz, Daniel Keyser, and Lance F. Bosart. The Effect of Large-Scale Flow on Low-Level Frontal Structure and Evolution in Midlatitude Cyclones. *Mon. Wea. Rev.*, 126:1767–1791, July 1998. ISSN 0027-0644. doi: 10.1175/1520-0493(1998)126<1767:TEOLSF>2.0.CO;2.

David M. Schultz, Lance F. Bosart, Brian A. Colle, Huw C. Davies, Christopher Dearden, Daniel Keyser, Olivia Martius, Paul J. Roebber, W. James Steenburgh, Hans Volkert, and Andrew C. Winters. Extratropical Cyclones: A Century of Research on Meteorology's Centerpiece. *Meteorol. Monogr.*, 59:16.1–16.56, January 2018. ISSN 0065-9401. doi: 10.1175/AMSMONOGRAPHS-D-18-0015.1.

E. W. Schulz, S. A. Josey, and R. Verein. First air-sea flux mooring measurements in the Southern Ocean. *Geophys. Res. Lett.*, 39, 2012. ISSN 1944-8007. doi: 10.1029/2012GL052290.

M. A. Shapiro and D. Keyser. Fronts, jet streams, and the tropopause. Extratropical Cyclones, The Erik Palmen Memorial Volume, CW Newton and E. Holopainen, Eds. *Amer Meteor Soc*, page 167, 1990.

T. A. Shaw, M. Baldwin, E. A. Barnes, R. Caballero, C. I. Garfinkel, Y.-T. Hwang, C. Li, P. A. O'Gorman, G. Rivière, I. R. Simpson, and A. Voigt. Storm track processes and the opposing influences of climate change. *Nature Geosci*, 9:656–664, September 2016. ISSN 1752-0894. doi: 10.1038/ngeo2783.

Andrew Shepherd, Erik R. Ivins, Geruo A, Valentina R. Barletta, Mike J. Bentley, Srinivas Bettadpur, Kate H. Briggs, David H. Bromwich, René Forsberg, Natalia Galin, Martin Horwath, Stan Jacobs, Ian Joughin, Matt A. King, Jan T. M. Lenaerts, Jilu Li, Stefan R. M. Ligtenberg, Adrian Luckman, Scott B. Luthcke, Malcolm McMillan, Rakia Meister, Glenn Milne, Jeremie Mouginot, Alan Muir, Julien P. Nicolas, John Paden, Antony J. Payne, Hamish Pritchard, Eric Rignot, Helmut Rott, Louise Sandberg Sørensen, Ted A. Scambos, Bernd Scheuchl, Ernst J. O. Schrama, Ben Smith, Aud V. Sundal, Jan H. van Angelen, Willem J. van de Berg, Michiel R. van den Broeke, David G. Vaughan, Isabella Velicogna, John Wahr, Pippa L. Whitehouse, Duncan J. Wingham, Donghui Yi, Duncan Young, and H. Jay Zwally. A Reconciled Estimate of Ice-Sheet Mass Balance. *Science*, 338:1183–1189, November 2012. ISSN 0036-8075, 1095-9203. doi: 10.1126/science.1228102.

Ian Simmonds and Kevin Keay. Mean Southern Hemisphere Extratropical Cyclone Behavior in the 40-Year NCEP–NCAR Reanalysis. *J. Climate*, 13:873–885, March 2000. ISSN 0894-8755. doi: 10.1175/1520-0442(2000)013<0873:MSHECB>2.0.CO;2.

Ian Simmonds and Ross J. Murray. Southern Extratropical Cyclone Behavior in ECMWF Analyses during the FROST Special Observing Periods. *Wea. Forecasting*, 14:878–891, December 1999. ISSN 0882-8156. doi: 10.1175/1520-0434(1999)014<0878:SECBIE>2.0.CO;2.

Ian Simmonds and Irina Rudeva. A comparison of tracking methods for extreme cyclones in the Arctic basin. *Tellus A*, 66, September 2014. ISSN 1600-0870. doi: 10.3402/tellusa.v66.25252.

Ian Simmonds, Kevin Keay, and Eun-Pa Lim. Synoptic Activity in the Seas around Antarctica. *Mon. Wea. Rev.*, 131:272–288, February 2003. ISSN 0027-0644. doi: 10.1175/1520-0493(2003)131<0272:SAITSA>2.0.CO;2.

Adrian J. Simmons and Brian J. Hoskins. The Life Cycles of Some Nonlinear Baroclinic Waves. *J. Atmos. Sci.*, 35:414–432, March 1978. ISSN 0022-4928. doi: 10.1175/1520-0469(1978)035<0414:TLCOSN>2.0.CO;2.

R. Justin Small, Robert A. Tomas, and Frank O. Bryan. Storm track response to ocean fronts in a global high-resolution climate model. *Clim. Dyn.*, 43:805–828, August 2014. ISSN 0930-7575. doi: 10.1007/s00382-013-1980-9.

S. D. Smith. Coefficients for sea surface wind stress, heat flux, and wind profiles as a function of wind speed and temperature. *Journal of Geophysical Research: Oceans*, 93:15467–15472, September 2012. ISSN 0148-0227. doi: 10.1029/JC093iC12p15467.

F. E. Snodgrass, G. W. Groves, K. F. Hasselmann, G. R. Miller, W. H. Munk, and W. H. Powers. Propagation of Ocean Swell across the Pacific. *Philos. Trans. R. Soc. Lond. Math. Phys. Eng. Sci.*, 259:431–497, May 1966. ISSN 1364-503X, 1471-2962. doi: 10.1098/rsta.1966.0022.

Alexander Soloviev and Roger Lukas. *The Near-Surface Layer of the Ocean: Structure, Dynamics and Applications*. Springer Science & Business Media, December 2013. ISBN 978-94-007-7621-0.

Xiangzhou Song. Explaining the Zonal Asymmetry in the Air-Sea Net Heat Flux Climatology Over the Antarctic Circumpolar Current. *J. Geophys. Res. Oceans*, 125:e2020JC016215, 2020. ISSN 2169-9291. doi: 10.1029/2020JC016215.

V.A. Squire. Of ocean waves and sea-ice revisited. *Cold Reg. Sci. Technol.*, 49:110–133, August 2007. ISSN 0165232X. doi: 10.1016/j.coldregions.2007.04.007.

Vernon Squire and Alastair J. Allan. Propagation of Flexural Gravity Waves in Sea Ice. In *Sea Ice Processesand Models*, pages 327–338. University of Washington Press,Seattle, edited by r. s. pritchard edition, 1980.

Vernon A. Squire, William H. Robinson, Michael Meylan, and Timothy G. Haskell. Observations of flexural waves on the Erebus Ice Tongue, McMurdo Sound, Antarctica, and nearby sea ice. *J. Glaciol.*, 40:377–385, 1994/ed. ISSN 0022-1430, 1727-5652. doi: 10.3189/S0022143000007462.

Thomas F. Stocker and Sigfùs J. Johnsen. A minimum thermodynamic model for the bipolar seesaw. *Paleoceanography*, 18, 2003. ISSN 1944-9186. doi: 10.1029/2003PA000920.

Justin E. Stopa and Kwok Fai Cheung. Intercomparison of wind and wave data from the ECMWF Reanalysis Interim and the NCEP Climate Forecast System Reanalysis. *Ocean Modelling*, 75: 65–83, March 2014. ISSN 1463-5003. doi: 10.1016/j.ocemod.2013.12.006.

Justin E. Stopa, Peter Sutherland, and Fabrice Ardhuin. Strong and highly variable push of ocean waves on Southern Ocean sea ice. *PNAS*, 115:5861–5865, June 2018. ISSN 0027-8424, 1091-6490. doi: 10.1073/pnas.1802011115.

Hans von Storch and Francis W. Zwiers. *Statistical Analysis in Climate Research*. Cambridge University Press, first edition, 1999. ISBN 978-0-521-01230-0 978-0-521-45071-3 978-0-511-61233-6. doi: 10.1017/CBO9780511612336.

Julienne C. Stroeve, Vladimir Kattsov, Andrew Barrett, Mark Serreze, Tatiana Pavlova, Marika Holland, and Walter N. Meier. Trends in Arctic sea ice extent from CMIP5, CMIP3 and observations. *Geophys. Res. Lett.*, 39, 2012. ISSN 1944-8007. doi: 10.1029/2012GL052676.

Neil C. Swart, Sarah T. Gille, John C. Fyfe, and Nathan P. Gillett. Recent Southern Ocean warming and freshening driven by greenhouse gas emissions and ozone depletion. *Nat. Geosci.*, 11:836, November 2018. ISSN 1752-0908. doi: 10.1038/s41561-018-0226-1.

Fernando G. Taboada, Charles A. Stock, Stephen M. Griffies, John Dunne, Jasmin G. John, R. Justin Small, and Hiroyuki Tsujino. Surface winds from atmospheric reanalysis lead to contrasting oceanic forcing and coastal upwelling patterns. *Ocean Model.*, 133:79–111, January 2019. ISSN 1463-5003. doi: 10.1016/j.ocemod.2018.11.003.

Veronica Tamsitt, Ivana Cerovečki, Simon A. Josey, Sarah T. Gille, and Eric Schulz. Mooring Observations of Air–Sea Heat Fluxes in Two Subantarctic Mode Water Formation Regions. *J. Clim.*, 33:2757–2777, April 2020. ISSN 0894-8755, 1520-0442. doi: 10.1175/JCLI-D-19-0653.1.

Karl E. Taylor, Ronald J. Stouffer, and Gerald A. Meehl. An Overview of CMIP5 and the Experiment Design. *Bull. Amer. Meteor. Soc.*, 93:485–498, April 2012. ISSN 0003-0007. doi: 10.1175/BAMS-D-11-00094.1.

David W. J. Thompson and Elizabeth A. Barnes. Periodic Variability in the Large-Scale Southern Hemisphere Atmospheric Circulation. *Science*, 343:641–645, February 2014. ISSN 0036-8075, 1095-9203. doi: 10.1126/science.1247660.

David W. J. Thompson and Susan Solomon. Interpretation of Recent Southern Hemisphere Climate Change. *Science*, 296:895–899, May 2002. ISSN 0036-8075, 1095-9203. doi: 10.1126/science.1069270.

David W. J. Thompson and John M. Wallace. Annular Modes in the Extratropical Circulation. Part I: Month-to-Month Variability. *J. Climate*, 13:1000–1016, March 2000. ISSN 0894-8755. doi: 10.1175/1520-0442(2000)013<1000:AMITEC>2.0.CO;2.

David W. J. Thompson and Jonathan D. Woodworth. Barotropic and Baroclinic Annular Variability in the Southern Hemisphere. *J. Atmos. Sci.*, 71:1480–1493, November 2013. ISSN 0022-4928. doi: 10.1175/JAS-D-13-0185.1.

David W. J. Thompson, John M. Wallace, and Gabriele C. Hegerl. Annular Modes in the Extratropical Circulation. Part II: Trends. *J. Climate*, 13:1018–1036, March 2000. ISSN 0894-8755. doi: 10.1175/1520-0442(2000)013<1018:AMITEC>2.0.CO;2.

Richard E. Thomson and W. Stanford Huggett. Wind-driven inertial oscillations of large spatial coherence. *Atmosphere-Ocean*, 19:281–306, December 1981. ISSN 0705-5900. doi: 10.1080/07055900.1981.9649116.

Hendrik L. Tolman. User manual and system documentation of WAVEWATCH III TM version 3.14. *Tech. Note MMAB Contrib.*, 276:220, 2009.

Leif Toudal Pedersen, Gorm Dybkjær, Steinar Eastwood, Georg Heygster, Natalia Ivanova, Stefan Kern, Thomas Lavergne, Roberto Saldo, Stein Sandven, Atle Sørensen, and Rasmus Tonboe. ESA Sea Ice Climate Change Initiative (Sea_Ice_cci): Sea Ice Concentration Climate Data Record from the AMSR-E and AMSR-2 instruments at 50km grid spacing, version 2.1, 2017.

Kevin E. Trenberth. Storm Tracks in the Southern Hemisphere. *J. Atmos. Sci.*, 48:2159–2178, October 1991. ISSN 0022-4928. doi: 10.1175/1520-0469(1991)048<2159:STITSH>2.0.CO;2.

Ana Trindade, Marcos Portabella, Ad Stoffelen, Wenming Lin, and Anton Verhoef. ERAstar: A High-Resolution Ocean Forcing Product. *IEEE Trans. Geosci. Remote Sensing*, 58:1337–1347, February 2020. ISSN 0196-2892, 1558-0644. doi: 10.1109/TGRS.2019.2946019.

Constantino Tsallis. Possible generalization of Boltzmann-Gibbs statistics. *J Stat Phys*, 52: 479–487, July 1988. ISSN 1572-9613. doi: 10.1007/BF01016429.

Constantino Tsallis and Daniel A. Stariolo. Generalized simulated annealing. *Physica A: Statistical Mechanics and its Applications*, 233:395–406, November 1996. ISSN 0378-4371. doi: 10.1016/S0378-4371(96)00271-3.

Stanton E. Tuller and Arthur C. Brett. The Characteristics of Wind Velocity that Favor the Fitting of a Weibull Distribution in Wind Speed Analysis. *J. Climate Appl. Meteor.*, 23:124–134, January 1984. ISSN 0733-3021. doi: 10.1175/1520-0450(1984)023<0124:TCOWVT>2.0.CO;2.

Geoffrey K. Vallis, Edwin P. Gerber, Paul J. Kushner, and Benjamin A. Cash. A Mechanism and Simple Dynamical Model of the North Atlantic Oscillation and Annular Modes. *J. Atmospheric Sci.*, 61:264–280, February 2004. ISSN 0022-4928, 1520-0469. doi: 10.1175/1520-0469(2004)061<0264:AMASDM>2.0.CO;2.

D.G. Vaughan, J.C. Comiso, I. Allison, J. Carrasco, G. Kaser, R. Kwok, P. Mote, T. Murray, F. Paul, J. Ren, E. Rignot, O. Solomina, K. Steffen, and T. Zhang. Observations: Cryosphere. In: Climate Change 2013: The Physical Sci- ence Basis. Contribution of Working Group I to

the Fifth Assessment Report of the Intergovernmental Panel on Climate Change [Stocker, T.F., D. Qin, G.-K. Plattner, M. Tignor, S.K. Allen, J. Boschung, A. Nauels, Y. Xia, V. Bex and P.M. Midgley (eds.)]. In *Climate Change 2013: The Physical Sci- Ence Basis. Contribution of Working Group I to the Fifth Assessment Report of the Intergovernmental Panel on Climate Change [Stocker, T.F., D. Qin, G.-K. Plattner, M. Tignor, S.K. Allen, J. Boschung, A. Nauels, Y. Xia, V. Bex and P.M. Midgley (Eds.)].* Cambridge University Press, Cambridge, United Kingdom and New York, NY, USA., 2013.

Gareth L. Vaughan, Luke G. Bennetts, and Vernon A. Squire. The decay of flexural-gravity waves in long sea ice transects. *Proc. R. Soc. Lond. Math. Phys. Eng. Sci.*, 465:2785–2812, September 2009. ISSN 1364-5021, 1471-2946. doi: 10.1098/rspa.2009.0187.

Ana B. Villas Bôas and William R. Young. Directional diffusion of surface gravity wave action by ocean macroturbulence. *J. Fluid Mech.*, 890, May 2020. ISSN 0022-1120, 1469-7645. doi: 10.1017/jfm.2020.116.

Ana B. Villas Bôas, Sarah T. Gille, Matthew R. Mazloff, and Bruce D. Cornuelle. Characterization of the Deep Water Surface Wave Variability in the California Current Region. *J. Geophys. Res. Oceans*, 122:8753–8769, November 2017. ISSN 21699275. doi: 10.1002/2017JC013280.

Ana B. Villas Bôas, Fabrice Ardhuin, Alex Ayet, Mark A. Bourassa, Peter Brandt, Betrand Chapron, Bruce D. Cornuelle, J. T. Farrar, Melanie R. Fewings, Baylor Fox-Kemper, Sarah T. Gille, Christine Gommenginger, Patrick Heimbach, Momme C. Hell, Qing Li, Matthew R. Mazloff, Sophia T. Merrifield, Alexis Mouche, Marie H. Rio, Ernesto Rodriguez, Jamie D. Shutler, Aneesh C. Subramanian, Eric J. Terrill, Michel Tsamados, Clement Ubelmann, and Erik van Sebille. Integrated Observations of Global Surface Winds, Currents, and Waves: Requirements and Challenges for the Next Decade. *Front. Mar. Sci.*, 6, 2019. ISSN 2296-7745. doi: 10.3389/fmars.2019.00425.

Peter Wadhams and Martin J. Doble. Sea ice thickness measurement using episodic infragravity waves from distant storms. *Cold Reg. Sci. Technol.*, 56:98–101, May 2009. ISSN 0165232X. doi: 10.1016/j.coldregions.2008.12.002.

David J. Wales and Jonathan P. K. Doye. Global Optimization by Basin-Hopping and the Lowest Energy Structures of Lennard-Jones Clusters Containing up to 110 Atoms. *J. Phys. Chem. A*, 101:5111–5116, July 1997. ISSN 1089-5639. doi: 10.1021/jp970984n.

John M. Wallace, Gyu-Ho Lim, and Maurice L. Blackmon. Relationship between Cyclone Tracks, Anticyclone Tracks and Baroclinic Waveguides. *J. Atmos. Sci.*, 45:439–462, February 1988. ISSN 0022-4928. doi: 10.1175/1520-0469(1988)045<0439:RBCTAT>2.0.CO;2.

Xiaolan L. Wang, Yang Feng, Rodney Chan, and Victor Isaac. Inter-comparison of extra-tropical cyclone activity in nine reanalysis datasets. *Atmospheric Research*, 181:133–153, November 2016. ISSN 0169-8095. doi: 10.1016/j.atmosres.2016.06.010.

Rik Wanninkhof. Relationship between wind speed and gas exchange over the ocean. *J. Geophys. Res. Oceans*, 97:7373–7382, 1992. ISSN 2156-2202. doi: 10.1029/92JC00188.

Rik Wanninkhof. Relationship between wind speed and gas exchange over the ocean revisited. *Limnol. Oceanogr. Meth.*, 12:351–362, June 2014. ISSN 1541-5856. doi: 10.4319/lom.2014.12.351.

Rik Wanninkhof, Scott C. Doney, Taro Takahashi, and Wade R. McGillis. The effect of using time-averaged winds on regional air-sea CO 2 fluxes. *GMS*, 127:351–356, 2002.

Andreas Weber. *Enlivenment: Toward a Poetics for the Anthropocene*. Untimely Meditations. MIT Press, Cambridge, Massachusetts, 2019. ISBN 978-0-262-53666-0.

Caihong Wen, Arun Kumar, and Yan Xue. Uncertainties in reanalysis surface wind stress and their relationship with observing systems. *Clim. Dyn.*, 52:3061–3078, March 2019. ISSN 0930-7575. doi: 10.1007/s00382-018-4310-4.

F. J. Wentz, S. Peteherych, and L. A. Thomas. A model function for ocean radar cross sections at 14.6 GHz. *J. Geophys. Res. Oceans*, 89:3689–3704, 1984. ISSN 2156-2202. doi: 10.1029/JC089iC03p03689.

F. J. Wentz, R. Scott, R. Hoffman, S. Mark Leidner, Robert Atlas, and Joseph Ardizzone. Remote Sensing Systems Cross-Calibrated Multi-Platform (CCMP) 6-hourly ocean vector wind analysis product on 0.25 deg grid, Version 2.0. Remote Sensing Systems, Santa Rosa, CA. Available online at www.remss.com/measurements/ccmp, 2015.

Heini Wernli and Cornelia Schwierz. Surface Cyclones in the ERA-40 Dataset (1958–2001). Part I: Novel Identification Method and Global Climatology. *J. Atmos. Sci.*, 63:2486–2507, October 2006. ISSN 0022-4928. doi: 10.1175/JAS3766.1.

Heini Wernli, Sebastien Dirren, Mark A. Liniger, and Matthias Zillig. Dynamical aspects of the life cycle of the winter storm 'Lothar' (24–26 December 1999). *Q. J. R. Meteorol. Soc.*, 128: 405–429, 2002. ISSN 1477-870X. doi: 10.1256/003590002321042036.

Christopher J. White, Henrik Carlsen, Andrew W. Robertson, Richard J. T. Klein, Jeffrey K. Lazo, Arun Kumar, Frederic Vitart, Erin Coughlan de Perez, Andrea J. Ray, Virginia Murray, Sukaina Bharwani, Dave MacLeod, Rachel James, Lora Fleming, Andrew P. Morse, Bernd Eggen, Richard Graham, Erik Kjellström, Emily Becker, Kathleen V. Pegion, Neil J. Holbrook, Darryn McEvoy, Michael Depledge, Sarah Perkins-Kirkpatrick, Timothy J. Brown, Roger Street, Lindsey Jones, Tomas A. Remenyi, Indi Hodgson-Johnston, Carlo Buontempo, Rob Lamb, Holger Meinke, Berit Arheimer, and Stephen E. Zebiak. Potential applications of subseasonal-to-seasonal (S2S) predictions. *Meteorol. Appl.*, 24:315–325, 2017. ISSN 1469-8080. doi: 10.1002/met.1654.

Douglas Wiens, Peter D. Bromirski, R. C. Aster, Ralph A. Stephen, Peter Gerstoft, and A. Nyblade. Collaborative Research: Dynamic Response of the Ross Ice Shelf to Wave-Induced Vibrations

and Collaborative Research: Mantle Structure and Dynamics of the Ross Sea from a Passive Seismic Deployment on the Ross Ice Shelf. 2014. doi: 10.7914/sn/xh_2014.

G. Williams, T. Maksym, J. Wilkinson, C. Kunz, C. Murphy, P. Kimball, and H. Singh. Thick and deformed Antarctic sea ice mapped with autonomous underwater vehicles. *Nature Geosci*, 8: 61–67, January 2015. ISSN 1752-0908. doi: 10.1038/ngeo2299.

B.W. Wilson. Origin and effects of long period wave in ports. *Proc 19th Int Navig Cong Sect II Commun I*, pages 13–61, 1957.

Y Xiang, D. Y Sun, W Fan, and X. G Gong. Generalized simulated annealing algorithm and its application to the Thomson model. *Physics Letters A*, 233:216–220, August 1997. ISSN 0375-9601. doi: 10.1016/S0375-9601(97)00474-X.

J.-H. Xie and J. Vanneste. A generalised-Lagrangian-mean model of the interactions between near-inertial waves and mean flow. *J. Fluid Mech.*, 774:143–169, July 2015. ISSN 0022-1120, 1469-7645. doi: 10.1017/jfm.2015.251.

Masafumi Yagi and Kunio Kutsuwada. Validation of different global data sets for sea surface wind-stress. *Int. J. Remote Sens.*, 41:6022–6049, August 2020. ISSN 0143-1161. doi: 10.1080/01431161.2020.1714784.

I. R. Young, S. Hasselmann, and K. Hasselmann. Computations of the Response of a Wave Spectrum to a Sudden Change in Wind Direction. *J. Phys. Oceanogr.*, 17:1317–1338, September 1987. ISSN 0022-3670. doi: 10.1175/1520-0485(1987)017<1317:COTROA>2.0.CO;2.

V. E. Zakharov. Energy balance in a wind-driven sea. *Phys. Scr.*, T142:014052, December 2010. ISSN 1402-4896. doi: 10.1088/0031-8949/2010/T142/014052.

V. E. Zakharov and S. I. Badulin. On energy balance in wind-driven seas. *Dokl. Earth Sc.*, 440: 1440–1444, October 2011. ISSN 1531-8354. doi: 10.1134/S1028334X11100175.

Vladimir E. Zakharov, Sergei I. Badulin, Vladimir V. Geogjaev, and Andrey N. Pushkarev. Weak-Turbulent Theory of Wind-Driven Sea. *Earth Space Sci.*, 6:540–556, 2019. ISSN 2333-5084. doi: 10.1029/2018EA000471.

Giuseppe Zappa, Len C. Shaffrey, and Kevin I. Hodges. The Ability of CMIP5 Models to Simulate North Atlantic Extratropical Cyclones. *J. Climate*, 26:5379–5396, February 2013. ISSN 0894-8755. doi: 10.1175/JCLI-D-12-00501.1.

Zhongshui Zou, Shuiqing Li, Jian Huang, Peiliang Li, Jinbao Song, Jun A. Zhang, and Zhanhong Wan. Atmospheric Boundary Layer Turbulence in the Presence of Swell: Turbulent Kinetic Energy Budget, Monin–Obukhov Similarity Theory, and Inertial Dissipation Method. *J. Phys. Oceanogr.*, 50:1213–1225, May 2020. ISSN 0022-3670. doi: 10.1175/JPO-D-19-0136.1.